Prognostic significance and functional activity of voltage-gated sodium channels in breast cancer

Theresa Leslie

PhD

University of York

Biology

March 2022

Abstract

Voltage gated sodium channels (VGSCs), specifically the cardiac isoform $Na_v1.5$, have previously been shown to increase invasion and metastasis in breast cancer. In this thesis, results from immunohistochemical analysis of 1480 breast tumours showed that $Na_v1.5$ expression correlates with worse prognosis, increased metastasis and higher grade and stage cancer. Breast cancer tissue from patients and primary breast cancer cells were assessed using patch clamp recording for the presence of Na^+ currents through VGSCs and some cells showed small inward currents consistent with VGSCs.

VGSCs have previously been shown to increase cancer cell invasion through increased H^+ efflux from cancer cells through the Na^+/H^+ exchanger NHE1. This acidifies the extracellular fluid, thereby aiding enzymes which degrade the extracellular matrix. In this project, the mechanism by which VGSCs increase H^+ efflux was investigated and evidence is presented suggesting that VGSCs increase the rate of glycolysis and therefore H^+ production, via increasing activity of the Na^+/K^+ ATPase. Gene expression changes dependent on VGSCs in breast cancer were explored in an RNAseq analysis of $Na_v1.5$ knock-down in MDA-MB-231 xenograft tumours. As well as downregulation of invasion- and migration-related genes with $Na_v1.5$ knock-down, there were changes related to pH control, Ca^{2+} signalling and immune function. Gene set enrichment analysis revealed that the differentially expressed genes were important in cancer.

Previously an antiepileptic drug and VGSC inhibitor, phenytoin was shown to slow breast tumour growth and metastasis in MDA-MB-231 xenograft tumours. This project assessed a newer antiepileptic VGSC inhibitor with an improved safety profile, eslicarbazepine acetate. This drug inhibited transient and persistent Na^+ current through $Na_v1.5$ so it could be used *in vivo* to assess its activity against breast cancer.

In conclusion, evidence is presented confirming the prognostic significance of VGSCs in breast cancer and showing new insight into the mechanism by which VGSCs increase metastasis.

List of contents

List of tables

List of figures

Acknowledgements

I would like to thank my supervisor, Will Brackenbury for being open-minded enough to allow a vet into the lab. He has introduced me to a fascinating and worthwhile field, and a diverse array of projects, and helped me a great deal to develop as a researcher. I would also like to thank my second supervisor Sangeeta Chawla for her cheerfulness, wisdom and perspective. Also, Miles Whittington, whom we have sadly lost, provided essential support, allowing me to develop a new recording technique. I was lucky to have a brilliant colleague Andy James who shared his optimism, scientific ideas and game recommendations. Many others have helped me in the Department, including John Davey who did an amazing job of educating me about bioinformatics, Andrew Leech who was always willing to share his knowledge, and Peter O'Toole who gave useful advice on microscopy and swimming!

Michaela Nelson, Ming Yang and Alex Haworth were excellent lab mates. I thank Ming for teaching me how to patch clamp, and Michaela and Alex for their general good humour and kindness. I also met some other lovely PhD students, Jack Munns, Iulia Gherman and Lotte van Beek. I'm very grateful to my buddy Eleanor Drinkwater for getting me out of the lab occasionally to hunt for woodlice and to my musical collaborator and good friend John Armstrong who helped to keep me sane and realise that there was more to life than work.

Lastly I am so grateful to my husband Dave who was extremely supportive with the whole idea of doing a PhD, and endured my frustrations with remarkable good grace. Also Emma is a wonderful friend who supported me wholeheartedly and lifted my spirits despite being unwell, and my dear parents who moved back to Nova Scotia at the start of a pandemic but survived and continued to provide listening ears and occasional advice. I couldn't have got through the PhD without my marvellous family.

Declaration

Three publications have so far arisen from this thesis:

1. Leslie TK, James AD, Zaccagna F, Grist JT, Deen S, Kennerley A, Riemer F, Kaggie JD, Gallagher FA, Gilbert FJ & Brackenbury WJ. (2019). Sodium homeostasis in the tumour microenvironment. Biochim Biophys Acta Rev Cancer 1872, 188304.

https://www.sciencedirect.com/science/article/pii/S0304419X19300629?via%3Dihub

2. Leslie TK, Brückner L, Chawla S & Brackenbury WJ. (2020). Inhibitory Effect of Eslicarbazepine Acetate and S-Licarbazepine on $Na_v1.5$ channels. Front Pharmacol 11, 555047.

https://www.frontiersin.org/articles/10.3389/fphar.2020.555047/full

3. James AD, Leslie TK, Kaggie JD, Wiggins L, Patten L, O'Duinn JM, Langer S, Labarthe M-C, Riemer F, Baxter G, McLean MA, Gilbert FJ, Kennerley AJ & Brackenbury WJ. (2022). Sodium accumulation in breast cancer predicts malignancy and treatment response. Br. J. Cancer

https://www.nature.com/articles/s41416-022-01802-w

I declare that this thesis is a presentation of original work and I am the sole author. This work has not previously been presented for an award at this, or any other, University. All sources are acknowledged as references.

1 Introduction

Breast cancer is the leading cause of cancer-related deaths in women worldwide (Bray *et al.*, 2004; Schnitt, 2014; Bray *et al.*, 2018) and most deaths are due to metastasis, which commonly occurs in the lung, pleura, bone, liver and brain (Weigelt *et al.*, 2005). Around 20-30% of patients with primary breast cancer will go onto develop distant metastasis and once this has occurred the average survival time is 2-3 years despite treatment (Cardoso *et al.*, 2012). Treatment of oestrogen-receptor (ER) and human epidermal growth factor receptor (HER2) positive tumours has improved with the development of medications targeting these receptors but triple-negative breast cancer remains difficult to treat. This type of breast cancer has no specific treatments and even with local therapy and cytostatic CDK4/6 inhibitor therapies or cytotoxic chemotherapy the survival rate is reduced in comparison with other types of breast cancer (Li *et al.*, 2017). Clearly, there is a great need for improved treatments for triple-negative breast cancer in particular, and prevention of metastasis in all types of breast cancer.

1.1 Voltage-gated sodium channel α subunits

Voltage-gated sodium channels (VGSCs) consist of one pore-forming α subunit and one or more β subunits. Several α subunits have been discovered to be aberrantly expressed in many types of epithelial cancers (carcinomas), including breast cancer (Roger *et al.*, 2003). These channels are normally found in electrically excitable cells such as neurons and myocytes where they are responsible for initiating and propagating action potentials (Hille, 2001). When they open in response to depolarisation of the cell membrane potential (V_m), they allow fast entry of Na^+ ions into the cell, further depolarising the V_m. The pore-forming α subunit is a ~270 kD protein with four homologous domains, each containing six transmembrane α helices (Figure 1.1 A) (Noda *et al.*, 1984). There are nine isoforms of the α subunit, $Na_v1.1$-1.5, encoded by the genes *SCN1A*- *SCN5A* and $Na_v1.6$-1.9 encoded by

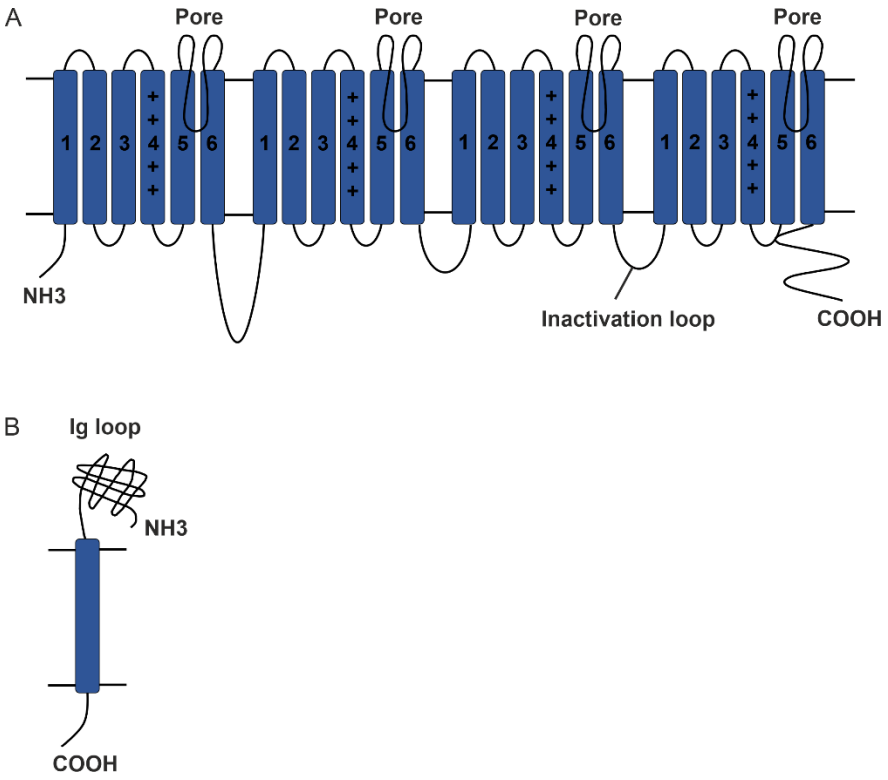

Figure 1.1 Structure of VGSC α and β subunits.
The upper surface indicates the extracellular side of the plasma membrane. **A**. VGSC α subunits contain four homologous domains, each of which contains six transmembrane segments. The ion pore is formed by a loop between segments 5 and 6 of each domain, and the voltage sensor (segment 4) can move towards and away from the extracellular side of the membrane. The inactivation loop is formed by the amino acids between domains 3 and 4. **B**. β subunits have a single transmembrane segment, an extracellular Ig loop and a small intracellular C terminus.

SCN8A- SCN11A with specific tissue distribution (Savio-Galimberti *et al.*, 2012). $Na_v1.1$-1.3 and 1.6 are primarily found in the central nervous system (CNS), $Na_v1.4$ is the skeletal muscle isoform, $Na_v1.5$ is the cardiac isoform but is also present in CNS and peripheral nervous system (PNS), and $Na_v1.7$-1.9 are primarily found in the PNS (Wang *et al.*, 2017). The isoforms are commonly classified into those relatively sensitive to tetrodotoxin (TTX) ($Na_v1.1$- $Na_v1.4$ and $Na_v1.6$) and those relatively resistant to it ($Na_v1.5$, $Na_v1.8$ and $Na_v1.9$) (Savio-Galimberti *et al.*, 2012).

The ion-conducting selectivity filter is made up of the 5th and 6th transmembrane segments of each domain with a re-entrant loop between these segments which forms the outer part of the pore. This structure was predicted by molecular modelling (Guy & Seetharamulu, 1986) and visualised for the first time by crystallographic analysis of a bacterial Na_v channel (Payandeh *et al.*, 2011). The voltage sensor is made of up the 4th segment from each domain (Guy & Seetharamulu, 1986; Yarov-Yarovoy *et al.*, 2006). This moves across the membrane upon depolarisation of the V_m and drags segments 1-3 around it, pulling the channel into the open state. After 1-2 ms, channel opening is followed by fast inactivation as the intracellular inactivation loop, located between domains III and IV comes in to "block" the channel (Armstrong & Bezanilla, 1977; Bezanilla & Armstrong, 1977; Vassilev *et al.*, 1988). Recent crystallographic analysis of human $Na_v1.4$ shows that the inactivation loop acts allosterically to cause channel blockage (Pan *et al.*, 2018). While VGSCs are inactivated in this way, the passage of ions is blocked. A second mode of inactivation in VGSCs is slow inactivation (Rudy, 1978). This takes place hundreds of milliseconds after the channel opens and is not yet well understood, although it appears to involve changes to the pore conformation (Vilin & Ruben, 2001). In a small percentage of channel opening events, there is failure of the fast inactivation gate to close, allowing a "persistent" Na^+ current through a small percentage of channels. This persistent current is typically 1-3% the size of the transient current across the whole cell membrane (Alzheimer *et al.*, 1993; Eijkelkamp *et al.*, 2012). Since there are no sudden changes in V_m in non-electrically excitable cells such as breast cancer cells, transient

whole-cell Na^+ currents are unlikely to occur but due to the probabilistic intermittent opening of voltage-gated channels, some channels do open at the resting V_m, and since a small percentage of these channels fail to inactivate, breast cancer cells do experience a persistent Na^+ current through their VGSCs (Roger *et al.*, 2007; Driffort *et al.*, 2014).

1.1.1 Protein interactions with α subunits

There is evidence that VGSC α subunits interact with the cytoskeleton, as they are recruited and regulated by ankyrin G to the axon initial segment in neurons (Srinivasan *et al.*, 1988; McEwen *et al.*, 2004; Shirahata *et al.*, 2006). Ankyrin G also recruits many other proteins including β IV spectrin which interacts with actin, a major component of the cytoskeleton (Zhou *et al.*, 1998; Jenkins & Bennett, 2001). At the nodes of Ranvier in myelinated axons, ankyrin interacts with Nr-CAM and neurofascin to recruit VGSCs (Lustig *et al.*, 2001). In cardiomyocytes, the gap junctional protein connexin 43 is required for $Na_v1.5$ localisation to the intercalated disc, probably through interaction with the plus-end of microtubules (Agullo-Pascual *et al.*, 2014). Since the cardiac isoform $Na_v1.5$ clusters in caveolae in cardiomyocytes (Yarbrough *et al.*, 2002) and in breast cancer cells (Brisson *et al.*, 2011) and the sensory neuronal isoform $Na_v1.8$ is associated with lipid rafts (Pristerà *et al.*, 2012), there may be other direct interactions of α subunits with proteins.

1.1.2 Regulation of VGSC activity in cancer cells

1.1.2.1 Splicing

Alternative splicing of the *SCN5A* gene leads to expression of the neonatal variant of $Na_v1.5$ in MDA-MB-231 breast cancer cells (Fraser *et al.*, 2005) and colon cancer cells (Guzel *et al.*, 2018). The regulation of splicing is not fully understood but it may involve cAMP signalling and activity dependence (Fraser *et al.*, 2014). This feature of neonatal splice variants appearing in cancer cells is consistent with the theory that cancer cells revert to an embryonic-like phenotype, with increased proliferative and invasive potential (Monk & Holding, 2001).

1.1.2.2 Autoregulation

In excitable tissues VGSC activity normally leads to negative feedback at the translational level, resulting in lower density of VGSCs on the cell membrane (Klein *et al.*, 2003; Shiraishi *et al.*, 2003). In prostate and breast cancer cell lines, activity in these channels instead leads to positive feedback (Brackenbury & Djamgoz, 2006; Chioni *et al.*, 2010). The authors showed that this occurs via cAMP-dependent activation of protein kinase A (PKA) which leads to transcriptional upregulation of $Na_v1.7$ in prostate cancer and $Na_v1.5$ in breast cancer, and an increase in trafficking of these α subunits to the cell membrane. This same cAMP/PKA pathway upregulates trafficking of $Na_v1.5$ to the cell membrane in cardiomyocytes upon beta-adrenergic stimulation (Ono *et al.*, 1993), and may be responsible for the inhibition of VGSCs by the beta-blocker propranolol (Lee *et al.*, 2019a).

1.1.2.3 Steroid hormone regulation

Commonly hormone-sensitive cancers such as prostate and breast cancer become hormone-insensitive as they become more aggressive (Fujita & Nonomura, 2019; Zattarin *et al.*, 2020). The oestrogen receptor ERα appears to have a negative association with VGSC expression. Some circumstantial evidence for this comes from the low expression of VGSCs in the ERα-positive cell line MCF7, and high expression of VGSCs in the ERα-negative cell line MDA-MB-231 cells (Fraser *et al.*, 2005). When ERα was upregulated in MDA-MB-231 cells, the expression of $Na_v1.5$ was reduced, and when ERα was inhibited pharmacologically, the expression of $Na_v1.5$ was increased (Özerlat, 2009). Also, silencing the ERα in MCF7 cells induced a VGSC Na^+ current (Mohammed *et al.*, 2016). Similarly in dorsal root ganglion neurons, ERα expression and the presence of oestrogen decreased expression of many isoforms of VGSC (Hu *et al.*, 2012). The effect of stimulation of the cell membrane ERβ receptors is currently less clear but it appears to have the opposite effect of ERα, in that it increases VGSC currents in MDA-MB-231 cells (Fraser *et al.*, 2010). Like the positive feedback of VGSC activity on VGSC expression in cancer cells, this system acts through PKA activation.

Androgen receptors (AR) appear to have a similar relationship to VGSCs in prostate cancer cells as ERα does in breast cancer cells, in that AR expression and stimulation reduces VGSC current. Less is known in the case of AR, however and the story is not completely clear (Fraser *et al.*, 2014). The effect of progesterone on VGSC activity is also unclear but a study in neuroblastoma cells has indicated that there may be a negative association between progesterone and VGSC current (Barann *et al.*, 1999). Glucocorticoids can inhibit $Na_v1.5$ current in oocytes through activation of the serum- and glucocorticoid-inducible kinase (SGK1) (Boehmer *et al.*, 2003).

1.1.2.4 Growth factor regulation

Epidermal growth factor (EGF) upregulates $Na_v1.7$ and thereby increases motility and invasion in prostate cancer cells (Ding *et al.*, 2008). Similarly in non-small cell lung cancer cells, EGF has been shown to increase invasiveness largely through upregulation of $Na_v1.7$ (Campbell *et al.*, 2013). Nerve growth factor (NGF) also increases $Na_v1.7$ and invasion in prostate cancer cells in a mechanism involving PKA (Brackenbury & Djamgoz, 2007).

Vascular endothelial growth factor (VEGF), which drives angiogenesis, has a less clear relationship with VGSCs. In cervical cancer cells VEGF increases $Na_v1.6$ expression via p38 mitogen-activated protein kinase (MAPK) signalling. In neurons however, VEGF can either upregulate or downregulate VGSC expression depending on the type of neuron (Fraser *et al.*, 2014).

1.1.2.5 Other regulatory protein interactions

Calmodulin (CaM) has been shown to interact with the intracellular C-terminus of all human VGSC α-subunits (Abriel & Kass, 2005) but the effect of Ca^{2+}-bound CaM on $Na_v1.5$ is not clear. CaM binding to $Na_v1.5$ may stabilise the inactivated state of the channel by interfering with interactions between the inactivation gate (located in the domain III-domain IV linker) and the C-terminus (Kim *et al.*, 2004; Motoike *et al.*, 2004; Abriel & Kass, 2005). This

mechanism gives a way in which intracellular Ca^{2+} could regulate $Na_v1.5$ activity. A related mechanism is seen in rat cardiomyocytes, where the Ca^{2+}/CaM dependent protein kinase II (CAMKII) immunoprecipitates with $Na_v1.5$. In these cells inhibition of CAMKII reduces $Na_v1.5$ current (Yoon *et al.*, 2009). Similarly in neurons, CAMKII increases both transient and persistent current through $Na_v1.6$ (Zybura *et al.*, 2020).

Like many proteins, $Na_v1.5$ can be ubiquitinated which leads to trafficking into lysosomes and degradation of the protein. The PPxY protein domain required for Nedd4-2 E3 ubiquitinase activity is located on the C-terminal part of $Na_v1.5$ (Abriel & Kass, 2005). Binding of Nedd4-2 to this domain of $Na_v1.5$ reduced VGSC currents at the cell membrane in cardiac myocytes (van Bemmelen *et al.*, 2004).

The sigma-1 receptor is upregulated in breast cancer cells, and it forms a complex with $Na_v1.5$ in these cells (Balasuriya *et al.*, 2012). Sigma-1 receptor activity increases plasma membrane expression of $Na_v1.5$, (Aydar *et al.*, 2016), so this is a potential mechanism for increased $Na_v1.5$ activity in breast cancer cells. Similarly, salt-inducible kinase-1 (SIK1) acts as a tumour suppressor (Selvik *et al.*, 2014). Its canonical function is to detect increases in intracellular Na^+ concentration ($[Na^+]_i$) and increase the activity of the Na^+/K^+ ATPase (NKA) to reduce $[Na^+]_i$ (Sjöström *et al.*, 2007). SIK1 is downregulated in breast cancer, and knock-down of SIK1 in breast cancer cells promotes $Na_v1.5$ expression and $Na_v1.5$-dependent invasion and EMT (Gradek *et al.*, 2019). SIK1 downregulation is therefore another potential mechanism which increases $Na_v1.5$ activity in breast cancer.

In cardiomyocytes, $Na_v1.5$ forms a multiprotein complex with dystrophin and syntrophin, and dystrophin deficient mice have decreased total $Na_v1.5$ and plasma membrane VGSC current in their cardiomyocytes (Gavillet *et al.*, 2006). Also in cardiomyocytes, the gap junctional protein connexin 43 (Cx43) forms a complex with $Na_v1.5$ (Rhett *et al.*, 2012). This interaction leads to recruitment of $Na_v1.5$ to the intercalated disc (Agullo-Pascual *et al.*,

2014). It is not known whether a similar interaction between $Na_v1.5$ and Cx43 occurs in cancer cells. In breast cancer cells, Cx43 acts as a tumour suppressor, reducing proliferation and invasive behaviour at least partly by reducing nuclear localisation of β-catenin (Talhouk *et al.*, 2013). High Cx43 expression also correlates with longer relapse-free survival in breast cancer patients (Teleki *et al.*, 2014).

1.2 Voltage-gated sodium channel β subunits

VGSC α subunits can form functional channels on their own, but they may be linked one or two β subunits. The β subunits β1-4 encoded by the genes *SCN1B* to *SCN4B* are much smaller proteins of ~35 kD with a small intracellular domain, a single transmembrane domain and a large extracellular domain containing an immunoglobulin (Ig) loop (Brackenbury & Isom, 2011) (Figure 1.1 B). The exception to this is the splice variant of β1, β1B, which has no transmembrane domain and is therefore a secreted molecule (Kazen-Gillespie *et al.*, 2000). Each α subunit may be linked to one of either β2 or β4 via a covalent interaction with the Ig loop, and one of β1 or β3 via non-covalent interactions (Isom *et al.*, 1992). These non-covalent interactions require both the intracellular C-terminals (Meadows *et al.*, 2001) and the extracellular Ig domains (McCormick *et al.*, 1998).

The canonical function of β-subunits is to modulate the activity of the α-subunits. They can do this by altering expression and trafficking of α-subunits to the cell membrane (Brackenbury & Isom, 2011). These effects are α-subunit and cell-type specific. There is substantial evidence for certain β-subunits increasing α-subunit expression at the cell membrane. Co-expression of β1 with $Na_v1.2$ increases $Na_v1.2$ density at the plasma membrane in glial cells and neurons (McEwen *et al.*, 2004). Similarly, both β1 and β3 increase plasma membrane expression of $Na_v1.7$ in human embryonic kidney (HEK-293) cells (Laedermann *et al.*, 2013). In cancer cells, β1 appears to have a variable effect on α-subunit transcription. In MCF7 breast cancer cells, β1 downregulation using siRNA increased $Na_v1.5$ expression (Chioni *et al.*, 2009) and in A549 non-small cell lung cancer

cells β1 downregulation enhanced TTX-sensitive invasion (Campbell *et al.*, 2013). Conversely, overexpressing β1 reduced invasion H460 non-small cell lung cancer cells (Campbell *et al.*, 2013). In MDA-MB-231 breast cancer cells however, overexpressing β1 reduced migration but it *in*creased the VGSC current as occurred in HEK-293 cells (Chioni *et al.*, 2009). Clearly the relationship between β1 and α-subunit expression is complex.

Like β1, β2 also appears to be important in trafficking α-subunits to the plasma membrane. β2 increases expression of the TTX sensitive isoform $Na_v1.7$ at the plasma membrane of dorsal root ganglion neurons, but does not change TTX-resistant Na^+ current (Lopez-Santiago *et al.*, 2006) and β2 increases expression of $Na_v1.5$ at the cell membrane in ventricular cardiomyocytes without changing the total amount of $Na_v1.5$ protein (Bao *et al.*, 2016). However, in neuroblastoma cells, β2 was found to increase transcription of $Na_v1.1$, so it does not just affect trafficking of α-subunits (Kim *et al.*, 2007a). More recently, the intracellular domain of β1 (β1-ICD), after sequential cleavage of β1 by BACE1 then γ secretase, was shown to concentrate in the nucleus where it leads to transcriptional changes. β1-ICD acts as a transcriptional repressor in cardiomyocytes and Chinese hamster lung (CHL) cells (Bouza *et al.*, 2021). This same study also assessed the effect of overexpressing the β1 intracellular domain in CHL and HEK cells stably expressing $Na_v1.5$ cells. The β1 intracellular domain did not induce VGSC currents in CHL cells, nor did it alter VGSC current or gating in HEK-$Na_v1.5$ cells. Concentration of β1-ICD in the nucleus was also shown to occur in MDA-MB-231 cells, but unlike in CHL and HEK-$Na_v1.5$ cells, in MDA-MB-231 cells expression of the β1-ICD was shown to be necessary and sufficient to induce a TTX-sensitive VGSC current (Haworth *et al.*, 2021).

As well as regulating expression of α-subunits, β subunits can affect the kinetics and voltage-dependence of the α-subunits. Early studies co-expressing β1 and β2 with $Na_v1.2$ showed that these β subunits accelerated VGSC fast inactivation and caused inactivation to occur at more negative voltages in oocytes (Isom *et al.*, 1992; Isom *et al.*, 1995a). In

contrast, β3 caused fast inactivation of $Na_v1.3$ to occur at more positive voltages in HEK-293 cells (Cusdin *et al.*, 2010). β4 increases the ability of neurons to fire rapidly by causing a highly reversible open channel block, and by slowing inactivation (Grieco *et al.*, 2005). It acts antagonistically to β1 in regulating excitability, since β1 reduces excitability by enhancing inactivation.

The extracellular Ig domain gives β subunits their ability to act as cell adhesion molecules (CAMs) (Srinivasan *et al.*, 1998; Malhotra *et al.*, 2000; Ratcliffe *et al.*, 2001). They can bind to β subunits on adjacent cells (*trans*-homophilic interactions) but can also form *trans*-heterophilic interactions with other CAMs. For example, β1 can bind to β2, contactin-1, N-cadherin, Nr-CAM, and the extracellular matrix (ECM) proteins tenascin-C and tenascin-R (Srinivasan *et al.*, 1998; Xiao *et al.*, 1999; Kazarinova-Noyes *et al.*, 2001; Malhotra *et al.*, 2004; McEwen & Isom, 2004).

Another function of β subunits is intracellular signalling. Like the α subunits, β1 and β2 interact with the cytoskeleton by recruiting ankyrin to points of cell-cell contact (Malhotra *et al.*, 2000). In neurons, this is important for formation of the axon-initial segment and the nodes of Ranvier, areas with a high concentration of VGSCs. Additionally, β1 homophilic interaction via fyn kinase leads to neurite outgrowth in cerebellar granule neurons, aiding in pathfinding and development (Brackenbury *et al.*, 2008; Brackenbury *et al.*, 2010).

1.3 Evidence for functional VGSC expression in cancer

In the earliest studies of VGSCs in cancer, a TTX-sensitive VGSC current was found in small-cell lung cancer cell lines (Pancrazio *et al.*, 1989), and in thymoma cells (Marx *et al.*, 1991). In 1995, the presence of VGSCs was found in two prostate cancer cell lines (Grimes *et al.*, 1995), where inhibition of the VGSC currents with TTX was found to decrease *in vitro* invasive behaviour. Since then, VGSC currents have been found in ovarian (Gao *et al.*, 2010), colon (House *et al.*, 2010), melanoma (Allen *et al.*, 1997), neuroblastoma (Ou *et al.*,

2005), cervical (Diaz *et al.*, 2007; Hernandez-Plata *et al.*, 2012), and breast cancer (Roger *et al.*, 2003). VGSC currents have also been found in non-epithelial cancers: glioma (Schrey *et al.*, 2002) and leukaemia (Yamashita *et al.*, 1987; Fraser *et al.*, 2004). Specific carcinomas express different VGSC α subunits (Table 1.1). In breast cancer and ovarian cancer $Na_v1.5$ is most common (specifically the neonatal splice variant in the case of breast cancer) (Fraser *et al.*, 2005; Gao *et al.*, 2010). $Na_v1.7$ is predominant in prostate cancer (Diss *et al.*, 2005) and $Na_v1.6$ and to a lesser extent $Na_v1.7$ are most prevalent in cervical cancer (Hernandez-Plata *et al.*, 2012). Interestingly, the location of the α subunits is cytoplasmic as well as at the plasma membrane in cervical cancer biopsies, whereas it is only at the plasma membrane in non-cancer biopsies (Hernandez-Plata *et al.*, 2012). Cytoplasmic expression of $Na_v1.5$ is also seen in breast cancer (Nelson *et al.*, 2015a). Many non-cancer cells show large pools of cytoplasmic VGSC expression however, so this may not be a cancer-specific intracellular location (Bao, 2015). It is possible that the α subunits function on intracellular membranes since in macrophages, expression of $Na_v1.5$ in the late endosome increases its acidification, allowing greater phagocytic ability (Carrithers *et al.*, 2007).

Expression of VGSC α-subunits correlates with metastatic ability in breast cancer cell lines (Roger *et al.*, 2003; Fraser *et al.*, 2005) and prostate cancer cell lines (Grimes *et al.*, 1995; Bennett *et al.*, 2004). This pattern extends to patients as VGSC expression correlates positively with cancer in prostate biopsies (Diss *et al.*, 2005), colon biopsies (House *et al.*, 2010) and ovarian biopsies (Gao *et al.*, 2010) and with worse prognosis in breast cancer patients (Yang *et al.*, 2012). Specifically, in breast cancer, *SCN5A* mRNA coding for the $Na_v1.5$ α subunit correlates with increased incidence of metastasis, recurrence and decreased 5-year survival (Fraser *et al.*, 2005).

VGSC β subunit expression is also altered in cancer (Table 1.1), although the situation is less clear than with α subunits. In normal cervix and cervical cancer tissue β1 is the most abundant β subunit at the mRNA level, and β2 and β4 are downregulated in cervical cancer

(Hernandez-Plata *et al.*, 2012; Sanchez-Sandoval & Gomora, 2019). Similarly, in breast cancer cell lines β1 is the most abundant β subunit at the mRNA level (Chioni *et al.*, 2009), and in breast cancer, as in cervical cancer, β4 is downregulated (Bon *et al.*, 2016). β1 is also the most abundant β subunit in prostate cancer cell lines (Diss *et al.*, 2008). β1 expression is positively associated with metastatic potential in prostate cancer cell lines, but not in breast cancer cell lines (Diss *et al.*, 2008; Chioni *et al.*, 2009; Nelson *et al.*, 2014). In patient breast tissue, however, β1 protein expression was higher in breast cancer vs normal breast (Nelson *et al.*, 2014).

Table 1.1 VGSC subunits expressed in cancer, from (Brackenbury, 2012)

α-subunits of VGSCs		
Protein	**Cancer types**	**References**
$Na_v1.1$	Ovarian	(Gao *et al.*, 2010)
$Na_v1.2$	Cervical, mesothelioma, ovarian, prostate	(Diss *et al.*, 2001; Fulgenzi *et al.*, 2006; Diaz *et al.*, 2007; Gao *et al.*, 2010)
$Na_v1.3$	Ovarian, prostate, small cell lung cancer	(Diss *et al.*, 2001; Onganer & Djamgoz, 2005; Gao *et al.*, 2010)
$Na_v1.4$	Cervical, ovarian, prostate	(Diss *et al.*, 1998; Diaz *et al.*, 2007; Gao *et al.*, 2010)
$Na_v1.5$	Breast*, colon*, lymphoma*, neuroblastoma*, non-small cell lung cancer, ovarian, small cell lung cancer	(Fraser *et al.*, 2004; Fraser *et al.*, 2005; Onganer & Djamgoz, 2005; Ou *et al.*, 2005; Roger *et al.*, 2007; Gao *et al.*, 2010; House *et al.*, 2010)
$Na_v1.6$	Breast, cervical, lymphoma, melanoma, mesothelioma, non-small cell lung cancer, prostate, small cell lung cancer	(Diss *et al.*, 2001; Fraser *et al.*, 2004; Fraser *et al.*, 2005; Onganer & Djamgoz, 2005; Fulgenzi *et al.*, 2006; Diaz *et al.*, 2007; Roger *et al.*, 2007; Hernandez-Plata *et al.*, 2012)
$Na_v1.7$	Breast, cervical, lymphoma, mesothelioma, non-small cell lung cancer, ovarian, prostate*	(Diss *et al.*, 2001; Fraser *et al.*, 2004; Fraser *et al.*, 2005; Fulgenzi *et al.*, 2006; Diaz *et al.*, 2007; Roger *et al.*, 2007; Gao *et al.*, 2010)
$Na_v1.8$	—	
$Na_v1.9$	Lymphoma, small-cell lung cancer	(Fraser *et al.*, 2004; Onganer & Djamgoz, 2005)
β-subunits of VGSCs		
β1	Breast*, cervical*, non-small cell lung cancer, prostate*	(Roger *et al.*, 2007; Diss *et al.*, 2008; Chioni *et al.*, 2009; Hernandez-Plata *et al.*, 2012)
β2	Breast, cervical, non-small cell lung cancer, prostate	(Roger *et al.*, 2007; Diss *et al.*, 2008; Chioni *et al.*, 2009; Hernandez-Plata *et al.*, 2012; Jansson *et al.*, 2012)
β3	Non-small cell lung cancer, prostate	(Roger *et al.*, 2007; Diss *et al.*, 2008)
β4	Breast, cervical, non-small cell lung cancer, prostate	(Roger *et al.*, 2007; Diss *et al.*, 2008; Chioni *et al.*, 2009; Hernandez-Plata *et al.*, 2012; Jansson *et al.*, 2012)

1.4 Function of VGSCs in cancer

The first and most commonly described role of VGSCs in cancer is to increase cells' ability to invade through extracellular matrix (ECM) *in vitro* (Grimes *et al.*, 1995; Laniado *et al.*, 1997; Roger *et al.*, 2003; Bennett *et al.*, 2004; Fraser *et al.*, 2005; Brackenbury *et al.*, 2007; House *et al.*, 2010). The increase in invasive ability may explain why expression correlates with metastasis in patients as described above. It can also explain why $Na_v1.5$ expression and activity increase local invasion and metastasis in mouse xenograft breast tumours (Driffort *et al.*, 2014; Nelson *et al.*, 2015a; Nelson *et al.*, 2015b). In many cases, migration has also been linked to VGSC activity (Fraser *et al.*, 2003; Brackenbury & Djamgoz, 2006; Fulgenzi *et al.*, 2006; Chioni *et al.*, 2010; Yang *et al.*, 2020). In one study, VGSCs have been shown to increase the length of plasma membrane processes, which is likely an indicator of migration ability (Fraser *et al.*, 1999). Another cancer cell feature that is linked to VGSC activity is an elongated morphology (Brisson *et al.*, 2013; Driffort *et al.*, 2014; Nelson *et al.*, 2015b; Yang *et al.*, 2020), which is often associated with epithelial to mesenchymal transition (EMT), one of the steps required for metastasis of carcinomas. More evidence for a causative link between VGSCs and EMT was published more recently. In this, knockdown of $Na_v1.5$ expression in MDA-MB-231 cells was shown to reduce expression of the EMT marker *SNAI1* whereas overexpression of $Na_v1.5$ in MCF7 cells increased expression of the EMT markers *SNAI1* and *ZEB1*. In addition, an initiator of EMT, TGFβ1 was shown to increase $Na_v1.5$ expression (Gradek *et al.*, 2019).

VGSCs have been shown to promote proliferation in some prostate cancer cell lines (Abdul & Hoosein, 2002; Anderson *et al.*, 2003). However, the evidence for VGSC-mediated promotion of proliferation is not as strong as for promotion of invasion and migration, as many *in vitro* studies have shown no change in proliferation when VGSCs are blocked pharmacologically (Roger *et al.*, 2003; Fraser *et al.*, 2005; Gillet *et al.*, 2009; Hernandez-Plata *et al.*, 2012; Yang *et al.*, 2012; Driffort *et al.*, 2014; Nelson *et al.*, 2015a). VGSCs may also affect apoptosis: shRNA knock-down of $Na_v1.5$ in the breast cancer cell line MDA-MB-

231 reduced the number of apoptotic cells expressing activated caspase 3 in xenograft tumours but did not affect apoptosis of the same cells *in vitro* (Nelson *et al.*, 2015b). Levobupivacaine (a VGSC-inhibiting local anaesthetic) treatment of the breast cancer cell lines MCF7 and MDA MB 231 increased activated caspase 3 expression measured by western blot (Kwakye *et al.*, 2020). In a few studies VGSC activity has been linked to chemoresistance; in K562 leukaemia cells, a subset of multi-drug resistant cells were found to express VGSC currents (Yamashita *et al.*, 1987). In addition, local anaesthetics augmented the pro-apoptotic effect of chemotherapeutic drugs on an esophageal carcinoma cell line, and they also enhanced the inhibitory effect of chemotherapeutic drugs on proliferation and invasion (Zhu *et al.*, 2020).

1.5 Function of VGSC β subunits in cancer

The different VGSC β subunits have very different effects in tumours, so these will be addressed separately. The most abundant β subunit in carcinomas is β1. *In vitro*, this increases cell-cell and cell-substrate adhesion, elongates the cell, and decreases migration (Chioni *et al.*, 2009). Overexpression of β1 in MDA-MB-231 cells, which have very little endogenous β1, leads to a larger VGSC Na^+ current. This could be explained by an increase in functional $Na_v1.5$, since β1 downregulation increases levels of $Na_v1.5$ mRNA and protein (Chioni *et al.*, 2009), or it could be explained by increase in cell surface expression of $Na_v1.7$, as β1 expression has this effect in HEK293 cells (Laedermann *et al.*, 2013). Indeed, the increased Na^+ current induced by β1 in MDA-MB-231 cells was shown to be TTX-sensitive, which makes it likely that $Na_v1.7$ is the β1-induced channel (Haworth, 2019). As in cerebellar granule neurons, β1 trans-homophilic adhesion increases the length of cell membrane outgrowths in MDA-MB-231 cells (Brackenbury *et al.*, 2008). β1 trans-homophilic adhesion between MDA-MB-231 cells and fibroblasts has the same effect (Nelson *et al.*, 2014). Interestingly, in both the studies in neurons and cancer cells, β1-induced formation of cell membrane outgrowths is dependent on fyn kinase activity and Na^+

current, so α-subunits must be involved in this mechanism (Davis *et al.*, 2004; Brackenbury *et al.*, 2008; Brackenbury *et al.*, 2010).

The role of β2 in cancer has not been extensively studied. It is upregulated in the metastatic prostate cancer cell line C4-2B compared to the weakly-metastatic cell line LNCaP from which it is derived (Jansson *et al.*, 2012). Overexpression in LNCaP cells elongates the cell morphology and increases adhesion to certain substrates but not others. It also decreased the rate of tumour growth when these cells were implanted to form xenograft tumours (Jansson *et al.*, 2012).

In contrast to β1, β3 appears to be a tumour-suppressor. It is activated by p53 and induces apoptosis in response to DNA damage (Adachi *et al.*, 2004). This might explain its low expression in breast cancer and small-cell lung cancer (Roger *et al.*, 2007; Gillet *et al.*, 2009; Campbell *et al.*, 2013). β4 is another tumour suppressor. It represses invasive behaviour and is downregulated in both breast cancer and cervical cancer (Bon *et al.*, 2016; Sanchez-Sandoval & Gomora, 2019).

1.6 Potential mechanisms of VGSC-induced invasion and migration

There are several putative mechanisms by which VGSCs potentiate invasion and migration (Figure 1.3). Given that the channels have many direct protein interactions, they depolarise the cell V_m and they affect Na^+ homeostasis, this is not surprising. The following section will discuss the various mechanisms which have been experimentally confirmed.

1.6.1 Cytoskeletal reorganization and migration

VGSC expression and activity in breast cancer cells promotes cortactin phosphorylation on Y421 (Brisson *et al.*, 2013). This phosphorylation activates cortactin to act as an actin nucleation-promoting factor (Wang *et al.*, 2011b). Cortactin binds and activates the actin-related protein 2/3 (Arp2/3) complex resulting in F-actin polymerisation in a branching

pattern (MacGrath & Koleske, 2012). This is needed to form lamellipodia at the invading edge of cells, so cortactin aids cell migration in cancer (MacGrath & Koleske, 2012). Given that VGSC activity also activates src (Brisson *et al.*, 2013), and src can activate cortactin, it is likely that the effect of VGSCs on cortactin is mediated by src. In neurons β1 and $Na_v1.6$ subunits together lead to activation of the src family kinase fyn to stimulate outgrowth of neurites (Brackenbury *et al.*, 2008; Brackenbury *et al.*, 2010). A similar process occurs in breast cancer cells, resulting in increased invasion and metastasis (Nelson *et al.*, 2014). Reciprocally, src can phosphorylate $Na_v1.5$ in cardiomyocytes which depolarises the voltage dependence of inactivation (Ahern *et al.*, 2005). This would mean that src would increase $Na_v1.5$ channel availability at the resting membrane potential and likely increase the persistent Na^+ current through the channel. Given that VGSC activity can increase src activity in some cell lines and vice versa in other cell lines, there may positive feedback between these proteins.

In colon and breast cancer, VGSC activity increases the expression of several invasion-related genes that are regulated by the ERK1 and ERK2 mitogen-activated protein kinases (MAPK). These genes include VEGFC (vascular endothelial growth factor C), WNT9A, HIF1A (hypoxia-inducible factor 1α), and CD44. (House *et al.*, 2010; House *et al.*, 2015; Nelson *et al.*, 2015b). CD44 is a CAM which binds to the ECM component hyaluronan, and this binding promotes the cell's invasive ability. CD44 expression increases with VGSC activity in breast cancer cells (Nelson *et al.*, 2015b). Interestingly, CD44 activates src in ovarian cancer cells (Bourguignon *et al.*, 2001), so this could explain how VGSC activity activates src and cortactin in breast cancer cells in (Brisson *et al.*, 2013), by the pathway VGSC → CD44 → src → cortactin. CD44 interacts with a Rac1-activated protein kinase, PKN-γ, and this complex leads to cortactin activation (and Ca^{2+} mobilisation) in keratinocytes (Bourguignon *et al.*, 2004). In these cells, invasion and migration were not assessed, but cortactin activation and Ca^{2+} mobilisation led to cell adhesion and differentiation.

In summary, VGSC α-subunits and β1 subunits lead to activation of cortactin which stimulates initiation of actin polymerisation in a branching shape, important for migration. VGSCs also activate src and fyn tyrosine kinases which activate cortactin, and VGSCs also activate CD44, which in turn activates src. VGSCs may therefore be players in an interlinked network of proteins controlling actin polymerisation, as well as a gene network controlling invasion.

1.6.2 V_m depolarisation

1.6.2.1 Effect of V_m on proliferation

The classical function of VGSCs is to depolarise the V_m to initiate and propagate action potentials in neurons and myocytes (Hille, 2001). Although carcinoma cells have not been demonstrated to fire action potentials, VGSC opening does lead to depolarisation of the V_m in these cells (Yang *et al.*, 2020). This is intriguing, since cancer cells and rapidly proliferating cells have relatively a depolarised V_m compared to their healthy or slowly proliferating equivalents (Figure 1.2). There is evidence that V_m could be a direct regulator of proliferation since depolarisation of the V_m in *Xenopus* embryos triggers the development of a neoplastic phenotype (Lobikin *et al.*, 2012). This may be linked to the changes in V_m that accompany the stages of the cell cycle (Sachs *et al.*, 1974), since hyperpolarising the V_m prevents DNA synthesis and mitosis (Cone, 1970) and prevents progression through the cell cycle in Chinese hamster ovary (CHO) cells (Cone & Tongier, 1971).

The mechanism by which V_m controls proliferation is not clear, but there are several possibilities. The oncogene K-ras, which increases proliferation via the MAPK pathway, increases its activity when the V_m is depolarised. This is due to reorganisation of charged phospholipids in the inner leaflet of the plasma membrane, leading to nano-clustering and therefore activation of K-ras (Zhou *et al.*, 2015). VGSC activity increases MAPK signalling in colon cancer cells (House *et al.*, 2010; House *et al.*, 2015). It is possible that VGSCs do

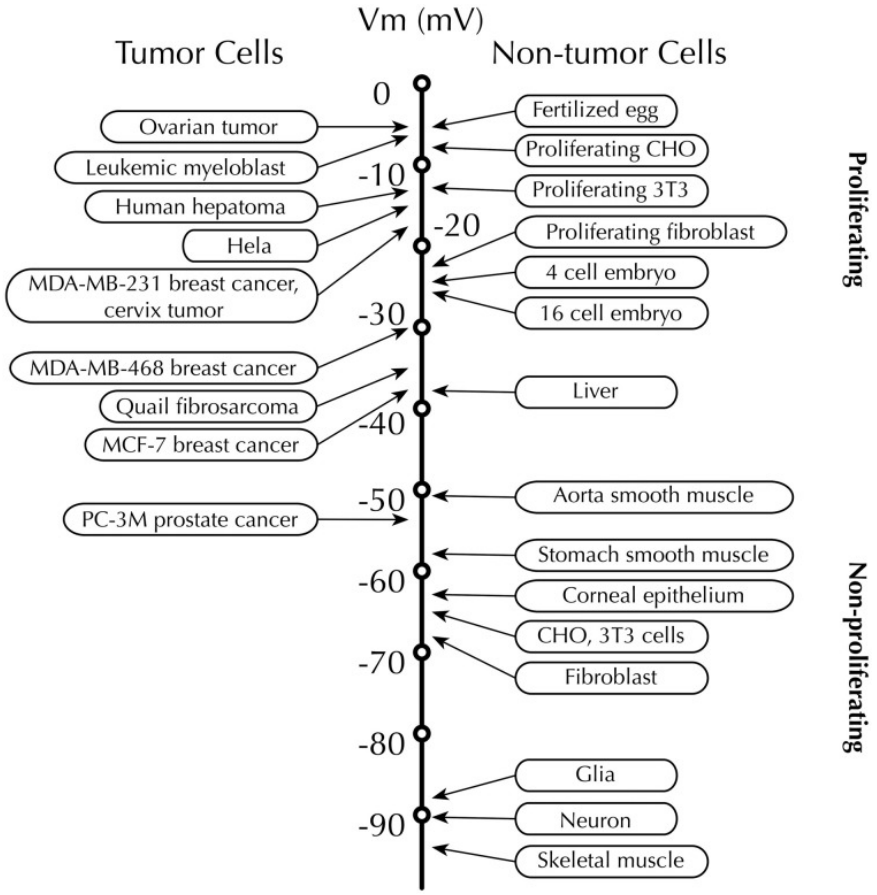

Figure 1.2 Comparison between V_m in rapidly healthy and cancer cells, and between rapidly proliferating and non-proliferating cell types.
Taken from (Yang & Brackenbury, 2013)

this at least partly via modulation of the V_m as well as the PKA/Rap1B/MEK/ERK pathway delineated in (House *et al.*, 2015).

1.6.2.2 Effect of V_m on galvanotaxis

In addition to the effect on cellular proliferation, V_m changes also regulate cell migration. Intact epithelial layers develop a potential difference across them due to the polarity of the cells (Barratt, 1976). The strength of this electric field is between 50-500 mV/mm (Mycielska & Djamgoz, 2004), and when the layer is breached, a lateral electric field is generated across the wound (du Bois-Reymond, 1843), with the negative pole in the centre of the wound (Borgens *et al.*, 1977). Interestingly, amiloride, an inhibitor of the epithelial Na^+ channel (ENaC), collapsed this electrical gradient across wounds in newts (Borgens *et al.*, 1977). The electrical field generated across wounds aids directional migration of cells to close the wound (Borgens *et al.*, 1977; Barker *et al.*, 1982). Electric field-induced wound healing is due to galvanotaxis: the motion of cells in the direction of an electric field. For example, skin-derived keratinocytes migrate towards the negative pole in electric fields similar to those found in wounds (Nishimura *et al.*, 1996). Similarly, cancer cells display galvanotaxis, although the direction of movement may depend on the metastatic ability of the cells (Mycielska & Djamgoz, 2004). Galvanotaxis of Mat-Ly-Lu prostate cancer cells was shown to be VGSC-sensitive (Djamgoz *et al.*, 2001). Galvanotaxis is controlled by several signalling mechanisms. It usually requires extracellular Ca^{2+} and total intracellular $[Ca^{2+}]$ increases when the electric field is present (Onuma & Hui, 1988). It is dependent on phosphoinositide-3-kinase (PI(3)K) signalling at the leading edge of cells, (the side towards the cathode) (Zhao *et al.*, 2006). Additionally, the small Rho guanosine triphosphatase Rac1 is required for migration towards the cathode, where it is the common downstream effect of both β4 integrin and epidermal growth factor receptor (EGFR)-induced galvanotaxis (Pullar *et al.*, 2006). Similarly, Rac1 has been shown to be important in electrically-induced migration of cancer cells. V_m depolarisation promotes migration but not invasion of MDA MB-231 cells, and V_m hyperpolarisation decreased the density of F-actin and active Rac-1 in

the leading edge of lamellipodia (Yang *et al.*, 2020). In this study, VGSC activity depolarised the V_m by around 4 mV, and this small change in V_m, when induced in a VGSC-independent manner was sufficient to increase cellular migration. In summary, cancer cells, like other epithelial cells, have the ability to migrate in a direction defined by an electric field

1.6.3 Increasing intracellular [Ca^{2+}]

Since Ca^{2+} influx is an integral feature of cell migration, it is possible that VGSCs might increase migration through regulation of Ca^{2+} dynamics. There are several ways in which Na^+ channels might do this:

1. Through direct control of Ca^{2+} influx through the Na^+/Ca^{2+} exchanger (NCX)

2. Through alteration of the V_m which regulates gating of voltage-gated Ca^{2+} channels (VGCCs) and which alters the driving force of Ca^{2+} into the cell through any Ca^{2+}-permeant channel

3. Through regulation of release of Ca^{2+} from intracellular stores

Na^+/Ca^{2+} exchange is a major mechanism for Ca^{2+} removal from cells, and this is powered by the electrochemical Na^+ gradient, where entry of 3 Na^+ ions is linked to exit of one Ca^{2+} ion (Bers & Ginsburg, 2007). Reduction of the inward Na^+ gradient through VGSC activity would be expected to reduce Ca^{2+} clearance from the cell and increase intracellular [Ca^{2+}]. There are some studies showing that reducing this Ca^{2+}-clearance function of NCX induces a cancerous phenotype. Reducing NCX expression at the cell membrane in kidney epithelial cells leads to increased [Ca^{2+}] and increased migration through Ca^{2+}/calmodulin activation of PI(3)K (Balasubramaniam *et al.*, 2015). In addition, NCX knock-down in kidney cells leads to EMT, and as expected from this, the expression of NCX is reduced in kidney tumours (Balasubramaniam *et al.*, 2017). There is even evidence for NCX1 functioning in reverse

mode (Na^+ exit and Ca^{2+} entry mode) in pancreatic cancer cells, since a specific inhibitor of reverse-mode function of NCX and knock-down of NCX1 both abrogated TGFβ-induced elevation of intracellular Ca^{2+} and migration (Dong *et al.*, 2010). Acidic intracellular pH inhibits forward action (Na^+ entry and Ca^{2+} exit) of NCX (Philipson *et al.*, 1982), which could lead to elevation of intracellular [Ca^{2+}] in severely hypoxic tumours, although most cancer cells have a slightly alkaline intracellular pH (White *et al.*, 2017).

Another Na^+/Ca^{2+} exchanger, NCLX is present on mitochondrial membranes. In melanoma and monocytic cell lines, Na^+ entry into the cytoplasm through $Na_v1.6$ leads to Na^+ entry into mitochondria, resulting in release of Ca^{2+} from mitochondria into the cytoplasm. The elevation in Ca^{2+} increases melanoma and monocyte invasiveness (Carrithers *et al.*, 2009). The VGSC-induced increase in cytosolic Ca^{2+} is likely mediated through NCLX since it is inhibited by the NCLX blocker CGP-37157 in the monocytic cell line.

The driving force for Ca^{2+} entry is larger the more negative the V_m and since VGSC activity makes the V_m less negative (Yang *et al.*, 2020), VGSCs might be expected to reduce Ca^{2+} entry through plasma membrane Ca^{2+} channels. However, VGCCs open in response to depolarisation of the V_m. Therefore, despite reducing the driving force for Ca^{2+} entry, VGSC activity might be able to increase Ca^{2+} entry by promoting opening of VGCCs. Many VGCC subtypes are downregulated at the mRNA level in breast cancer cells (Phan *et al.*, 2017), but others are upregulated in breast cancer (Wang *et al.*, 2015a), so it is possible that VGSCs could increase open probability of VGCCs to increase Ca^{2+} entry.

Release of Ca^{2+} from intracellular stores could potentially be affected by Na^+ homeostasis. In cardiomyocytes $Na_v1.5$ persistent current increases Ca^{2+}-calmodulin kinase II (CaMKII) autophosphorylation leading to CaMKII activation (Yao *et al.*, 2011). CaMKII has many oncogenic effects in cancer, for example it interacts with the MEK/ERK mitogenic pathway, increases Rac1 activation to increase migration and increases NF-κB signalling to promote

progression through the cell cycle (Wang *et al.*, 2015b). CaMKII autophosphorylation increases CaMKII phosphorylation of its many substrates including the ryanodine receptor 2 (RyR2). The result of CaMKII phosphorylation of RyR2 can either increase or decrease leak of Ca^{2+} out of the sarcoplasmic reticulum depending on the experimental conditions, (Couchonnal & Anderson, 2008). The consequences of RyR2 phosphorylation by CAMKII have not been investigated in cancer, but there is a potential for $Na_v1.5$ persistent current to affect RyR2 Ca^{2+} release from the ER in cancer via CAMKII phosphorylation of RyR2.

In contrast to Ca^{2+} entry through the plasma membrane which is often associated with increased migration, Ca^{2+} release from intracellular stores and uptake into mitochondria more often promotes apoptosis in cancer cells (Akl & Bultynck, 2013). In fact, many well-known tumour suppressors such as BRCA1 and PTEN promote ER release of Ca^{2+} via inositol triphosphate receptors (IP3Rs). Conversely, several oncogenes such as Bcl-2 and PKB/Akt suppress IP3R activity (Bultynck & Campanella, 2017). There is no direct evidence for connection of involvement of VGSCs in release of Ca^{2+} from the endoplasmic reticulum in non-excitable cells, but possible evidence for Na^+ channels promoting Ca^{2+} entry through the plasma membrane. For example, depolarisation of the V_m (an effect of VGSC activity) does not affect intracellular release of Ca^{2+} in salivary acinar cells, but it does reduce Ca^{2+} entry through the cell membrane (Zhang & Melvin, 1993).

1.6.4 Increasing intracellular [Na^+]

An influx of Na^+ may be expected to raise $[Na^+]_i$. Indeed, a small increase in $[Na^+]_i$ can be attributed to VGSCs in H460 non-small cell lung cancer cells, where blockade of VGSCs with TTX reduced $[Na^+]_i$ from 22.3 to 10.8 mM (Campbell *et al.*, 2013). TTX also reduced the $[Na^+]_i$ of MDA-MB-231 breast cancer cells from 15.6 mM to ~ 11 mM (Yang *et al.*, 2020). In another study, H460 cells had a higher $[Na^+]_i$ (15.3 mM) than the "normal" lung cell line NL-20 which does not have a detectable Na^+ current and a $[Na^+]_i$ of 7.8 mM (Roger

et al., 2007). In the first two studies above TTX also reduced invasion or migration as well as reducing $[Na^+]_i$.

An increase in $[Na^+]_i$ will have myriad effects on cancer cells including changes in V_m and plasma $[Ca^{2+}]$ (sections 1.6.2 and 1.6.3). In addition, many processes essential to nutrient import in cancer cells are powered by the inward electrochemical Na^+ gradient, for example glucose import through SGLT2 and amino acid (particularly glutamine) import through Na^+-dependent transporters such as SLC1A5. These transporters are upregulated in cancer, for example SGLT2 is upregulated in lung cancer (Ishikawa *et al.*, 2001), and SLC1A5 is upregulated in lung cancer (Hassanein *et al.*, 2013), breast cancer (van Geldermalsen *et al.*, 2016), colorectal cancer (Witte *et al.*, 2002) and glioma (Dolinska *et al.*, 2003). Importantly, two of the main pH regulatory mechanisms, the Na^+/HCO_3^- cotransporter NBCn1 and the Na^+/H^+ exchanger NHE1 are powered by the Na^+ gradient. These transporters are also upregulated and highly active in cancer cells. NBCn1 is the most important pH control mechanism in breast cancer cells at intracellular pH > 6.6, whereas NHE1 is most important at pH < 6.6 (Boedtkjer *et al.*, 2013; Lee *et al.*, 2015). NHE1 is upregulated in glioma (McLean *et al.*, 2000), head and neck squamous cell carcinoma (Kaminota *et al.*, 2017), breast cancer (Amith *et al.*, 2015) and hepatocellular carcinoma (Yang *et al.*, 2011).

An increase in $[Na^+]_i$ would reduce the inward Na^+ gradient powering these important processes. Nonetheless, all of these processes are heavily used in cancer cells which will act to deplete the Na^+ gradient further. Cancer cells maintain the inward Na^+ gradient using NKA in the plasma membrane (Section 1.6.7).

1.6.5 Na^+ entry is linked to pH dysregulation

Unlike in normal tissue where the intracellular pH is acidic (~ pH 7.2) compared to the extracellular pH (~pH 7.4), in solid tumours there is an inversion of the pH across the plasma membrane (White *et al.*, 2017). Alkalinisation of the intracellular pH has been

shown to be an early event in malignant transformation when NIH3T3 fibroblasts were transformed by the HPV16 oncogene E7 (Reshkin *et al.*, 2000). In this study, NHE1-induced intracellular alkalinisation promoted proliferation, glycolysis and serum- and anchorage-independent growth. Acidification of the extracellular pH aids the spread of cancer in many ways. Low extracellular pH is sensed by several G-protein-coupled receptors such as GPR4 and GPR1/OGR1 and TDAG8, leading to cAMP production and thence to PI3K/Akt pathway activation and PKA/ERK pathway activation (Damaghi *et al.*, 2013). These are both pro-survival and mitogenic pathways. The amiloride-sensitive epithelial Na^+ channel ENaC, and the related acid-sensing ion channels (ASICs), also respond to low extracellular pH to permit entry of Na^+ into the cell. As well as contributing to an increase in $[Na^+]_{i,}$ activity of these ion channels has been linked to proliferation, migration, invasion and metastasis in various cancers (Xu *et al.*, 2016; Zhou *et al.*, 2017; Zhu *et al.*, 2017).

On top of the effects intrinsic to cancer cells, extracellular acidity hinders anti-tumour immunity by inducing cytotoxic T-cell anergy (Calcinotto *et al.*, 2012; Bellone *et al.*, 2013; Sukumar *et al.*, 2013). Low pH is optimal for secreted enzymes such as cathepsin B and matrix metalloproteinases 2 and 9 (MMP2 and MMP9) which break down the extracellular matrix, aiding invasion of cancer cells through basement membranes and eventual metastasis (Turk *et al.*, 1999; Rofstad *et al.*, 2006; Busco *et al.*, 2010).

VGSC activity has been shown to increase the H^+-extrusion activity of NHE1 in breast and lung cancer. This leads to extracellular acidification and increased activity of extracellular proteolytic enzymes (Roger *et al.*, 2007; Gillet *et al.*, 2009; Brisson *et al.*, 2011; Brisson *et al.*, 2013). Given that Na^+ entry through VGSCs would deplete the Na^+ gradient driving NHE1, VGSC activity would be expected to decrease rather than increase NHE1's ability to remove intracellular H^+. It was postulated that Na^+ allosterically modulates activity of NHE1 by binding to an intracellular binding site (Brisson *et al.*, 2013).

It is possible that VGSC activity may be affecting NHE1 through another mechanism. Lee *et al*. (2010) showed that the oncogene BAX inhibitor-1 promotes glycolysis and reduces mitochondrial respiration as well as increasing activity of NHE1 and MMP-2/9 in HT1080 fibrosarcoma cells (Lee *et al.*, 2010). The authors' conclusion was that the increase in NHE1 activity was a homeostatic mechanism to maintain intracellular pH, by removing H^+ generated by glycolytic respiration. An intriguing possibility, therefore, is that VGSC activity also leads to an increase in glycolytic respiration, thereby increasing NHE1 activity.

1.6.6 Na^+ entry increases glycolytic respiration

A common feature of cancer cells is their highly glycolytic metabolism, even in the presence of adequate oxygen. This is known as aerobic glycolysis, or the Warburg effect (Warburg, 1925). This effect is not completely understood and is the subject of much research (Parks *et al.*, 2013; Liberti & Locasale, 2016). Although Na^+ entry through VGSCs has not been linked to an increase in glycolytic rate, Na^+ entry through other means has been. In rat skeletal muscle, Na^+ entry was produced by incubation of whole muscles with monensin, an ionophore which equilibrates Na^+ (and to some extent H^+ and K^+) across the plasma membrane. This caused an increase in lactate production which was inhibited by incubating in a Na^+-free medium, or by adding the NKA-blocker ouabain (James *et al.*, 1996). This result indicates that Na^+ entry causes an increase in glycolysis which is mediated by NKA.

Further evidence for a link between Na^+ entry and glycolysis can be found by looking at another Na^+ channel. Mutations in the non-voltage-gated isoform of the VGSC family Na_x, encoded by *SCN7A* have recently been implicated as important in oesophageal cancer (Yuan *et al.*, 2022) and a recent transcriptomics study highlighted Na_x as the key gene associated with tumour mutation burden in gastric cancer (Li *et al.*, 2022). Na_x acts as a sensor of extracellular [Na^+] in the brain. This channel forms a complex with the α1 subunit of the NKA and activity of the channel leads to increased intracellular lactate production and glucose uptake in glial cells (Shimizu *et al.*, 2007; Berret *et al.*, 2013). Nomura *et al*. showed

that this Na_x activation in glial cells releases H^+ as well as lactate, and this goes on to activate ASIC1a channels in neighbouring neurons (Nomura *et al.*, 2019). The increase in glucose uptake combined with lactate and H^+ production caused by increased activity of Na_x is most likely due to an increase in the rate of glycolysis. The fact that Na_x forms a functional complex with NKA suggests that Na^+ entry drives Na^+ pumping by NKA as part of this mechanism. Indeed, an increase in $[Na^+]_i$ will increase activity of NKA to maintain homeostasis. Na^+ binds to the cytoplasmic side of the NKA and increases its rate of activity (Pellerin & Magistretti, 1994; Chatton *et al.*, 2000; Humphrey *et al.*, 2002; Clarke *et al.*, 2003).

While the above studies indicate that increasing cytoplasmic $[Na^+]$ increases the rate of glycolysis, it has been shown that elevated mitochondrial $[Na^+]$ inhibits ATP production via the electron transport chain (Hernansanz-Agustín *et al.*, 2020). ATP would then need to be formed via an alternative route. Since raising cytoplasmic $[Na^+]$ may increase mitochondrial $[Na^+]$ via NCLX, it is possible that this is another mechanism by which glycolysis may be upregulated when cytoplasmic $[Na^+]$ is elevated.

1.6.7 Na^+/K^+ ATPase is fuelled by glycolysis

NKA is located on the plasma membrane and uses a large proportion of a cell's total ATP supply, ranging from 75% in neurons (Attwell & Laughlin, 2001) down to 34-60 % in hepatocytes and skeletal muscle (McBride & Early, 1989). Despite much interest in the NKA as a potential therapeutic target in cancer, we do not yet know the relative proportion of ATP used by NKA in cancer cells compared to normal cells.

NKA activity has been investigated in a tissue other than cancer which exhibits aerobic glycolysis: vascular smooth muscle. Increasing activity of NKA has been shown to increase the rate of lactate production in vascular smooth muscle (Paul *et al.*, 1979). By performing several ionic manipulations to control NKA activity and V_m and by inhibiting NKA with

ouabain, Paul *et al* showed that although vascular smooth muscle contractility was mainly fuelled by oxidative metabolism, NKA was mainly fuelled by glycolysis.

In cardiomyocytes, inhibition of NKA using ouabain did not affect O_2 consumption but greatly affected the total ATPase activity, as measured by NADH change where pyruvate kinase and lactate dehydrogenase were provided (Sepp *et al.*, 2014). These researchers also found that cellular ATPases are closely coupled to pyruvate kinase (PK), which catalyses a rate-limiting reaction in glycolysis (Sepp *et al.*, 2010). Similarly, NKA activity was shown to increase the rate of aerobic glycolysis but not O_2 consumption in renal cell lines (Lynch & Balaban, 1987a, b). Inhibition of NKA with ouabain in normal breast and breast cancer cell lines reduced the proton production rate (glycolytic rate) dramatically, but did not significantly affect the O_2 consumption rate, further supporting the notion that NKA is fuelled by glycolysis (Epstein *et al.*, 2014). Similar to NKA, the plasma membrane Ca^{2+} ATPase (PMCA) was confirmed to rely predominantly on glycolysis in pancreatic cancer cells (James *et al.*, 2015). The reason why NKA predominantly utilises glycolysis for its ATP supply was investigated in a model by Epstein *et al*. (2014). The model predicted that diffusion limitations in the cytoplasm and a fluctuating demand for ion pumping activity meant that NKA would require an ATP source close to where it is located in the plasma membrane, which can respond quickly to a fluctuating ATP demand. In this scenario, glycolytic enzymes would be found close to the plasma membrane and mitochondria much further away (Epstein *et al.*, 2014).

In summary, VGSCs have been shown to act via CD44, src and cortactin, and via depolarisation of Rac1, all of which increase branching of the actin cystoskeleton and promote migration. VGSCs may also alter Ca^{2+} signalling through increased Ca^{2+} entry through the plasma membrane via VGCCs and NCX. VGSCs increase extracellular acidification via increasing activity NHE1 which increases invasion by creating an optimal

pH for ECM-degrading enzymes. In addition, increasing Na^+ influx would be expected to increase activity of NKA (Figure 1.3).

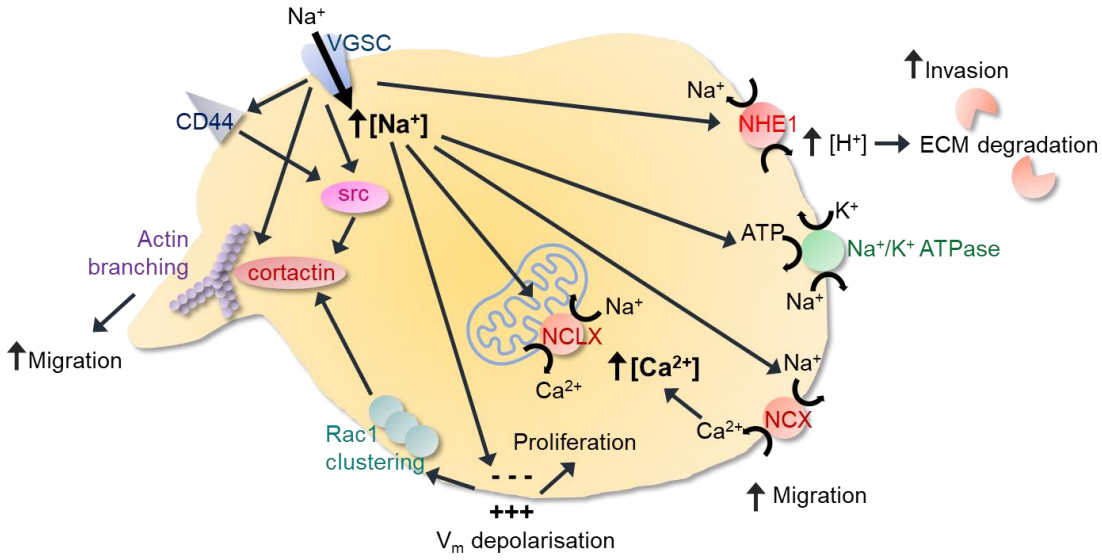

Figure 1.3 Some mechanisms of VGSC-induced malignant cell behaviours.
VGSCs can increase activation of cortactin to increase branching of the actin cytoskeleton, required for forming plasma membrane processes and cell migration. VGSC activity can also increase src activation, which activates cortactin. VGSC activity increases CD44 expression which increases src activation. VGSC-induced cell V_m depolarisation leads to clustering and activation of Rac1 which increases migration via cortactin. VGSCs increase $[Na^+]_i$ and this can increase cytosolic $[Ca^{2+}]$ through NCX. It may also increase mitochondrial $[Na^+]$ via NCLX, which disrupts the electron transport chain. Elevated $[Na^+]_i$ would increase the activity of the Na^+/K^+ ATPase and increase extracellular acidification via NHE1.

1.7 Hypotheses and aims

The overarching hypothesis tested in this thesis is that VGSCs are functionally upregulated in breast cancer cells, promoting invasion and metastasis. The main aims of this PhD project were:

1. To delineate the mechanisms by which VGSCs could regulate extracellular acidification (Chapter 3).
2. To study gene expression and networks regulated by $Na_v1.5$ (Chapter 4).
3. To evaluate expression and prognostic value of VGSCs in clinical specimens (Chapter 5).
4. To assess electrophysiological effects of a modern anti-epileptic VGSC inhibitor, eslicarbazepine acetate on $Na_v1.5$ *in vitro* (Chapter 6).

2 Materials and methods

2.1 Cell and tissue culture

2.1.1 Cell lines

The MDA-MB-231 and MCF7 breast cancer cell lines were gifts from M. Djamgoz, Imperial College, London. SKBR3 cells were a gift from J. Rae, University of Michigan. MCF-10A cells were a gift from N. Maitland, University of York. HEK293 cells stably expressing Nav1.5 were a gift from L. Isom, University of Michigan. Molecular identity was confirmed by short tandem repeat analysis (Sample reference JC 15 D1007544 6302 LW5000014 17). MDA-MB-231 cells stably expressing enhanced green fluorescent protein (GFP) and MDA-MB-231 cells over-expressing β1-GFP C-terminal fusion (hereafter called "MDA-MB-231-β1" cells) were gifts from M. Djamgoz (Chioni *et al.*, 2009). MDA-MB-231 cells stably expressing shRNA targeting *SCN5A* ($Na_v1.5$) were developed by M. Nelson, University of York.

2.1.2 Patient breast cancer tissue and primary cells

Table 2.1 Breast cancer patient tissue and primary cell samples.

Tumour	ER status	HER2 status	LN status	Age at diagnosis
T1	Borderline	Positive	Positive	79
T2	Positive	Negative	Unknown	81
T3	Positive	Negative	Positive	49
1° culture sample	**ER status**	**HER2 status**	**LN status**	**Age at diagnosis**
BC1	Negative	Negative	Positive	30
BC2	Positive	Borderline	Positive	57
BC3	Positive	Borderline	Positive	32
BC4	Positive	Positive	Positive	70
BC5	Negative	Positive	Negative	54
N1	N/A	N/A	N/A	N/A
N2	N/A	N/A	N/A	N/A

2.1.3 Maintenance of cells/tissue

MDA-MD-231, MCF7 and SKBr3 cells were cultured in Dulbecco's modified eagle medium (DMEM, Gibco) supplemented with 5 % (MDA-MB-231 and MCF7) or 10 % (SKBr3) foetal bovine serum (FBS) and 4 mM L-glutamine (all from Gibco). MCF10A cells were cultured in DMEM:F12 (Invitrogen), 5 % heat-inactivated horse serum, 0.5 μg/ml hydrocortisone, 20 ng/ml human EGF, 10 μg/ml insulin and 100 ng/ml cholera toxin. MDA-MB-231 xenograft tumour slices were cultured in 50% MEM with Glutamax (Gibco), 25% Earle's balanced salt solution, 35 mM glucose, 25% heat-inactivated horse serum, 1 ml/100ml pen/strep. Human primary cells and human breast tumour slices were cultured in DMEM:F12 (D8437 Sigma) with 1 ml/100ml pen/strep, 2.5 μg/ml Fungizone, 10 % FBS, 0.5 μg/ml hydrocortisone, 10 μg/ml apo-transferrin, 10 ng/ml human EGF and 5 μg/ml insulin. Human primary cells were cultured on collagen-coated glass coverslips and plastic-ware. MDA-MB-231-GFP and MDA-MB-231-β1 cells were maintained in medium containing hygromycin (100 μg/ml), HEK-293 cells stably expressing Nav1.5 and MDA-MB-231 cells transfected with shRNA were maintained in medium containing G418 (400 μg/ml). Cells and tissues were cultured at 37 °C and 5% CO_2 in a humidified Binder C150 incubator. Cells were grown in Corning tissue culture-treated cell culture dishes and were detached with 0.05 % (v/v) Trypsin-EDTA (Life Technologies) in phosphate buffer saline (PBS, Life Technologies). Cells were passaged approximately weekly when they reached near confluency and were discarded after 10 passages post-thawing. Cells were confirmed to be *Mycoplasma*-free every month using the 4′,6-diamidino-2-phenylindole (DAPI) method (Uphoff *et al.*, 1992).

2.1.4 Freezing and thawing cells

Cells were stored in cryovials in liquid nitrogen. To thaw cells, a 200 μl aliquot of frozen cells was thawed quickly in a waterbath at 37 °C, and the aliquot was diluted in 10 ml medium. The culture medium was replaced after 12-24 h to remove DMSO from the freezing medium. To freeze cells, a near-confluent 10 cm dish of cells was trypsinised then

suspended in cell culture medium. The cell suspension was centrifuged at 100 g for 5 minutes at room temperature and the supernatant was removed. The cells were resuspended in 1 ml freezing medium and aliquots of 200 µl were transferred into cryovials (Greiner) and stored at -80 °C for 2 days before moving to liquid nitrogen. For MDA-MB-231, MCF7 and HEK293-Nav1.5 cells, freezing medium contained 70 % (v/v) DMEM, 20 % (v/v) FBS and 10 % (v/v) cell culture grade dimethylsulfoxide (DMSO, PanReac AppliChem). For MCF10A cells, freezing medium was the same as for other cell lines apart from Horse serum (Invitrogen) was used instead of FBS.

2.2 Pharmacology

Drugs were dissolved in solvent at near-maximal solubility and were then aliquoted and frozen at -30 °C. On the day of use, an aliquot would be thawed and diluted in the assay medium (usually physiological saline solution (PSS) or cell culture medium), using serial dilutions where large changes in concentration were required. In control conditions equal volumes of solvent were added to assay media as in the test conditions.

Table 2.2 Drugs used in this thesis.

Drug	**Supplier**	**Stock concentration**	**Solvent**	**Working concentration**
TTX citrate	HelloBio (HB1035)	1 mM	Water	30 µM
Ouabain octahydrate	Sigma (O3125)	50 mM	DMSO	Various
Cariporide	SantaCruz Biotechnology (SC337619)	50 mM	DMSO	20 µM
Iodoacetic acid	Acros Organics (170970250)	400 mM (made fresh)	Water	2 µM
Oligomycin A	SantaCruz Biotechnology (SC201551)	10 mM	DMSO	1 µM
Eslicarbazepine acetate	TCI Chemicals (E1046)	67 mM	DMSO	100 µM or 300 µM
Licarbazepine	Tocris (3865)	300 mM	DMSO	100 µM or 300 µM

2.3 Whole cell patch clamp recording

2.3.1 Micropipettes

The whole-cell patch clamp technique was used to record cell membrane currents from cells grown on glass coverslips (Grimes *et al.*, 1995; Fraser *et al.*, 2005). Filamented borosilicate capillary tubes were pulled and fire-polished using a Narishige MF-830 microforge to a resistance of ~5 MΩ when measured containing intracellular pipette solution (IPS) in the recording bath. The resistance was changed to ~10 MΩ for recording from primary cells.

2.3.2 Recording solutions

Extracellular physiological saline solution (PSS) contained, in mM, NaCl 144, KCl 5.4, $MgCl_2$ 1, $CaCl_2$ 2.5, HEPES 5, D-glucose 5.6, and was adjusted to pH 7.2 (unless otherwise stated) using NaOH, with a final osmolarity of 315 ± 10 mOsm/kg. For the extracellular recording solution for HEK-293 cells expressing $Na_v1.5$, the extracellular [Na^+] was reduced to account for the much larger Na^+ currents and contained (in mM): NaCl 60, Choline Cl 84, KCl 5.4, $MgCl_2$ 1, $CaCl_2$ 2.5, D-glucose 5.6, and HEPES 5, and was adjusted to pH 7.2 with NaOH. In Na^+-free recording solution, Na^+ was replaced with NMDG. Intracellular recording solution for measuring Na^+ currents contained, in mM, NaCl 5, CsCl 145, $MgCl_2$ 2, $CaCl_2$ 1, HEPES 10, EGTA 11 and was adjusted to pH 7.4 (unless otherwise stated) using CsOH, with a final osmolarity of 295 ± 10 mOsm/kg (Brackenbury & Djamgoz, 2006). Intracellular recording solution for measuring K^+ currents contained, in mM, NaCl 5, KCl 145, $MgCl_2$ 2, $CaCl_2$ 1, HEPES 10, EGTA 11 and was adjusted to pH 7.4. Intracellular recording solution for measuring V_m contained, in mM, NaCl 5, KCl 145, $MgCl_2$ 2, $CaCl_2$ 1, HEPES 10, EGTA 1.57 and was adjusted to pH 7.4.

2.3.3 Recording set-up

Patch clamp recordings were made using a MultiClamp 700B amplifier (Molecular Devices) linked to a computer running MultiClamp 700B Commander 2.1.0 software (Molecular Devices). Currents were digitized using a Digidata 1440A interface (Molecular Devices),

low-pass filtered at 10 kHz, sampled at 50 kHz, and analysed using pCLAMP 10.7 software (Molecular Devices). Series resistance was compensated by 40-60% and linear components of leak were subtracted using a P/6 protocol (Armstrong & Bezanilla, 1977).

Cells were visualised with an Olympus BX51WI light microscope with a dry 10X and water-dipping 40X lens. GFP was excited by using a pE100 CoolLED at 470 nm and the fluorophore emission was gathered at 525 ± 50 nm. An open recording chamber (Warner Instruments RC-26GLP) was fixed to the microscope by a stage adaptor (Warner Instruments SAOLY/2) and cells on coverslips or tissue slices were perfused with PSS at a rate of ~ 1 ml/minute using a gravity-fed perfusion system. To change the solution, over four bath changes (4 ml) were perfused over the cells. Tissue slices were immobilised with a SHD-26GH/15 slice anchor (Warner Instruments).

The ground electrode was a Ag/AgCl pellet and the pipette electrode was a silver wire coated with AgCl. The electrode wire was re-coated by soaking in NaHClO for 20 minutes every two weeks. The pipette was moved using a PatchStar micromanipulator (Scientifica).

2.3.4 Recording protocols

Cells were clamped at a holding potential of -120 mV or -80 mV for 250 ms, dependent on experiment (detailed in the Figure legends). Five main voltage clamp protocols were used, as follows:

1. To assess the effect of drug/low pH perfusion and wash-out on peak current in real time, a simple one-step protocol was used where cells were held at -120 mV or -80 mV for 250 ms and then depolarised to -10 mV for 50 ms.

2. To assess the voltage-dependence of activation, cells were held at -120 mV for 250 ms and then depolarised to test potentials in 5-10 mV steps between -120 mV and +30 mV for

50 ms. The voltage of activation was taken as the most negative voltage which induced a visible transient inward current.

3. To assess the voltage-dependence of steady-state inactivation, cells were held at -120 mV for 250 ms followed by prepulses for 250 ms in 5-10 mV steps between -120 mV and +30 mV and a test pulse to -10 mV for 50 ms.

4. To assess recovery from fast inactivation, cells were held at -120 mV for 250 ms, and then depolarised twice to 0 mV for 25 ms, returning to -120 mV for the following intervals between depolarisations (in ms): 1, 2, 3, 5, 7, 10, 15, 20, 30, 40, 50, 70, 100, 150, 200, 250, 350, 500. In each case, the second current was normalized to the initial current and plotted against the interval time.

2.3.5 Noise reduction in recordings

1. For the simple one-step protocol the step voltage change was applied 20 times and the resulting current traces were averaged to reduce noise.

2. To assess voltage of activation or inactivation, peak currents were detected and the peak-to-peak noise during the quiescent period before depolarisation was calculated. Half of this peak-to-peak noise was subtracted from every peak current measurement.

3. For recordings from primary cells and cells in patient tumour slices, currents were low-pass filtered at 1 kHz.

2.3.6 Calculations

To calculate conductance, the noise-subtracted current was divided by the driving force for Na^+:

Driving force (mV) = Depolarisation voltage - reversal potential (V_{rev}) for Na^+

where V_{rev} was calculated using the Nernst equation:

$$V_{rev} = \frac{RT}{zF} \times \ln \frac{[Na^+]_e}{[Na^+]_i}$$

where $[Na^+]_e$ is the extracellular $[Na^+]$ and $[Na^+]_i$ is the intracellular $[Na^+]$, R is the universal gas constant (8.314 J K^{-1} mol^{-1}) , T is the temperature in Kelvin, z is the charge of the ion (+1) and F is the Faraday constant (96485 C mol^{-1}).

The V_{rev} for Na^+ was +85 mV for most experiments but due to different recording solutions used when recording Na^+ currents from HEK-$Na_v1.5$ cells, the V_{rev} was +63 mV.

The voltage-dependence of conductance and availability were normalized and fitted to a Boltzmann equation:

$G = G_{max}/[1 + \exp((V_{1/2} - V_m)/k)]$, where G_{max} is the maximum conductance, $V_{1/2}$ is the voltage at which the channels are half activated/inactivated, V_m is the membrane voltage and k is the slope factor.

The time course of inactivation was fitted to a double exponential function:

$I = A_f \exp(-t/\tau_f) + A_s \exp(-t/\tau_s) + C$, where A_f and A_s are maximal amplitudes of the slow and fast components of the current, τ_f and τ_s are the fast and slow decay time constants and C is the asymptote.

To analyse recovery data, currents were normalised to the initial current ($I_t / I_{t=0}$), plotted against recovery time (t) and fitted to a single exponential function:

$\tau = A1 + A2 \exp(-t/t_0)$, where A1 and A2 are the coefficients of decay of the time constant (τ), t is time and t_0 is a time constant describing the time dependence of τ.

To measure V_m, the amplifier was used in current clamp mode and the bridge balance and capacitance were compensated (Molecular-Devices, 2012). The gigaseal was formed and the membrane patch broken in voltage clamp mode then the amplifier was then switched to I = 0 mode (no current or voltage inputs) as soon as possible after breaking the membrane patch, and the voltage was measured over 60 seconds. The average voltage over this time was corrected for liquid junction potentials (-3.7 mV in the recording conditions) calculated using the pClamp 10.7 liquid junction potential calculator (Barry, 1994).

2.4 Orthotopic breast tumour model

All animal procedures were carried out after approval by the University of York Animal Welfare and Ethical Review Body and under authority of a UK Home Office Project Licence. *Rag2*$^{-/-}$ *Il2rg*$^{-/-}$ mice were bred in-house and females over the age of 6 weeks were used for tumour implantation. A suspension of 1 x 10^6 MDA-MB-231 cells in Matrigel (Corning) (50% v/v in PBS) was implanted into the left inguinal mammary fat pad of each animal whilst under isoflurane anaesthesia (Figure 2.1 A). For some experiments MDA-MB-231 cells stably transfected with shRNA directed against *SCN5A* or scrambled shRNA (Nelson *et al.*, 2015b) were implanted instead of wild-type MDA-MB-231 cells. Mice were weighed and their body condition and tumour size were checked at least every 2 days. Tumours were measured using callipers and the tumour volume was calculated using the modified ellipsoidal formula, volume = 1/2(length × width^2) (Tomayko & Reynolds, 1989). Mice were euthanized after approximately four weeks.

2.5 Tumour slice preparation

Tumours were dissected immediately after euthanasia and sliced in ice-cold PBS using a Campden 5100MZ vibratome to a thickness of 200 μm for patch clamp recording or 500 μm for ion selective microelectrode recording. They were then immediately transferred to a PSS bath at room temperature. To make lung tissue slices, the mouse was euthanised, the thorax was opened by splitting the sternum, the trachea was cannulated using a 20G IV cannula and

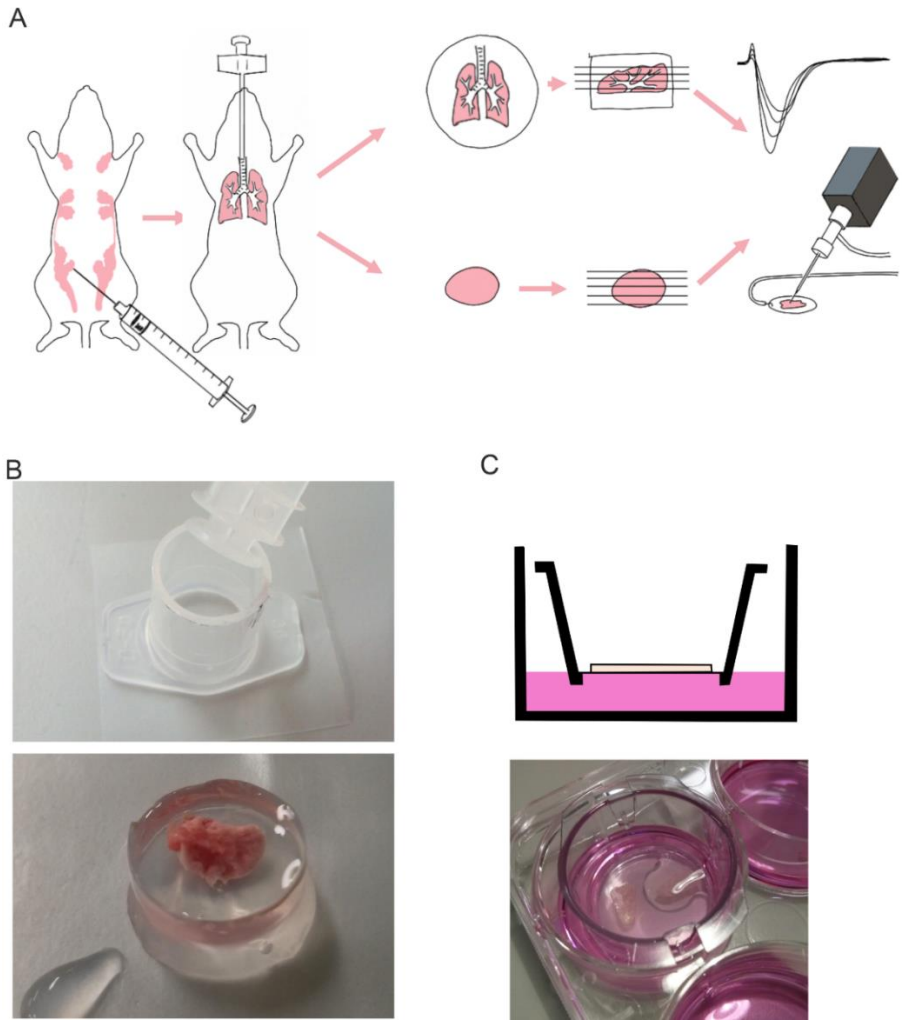

Figure 2.1 Tissue slice preparation.
A. Schematic showing protocol: 1 x 10^6 MDA-MB-231 cells in 50 % Matrigel were implanted into the mammary fat pad of $GC^{-/-}/Rag2^{-/-}$ mice. Mice were euthanised after 4 weeks. Lungs were filled with 1% low-melting-point agarose then dissected and embedded in low-melting-point agarose. Primary tumours were also dissected and tissues were sliced to a thickness of 250 µm. Whole cell patch clamp was used to measure Na^+ currents and V_m from cells in slices. **B**. Mould for embedding lungs in low melting point agarose. **C**. Some slices were maintained in culture on a transwell insert at the interface between the culture medium and the air.

1% low melting point agarose at 37 °C was injected through the cannula into the lungs (Figure 2.1 A). When this had reached room temperature and set, the lungs were dissected out and embedded in more 1% low melting point agarose at 37 °C. The resulting block was then sliced to a thickness of 250 μm. For long-term culture, tissue slices were held on a transwell insert at the interface between culture medium and air (Figure 2.1 C).

2.6 Ion sensitive microelectrodes (ISMEs)

2.6.1 Micropipettes

Unfilamented borosilicate capillary tubes were pulled to a resistance of ~5 MΩ (measured after silanization and when filled with PSS and in a recording bath). Pipettes were then coated with a hydrophobic layer (silanized) at 200 °C for 15 minutes with N,N-dimethyltrimethylsilyamine (TMSDMA) (Sigma).

2.6.2 Recording solutions

For measuring Na^+, microelectrodes were back filled with PSS (see section 2.3.2). For measuring H^+, they were back filled with the following solution, in mM: NaCl 100, HEPES 20, NaOH 10, adjusted to pH 7.5. After back-filling with aqueous solution, the microelectrodes were front-filled by suction with oil containing ionophores (Sigma hydrogen ionophore I – cocktail A to make H^+-selective electrodes, or Sigma sodium ionophore II – cocktail A to make Na^+-selective electrodes) (Voipio *et al.*, 1994). Tissue slices were perfused with PSS (see section 2.3.2). PSS solutions adjusted to pH 5.43, 6.4, 7.2 and 8.23 were made for calibration of H^+ ISMEs. PSS solutions with $[Na^+]$ of 48, 96, 144 or 192 mM (with no replacement ion) were made for calibration of Na^+ ISMEs.

2.6.3 Recording set-up

ISME recordings were made using a MultiClamp 900A amplifier (Molecular Devices) linked to a computer running MultiClamp 900A Commander software (Molecular Devices). The headstage amplifier was a high impedance 0.0001MU Axon HS-2 (Molecular Devices).

Currents were digitized using a ITC018 A/D converter (HEKA Instruments), regular oscillatory noise was reduced with a HumBug noise eliminator (Quest Scientific) and the voltage signal was low-pass filtered at 10 Hz. Voltage was recorded using Axograph software (version 1.7.6).

Tissue slices were magnified using a stereo microscope. A humidified recording chamber (designed by Prof. M. Whittington) housed the tissue slices on the interface between PSS at 30 °C and humidified, warmed air (Figure 2.2 A). PSS was perfused by a Gilson F117604 peristaltic pump (ThermoFisher) with a bubble trap to reduce mechanical noise from the pump. The ground electrode and the pipette electrode were silver wires coated with AgCl. The electrode wires were re-coated by soaking in NaHClO for 20 minutes every two weeks.

2.6.4 ISME recording from tumour slices

ISME measurements from tumour slices were made within one hour of mouse euthanasia. Sketches were made of the slices with grossly visible colour differences between "core" and "peripheral" regions identified in the drawing. ISMEs were placed on the top surface of tumour slices, since it was found that deeper placement would damage the ISME (Figure 2.2 A). After each placement the Faraday cage was closed and the voltage was monitored until a steady voltage was reached, then this voltage was recorded. In total, 12 measurements were made from each region of the slice, alternating between regions, with calibrations and bath measurements taken before, half-way through and at the end of the measurements.

2.6.5 Calibration of ISMEs

The ISMEs were calibrated just before use in microcentrifuge tubes outside the recording chamber. A separate ground electrode of the same material as in the recording chamber was used in the calibration tubes. Once the ground electrode and ISME were placed in each calibration tube, the Faraday cage was closed and the voltage was allowed to stabilise before a measurement was read from the Axoscope screen. This equilibration took ~1 minute for H^+

electrodes and ~3 minutes for Na^+ electrodes. If the electrode was found to be insensitive to changing ionic concentrations it was discarded. Given that the calibration could not be performed in the recording chamber with the same ground electrode as the test recordings, there was a voltage offset between the two conditions. The voltage offset between the PSS in the bath around the tumour and in the microcentrifuge tube containing the same ion concentrations was calculated. This offset was later subtracted from the measured voltages in the tumour slice. Calibration and offset calculation was performed before and after every 12 measurements since it could drift with repeated electrode placement. If the electrode had greatly reduced sensitivity, the electrode was discarded, along with the measurements made between the first and second calibrations.

Where there was only a small change in ISME sensitivity, the calibrations and offsets performed immediately before and after a set of 12 measurements were averaged, so each set of 12 measurements was calibrated separately. A straight line was fitted to the offset-corrected voltage/pH calibration points, and the equation of this straight line was calculated: voltage = (slope x pH) + y intercept. For each voltage measurement from the tumour slice, the corresponding pH was calculated by rearranging the equation for pH: pH = (voltage – y intercept)/slope (Figure 2.2 B). The same calibration method was used for Na^+-sensitive electrodes (Figure 2.2 C).

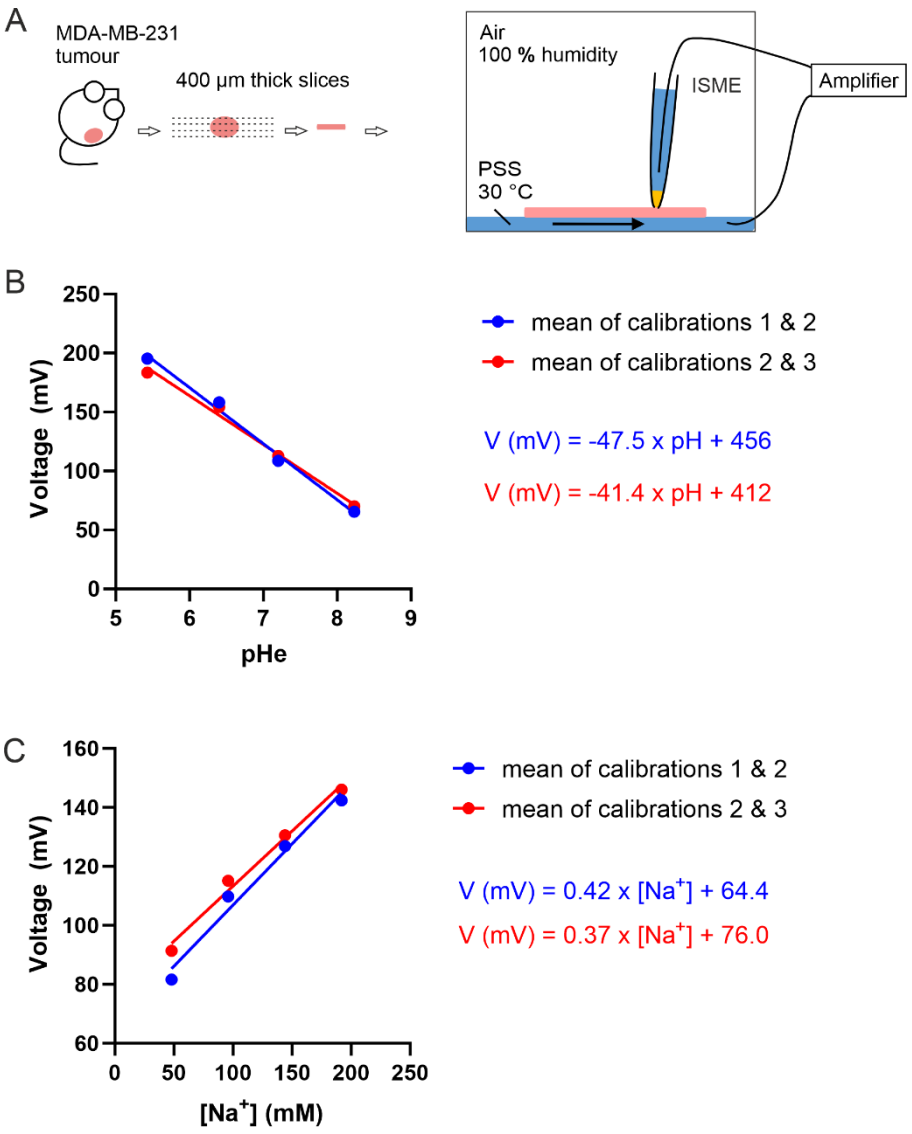

Figure 2.2. Ion-sensitive microelectrode recording from MDA-MB-231 xenograft slices. **A**. Schematic of protocol: tumour-bearing mouse was euthanised, the tumour dissected and sliced on a vibratome into 400 µm thick slices. These were maintained at the interface of air at 100 % humidity and perfused PSS at 30 °C. Ion sensitive microelectrodes were placed in various locations at the top surface of the slices and the voltage between the bath and the microelectrode was measured. **B**. Example of two averaged calibrations for a pH-sensitive electrode, showing a slight reduction in sensitivity after it had been used for several measurements. **C**. Example of two averaged calibrations for a Na^+-sensitive electrode, showing a slight reduction in sensitivity after it had been used for several measurements.

2.7 Xenograft tumour tissue

2.7.1 Tissue preservation and sectioning

After recording with ISMEs, tumour slices were fixed in 4% paraformaldehyde (PFA) for 1 h, cryoprotected in 10 % then 30 % sucrose in PBS over 48 h and frozen in optimal cutting temperature (OCT) compound (Agar scientific) before being sectioned to a thickness of 12 μm on a Leica CM1950 cryostat and mounted on SuperFrost plus slides (Epredia Menzel).

2.7.2 Haematoxylin and eosin staining

Tumour section slides were post-fixed in 4 % PFA for 10 minutes then washed for 3 x 5 minutes in 0.1 % PB, then in distilled water before being stained in 1 x Gills Hematoxylin (Richard Allan Scientific) for 5 minutes. Sections were then rinsed with water, acidified in 1% HCl in 70% ethanol for 2 minutes and rinsed again with water before being alkalinised in 0.1 % NH_4OH in water, then rinsed with water. Sections were then stained with Eosin-Y alcoholic (Richard Allan Scientific) for 1 minute then rinsed briefly with water and mounted with Faramount aqueous mounting medium (Dako).

2.7.3 Xenograft tumour immunohistochemistry

For immunohistochemical labelling, sections were drawn around with a hydrophobic PAP pen (Dako) then post-fixed in 4 % PFA for 10 minutes and washed in 0.1 M phosphate buffer (PB) (40.5 ml of 0.8 M Na_2HPO_4 and 9.5 ml of 0.8 M NaH_2PO_4, diluted to 400 ml with distilled water). Fixed sections were blocked in 0.1 M PB with 0.3 % Triton-X-100 and 10 % goat serum (PBTGS) for 1 h at room temperature, then primary antibodies were diluted in PBTGS and sections were incubated in these overnight at room temperature. Active caspase 3 antibody (R&D Systems AF835) was diluted 1:200 and Ki67 antibody (Abcam AB15580) was diluted to 1:5000. Both antibodies were raised in rabbits so they were used on separate tissue sections from each tissue slice. After incubating with primary antibody, sections were washed in 0.1 M PB for 3 x 5 minutes then incubated with Alexa-568 conjugated goat anti-rabbit secondary antibody (Invitrogen A11036) at 1:500 dilution in

PBTGS for 2 h at room temperature. After this sections were counterstained with DAPI by washing with 0.1 M PB containing DAPI (0.5 µg/ml) for 3 x 5 minutes, then mounted in Prolong Gold + DAPI (Thermofisher P36931).

2.7.4 Xenograft tumour IHC image analysis

Stained sections were imaged on a Zeiss AxioScan.Z1 slide scanner with a 20X objective. Images were viewed using Zen 3.4 (blue edition) software (Zeiss) and the maximal intensity in the red and blue (DAPI) channels were changed to maximise the visibility of positively stained cells. The minimum intensity was not changed. Images were then converted from .czi format to 8-bit .tif format. In ImageJ 1.53c software (NIH), a whole section was viewed at a time and the shape was matched to the drawing of the tissue slice during ISME recording. Regions of interest (1000 x 1000 pixels) were chosen in both "core" and "peripheral" regions identified during ISME recording. Six ROIs were selected from each region (often sampling the majority of the region). These ROIs were saved as numbered image files for analysis. The rest of the analysis was performed using an ImageJ macro (Section Appendix IV). Briefly, a nuclear count was performed by a particle count in the DAPI channel. A minimum level intensity cut-off was applied to remove background staining in the red channel, and this value was kept consistent within all ROIs from each tissue section. Nuclear Ki67 staining was quantified by a particle count where the DAPI signal colocalised with the red signal (using a mask generated from the DAPI channel). Since activated caspase 3 staining was not nuclear, the DAPI mask was not applied to these images before making a particle count. Particle counts were expressed as a percentage of the DAPI count in the same ROI to give the percentage of positively stained cells in each ROI for each antibody.

2.8 Human tumour tissue microarray immunostaining

A tumour microarray consisting of formalin-fixed, paraffin-embedded sections of 1740 primary breast tumour cores was obtained from the Breast Cancer Now Tissue Bank. Slides

were deparaffinised in Histoclear (National Diagnostics) then rehydrated in decreasing concentrations of ethanol. Antigen retrieval was achieved by incubating with citrate-based Target Retrieval Solution (Dako S1699) at 95 °C for 30 minutes. Samples were drawn around with a hydrophobic PAP pen (Dako S2002) then blocked with peroxidase block (Dako S202386-2) for 5 minutes. Samples were incubated with primary antibody diluted in antibody diluent (Dako S0809) at 1:25 for anti-β1 N-terminal (Abgent AP10645a) or 1:100 for anti-$Na_v1.5$ (Alomone ASC-013). Slides were incubated with primary antibody for 1 h (β1) or 3 h ($Na_v1.5$) at room temperature. After gentle rinsing and immersion in buffer solution, slides were stained with EnVision+ Dual Link System/HRP (DAB+) (Dako K401011), following the manufacturer's instructions. Slides were then counterstained with Mayer's haematoxylin (Dako S3309) and mounted in Faramount aqueous mounting medium (Dako S3025).

Negative control slides were not exposed to primary antibody. As a control to show specificity of staining, some protocol optimisation slides were stained with antibodies which had been preincubated with the immunising peptides. Preincubations were performed in Dako antibody diluent overnight at 4 °C, then the mixture was centrifuged at 16000 x g for 20 minutes and the supernatant used for immunostaining. Preincubation with immunising peptides required optimisation for both antibodies, increasing the proportion of peptide:antibody in both cases to maximal possible proportions given the volumes that were available. Final proportions were 0.2 µl (0.19 µg) antibody and 93 µl (139.5 µg) peptide in a total volume of 200 µl for Anti-$Na_v1.5$ antibody. The molar ratio was not clear as the molecular weight of the antibody was not specified but can be estimated at around 150 kDa. The molecular weight of the peptide is 33 kDa, giving a molar ratio of peptide:antibody of 3337.

For the anti-β1 antibody the proportions were 0.8 µl (0.2 µg) antibody 48 µl (48 µg) peptide in a total volume of 200 µl. Again, the molar ratio was not clear as the molecular weight of

both the antibody and peptide were not specified but estimates in Abgent's blocking peptide protocol (https://www.abcepta.com/assets/pdf/Blocking_Peptides_Protocol.pdf) are 150 kDa for an antibody and 1.65 kDa for a 15- residue peptide. This gives a molar ratio of peptide:antibody as 21825.

2.9 TMA imaging and staining quantification

Slides were imaged on a Zeiss AxioScan.Z1 slide scanner with a 20X objective and staining was visualised using Zen 3.4 (blue edition) software (Zeiss). Staining was quantified using a modification to the Allred scoring system (Allred *et al.*, 1998). In this system, the proportion of positively stained cells is scored, and the intensity of staining is scored separately (Table 2.3).

Table 2.3 Scoring of anti-$Na_v1.5$ or anti-β1 antibody staining of TMA sections.
The proportion score and intensity score were added together to make the final score for each tissue core section. Allred score = proportion score + intensity score

Positive cells %	Proportion score
0	0
<1	1
1-10	2
11-33	3
34-66	4
67-100	5

Intensity	Intensity score
None	0
Weak	1
Intermediate	2
Strong	3

2.10 Immunocytochemistry

2.10.1 Immunocytochemical staining

Cells on coverslips were fixed in 4 % PFA for 10 minutes, washed with PBS then blocked for 1 hour with PBTGS. They were then incubated with rabbit monoclonal anti ER-α [SP1] (ab16660) or rabbit monoclonal anti-ErbB 2 (HER2) antibody [EP1045Y] (ab134182), both at 1:250 dilution in PBTGS at room temperature overnight. After being washed for 3 x 5 minutes with PBS, coverslips were incubated with Alexa-488 conjugated goat anti-rabbit secondary antibody (Invitrogen A11034) at 1:500 dilution in PBTGS at room temperature for 3 hours. Coverslips were then counterstained with DAPI by being

washed in 0.1 M PB containing DAPI (0.5 µg/ml) for 3 x 5 minutes, then they were mounted in Prolong Gold + DAPI (Thermofisher P36931). Anti-ER-α staining was compared against the MCF7 cell line as a positive control and the MDA-MB-231 cell line as a negative control. Anti- HER2 staining was compared against the SKBr3 cell line as a positive control and the MDA-MB-231 cell line as a negative control.

2.10.2 Imaging of immunocytochemical staining

Slides were imaged on a Nikon Eclipse TE200 fluorescent microscope with a Plan Fluor 40X objective using a RoleraXR Fast1394 charge-coupled device (CCD) camera (QImaging) and SimplePCI 6.0 software. DAPI was excited at 340 nm and the fluorescence signal was gathered at 455 nm. Alexa 488 was excited at 490 nm and fluorescence signal was gathered at 512 nm. Files were saved as 8-bit .tif files at 150 pixels/inch.

2.11 RNA extraction and RT-PCR

2.11.1 RNA extraction

RNA was extracted using TRIzol reagent (Invitrogen) following a protocol from W.M. Keck Foundation Biotechnology Microarray Resource Laboratory at Yale University. Briefly, RNA was extracted from primary cells remaining on plasticware after coverslips had been removed and used for other experiments. Cells from each well were scraped in 1 ml TRIzol and vortexed. Xenograft tumour samples were frozen in TRIzol (1 ml TRIzol per 100 mg tissue) at -80 °C until RNA extraction. On the day of extraction, the samples were thawed then homogenised using a Dounce homogeniser, then centrifuged at 4°C and 12000 x g for 5 minutes to pellet debris. The vortexed primary cell samples in TRIzol and the TRIzol supernatant from homogenised tissue samples were then treated by adding 0.2 ml chloroform per ml TRIzol to each sample. Samples were then incubated at room temperature for 3 minutes and centrifuged at 4 °C and 12000 x g for 15 minutes. The upper aqueous phase was kept and into this was added 0.5 ml isopropanol and 1 µl Glycoblue (Thermofisher AM9516) to aid detection of the RNA pellet. Samples were then incubated at

room temperature for 10 minutes and centrifuged at 4 °C and 12000 x g for 20 minutes. The supernatant was removed and the pellet was washed twice in 75 % ethanol. The pellet was then dried and dissolved in 10 µl RNAase-free water. RNA concentrations were checked using a Nanodrop (Thermo Scientific).

2.11.2 RT PCR – cDNA synthesis

Samples were treated with DNAseI (Sigma AMPD1) to remove any contaminating DNA. They were incubated with DNAseI at a concentration of 1 unit per 10 µl reaction, at 21 °C for 15 minutes. DNAseI was then inactivated by addition of 1 µl stop solution to each sample and heating to 70 °C for 15 minutes. cDNA was made using Superscript II reverse transcriptase (Invitrogen) by adding 1 µg RNA (5-8 µl depending on RNA concentration) to 250 ng random hexamer (2.5 µl of 100 ng/µl solution) and the reaction was made up to 11.5 µl with water. The sample was incubated at 70 °C for 10 minutes to separate RNA to single strands, then rapidly cooled on ice. A reaction mixture of 2 µl of 0.1 M dithiothreitol (DTT), 4 µl Supercript II first strand buffer (5X), 1 µl 10 mM dNTP mix and 0.5 µl (20 U) RNAse inhibitor was added to the sample, mixed and incubated at room temperature for 2 minutes. 1 µl (200 U) of Superscript II reverse transcriptase enzyme was added to the sample, stirred and incubated at room temperature for 10 minutes. The reaction mixture was incubated at 42 °C for 1.5 hours then the reaction was halted by heating to 70 °C for 15 minutes then cooled on ice.

2.11.3 PCR method

Using GoTaq Hot Start DNA polymerase (Promega) kit and protocol, a master mix of PCR reagents was produced for each primer pair or template DNA, depending on the experiment.

A 50 µl PCR reaction contained:

10 µl Green GoTaq Flexi Buffer (5X), 4 µl $MgCl_2$ (25 mM), 1 µl dNTPs (10 mM each base), 1 µl each of the forward and reverse primers (100 nM), 0.25 µl GoTaq Hot Start Polymerase

(5 U/µl) and 100 ng of template DNA, made up to 50 µl with nuclease-free water. For no template controls, water was added instead of cDNA.

The annealing temperature of each primer pair was first calculated by the Promega online Tm calculator (https://www.promega.co.uk/resources/tools/biomath/tm- calculator/) and then optimised experimentally. In a typical PCR program, DNA was denatured at 95 °C for 2 min then it was subjected to 35 cycles of 30 s denaturation at 94 °C then 30 s annealing at the optimal annealing temperature then 60 s extension at 72 °C.

Gel electrophoresis of samples was performed in 1-2 % agarose gels made with TBE buffer (0.1 M Tris base, 0.1 M boric acid, 2 mM EDTA). SYBR safe DNA stain (Invitrogen) was added at 10 µl per 100 ml gel to visualise DNA bands. Gels were run in TBE buffer at 100 V for ~45 min. Gels were visualised and photographed using a Gel Doc EZ Imager (Bio-Rad).

2.12 Trypan blue viability assay

Cells were cultured in 6 well plates. Culture medium from each well was removed from wells into 14 ml Falcon tubes using a pipette then adherent cells were detached from wells using Trypsin-EDTA. The trypsin was inactivated using double the volume of serum-containing medium. Suspended cells were recombined with their used medium in the 14 ml Falcon tubes. These tubes were centrifuged at 800 x g for 5 minutes. The pellet was resuspended in a known volume of DMEM and a 10 µl sample was mixed with an equal volume of Trypan blue. Cells were counted using an Invitrogen Countess automated cell counter.

2.13 Ratiometric ion indicators

2.13.1 SBFI-AM experiments in individual cells on coverslips

Cells were grown on glass coverslips for 48 h, then incubated for 1 h at 37°C in 10 µM SBFI-AM (Thermofisher S1263) with 0.1% Pluronic F-127 (Sigma P2443) in DMEM. To

allow esterified dye to diffuse out of the cells before recording, coverslips were washed twice then left in PSS for 30 minutes before recording. Coverslips were mounted in a Warner RC-20H recording chamber used in open configuration with PSS perfusion at 1 ml/min by a perfusion system with peristaltic pumps to control inflow and outflow. Solutions were changed using the perfusion system except the calibration solutions at the end of the experiment which were introduced drop-wise by syringe. Two-point calibration was performed at the end of every experiment. For SBFI-AM, 10 mM Na^+ PSS (with K^+ as replacement ion) containing 20 μM gramidicin D (Sigma), was applied for 12 minutes, followed by 20 mM Na^+ for a further 12 minutes. Each cell's fluorescence ratio was calibrated to its own calibration line.

2.13.2 BCECF-AM experiments in individual cells on coverslips

Cells were grown on glass coverslips for 48 h, then were incubated for 10 minutes at 21°C in 1 μM BCECF-AM (Biotium 51011) without Pluronic F-127. The perfusion apparatus and recording chamber were the same as for the SBFI-AM experiments. Solutions were changed using the perfusion system, apart from ionophore-containing calibration solutions, which were introduced drop-wise by syringe. Two-point calibration was performed at the end of every experiment using K^+-based PSS (where Na^+ was replaced by K^+) at pH 7 with 13 μM nigericin (Sigma) for 7 minutes, followed by K^+-based PSS at pH 8 for a further 7 minutes. Each cell's fluorescence ratio was calibrated to its own calibration line.

2.13.3 Imaging of ratiometric fluorescent indicators

Exposures of 0.15 s duration were taken every 15 s with a Nikon Eclipse TE200 epi-fluorescent microscope using SimplePCI 6.0 software to control the imaging system. Images were captured with a RoleraXR Fast1394 CCD camera (Q-imaging) with a 20X Plan Fluor lens and 2X binning (SBFI-AM) or with a 10X Plan Fluor objective and no binning (BCECF-AM). Filters used in imaging were for SBFI-AM: Chroma 71000a (340 nm and 380 nm excitation, dichroic 400 nm LP and emission 510 ± 80 nm) and for BCECF-AM:

Chroma 31044v2 (436 ± 20 nm and 480 ± 40 nm excitation, dichroic 505 nm LP and emission 540 nm LP). Images were saved as 16-bit .tif files and analysed in NIH ImageJ 1.53c. Circular ROIs were placed over cells which had a healthy appearance (not unusually small or bright, and which did not move appreciably during the recording period.) The mean intensity at each wavelength was calculated for each ROI. Background fluorescence was calculated for each excitation wavelength by selecting a ROI where there were no cells. Background fluorescence was subtracted from the mean intensity of each ROI before fluorescence ratio calculation. Each experimental repeat was the mean measurement from ~ 40 cells per coverslip.

2.13.4 Plate reader-based SBFI-AM measurement

Cells were seeded at 2 x 10^4 (MCF7 and SKBr3), 2.5 x 10^4 (MDA-MB-231) or 4 x 10^4 (MCF10A) cells/well in a Greiner 96 well, black walled, micro-clear polymer-bottomed plate. Medium was exchanged and drug incubations started after 36 h. Before dye loading, wells were washed with PBS, and 60 µl DMEM containing SBFI-AM (10 µM) and Pluronic F-127 (0. 1%) ± drug treatment was added to each well. Cells were incubated in SBFI-AM at 37 °C for 2 h. Wells were then washed twice in PSS ± drug and left in PSS ± drug for imaging on a BMG Clariostar plate reader with excitation at 340 and 380 nm and emission collected at 510 nm. Simultaneous calibration of $[Na^+]_i$ was performed in separate wells of the plate using 0 mM, 10 mM, 20 mM, 30 mM and 40 mM Na^+ PSS (with K^+ as the replacement ion). Intracellular and extracellular $[Na^+]$ was equilibrated with 20 µM gramidicin D until fluorescence ratios stabilised (~15 minutes). Background fluorescence was subtracted from each wavelength before fluorescence ratio calculation. Calibration was performed in each plate for each cell line separately. Each experimental repeat or calibration point was the average fluorescence ratio of five wells from a single plate.

2.14 Inductively coupled plasma mass spectrometry

Normal mammary glands from ex-breeding female $GC^{-/-}Rag2^{-/-}$ mice or MDA-MB-231 xenograft tumours from the same genotype of mice were dissected and weighed. These were freeze-dried overnight and re-weighed. The dried sample was transferred to a PTFE digestion vessel which was then digested with nitric acid and hydrogen peroxide [4:1] (trace metal grade) using a microwave digestion system (Ethos Up, Milestone). Digestion method "SK-CL-002-Animal Tissue" was employed from the Ethos up library (Milestone). After digestion was complete, the digestate was transferred to a 50 ml volumetric flask and diluted to volume using deionised water (18 MΩ). All digestion vessels and glassware were cleaned beforehand using an acid steam cleaning system (traceClean, Milestone) to reduce the risk of trace metal contamination. Na^+ content was quantified using calibration standards prepared using certified reference standards (multi-element environmental calibration standard, Agilent 5183-4688). In addition, a 10 ppb internal standard solution was prepared from a certified reference solution (Agilent 5188-6526). Samples were analysed by ICP-MS to give sodium content as ppm (dry mass). This value was converted to mmol/kg fresh mass by multiplying by the fresh mass/dry mass ratio. Sample digestion and ICP-MS was performed by Darren Phillips at the Biorenewables Development Centre, Dunnington, York.

2.15 RNA sequencing

2.15.1 Sample preparation and quality control

Xenograft tumours which had grown to a mean diameter of 10 mm were halved and half of each was placed in TRIzol reagent immediately after dissection and stored at -80 °C. RNA was extracted as described in Section 2.11.1. Library preparation and sequencing were performed by Novogene. Firstly, RNA quantity, integrity and purity were assessed using agarose gel electrophoresis and an Agilent 2100 bioanalyzer (Figure 2.3 A-C). Secondly, a cDNA library was prepared and sequenced using an Illumina sequencer, generating > 2 x 10^7 clean reads per sample (Figure 2.3 D).

2.15.2 Analysis of RNAseq data

RNASeq analysis was provided as a service by Novogene. FASTQ read files (Cock *et al.*, 2010) were mapped to the human genome or mouse genome using STAR aligner (Dobin *et al.*, 2013) creating BAM files. Count matrices were generated using HTSeq. To produce heatmaps, samples were clustered using gene expression in Z scores which are produced using $\log_2$(FPKM+1). Specifically, the distance between the $\log_2$(FPKM+1) of each gene from the mean $\log_2$(FPKM+1) of all genes was calculated, then each value was divided by the standard deviation of $\log_2$(FPKM+1) for each gene. using the hierarchical clustering distance method in R. DESeq2 was then used to make differentially expressed gene (DEG) tables (Anders & Huber, 2010). DESeq2 compared the expression of each gene between samples by empirically fitting a negative binomial distribution to the raw read counts for each transcript, using the trimmed mean read count (mean of the middle 50% of the total gene expression distribution) as a reference value to normalise the read count to account for read depth (Dillies *et al.*, 2013). ClusterProfiler (Yu *et al.*, 2012) was used to create functional profiles for gene clusters for both human and mouse reads using the Gene Ontology (GO) database (http://www.geneontology.org), the Reactome database (https://reactome.org) and the Kyoto Encyclopedia of Genes and Genomes (KEGG) (http://www.kegg.jp). In addition, for the human gene data set only, disease ontology (DO) analysis was performed using the Disease Ontology database (http://www.disease-ontology.org) and the DisGeNET database (https://www.disgenet.org). Protein-protein interactions within the differentially expressed gene set were explored using the STRING database (http://string-db.org) (Shannon *et al.*, 2003).

Since reads from a xenograft tumour could potentially be mapped both to the human and to the mouse genome, ambiguously mapped genes were identified by Dr John Davey of the Technology Facility, Department of Biology, University of York. This was performed using BBsplit from the BBtools suite (Bushnell, 2021) which breaks reads into shorter sequences (kmers) and assesses when reads have kmers found in both human and mouse genomes. The

ambiguous reads were mapped back to the human genome using STAR aligner and this information was added to the DEG table.

2.16 Quantification of lactate production

Cells were seeded at 5 x 10^5 cells/well of a 6 well plate. After 24 h, wells were washed twice with PBS and 2 ml DMEM or FBS was added to each well. At this stage 24 h drug treatments were added. For shorter drug incubations, wells were washed again and drugs were included with a further change of DMEM. At the end of the drug incubations, 1 ml DMEM was collected from each well and frozen at -80 °C until all experiments had been performed. These were thawed and used in a colorimetric L-lactate assay (AAT Bioquest 13815). Absorbance from each well was measured at 575 nm and 605 nm on a BMG Clariostar plate reader. Blank subtraction was not used since phenol red was present in the culture medium. Each well in the lactate assay plate was from one well of cells in a 6 well plate. Each experimental repeat was composed of three technical repeats (three wells). A standard curve of known lactate concentrations was produced following the manufacturer's directions. This was not used to calibrate absorbance ratios because phenol red was present in the culture medium in test samples.

A

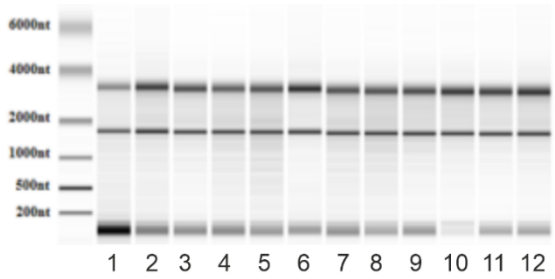

B

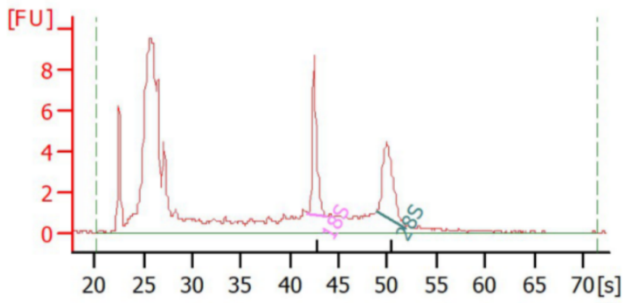

C

Sample	Concentration (ng/μl)	Volume (μl)	Total RNA (μg)	Integrity value	Sample QC result
ctrl 1	2010	18	36.18	6.6	Pass
ctrl 2	11190	21	234.99	7.1	Pass
ctrl 3	4020	15	60.3	8.8	Pass
ctrl 4	11100	18	199.8	7.1	Pass
ctrl 5	7260	18	130.68	8.5	Pass
ctrl 6	5970	17	101.49	8.5	Pass
shRNA 1	4040	18	72.72	7.9	Pass
shRNA 2	6810	16	108.96	8	Pass
shRNA 3	12830	15	192.45	7.2	Pass
shRNA 4	8320	16	133.12	7.5	Pass
shRNA5	10630	17	180.71	7.7	Pass
shRNA 6	9170	18	165.06	8.2	Pass

D

Sample name	Raw reads	Clean reads	Raw bases	Clean bases	Error rate(%)	Q20(%)	Q30(%)	GC content(%)
ctrl_1	24196727	23723856	7.3G	7.1G	0.03	97.84	93.98	48.75
ctrl_2	28516955	27951991	8.6G	8.4G	0.03	97.15	92.46	50.06
ctrl_3	20994395	20523243	6.3G	6.2G	0.03	97.72	93.79	49.69
ctrl_4	25423132	24940073	7.6G	7.5G	0.03	97.82	93.88	49.17
ctrl_5	21365625	20882636	6.4G	6.3G	0.03	97.79	93.89	49.66
ctrl_6	23242508	22688995	7.0G	6.8G	0.03	97.92	94.16	49.11
shRNA_1	24536101	23708564	7.4G	7.1G	0.03	97.93	94.15	49.36
shRNA_2	25110851	24657959	7.5G	7.4G	0.03	97.2	92.6	50.34
shRNA_3	23391450	22977730	7.0G	6.9G	0.03	97.21	92.65	50.37
shRNA_4	22660735	22256953	6.8G	6.7G	0.03	97.85	93.98	49.66
shRNA_5	21910069	21364601	6.6G	6.4G	0.03	98	94.09	50.36
shRNA_6	22697078	22063831	6.8G	6.6G	0.03	97.87	94.01	48.28

Figure 2.3. RNA sequencing sample quality control.
A. Agarose gel electrophoresis showing ribosomal RNA bands to check RNA integrity from the 12 samples. **B**. Sample 1 from **A**., further examined for purity and integrity with an Agilent 2100 bioanalyzer. **C**. RNA quality results from an Agilent 2100 bioanalyzer. **D**. Quality and number of reads from each sample by an Illumina sequencer.

2.17 Statistical analysis

Linear regression was used for calibration of ratiometric indicators and ISMEs, since the calibration curves approximated linear relationships over the ranges used. Linear regression was also used for determining rates of pH change in BCECF experiments. Statistical analysis was performed on raw (non-normalized) data using GraphPad Prism 8.4.0 for most analyses, or IBM SPSS Statistics 27 for Intraclass Correlation Coefficient, Cohen's weighted kappa and Cox multivariate proportional hazard analysis. RNAseq statistics were handled with DESeq2 and ClusterProfiler Pairwise statistical significance was determined with Student's paired or unpaired, or one-sample t-tests where data were normally distributed and using Mann-Whitney u tests where there were not. Multiple comparisons were made using ANOVA and Tukey's or Dunnett's multiple comparisons tests, where data were normally distributed and using Kruskal-Wallis or Friedman's tests where they were not. Results were considered significant at $P < 0.05$ or Padj <0.05 for differential gene expression. Padj values were corrected for false discovery rate (FDR) in DESeq2 using an interpretation of the Benjamini and Hochberg method (Benjamini & Hochberg, 1995). In this method genes are ranked by P value and then each P value is multiplied by the total number of tests and divided by the rank number of the gene. P values adjusted for false discovery rate (Padj) of < 0.25 are often considered in overrepresentation analysis (Subramanian *et al.*, 2005; Tamayo *et al.*, 2016) and when performing an exploratory experiment, especially when there are very few significantly enriched terms as in the Gene Ontology analysis of mouse genes and Reactome and Disease Ontology analysis of human genes in this study.

3 Investigating involvement of VGSCs in Na^+ and pH homeostasis

3.1 Introduction

Recent studies from the Brackenbury lab have shown that both $Na_v1.5$ and β1 subunits contribute to increased local invasion and metastasis in the MDA-MB-231 mouse model of breast cancer (Nelson *et al.*, 2014; Nelson *et al.*, 2015b). The mechanisms by which these two subunits increase metastasis may be unrelated, but since β1 increases size of whole-cell VGSC Na^+ currents (Isom *et al.*, 1992; Isom *et al.*, 1995b; Chioni *et al.*, 2009), it is possible that its pro-metastatic effects are mediated through an increased Na^+ current. For this to be the case, it would be expected that β1 would increase VGSC Na^+ currents in MDA-MB-231 cells *in vivo* as it does *in vitro*. However, this possibility has not yet been investigated. Yang et al (2020) showed that $Na_v1.5$ activity depolarised the V_m in MDA-MB-231 cells (Yang *et al.*, 2020). It is therefore possible that overexpressing β1 in MDA-MB-231 cells and tumours will depolarise the V_m as a consequence of an increased Na^+ current.

Another way in which VGSCs may alter cancer cell behaviour is through increasing the $[Na^+]_i$. This is of particular interest because tumours contain an elevated Na^+ concentration as determined by ^{23}Na MRI (Ouwerkerk *et al.*, 2003; Ouwerkerk *et al.*, 2007; Jacobs *et al.*, 2010; Zaric *et al.*, 2016; James *et al.*, 2021). If VGSCs promote invasion by elevating $[Na^+]_i$, $[Na^+]_i$ may correlate with VGSC current in cancer cell lines.

In breast cancer cells, $Na_v1.5$ activity leads to extracellular acidification via NHE1, and this increases invasion and migration *in vitro* (Brisson *et al.*, 2013; Driffort *et al.*, 2014). From the results of these studies, it is likely that the connection between $Na_v1.5$ activity and NHE1 is via an increase in $[Na^+]_i$. Since Na^+ influx into cells through VGSCs would decrease the inward Na^+ gradient powering H^+ efflux through NHE1, there may be some intermediary steps in the VGSC-induced H^+-efflux mechanism. A likely candidate for an intermediary step is NKA, since this is the only protein which removes Na^+ from the cell. NKA activity is

increased by elevated $[Na^+]_i$ (Pellerin & Magistretti, 1994) and is largely fuelled by glycolysis in many tissues (James *et al.*, 1996; Dutka & Lamb, 2007). Glycolysis produces H^+ which is then extruded by NHE1, thus lowering pH_e. There are many reports of low extracellular pH (pH_e) in solid tumours. This has been measured by pH electrodes in peripheral malignant melanoma tumours (Ashby, 1966), mammary tumours (van den Berg *et al.*, 1982) and other tumours (Wike-Hooley *et al.*, 1985). However, the links between VGSC function, Na^+ homeostasis and pH have not yet been delineated.

An additional consequence of the possible link between high intracellular $[Na^+]$ and low pH_e is the potential feedback on VGSC function in breast cancer cells. Of all of the isoforms of VGSC α subunit, at least $Na_v1.1$, $Na_v1.2$, $Na_v1.3$, $Na_v1.4$ and $Na_v1.5$ show some degree of H^+ block of the transient current, due to H^+ interactions with the pore of the channel (Khan *et al.*, 2002; Ghovanloo *et al.*, 2018). $Na_v1.5$ is the most sensitive to pH (Vilin *et al.*, 2012; Ghovanloo *et al.*, 2018). The reduced slow inactivation of $Na_v1.5$ in low pH increases the persistent Na^+ current in the heart, leading to ischaemia-induced arrhythmia (Khan *et al.*, 2006; Jones *et al.*, 2011). Recently low pH was shown to inhibit transient current through $Na_v1.5$ in breast cancer cells (Onkal *et al.*, 2019) but the effect of pH on persistent current has not been studied. The proposed interactions between VGSCs, $[Na^+]_i$ and pH are shown in Figure 3.1.

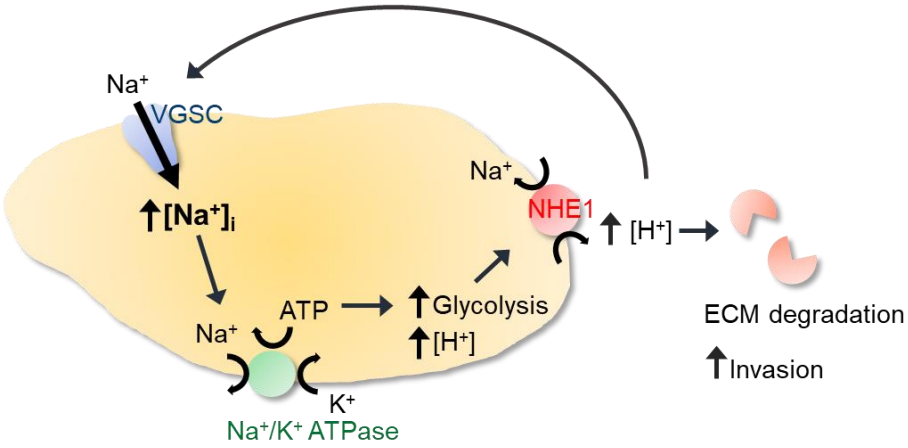

Figure 3.1 Schematic of hypothesis linking VGSC activity to pH regulation and invasion. VGSCs allow Na^+ into cancer cells, increasing $[Na^+]_i$. This upregulates NKA activity which consumes ATP. Glycolysis is upregulated to supply ATP to NKA. Acidic metabolites of glycolysis are removed from the cell via NHE1 along with other mechanisms, acidifying the extracellular space. This aids digestion of the extracellular matrix by cathepsins and MMP-2/9. Extracellular H^+ increases persistent VGSC current, further increasing Na^+ influx.

The aims of this chapter were to investigate:

1. The effect of β1 overexpression on Na^+ current and V_m on MDA-MB-231 cells and xenograft tumour tissue.

2. The functional relationship between VGSC expression, pH and $[Na^+]_i$ in breast cancer tumour tissue and cell lines.

5. The effect of pH_e on VGSC activity in MDA-MB-231 cells.

3.2 Results

3.2.1 Effect of β1 on Na^+ current and V_m in tumour slices

First, the effect of β1 on VGSC current and V_m was assessed *in vitro* in MDA-MB-231 cells. As previously reported in (Chioni *et al.*, 2009), expression of a β1-GFP construct in these cells increased the whole cell VGSC current *in vitro* (Figure 3.2 A-D). The V_m was assessed by whole-cell patch technique in I=0 mode over the course of the first 60 s after breaking the membrane patch, and the mean V_m over this time was calculated (Figure 3.2 E). Contrary to our hypothesis, the V_m was unchanged with β1-GFP expression (Figure 3.2 F).

To assess the impact of β1 on electrophysiological aspects of MDA-MB-231 cells *in vivo*, MDA-MB-231 cells stably expressing a β1-GFP construct or GFP were implanted into the mammary fat pad of *Rag2*$^{-/-}$ *Il2rg*$^{-/-}$ mice. Mice were euthanised once tumours were large enough to make tissue slices for patch clamp analysis. Tumour cells were identified in slices of primary tumours and lungs using fluorescence microscopy to detect GFP (Figure 3.3 B). Patch clamp recording was performed on cells at the top surface of the slice. After filling the lungs with low-temperature agarose, it was possible to make slices which maintained the delicate lung structure, and this allowed patch clamp recording of Na^+ currents in metastases. There is no report of microelectrode recordings previously having been made from metastases, so this was a novel technique. Cell fluorescence was vital to allow identification of cancer cells and for correct placement of the microelectrode (Figure 3.3 C and D).

Contrary to the situation *in vitro* (Chioni *et al.*, 2009), the VGSC current in tumours was not affected by β1 expression (Figure 3.3 E). Instead, the peak current density in both control and β1-expressing cells in tumour slices was of a similar size to that in control cells *in vitro* (Figure 3.3 F). Importantly, Na^+ currents were maintained when cells metastasised to the lungs and were unchanged from the currents in the primary tumours (Figure 3.3 G). There was no effect of β1 on V_m in the tumour slices (Figure 3.3 H). In addition, there was no difference in V_m between primary tumours and metastases (Figure 3.3 I).

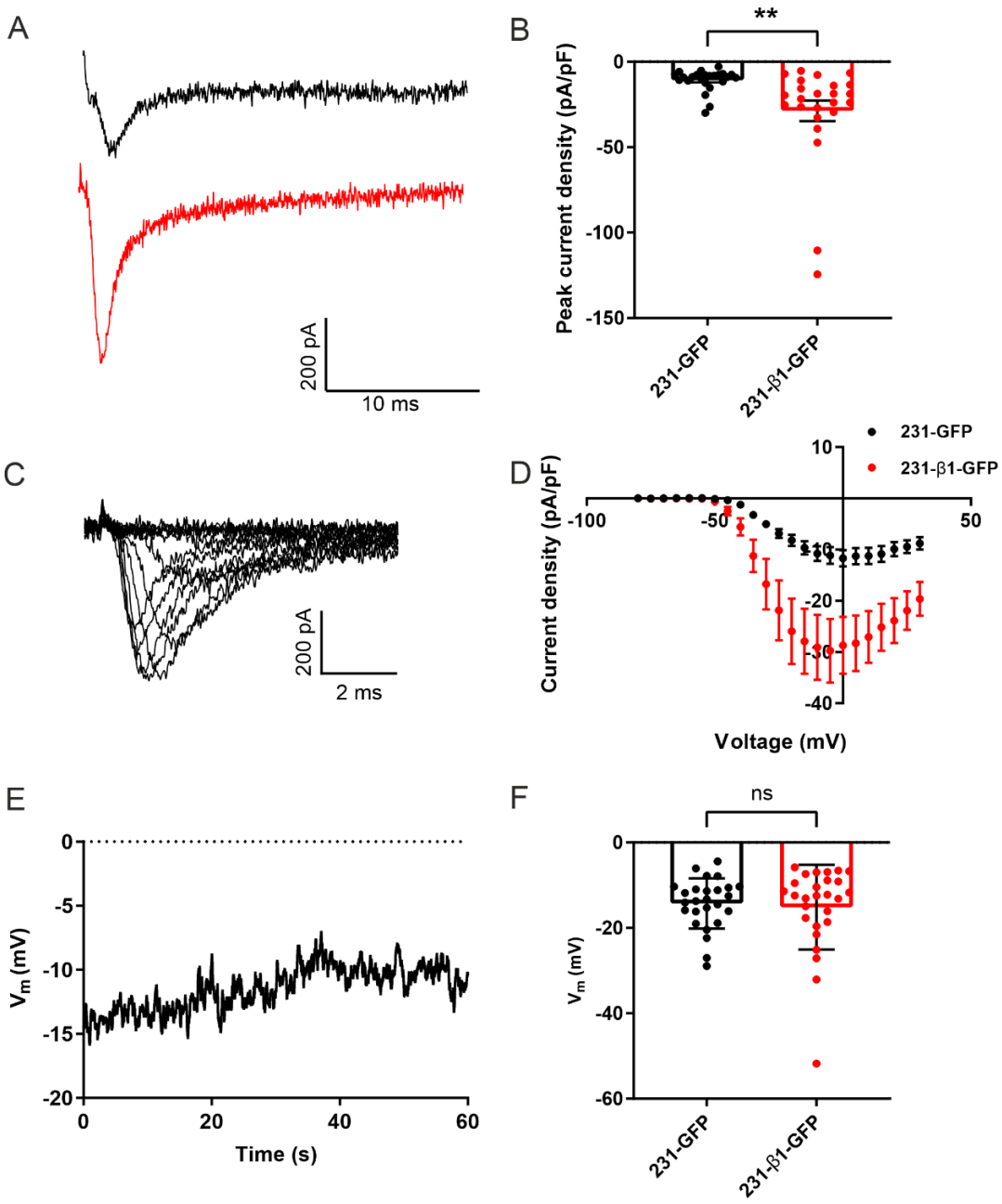

Figure 3.2 Electrophysiological comparison between control and β1-expressing MDA-MB-231 cells *in vitro*.
A. Example VGSC currents from isolated control and β1-expressing MDA-MB-231 cells elicited by a depolarisation from -120 mV to -5 mV. **B**. Peak current density of VGSC currents elicited by a depolarisation from -120 mV to -5 mV in isolated control and β1-expressing MDA-MB-231 cells. **C**. Example family of VGSC currents elicited by depolarisation to a range of voltages in a β1-expressing MDA-MB-231 cell. **D**. Current-voltage relationship of VGSC currents in isolated control and β1-expressing MDA-MB-231 cells. **E**. Example V_m recording in an isolated control MDA-MB-231 cell, during the first 60 s after breaking the membrane patch. **F**. Comparison between the V_m of isolated control and β1-expressing MDA-MB-231 cells. Results are mean ± SEM, Student's *t* tests.

In summary, β1 did not alter Na^+ current or V_m in MDA-MB-231 xenograft tumours, so it is likely that the promotion of migration due to β1 expression is through a mechanism other than V_m depolarisation via increased Na^+ current through the α subunit. Because of this, I decided to focus instead on the relationship between the α subunit $Na_v1.5$ and $[Na^+]_i$.

3.2.2 Total $[Na^+]$ is elevated in tumours compared to normal mammary glands, but extracellular $[Na^+]$ is normal

To quantify $[Na^+]$ in the MDA-MB-231 model of breast cancer, tumour tissue was compared to normal mammary glands from ex-breeding mice of the same strain. Analysis of total tissue $[Na^+]$ was performed using ICP-MS to quantify Na^+ content in freeze-dried tissue samples. The calculated total tissue $[Na^+]$ was 30.6 ± 2.7 mM in normal mammary glands and 45.7 ± 4.2 mM in xenograft tumours, showing that the sodium content of tumours was significantly increased (45.7 ± 4.2 mM) compared to normal mammary tissue (30.6 ± 2.8 mM) ($P < 0.01$; n = 7-8; Figure 3.4A). To further investigate whether $[Na^+]$ was elevated in the extracellular compartment of the tumour tissue, $[Na^+]_e$ was measured using ion-sensitive microelectrodes (ISMEs) sensitive to Na^+. The mean $[Na^+]_e$ was found to be 157.8 ± 1.3 mM. This is within the normal range of plasma $[Na^+]$ for mice of this age and strain (Sinke *et al.*, 2011). $[Na^+]_e$ was not significantly different between the peripheral and core regions of the tumour (Figure 3.4 B, regions illustrated in Figure 3.6 A). In summary, the tumour tissue total $[Na^+]$ was elevated compared to normal mammary tissue but the $[Na^+]_e$ in tumour tissue was physiologically normal. Together these results indicate that either $[Na^+]_i$ and/or the ratio of extracellular fluid volume to intracellular fluid volume is elevated in the tumour tissue.

3.2.3 Intracellular $[Na^+]$ and VGSC Na^+ current measurement in breast cancer cell lines

Since the results from section 0 indicated that in tumour tissue the total $[Na^+]$ was elevated but $[Na^+]_e$ was within normal limits, it was hypothesised that $[Na^+]_i$ might be elevated in breast cancer cells compared to normal breast cells. Therefore, $[Na^+]_i$ was assessed in several

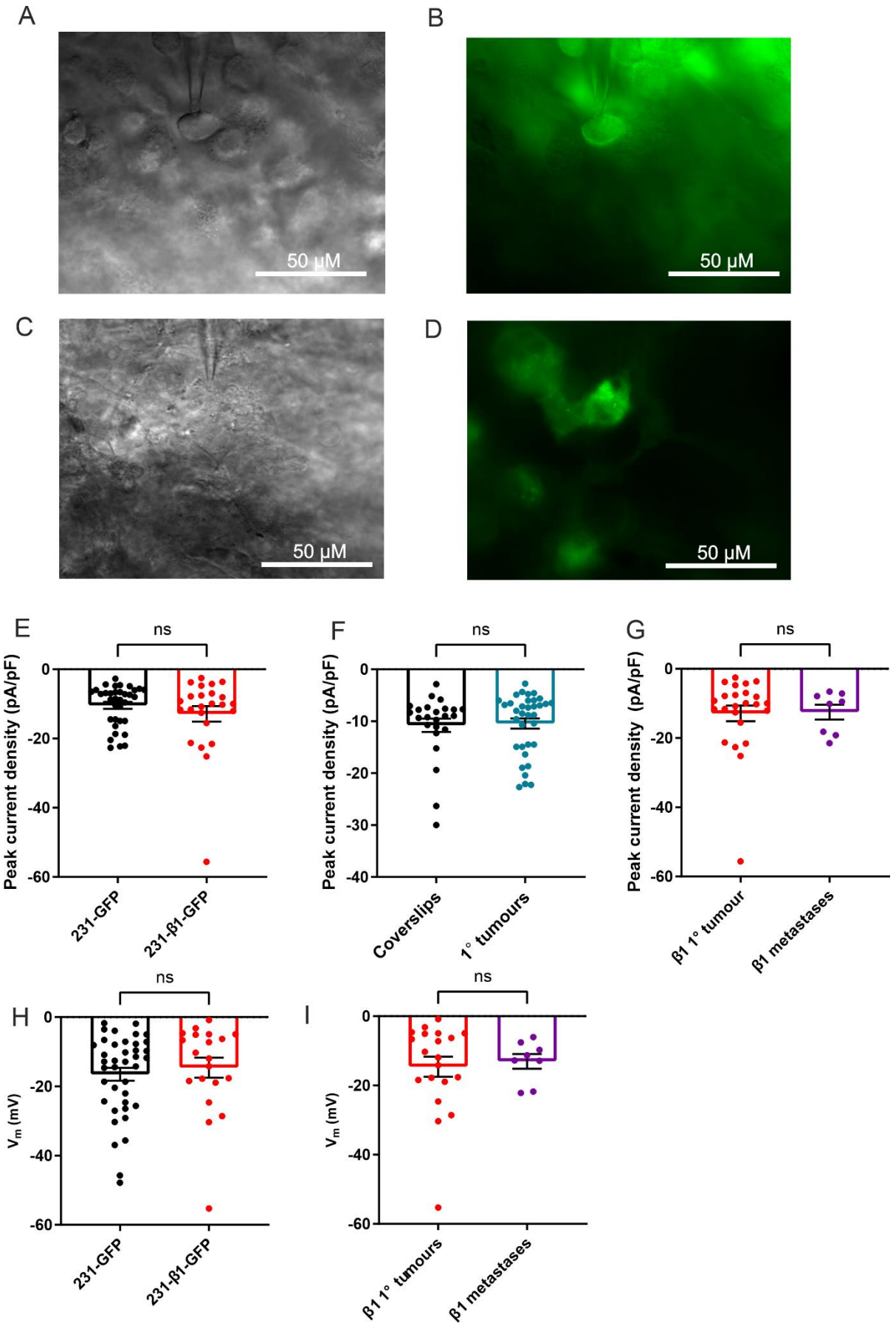
A
50 μM
B
50 μM
C
50 μM
D
50 μM
E
ns
Peak current density (pA/pF)
0
-20
-40
-60
231-GFP
231-β1-GFP
F
ns
Peak current density (pA/pF)
0
-10
-20
-30
-40
Coverslips
1° tumours
G
ns
Peak current density (pA/pF)
0
-20
-40
-60
β1 1° tumour
β1 metastases
H
ns
V_m (mV)
0
-20
-40
-60
231-GFP
231-β1-GFP
I
ns
V_m (mV)
0
-20
-40
-60
β1 1° tumours
β1 metastases

Figure 3.3 Electrophysiological comparison between control and β1-expressing MDA-MB-231 cells *in vivo*.
A. Bright field micrograph of patch clamp recording from a MDA-MB-231-GFP cell in a tumour slice **B**. Fluorescence micrograph of patch clamp recording from a MDA-MB-231-GFP cell in a tumour slice. **C**. Bright field micrograph of patch clamp recording in a lung slice **D**. Fluorescence micrograph of same field of view as in **C**, showing β1-expressing MDA-MB-231 cells in a lung slice. **E**. Peak VGSC current density in β1-expressing and control MDA-MB-231 cells in slices made from primary tumours **F**. Peak VGSC current density in control MDA-MB-231 cells in slices made from primary tumours compared to those on coverslips. **G**. Peak VGSC current density in β1-expressing MDA-MB-231 primary tumours compared to those in lung metastases. **H**. V_m of control and β1-expressing MDA-MB-231 cells in slices made from primary tumours. **I**. V_m of β1-expressing MDA-MB-231 cells in slices made from primary tumours or lungs. Results are mean ± SEM, Student's *t* tests.

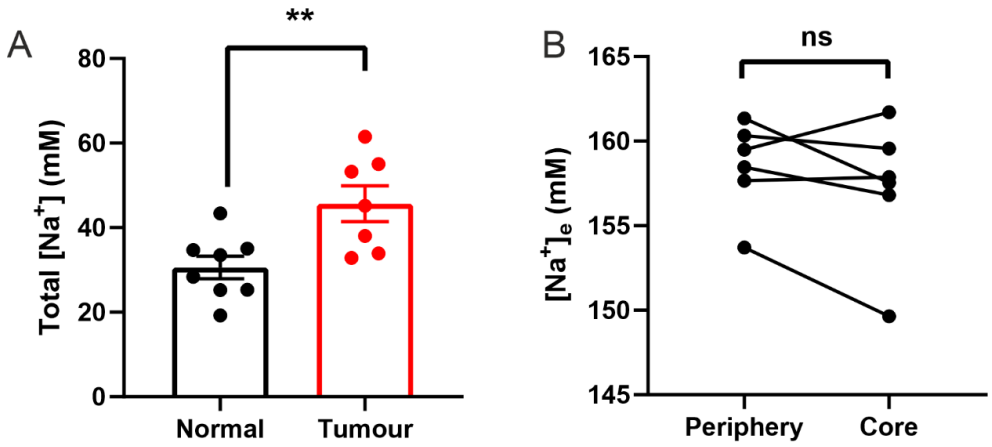

Figure 3.4 Measuring total tumour [Na^+] and extracellular [Na^+] ($[Na^+]_e$).
A. Comparison between total tumour [Na^+] in normal mammary gland tissue and MDA-MB-231 xenograft mammary tumours. Total tumour Na^+ content was quantified in freeze-dried tissue using ICP-MS. ($P < 0.01$; $n = 7$ or 8 glands; unpaired *t* test) **B**. Tumour slice $[Na^+]_e$ measured using ion selective microelectrodes, showing no difference between the core and peripheral regions in each slice ($P = 0.24$; $n = 6$ tumours; results of paired *t* test). Results are mean ± SEM, Student's *t* tests.

Table 3.1 Properties of breast cell lines used in this project.
(Subik *et al.*, 2010; Holliday & Speirs, 2011)

Cell line	Source	Subtype	ER	PR	HER2	Ki67	Tumourogenicity
MDA-MB-231	Pleural effusion	Basal	-	-	-	100%	High
MCF7	Pleural effusion	Luminal A	+	+	-	90%	High if oestrogen is present
SKBr3	Pleural effusion	HER2	-	-	+	20%	Low
MCF10A	Normal breast	Normal	N/A	N/A	N/A	30%	None

breast cancer cell lines (Table 3.1), including the triple-negative cell line MDA-MB-231, the ER/PR positive MCF7, the HER2 positive SKBr3 and the non-cancerous breast epithelial cell line MCF10A. $[Na^+]_i$ was assessed using the ratiometric fluorescent indicator SBFI-AM in plate-reader experiments (Section 2.13.4). MDA-MB-231 cells had a $[Na^+]_i$ of 9.3 ± 0.8 mM, MCF7 cells had a $[Na^+]_i$ of 10.2 ± 2.6 mM, SKBr3 cells had a $[Na^+]_i$ of 21.4 ± 4.7 mM and the normal breast cell line MCF10A had a $[Na^+]_i$ of 7.9 ± 3.0 mM (Figure 3.5 A). The expected intracellular $[Na^+]_i$ of healthy cells is 5-15 mM (Iamshanova *et al.*, 2016). All of the cell lines had $[Na^+]_i$ within this range apart from SKBr3 cells. There was no statistically significant difference between the measured $[Na^+]_i$ of any of the cell lines, except between SKBr3 and MCF10A cells ($P < 0.05$; n = 4-5 experiments of 5 wells each; one-way ANOVA with Tukey's multiple comparisons test).

Even though there was no obvious relationship between $[Na^+]_i$ and malignant phenotype in the four cell lines studied, it was possible that there could be a correlation between functional VGSC expression and $[Na^+]_i$ as VGSC activity has been shown to increase $[Na^+]_i$ (Campbell *et al.*, 2013; Yang *et al.*, 2020). To test this hypothesis, presence of VGSC Na^+ currents was assessed using whole cell patch clamp recording in the same four cell lines in which $[Na^+]_i$ had been assessed. Only the breast cancer cell line MDA MB-231 had large whole-cell Na^+ currents (Figure 3.5 B) and obvious Na^+ currents were present in 16/18 cells tested (Figure 3.5 C). Unexpectedly, a small number of MCF10A cells (2/16 cells) also displayed a very small VGSC-like inward current (Figure 3.5 B and C). Given the rarity and small size of the currents found in MCF10A cells, the sensitivity of the currents to TTX was not assessed. No VGSC Na^+ currents were detected in MCF7 or SKBr3 cells.

In summary, there was no relationship between cell line malignancy and $[Na^+]_i$, and there was no relationship between mean $[Na^+]_i$ and mean VGSC Na^+ current across the four cell lines ($P = 0.65$; Figure 3.5 D).

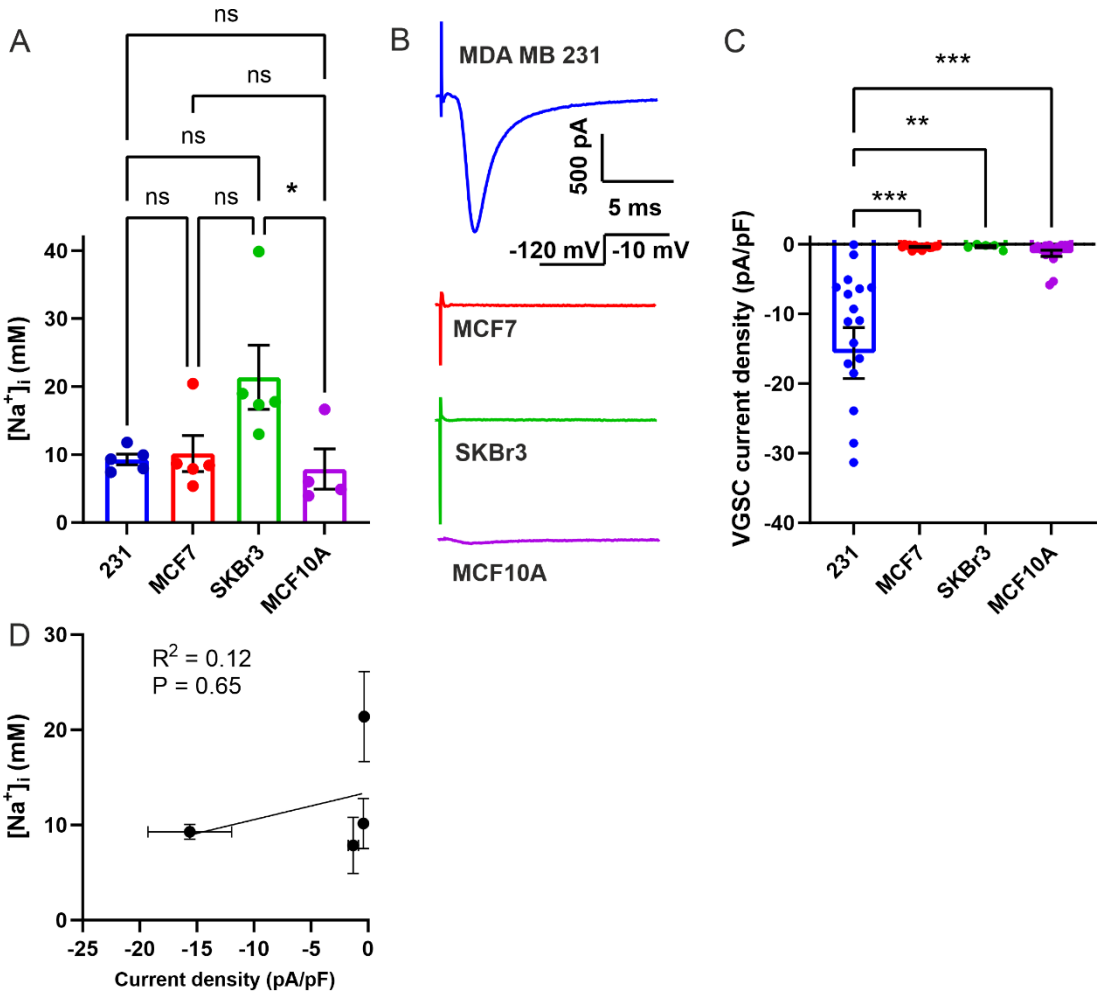

Figure 3.5. Intracellular [Na^+] and VGSC Na^+ currents in breast cell lines.
A. Quantification of $[Na^+]_i$ in the four cell lines (n = 4-5 experiments, of which each is the average of 5 wells, and each with its own calibration curve). **B**. Example VGSC Na^+ currents (or lack thereof) measured using whole cell patch clamp in the four cell lines. **C**. Quantification of the VGSC Na^+ current density measured in the four cell lines (n = 5-18 cells). **D**. Plot of $[Na^+]_i$ against mean VGSC current density in the four cell lines. Results are mean ± SEM, one-way ANOVA with Tukey's multiple comparisons tests.

3.2.4 Extracellular pH is lower in peripheral regions of tumour

Since the tumour microenvironment is reported to be acidic (White *et al.*, 2017), the pH_e of MDA-MB-231 xenograft tumour tissue slices was measured to ascertain whether this model followed the same pattern. pH-sensitive ISMEs were placed on the top surface of tumour slices and measurement of the voltage was recorded in at least 12 locations on each slice. Measurements were taken alternately from the more opaque regions which roughly correlated with the core of the tumour, and from the more translucent regions which were generally more peripheral (see Figure 3.6 A).

The mean overall pH_e was 6.9 ± 0.1, which is significantly lower than pH 7.4 normally found in healthy tissue ($P = 0.001$; $n = 9$; one sample *t* test) (White *et al.*, 2017). The mean pH_e in the peripheral regions was 6.8 ± 0.1 and in the core regions it was significantly higher, at 7.0 ± 0.1 ($P < 0.01$; $n = 9$; paired *t* test; Figure 3.6 B).

3.2.5 Low extracellular pH correlates with high cellularity and proliferative capacity

Given that there was a difference in pH_e between the core and peripheral regions of the tumour, next the differences between these regions were investigated in more detail using H&E staining and immunohistochemistry (Sections 2.7.2 and 2.7.3). Proliferation was assessed with an anti-Ki67 primary antibody (Figure 3.8), and apoptosis with an antibody against cleaved caspase 3 (Figure 3.9).

In the H&E-stained sections, nuclei in core regions appeared less well-defined giving the appearance of poor viability (Elmore *et al.*, 2016) (Figure 3.7 A). DAPI-stained nuclei were counted to assess cellularity in the two regions (Figure 3.7 A and B). The peripheral regions were more cellular than core regions. The mean nuclear count per ROI in the peripheral regions was 988 ± 29 compared to 838 ± 47 in the core regions ($P < 0.01$; $n = 9$ tumours; paired *t* test). Ki67 staining was more prevalent in peripheral regions than core regions; 20.1 ± 7.0 % cells were Ki67 positive in the peripheral region, compared to 6.9 ± 2.4 % cells in

the core region ($P < 0.05$; n = 9 tumours; paired *t* test; Figure 3.8 A and B). Conversely, cleaved caspase 3 staining was greater in core regions (10.9 ± 3.5 % positive cells) than peripheral regions (2.1 ± 0.7 % positive cells) ($P < 0.05$; n = 9 tumours; paired *t* test, Figure 3.9 A and B).

Taken together with the ISME recordings, these results suggest that the pH_e is lower in regions with high cellularity which are proliferating rapidly, generally towards the periphery of the tumour. The pH is higher where there is more apoptosis, towards the core of the tumour.

3.2.6 Low extracellular pH decreases transient current but increases persistent current in MDA-MB-231 cells

To assess the effect of the acidic tumour microenvironment on VGSC activity in MDA-MB-231 cells, the pH of the extracellular recording solution was changed and Na^+ currents were measured. For recording from this cell line, the pH of the PSS is normally adjusted to 7.2 (Fraser *et al.*, 2005), which is already slightly more alkaline than the pH_e of healthy tissue (pH 7.4). This was compared with a pH_e of 6.2 or 6.0 since the measured pH_e of solid tumours can approach this level of acidity (Gatenby & Gillies, 2004). After achieving the whole cell patch clamp configuration in PSS at pH_e 7.2 and performing several recording protocols, the pH_e was changed to 6.2 and the protocols repeated. The effects of changing pH_e on VGSC currents were found to be reversible upon change back to pH 7.2. First the transient Na^+ current elicited by a depolarisation from -120 mV to -10 mV was assessed. At pH_e 6.2 the transient current was reduced to -9.6 ± 1.5 pA/pF from -13.6 ± 2.3 pA/pF at pH_e 7.2 ($P < 0.01$; n = 11 cells; Wilcoxon matched pairs test; Figure 3.10 A and C). In contrast, the persistent Na^+ current measured between 20 and 25 ms after depolarisation was increased on acidification of the PSS. At pH_e 6.2, the persistent Na^+ current was increased to -0.71 ± 0.11 pA/pF from -0.31 ± 0.04 pA/pF at pH_e 7.2 ($P < 0.01$; n = 10 cells; paired *t* test; (Figure 3.10 B and D).

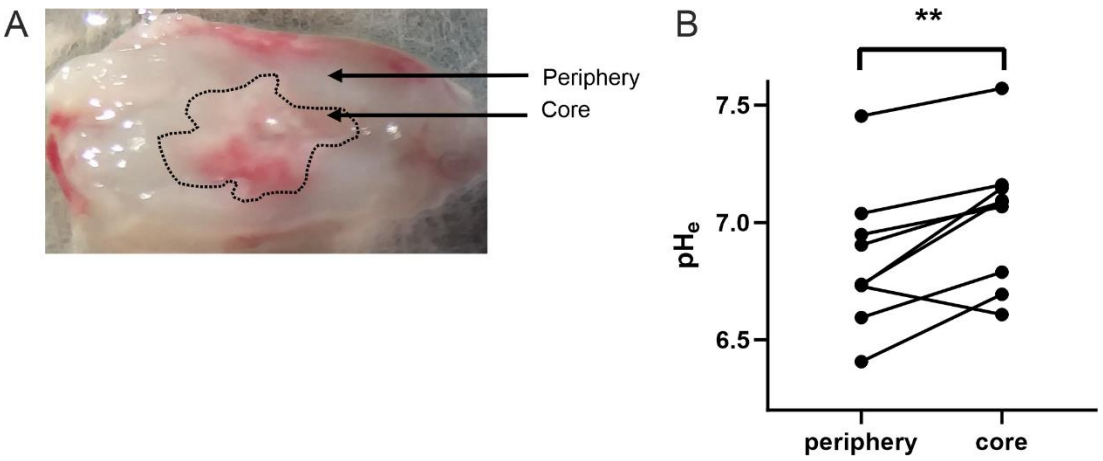

Figure 3.6 pH-sensitive microelectrode recording from MDA-MB-231 xenograft tumour slices.
A. Photograph of a tumour slice showing the difference in appearance between the more translucent periphery and more opaque core of the tumour. **B**. Tumour slice pH measured using pH-sensitive microelectrodes, showing the difference between the core and peripheral regions in each slice ($P < 0.0.1$; n = 9 tumours (one slice from each); results of paired *t* test).

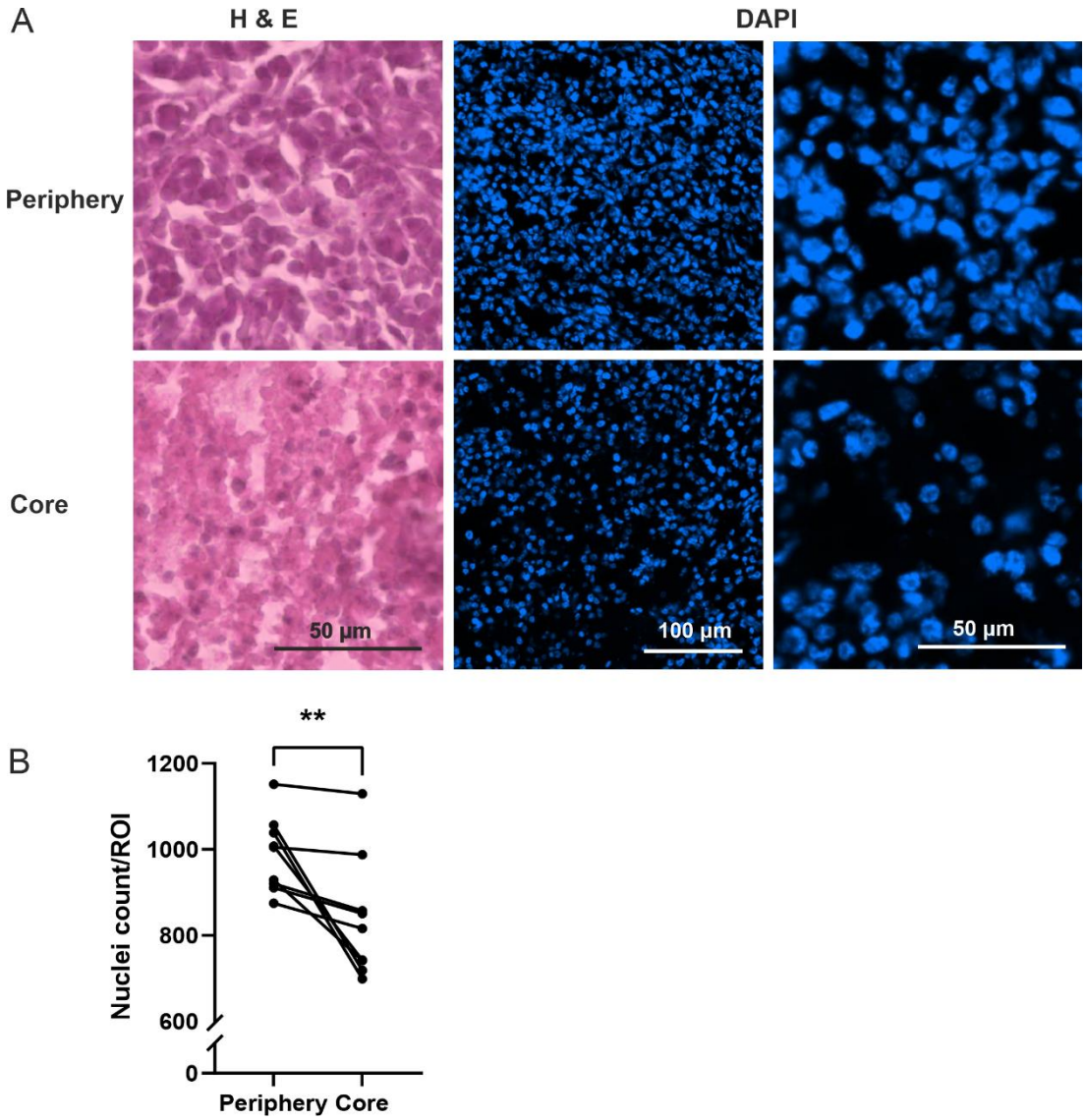

Figure 3.7 Cellularity of MDA-MB-231 xenograft tumour sections made after ISME pH measurement from tissues slices.
A. Examples of sections with DAPI-stained nuclei (blue), taken from the peripheral or core regions of a tumour slice. **B**. Assessment of cellularity in the peripheral and core regions of each section, made by counting DAPI-stained nuclei in anti-activated caspase 3 stained sections ($P < 0.01$; $n = 9$ tumours (one section from each); paired *t* test). Results are mean ± SEM.

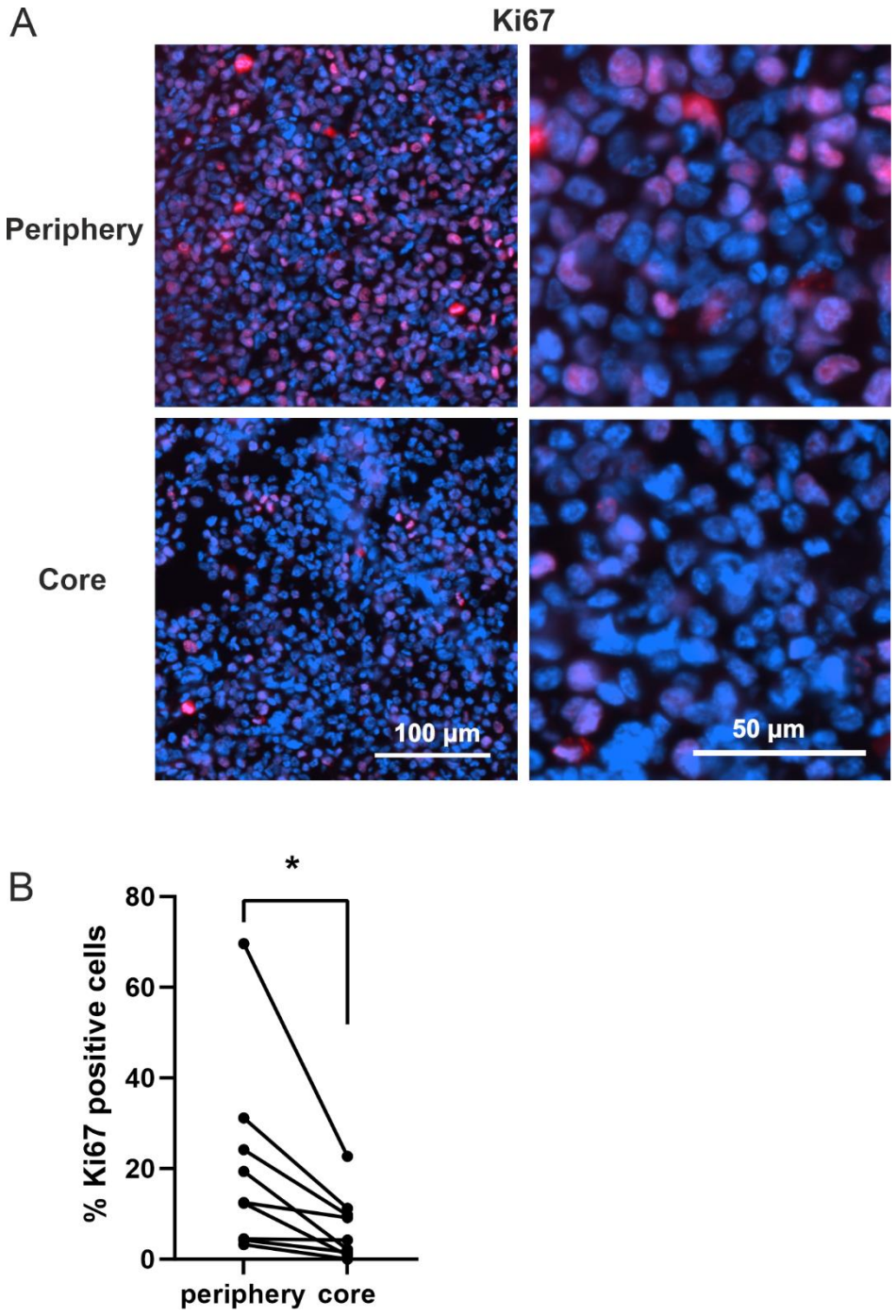

Figure 3.8 Ki67 staining in MDA-MB-231 xenograft tumour sections made after ISME pH measurement from tissues slices.
A. Examples of anti-Ki67 (red) antibody-stained sections with DAPI-stained nuclei (blue), taken from the peripheral or core regions of a tumour slice. **B**. Quantification of Ki67 staining in peripheral and core regions of sections ($P < 0.05$; $n = 9$ tumours (one section from each); paired *t* test). Results are mean ± SEM.

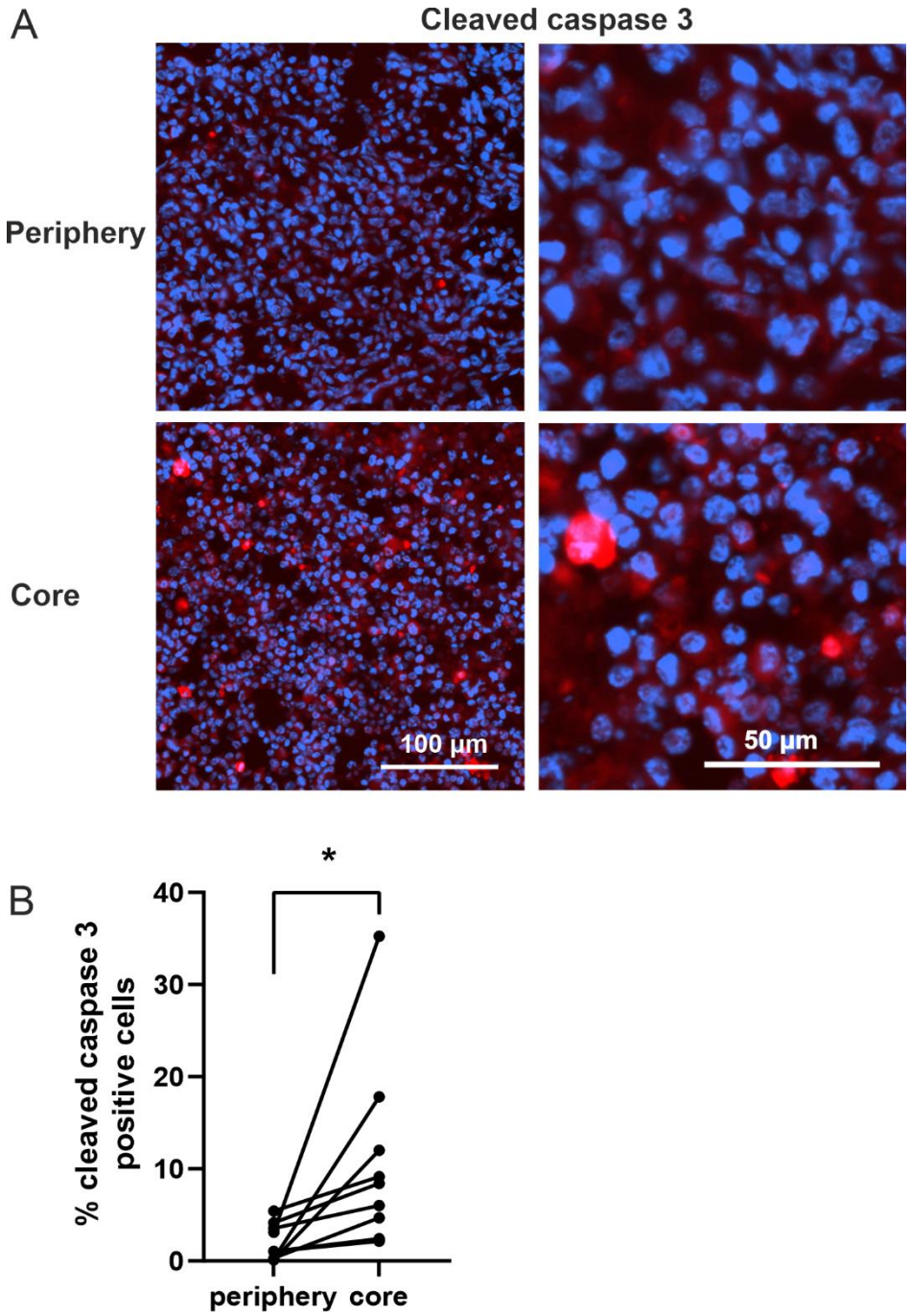

Figure 3.9 Activated caspase 3 staining in MDA-MB-231 xenograft tumour sections made after ISME pH measurement from tissues slices.
A. Examples of anti-activated caspase 3 (red) antibody-stained sections with DAPI-stained nuclei (blue), taken from the peripheral or core regions of a tumour slice. **B**.Quantification of activated caspase 3 staining in peripheral and core regions of sections ($P < 0.05$; n = 9 tumours (one section from each); paired *t* test). Results are mean ± SEM.

Next the effect of pH_e on voltage dependence of activation and inactivation of VGSCs in MDA-MB-231 cells was investigated. To assess voltage dependence of activation, cells were depolarised to a range of voltages, from a holding voltage of -120 mV (Figure 3.11 Ai) to produce an IV relationship (Figure 3.11 B). There was no effect of low pH on the activation curve (Figure 3.11 C). The activation slope (*k*) and voltage of half activation (V½) did not change when the pH_e was reduced from 7.2 to 6.2 (P = 0.077 (*k*) and 0.087 (V½); n = 10 cells; paired *t* tests, (Table 3.2).

3.2.7 Low extracellular pH depolarises VGSC voltage dependence of inactivation in MDA-MB-231 cells.

The voltage dependence of fast inactivation was investigated by changing the holding voltage before the depolarisation pulse (Figure 3.11 Aii and C). The inactivation curve V½ was significantly shifted towards more depolarised voltages, from -80.4 ± 1.4 mV at pH_e 7.2 to -73.3 ± 2.8 mV at pH_e 6.2 ($P < 0.01$; n = 10 cells; paired *t* tests; Table 3.2). The slope of the inactivation curve was also significantly reduced: *k* changed from 8.4 ± 0.8 mV at pH_e 7.2 to 11.9 ± 0.9 mV at pH_e 6.2 ($P < 0.01$; n = 10 cells; paired *t* tests; Table 3.2). The effect of this shift in activation increased the size of the window current, which is the region under both activation and inactivation curves where some channels are open but not all channels are inactivated. The window current is more easily visualised when the y axes from Figure 3.11 C are expanded (Figure 3.11 D). This shows that at the reported resting V_m of MDA-MB-231 cells, -18.9 mV (Fraser *et al.*, 2005), the availability of VGSCs more than doubled from 1.9 ± 0.6 % to 4.9 ± 0.7 % of the maximal availability ($P < 0.05$; n = 10 cells; paired *t* test) when the pH_e was reduced from 7.2 to 6.2 (Figure 3.11 G).

When the pH_e was reduced further to 6.0, the effect on the inactivation curve and the window current was even larger than at pH_e 6.2. The inactivation V½ changed from -78.2 ± 2.1 mV at pH_e 7.2 to 71.8 ± 2.9 mV at pH_e 6.0 ($P < 0.01$; n = 8 cells; paired *t* test; Figure 3.11 E and F), although the inactivation *k* was not significantly different (P= 0.13; n = 8 cells; paired *t* test; Figure 3.11 E and F). The activation curve was also shifted to less

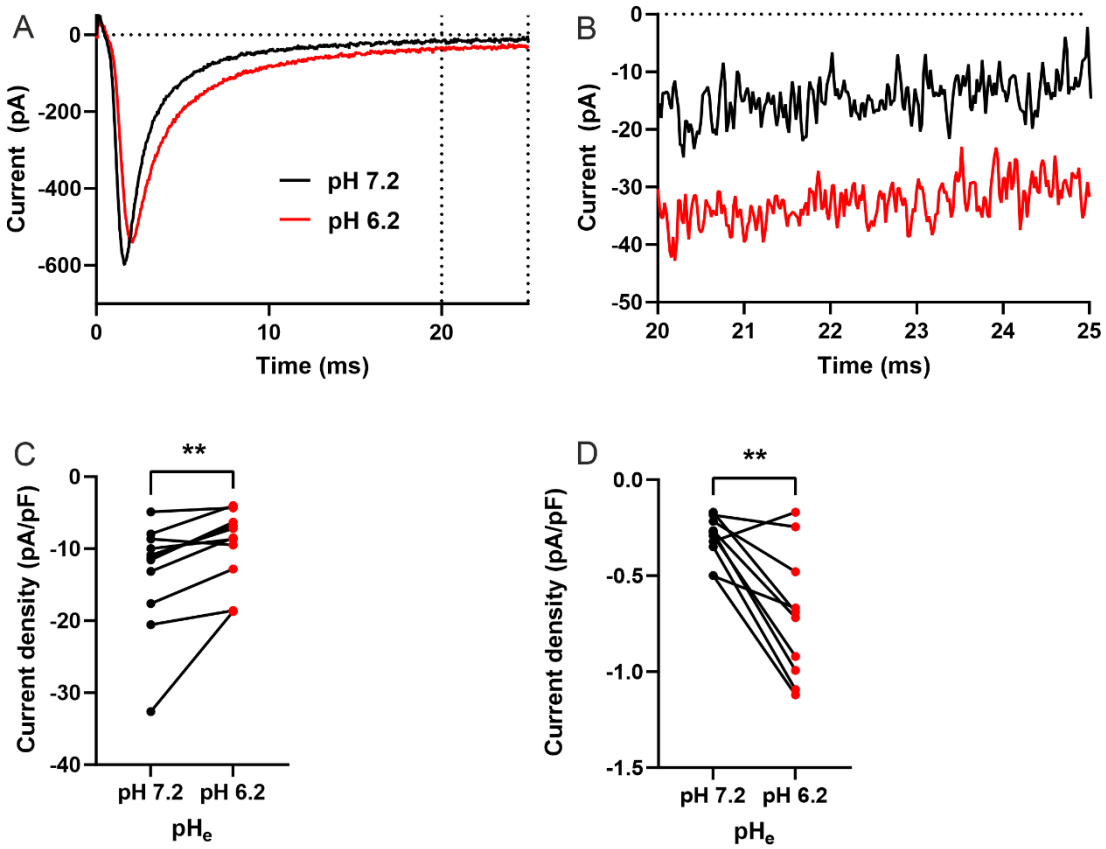

Figure 3.10. Low pH_e inhibits transient VGSC Na^+ currents but increases persistent currents. **A**. Example VGSC Na^+ currents elicited by depolarisation to 0 mV from a holding voltage of -120 mV. **B**. Expanded graph from **A**. between 20 and 25 ms after depolarisation. **C**. Peak current density of Na^+ currents as in **A**. ($P < 0.01$; n = 11 cells, Wilcoxon matched pairs test). **D**. Mean persistent Na^+ current density measured between 20 and 25 ms after depolarisation ($P < 0.01$; n = 10 cells; paired *t* test). Results are mean ± SEM.

negative voltages at pH 6.0 (V½ shifted from -17.7 ± 1.1 mV at pH 7.2 to -9.5 ± 1.1 mV at pH 6.0; $P < 0.0001$; n = 8 cells; paired *t* test; Figure 3.11 E and F). A depolarising shift in the activation curve has the potential to reduce the window current, but this shift did not limit the window current at the resting V_m of -18.9 mV. Indeed, due to the larger shift in the inactivation curve at pH 6.0, the window current increased nearly five-fold from 2.1 ± 0.9 % to 10.3 ± 2.2 % of the maximal available current when the pH_e was reduced from 7.2 to 6.0 ($P < 0.001$; n = 8 cells, paired *t* test; Figure 3.11 H).

Although transient currents have not been demonstrated to occur in non-excitable cells such as breast cancer cells, for completeness the activation kinetics were assessed by measuring time to peak current at various depolarisation voltages. When depolarising from -120 mV to -10 mV, the time from depolarisation to the peak of the transient current was longer at pH_e 6.2 (3.02 ± 0.35 ms compared to 2.07 ± 0.24 ms at pH 7.2) ($P < 0.001$; n = 10; paired *t* test; Table 3.2). When assessing the time to peak at each voltage, qualitatively, the time to peak appeared to be longer at each voltage when the pH_e was 6.2 than when it was 7.2 (Figure 3.11 I), however there was no significant difference in τ of the single exponential line of best fit between the two pHs ($P = 0.24$; n = 10; paired *t* test).

3.2.8 Low extracellular pH decreases intracellular pH

Changing the pH of the PSS could affect VGSCs in a variety of ways. In particular, H^+ could be binding to channels on the intracellular or extracellular side. This is important to ascertain in the context of cancer, because although the pH_e in tumours is usually lower than normal, the pH_i is usually slightly higher than normal (White *et al.*, 2017). To investigate how pH_i is affected by changes in pH_e in this experimental context, pH_i was measured using the ratiometric, fluorescent H^+ indicator BCECF-AM (Section 2.13.2). In these experiments, pH_i followed changes in pH_e, indicating that it was possible that H^+ was altering gating by binding to the intracellular side of VGSCs (Figure 3.12).

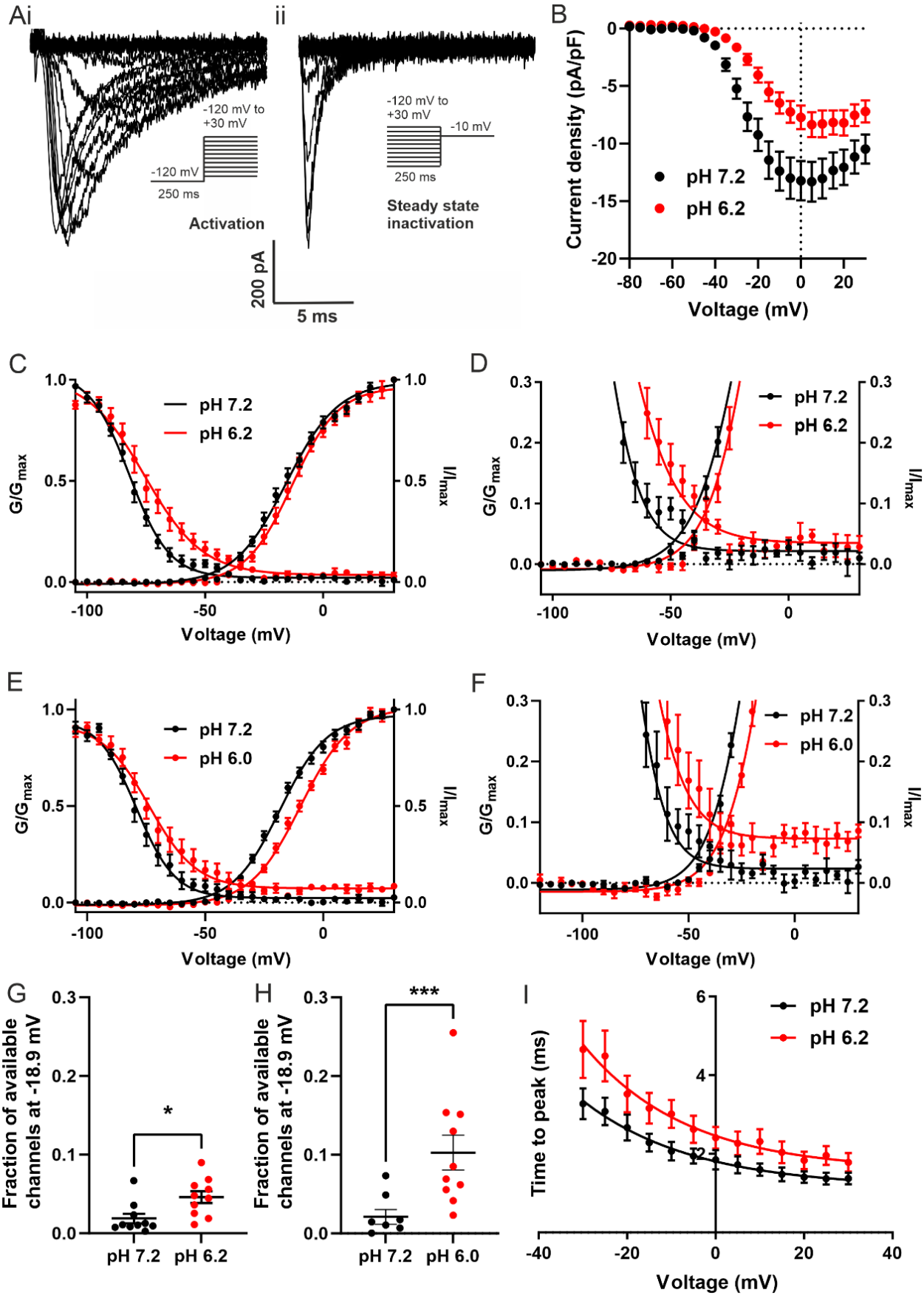
Ai
ii
-120 mV to
+30 mV
-120 mV
250 ms
Activation
-120 mV to
+30 mV
-10 mV
250 ms
Steady state
inactivation
200 pA
5 ms
B
Current density (pA/pF)
pH 7.2
pH 6.2
Voltage (mV)
C
G/Gmax
I/Imax
pH 7.2
pH 6.2
Voltage (mV)
D
pH 7.2
pH 6.2
Voltage (mV)
E
pH 7.2
pH 6.0
Voltage (mV)
F
pH 7.2
pH 6.0
Voltage (mV)
G
Fraction of available channels at -18.9 mV
*
pH 7.2
pH 6.2
H
Fraction of available channels at -18.9 mV
***
pH 7.2
pH 6.0
I
Time to peak (ms)
pH 7.2
pH 6.2
Voltage (mV)

Figure 3.11. Effect of extracellular pH on voltage dependence of activation and inactivation of VGSCs.
A.**i**. Example family of Na^+ currents generated by the activation voltage clamp protocol (inset). **ii**. Example family of Na^+ currents generated by the steady-state inactivation voltage clamp protocol (inset). **B**. Average current density/voltage relationship generated by the activation voltage clamp protocol (inset) at pH 7.2 or 6.2 (n = 17 cells). **C**. Overlay of activation and inactivation curves at pH 7.2 and 6.2 (n = 10 cells with largest currents). **D**. Expanded graph from **C**. showing the window current which is the area under both activation and inactivation curves. This area is larger at pH 6.2 than at pH 7.2 and shifted towards less negative voltages. **E**. Overlay of activation and inactivation curves at pH 7.2 and 6.0 (n = 16 for activation and 8 for inactivation curves). **F**. Expanded graph from **E**. showing the window current which is the area under both activation and inactivation curves. This area is larger at pH 6.0 than at pH 7.2, and shifted towards less negative voltages. This shows a greater increase in window current with a larger reduction in pH. **G**. Fraction of channels available at the reported resting membrane potential in MDA-MB-231 cells of -18.9 mV, at pH 7.2 and 6.2, showing a greater proportion of channels are available at pH 6.2 (n = 10 cells with largest currents). **H**. Fraction of channels available at the reported resting membrane potential in MDA-MB-231 cells of -18.9 mV, at pH 7.2 and 6.0, showing a greater proportion of channels are available at pH 6.0 (P = 0.0007; n = 8 cells; paired *t* test). **I**. Time from depolarisation to peak current, at various depolarisation voltages. Comparison between pH 7.2 and pH 6.2, showing that transient currents are generally slower at pH 6.2 (n = 10 cells). Results are mean ± SEM.

Table 3.2. Effect of reduced pH on VGSC Na^+ current parameters.

Parameter	pH 7.2	pH 6.2	P	N
Peak current density (pA/pF)	-13.5 ± 2.3	9.6 ± 1.5	0.006	11
Persistent current density (pA/pF)	-0.31 ± 0.04	-0.71 ± 0.11	0.006	10
Activation V½ (mV)	-15.2 ± 2.0	-12.9 ± 1.8	0.087	10
Activation *k* (mV)	10.7 ± 0.5	9.5 ± 0.4	0.077	10
Inactivation V½ (mV)	-80.4 ± 1.4	-73.3 ± 2.8	0.003	10
Inactivation *k* (mV)	8.4 ± 0.8	11.9 ± 0.9	0.005	10
T_p at -10 mV (ms)	2.07 ± 0.24	3.02 ± 0.35	< 0.001	10

V½: half (in)activation voltage; k: slope factor for (in)activation; T_p: time to peak current; The holding potential was -120 mV. Results are mean ± SEM. Statistical comparisons were made with paired *t*-tests on non-normalised data.

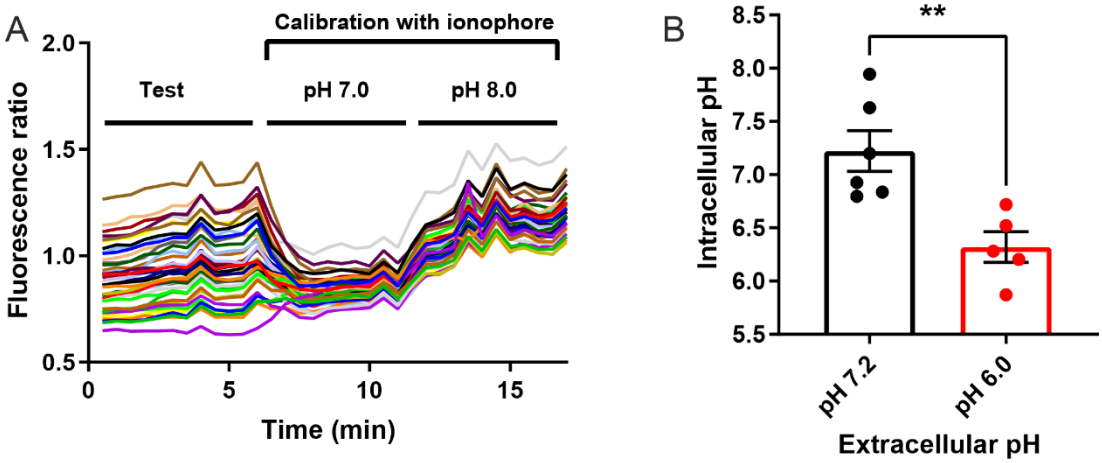

Figure 3.12 Effect of extracellular pH on intracellular pH.
A. Example two-point calibration of BCECF-AM fluorescence ratio in 40 MDA-MB-231 cells on a coverslip. **B**. Effect of 10-minute incubation with PSS at pH 7.2 or 6.0 on pH_i in MDA-MB-231 cells ($P < 0.01$; n = 5-6 experiments of 40 cells each; unpaired *t* test). Results are mean ± SEM.

3.2.9 Altering intracellular pH does not affect VGSC currents or gating

To investigate whether pH_i affects VGSC current or gating, the pH of the intracellular solution was altered in patch clamp experiments, and similar recording protocols were performed as in sections 3.2.6 and 3.2.7. The pH was changed in the range pH_i 7.2 to pH_i 7.6 to avoid affecting the quality of the glass to membrane seal necessary for patch clamp recording. This change did not affect peak VGSC Na^+ current (P = 0.36; n = 10 cells; unpaired *t* test; Figure 3.13 A); nor did it affect persistent Na^+ current (P = 0.89; n = 11 or 13 cells; unpaired *t* test; Figure 3.13 B). In addition, the change in pH_i did not affect the current/voltage relationship (Figure 3.13 C) or the voltage dependence of activation or inactivation (Figure 3.13 D and E). The V½ of activation was unchanged (P = 0.33; n = 10 or 11 cells; unpaired *t* test), the k (slope constant) of activation was unchanged (P = 0.30; n = 10 or 11 cells; unpaired *t* test). The V½ of inactivation was also unchanged (P = 0.14; n = 10 or 12 cells; unpaired *t* test) and the k (slope constant) of activation was unchanged (P = 0.55; n = 10 or 12 cells; unpaired *t* test).

In summary, the results from this section show that VGSCs in MDA-MB-231 cells are sensitive to pH_e but not sensitive to pH_i. If the pH_e is reduced from pH 7.2 to 6.2, a pH_e commonly found in the tumour microenvironment, transient Na^+ currents are decreased but persistent Na^+ currents are increased. The persistent current is increased due to a depolarising shift of the voltage dependence of inactivation at low pH_e. Thus, low pH_e in the tumour microenvironment might provide a physiological basis for $[Na^+]_i$ elevation via VGSC activity.

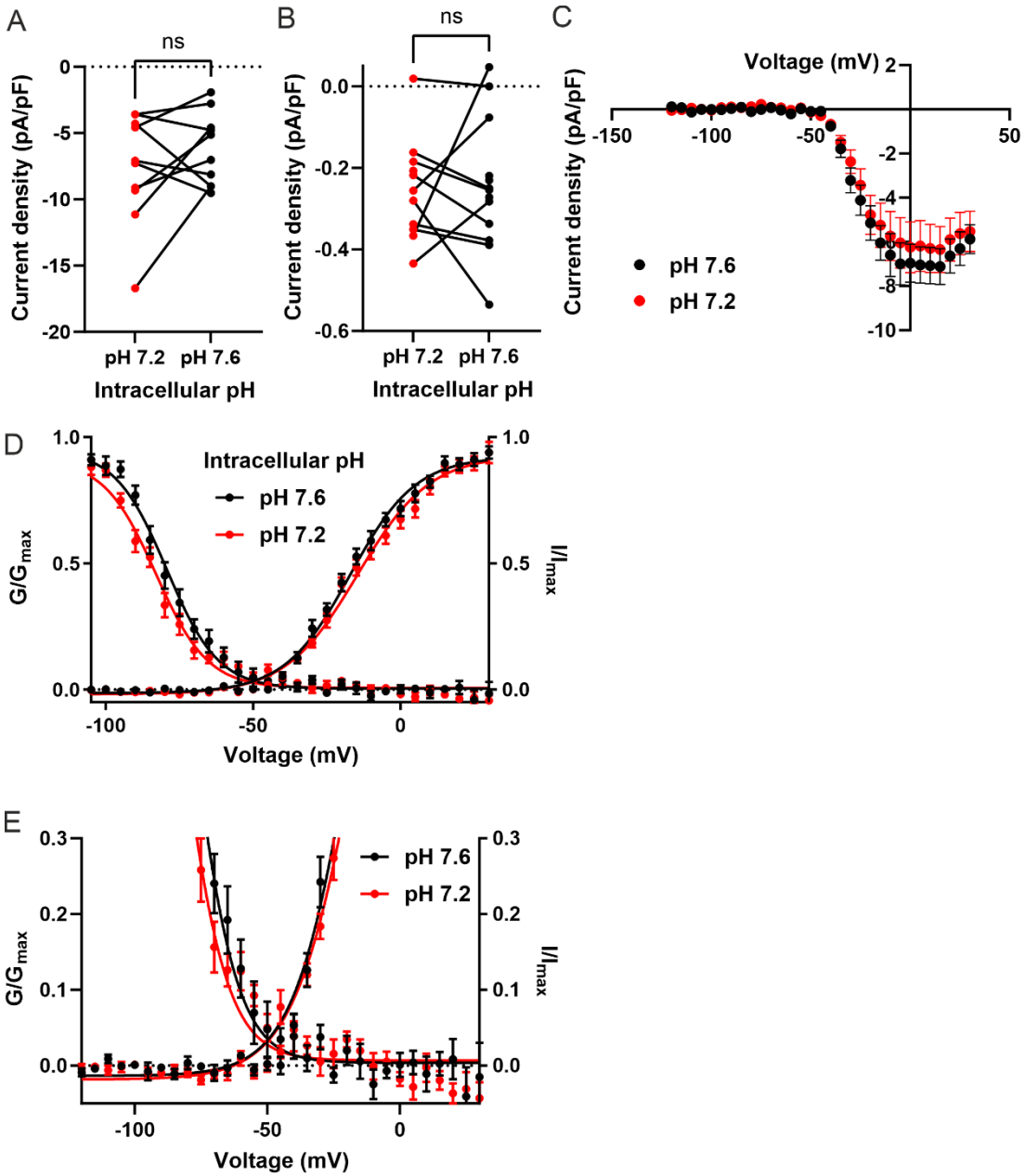

Figure 3.13 Effect of intracellular pH on VGSC currents and gating.
A. Peak current density of Na^+ currents (P = 0.36; n = 10 cells, unpaired *t* test). **B**. Mean persistent Na^+ current density measured between 20 and 25 ms after depolarisation (P = 0.89; n = 11-13 cells; unpaired *t* test). **C**. Average current density/voltage relationship generated by the activation voltage clamp protocol at pH_i 7.2 or 7.6 (n = 10-12 cells). **D**. Overlay of activation and inactivation curves at pH_i 7.2 and 7.6 (n = 10-12 cells). **E**. Expanded graph from **D**. showing the window current which is the area under both activation and inactivation curves. This area is unchanged between pH_i of 7.2 and 7.6. Results are mean ± SEM.

3.2.10 Investigating the mechanism of VGSC-induced extracellular acidification

Several publications have shown that VGSC activity in cancer cells increases H^+ extrusion through NHE1 (Brisson *et al.*, 2011; Brisson *et al.*, 2013), leading to increased invasion. The mechanism underlying this H^+ extrusion is not clear, since influx of Na^+ via VGSCs would be expected to reduce the inward Na^+ gradient which drives NHE1-dependent H^+ extrusion, therefore VGSC-induced extracellular acidification is counter-intuitive. In this thesis, the theory being tested is that VGSC activity increases activity of the NKA, which consumes ATP derived from glycolysis. VGSC activity might thereby increase the rate of glycolysis in cancer cells leading to the production of lactate and H^+, which is then extruded via NHE1, lowering the pH_e.

3.2.10.1 Na^+-dependent regulation of intracellular pH

First, an experiment was carried out to determine whether extracellular Na^+ is necessary for normal pH_i control in MDA-MB-231 cells. Extracellular Na^+ was replaced with NMDG for a period of 10 minutes and the pH_i response to this manoeuvre was assessed using BCECF-AM. Intracellular pH decreased when Na^+ was not present in the PSS ($P < 0.01$; $n = 3$ experiments of 40 cells each; one-way ANOVA with Tukey's multiple comparisons test), indicating that a Na^+-dependent mechanism is likely to be important for pH_i control in these experimental conditions (Figure 3.14).

Both the Na^+/HCO_3^- exchanger and NHE1 use the inward Na^+ gradient to regulate pH_i. Given there is no HCO_3^- in the standard electrophysiological solutions used here, NHE1 is likely a more important regulator of pH_i than the Na^+/HCO_3^- exchanger in these conditions. The next experiment was therefore designed to investigate the effect of the NHE1 inhibitor cariporide on pH_i. The rate of change in pH_i was assessed before and after addition of 20 μM cariporide to the PSS perfusate (Figure 3.15 A). This assay showed high variability in the

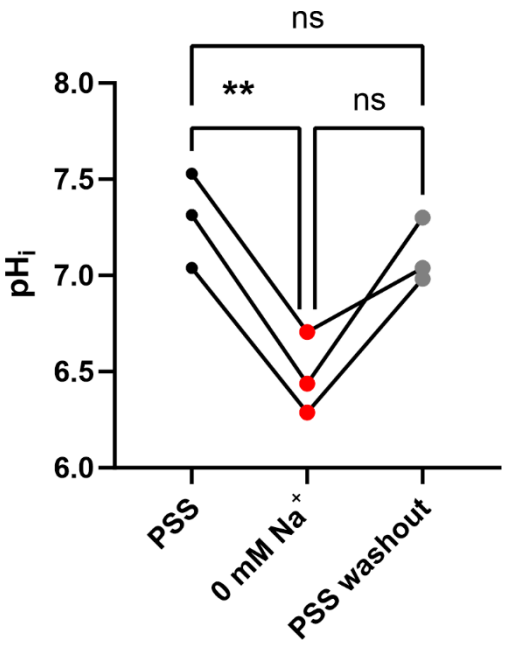

Figure 3.14 Effect of extracellular Na^+ depletion on intracellular pH in MDA-MB-231 cells. Cells loaded with BCECF-AM were first perfused with PSS with 144 mM Na^+ and then 0 mM Na^+ (replaced with NMDG) for 10 minutes, after which 144 mM Na^+ PSS was reintroduced. BCECF-AM fluorescence ratio was calibrated in each cell at the end of each experiment. ($P < 0.01$; n = 3 experiments of 40 cells each; one-way ANOVA with Tukey's multiple comparisons test). Results are mean ± SEM.

baseline pH change/min but cariporide induced an increased rate of pH_i acidification ($P < 0.01$; n = 6 experiments of 40 cells each; paired *t* test; Figure 3.15 B). These results are consistent with previously published data linking NHE1 to pH_i (Busco *et al.*, 2010; Brisson *et al.*, 2011).

Since NKA predominantly utilises ATP derived from glycolysis in many tissues (James *et al.*, 1996; Epstein *et al.*, 2014), this ATP consumption in turn would increase glycolytic production of acidic metabolites. NKA activity was expected to increase production of intracellular H^+, therefore pH_i was measured when NKA was inhibited with ouabain (Figure 3.15 C). Due to difficulties in assessing when the fluorescence ratio had reached a stable baseline, this experiment was performed differently from the cariporide experiment above. Instead of comparing the rate of pH change at the start of the experiment (control) with the end of the experiment (treatment), the rate of pH change was measured during 10 minutes at the end of the experiment, perfusing on PSS with/without treatment. There was considerable variability in rate of pH change and ouabain had no effect ($P = 0.78$; n = 4 experiments of 40 cells each; unpaired *t* test; Figure 3.15 D).

It is possible that due to the cell's buffering capacity, a change in the production rate of acidic metabolites might not significantly alter the pH_i. The above experiment was therefore repeated, while disabling the main pH control mechanism, NHE1 from removing excess H^+. The hypothesis was that cariporide would cause the pH_i to decrease rapidly, but when ouabain was present to inhibit NKA at the same time, (thereby reducing the glycolytic rate), the pH_i would reduce less rapidly. The rate of pH_i change in cariporide treatment was compared with the rate of pH_i change in cariporide + ouabain treatment (Figure 3.15 E). There was no significant difference in the rate of pH change between the treatments ($P = 0.17$; n = 7 experiments of 40 cells each; unpaired *t* test; Figure 3.15 F). These results show that there was no detectable change in intracellular pH_i due to perturbation of NKA activity.

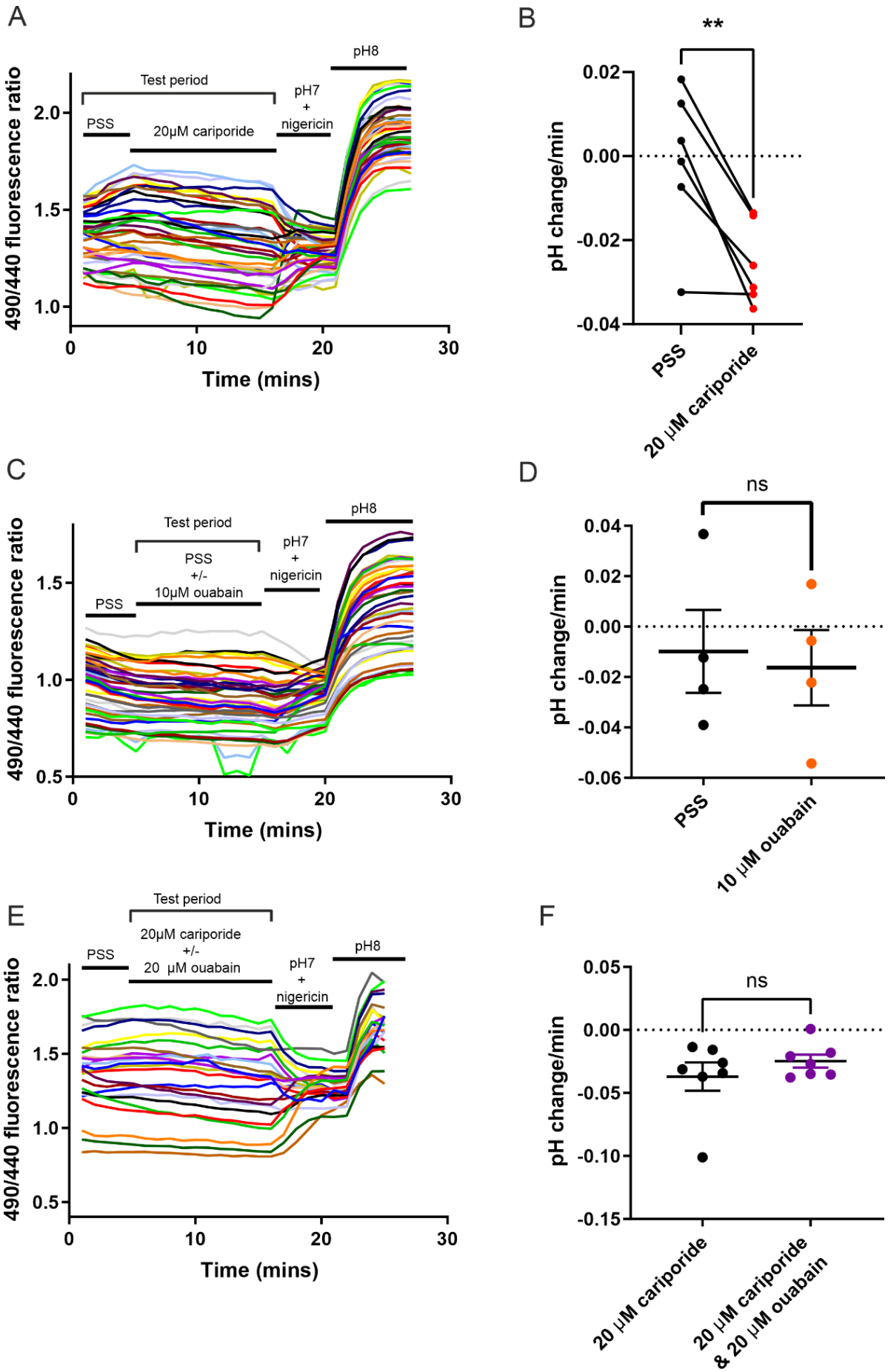
A
Test period
pH8
PSS
20μM cariporide
pH7
+
nigericin
490/440 fluorescence ratio
Time (mins)
B
**
pH change/min
PSS
20 μM cariporide
C
Test period
pH8
PSS
+/-
10μM ouabain
pH7
+
nigericin
490/440 fluorescence ratio
Time (mins)
D
ns
pH change/min
PSS
10 μM ouabain
E
Test period
20μM cariporide
+/-
20 μM ouabain
PSS
pH8
pH7
+
nigericin
490/440 fluorescence ratio
Time (mins)
F
ns
pH change/min
20 μM cariporide
20 μM cariporide
& 20 μM ouabain

Figure 3.15 Effects of NHE1 and NKA inhibition on rate of change of intracellular pH. **A**. Example BCECF-AM fluorescence ratio recordings from 40 cells on a coverslip, to measure the rate of change of pH_i in control PSS with that in 20 μM cariporide. Calibration was performed in each cell at the end of the experiment. **B**. Rate of change of pH_i before and after addition of cariporide to PSS perfusate ($P < 0.01$; n = 6 experiments with 40 cells in each; paired *t* test). **C**. Example BCECF-AM fluorescence ratio recordings to compare rate of pH change in control PSS with that in 10 μM ouabain treatment. **D**. Rate of change of pH_i in control PSS or 10 μM ouabain ($P = 0.78$; n = 4 experiments of 40 cells each; unpaired *t* test). **E**. Example BCECF-AM fluorescence ratio recordings to compare rate of pH change in 20 μM cariporide with that in 20 μM cariporide + 20 μM ouabain. **F**. Rate of change of pH_i in cariporide alone or cariporide + ouabain ($P = 0.17$; n = 7 experiments of 40 cells each; unpaired *t* test). Results are mean ± SEM.

3.2.10.2 Effect of VGSC and NKA inhibition on lactate production

To test whether VGSC activity and NKA activity increase the rate of glycolysis, lactate in the culture medium was assayed as a measure of glycolytic flux. First it was necessary to find a concentration of ouabain which would inhibit NKA activity without causing cell death within the time frame of the experiment. SBFI-AM was used in a plate reader to measure accumulation of $[Na^+]_i$ as a read-out of NKA inhibition (Section 2.13.4). Dose-response curves were generated for 2-hour and 6-hour incubations of MDA-MB-231 cells with ouabain (Figure 3.16 A). These results showed that 30 nM ouabain had little effect after 2 hours, but approximately 2/3 maximal effect after 6 hours. A concentration of 300 nM after 6 hours had a maximal effect. Ouabain concentrations as high as 3 μM for 6 hours caused no loss of viability of MDA-MB-231 cells as assessed by a Trypan blue assay ($P = 0.45$; $n = 3$ wells from one experiment; one-way ANOVA; Figure 3.16 B). Therefore a concentration of 300 nM ouabain was chosen for further experiments.

A colorimetric lactate assay was used to measure lactate secreted by MDA-MB-231 cells and MCF7 cells. To test the kit's ability to detect changes in lactate production, cells were incubated for two hours with oligomycin which inhibits oxidative phosphorylation by blocking ATP synthase, or iodoacetic acid which inhibits glycolysis by inhibiting GAPDH. The standard curve generated using the provided lactate reagent showed that the relationship of absorbance ratio to $\log_{10}$ [lactate] followed a sigmoid relationship (Figure 3.17 A).

Two-hour treatment with oligomycin to inhibit oxidative phosphorylation resulted in a significant increase in lactate production in MCF7 cells ($P < 0.05$; $n = 3$ experimental repeats; paired *t* test; Figure 3.17 C), but the increase was not significant in MDA-MB-231 cells ($P = 0.11$; $n = 3$ experimental repeats; paired *t* test) (Figure 3.17 G).

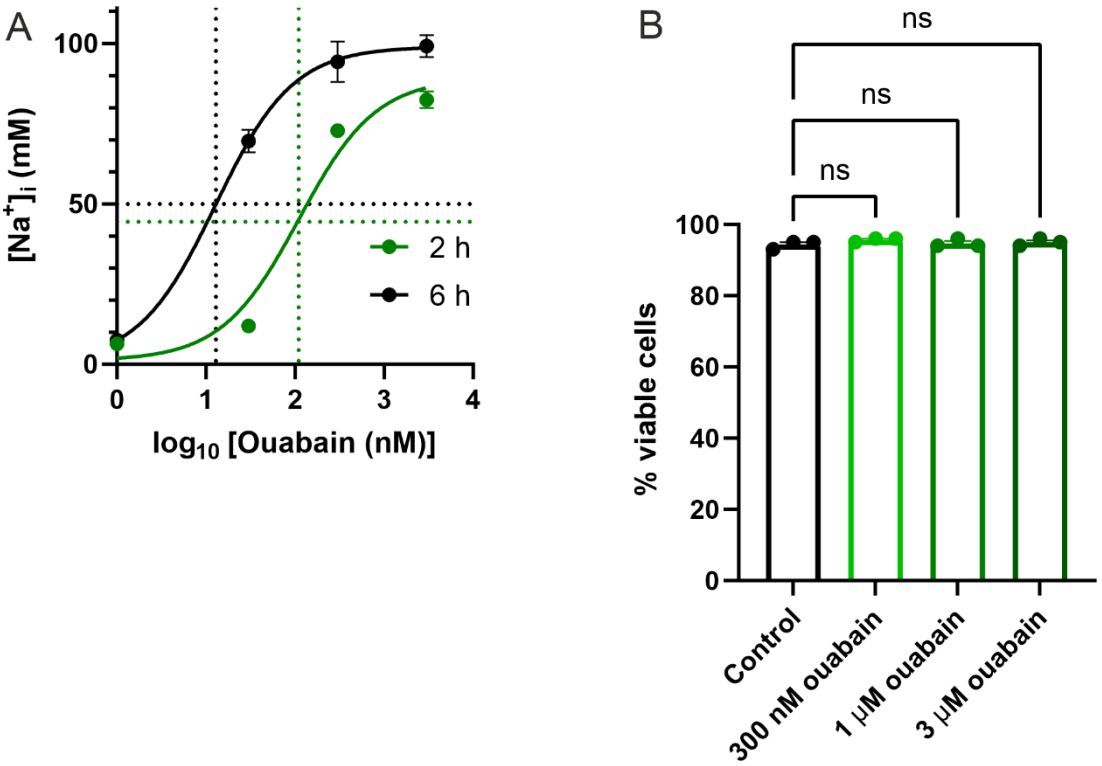

Figure 3.16 Optimisation of ouabain dose and incubation period for lactate assays.
A. Dose response curve showing the effect of ouabain on [Na+]i in MDA-MB-231 cells at two incubation durations (5 wells per condition). Dotted lines show IC50 for each incubation duration. B. Viability of MDA-MB-231 cells after incubation with various concentrations of ouabain for 6 h (P = 0.45; n = 3 wells from one experiment; one-way ANOVA with Dunnett's multiple comparisons test). Results are mean ± SEM.

Two hour treatment with iodoacetic acid to inhibit glycolysis resulted in a significant decrease in lactate production in MCF7 cells ($P < 0.05$; n = 3 experimental repeats; paired *t* test; Figure 3.17 D), but the decrease was not significant in MDA-MB-231 cells ($P = 0.16$; n = 3 experimental repeats; paired *t* test; Figure 3.17 H).These results show that the lactate assay kit was giving expected results, although the sample size may have been too small to reliably quantify changes in lactate production by MDA-MB-231 cells.

During the same assay, the effect of 24 h TTX incubation on lactate production was tested. TTX did not change lactate production by MCF7 cells ($P = 0.11$; n = 3 experimental repeats; paired *t* test; Figure 3.17 E) but it decreased apparent lactate production by MDA-MB-231 cells, although the latter effect was not significant ($P = 0.052$; n = 3 experimental repeats; paired *t* test; Figure 3.17 I). To assess whether NKA activity affects glycolytic rate, lactate production was assessed during incubation with ouabain. Surprisingly, a six-hour incubation with 300 nM ouabain significantly increased apparent lactate production by MCF7 cells ($P < 0.01$; n = 3 experimental repeats; paired *t* test; Figure 3.17 F) but did not change that of MDA-MB-231 cells ($P = 0.17$; n = 3 experimental repeats; paired *t* test; Figure 3.17 J). The lactate assay was repeated once more with a new kit to increase the sample sizes in these experiments but the findings could not be replicated due to experimental issues with the second kit.

3.2.11 Viability and Na^+ accumulation with metabolic inhibitors

Viability of MDA-MB-231 cells and MCF7 cells was assessed after incubation with oligomycin, iodoacetic acid and ouabain after the medium from these cells was used for the lactate assay. MCF7 cells were found to be far more sensitive to the effects of ouabain than MDA-MB-231 cells, since a six hour treatment with 300 nM ouabain reduced their viability by 16 % ($P < 0.05$; n = 3 experimental repeats; one sample *t* test; Figure 3.18 B) whereas 300 nM ouabain had no effect on MDA-MB-231 viability ($P = 0.18$; n = 3 experimental repeats; one sample *t* test; Figure 3.18 A). $[Na^+]_i$ accumulation was measured using SBFI-

AM in a plate reader and it was increased by a similar amount in MCF7 and MDA-MB-231 cells after 6 h incubation with 300 nM ouabain ($P < 0.001$ for both cell lines; $n = 3$ experimental repeats; one sample *t* tests; Figure 3.18 C and D).

Two hour incubation with a 1 μM oligomycin had no effect on viability in either cell line ($P = 0.74$ (MDA-MB-231) and $P = 0.84$ (MCF7); $n = 3$ experimental repeats; one sample *t* tests; Figure 3.18 A and B), whereas 2 h incubation with 2 mM iodoacetic acid greatly reduced viability in both cell lines ($P < 0.01$ (MDA-MB-231) and $P < 0.05$ (MCF7); $n = 3$ experimental repeats; one sample *t* tests; Figure 3.18 A and B), indicating that in these experimental conditions, both cell lines were reliant on glycolytic respiration but could cope with loss of oxidative phosphorylation capacity. Similarly, oligomycin treatment did not change the $[Na^+]_i$ in either cell line ($P = 0.62$ (MDA-MB-231) and $P = 0.14$ (MCF7); $n = 3$ experimental repeats; one sample *t* test; Figure 3.18 C and D), whereas iodoacetic acid increased $[Na^+]_i$ significantly in both cell lines, but to a greater extent in MDA-MB-231 cells than in MCF7 cells ($P < 0.01$ for both cell lines; $n = 3$ experimental repeats; one sample *t* test; Figure 3.18 C and D).

In summary, the results from this section suggest that both MDA-MB-231 and MCF7 cells rely on glycolysis for survival in these experimental conditions and they can survive without oxidative phosphorylation for at least two hours. In addition, NKA which drives Na^+ export in both cell lines, activity requires ATP derived from glycolysis, but not from oxidative phosphorylation.

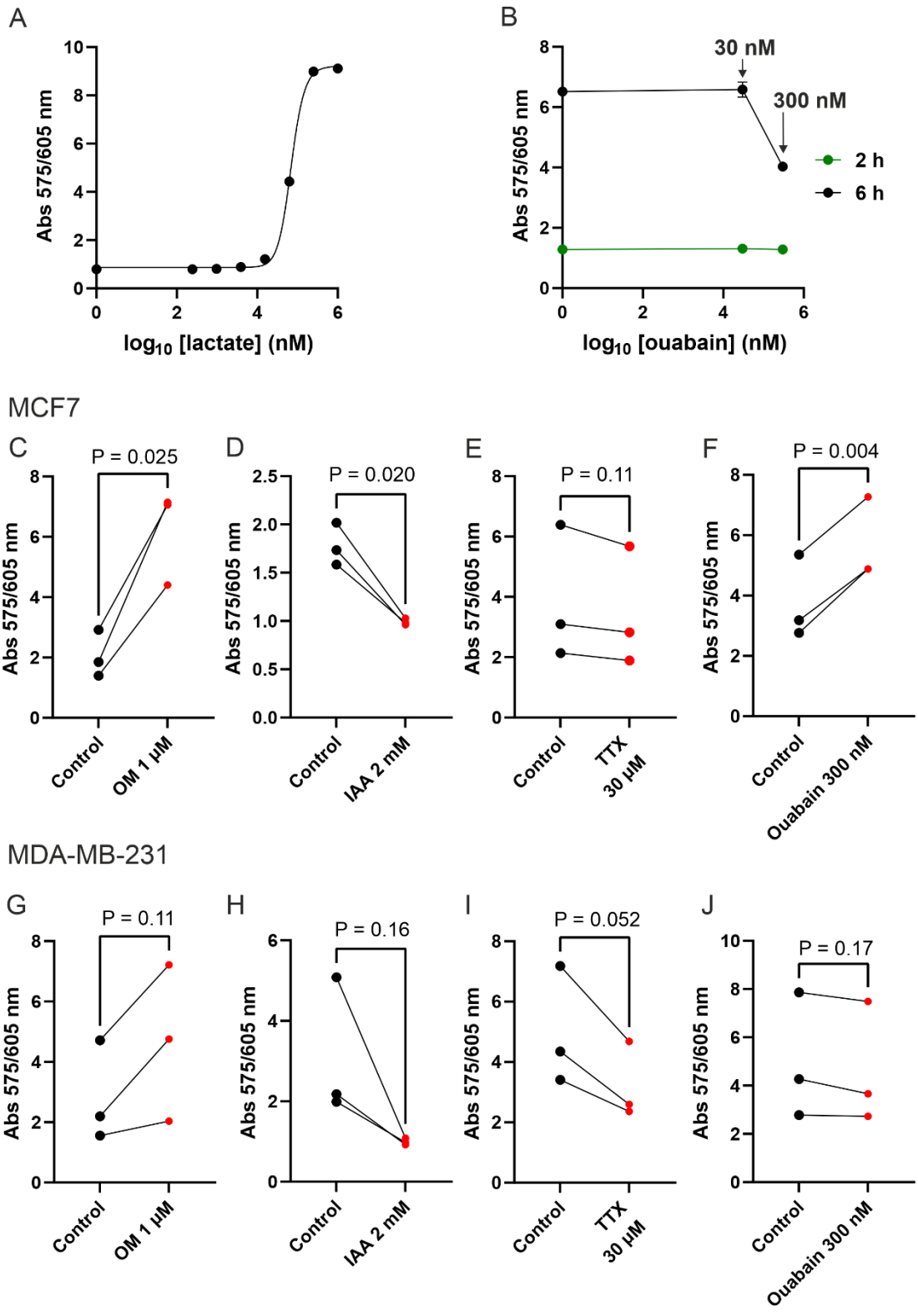
A
Abs 575/605 nm
log10 [lactate] (nM)
B
30 nM
300 nM
2 h
6 h
Abs 575/605 nm
log10 [ouabain] (nM)
MCF7
C
P = 0.025
Abs 575/605 nm
Control
OM 1 µM
D
P = 0.020
Control
IAA 2 mM
E
P = 0.11
Control
TTX 30 µM
F
P = 0.004
Control
Ouabain 300 nM
MDA-MB-231
G
P = 0.11
Control
OM 1 µM
H
P = 0.16
Control
IAA 2 mM
I
P = 0.052
Control
TTX 30 µM
J
P = 0.17
Control
Ouabain 300 nM

Figure 3.17 Lactate assays with inhibitors oligomycin (OM), iodoacetic acid (IAA), tetrodotoxin (TTX) and ouabain.
A. Standard curve generated using the provided lactate standard in the Amplite L-lactate assay kit. **B**. Initial experiment to determine a suitable dose and duration of ouabain treatment of MDA-MB-231 cells for a lactate assay, showing an approximately 2-fold reduction in lactate assay absorbance ratio with 300 nM ouabain for 6 h ($P < 0.001$; $n = 3$ wells in one experiment; unpaired *t* test). **C**. Lactate assay absorbance ratio in culture medium from MCF7 cells incubated for 2 h with 1 μM OM or control ($P < 0.05$; $n = 3$ experiments of 3 wells each; paired *t* test). **D**. Lactate assay absorbance ratio from MCF7 cells incubated for 2 h with 2 mM IAA or control. **E**. Lactate assay absorbance ratio from MCF7 cells incubated for 24 h with 30 μM TTX or control. **F**. Lactate assay absorbance ratio from MCF7 cells incubated for 6 h with 300 nM ouabain or control. **G-J**. As above in **C-F** but in MDA-MB-231 cells (P values for **C-J** stated on each graph; $n = 3$ experiments of 3 wells each; paired *t* tests). Results are mean ± SEM.

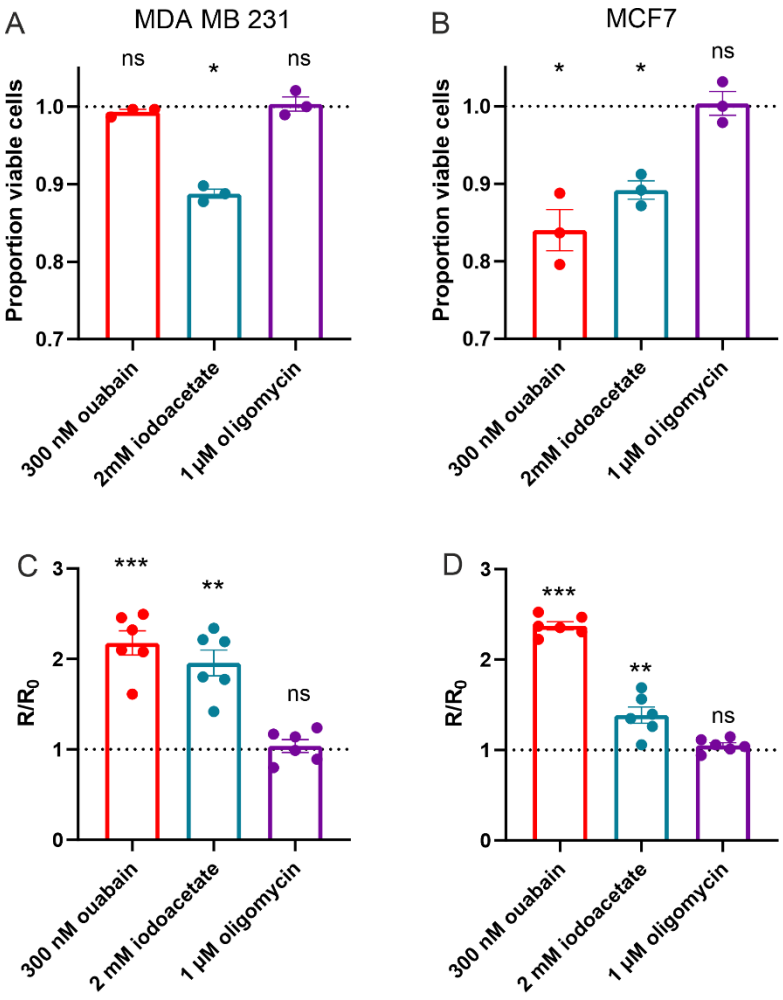

Figure 3.18 Effect of ouabain and metabolic inhibitors on viability and $[Na^+]_i$ accumulation in MCF7 and MDA-MB-231 cells.
A. Trypan blue viability of MCF7 cells after 6 h treatment with the NKA inhibitor ouabain ($P < 0.05$), or 2 h treatment with the glycolytic inhibitor iodoacetate ($P < 0.05$) or the inhibitor of oxidative phosphorylation, oligomycin ($P = 0.84$). (n = 3 experimental repeats; one sample *t* tests). **B**. Trypan blue viability of MDA-MB-231 cells after 6 h treatment with ouabain ($P = 0.18$) or 2 h treatment with iodoacetate ($P < 0.01$) or oligomycin ($P = 0.74$). (n = 3 experimental repeats; one sample *t* tests). **C**. SBFI-AM fluorescence ratios normalised to the ratio in the control condition of MDA-MB-231 cells after 6 h treatment with ouabain ($P < 0.001$), or 2 h treatment with iodoacetate ($P < 0.01$) or oligomycin ($P = 0.62$). **D**. Normalised SBFI-AM fluorescence ratios of MCF7 cells after 6 h treatment with ouabain ($P < 0.001$), or 2 h treatment with iodoacetate ($P < 0.01$) or oligomycin ($P = 0.14$). Results are mean ± SEM.

3.3 Discussion

3.3.1 Summary of main findings

- VGSC currents were present both in primary MDA-MB-231 tumours and in lung metastases and were of the same size in both locations. β1 over-expression did not change the size of VGSC Na^+ current in *ex vivo* tissue slice recordings, despite increasing Na^+ current *in vitro*.
    - Total [Na^+] is elevated in MDA-MB-231 tumours compared to normal mammary glands, but $[Na^+]_e$ is normal.
    - In *ex vivo* MDA-MB-231 tumour slices pH_e was lower in peripheral parts of the tumour than in the core. The peripheral regions were more cellular and had a higher proliferative index than the core regions. The peripheral regions also had a lower apoptotic index than the core.
    - The peak transient Na^+ current of VGSCs in MDA-MB-231 cells was reduced at low pH_e but the persistent Na^+ current was increased.
    - Inhibition of glycolysis decreased viability and increased $[Na^+]_i$ in both MDA-MB-231 cells and MCF7 cells, but inhibition of mitochondrial respiration with the ATP synthase blocker oligomycin did not affect viability or $[Na^+]_i$ in either cell line.

3.3.2 Effect of β1 on Na^+ current in tumours

Although the β1 subunit increased whole cell Na^+ currents in MDA-MB-231 cells *in vitro*, it did not have this effect *in vivo*. The reason for this disparity is not clear, but it is not due to loss of β1 expression *in vivo* because the cells that were chosen for recording were fluorescent and this must indicate the presence of β1 protein, since GFP was fused to β1. The mechanism by which β1 increases Na^+ current *in vitro* has not yet been fully elucidated, but it may be due to increased transcription of VGSC α subunits or recruitment of α subunits to the plasma membrane as discussed in Section 1.2. Given the differences in cell adhesion

interactions between isolated cells and cells in tissue slices, it is likely that the interactions of β1 with other CAMs will differ between the *in vitro* and *in vivo* situations.

There was no effect of β1 expression on V_m either *in vitro* or *in vivo*. This is understandable *in vivo* where β1 had no effect on the Na^+ current. However, this is a little unexpected in the *in vitro* situation where β1 increased the Na^+ current, since it has been shown that VGSC activity depolarises the V_m in MDA-MB-231 cells (Yang *et al.*, 2020). An explanation may be that β1 hyperpolarises the voltage dependence of inactivation (Isom *et al.*, 1992) and thereby decreases persistent Na^+ current through $Na_v1.1$ in HEK293 cells (Lopez-Santiago *et al.*, 2007; Aman *et al.*, 2009). If β1 decreases the persistent Na^+ current in MDA-MB-231 cells, it might be expected to hyperpolarise rather than depolarise the V_m in cancer cells. Since no electrophysiological effects of β1 were seen *in vivo*, it was not studied further in this thesis, and instead most work concentrated on the VGSC α subunit $Na_v1.5$.

3.3.3 VGSC currents and their relation to $[Na^+]$ and pH

Experiments in this chapter were performed to investigate steady-state concentrations of $[Na^+]$ and pH in intracellular and extracellular compartments of breast tumours. The contribution of VGSCs to $[Na^+]_i$ and glycolytic rate (and thus production of H^+) was also tested to test the hypothesis that VGSCs increase extracellular acidification through upregulation of glycolysis. The extracellular pH was found to be acidic in tumours, so the effect of this on VGSC activity in breast cancer cells was determined.

3.3.3.1 VGSC currents and $[Na^+]_i$ in breast cancer cell lines

The finding that VGSC currents were present in highly metastatic MDA-MB-231 cells but not in less metastatic MCF7 cells is consistent with (Fraser *et al.*, 2005). The small, voltage-gated inward currents found in a small proportion of MCF10A cells was unexpected, since no such currents were found in (Fraser *et al.*, 2005) or (Gillet *et al.*, 2009). In both of these previous studies, outward currents were present in MCF10A cell recordings which may have

obscured small inward currents, whereas Cs^+ was present in the pipette intracellular solution to inhibit outward currents in this study. Since TTX was not used to inhibit the inward currents in this study, it is possible that the inward currents were through VGCCs rather than VGSCs. There was no evidence that $[Na^+]_i$ correlated with expression of VGSC currents in these breast cancer cell lines, suggesting that other Na^+ transport mechanisms may be important in regulating $[Na^+]_i$.

3.3.3.2 $[Na^+]$ in MDA-MB-231 tumours

The finding that total tissue $[Na^+]$ was elevated in MDA-MB-231 tumours compared to normal mammary glands (Figure 3.4 A) agrees with much published research showing that $[Na^+]$ increases in line with tumour aggressiveness (Ouwerkerk *et al.*, 2003; Ouwerkerk *et al.*, 2007; Zaric *et al.*, 2016; Barrett *et al.*, 2018). The normal mammary glands used in this study were from lactating mice which contained milk, a component of the extracellular fluid that was not present in the tumours. This could not fully explain the difference in tissue $[Na^+]$ between normal glands and tumours however (see Appendix I).

An increase in total tumour $[Na^+]$ could be due to an increase in intracellular $[Na^+]$ ($[Na^+]_i$), extracellular $[Na^+]$ ($[Na^+]_e$), or both. Since $[Na^+]_e$ is an order of magnitude larger than $[Na^+]_i$ (Hille, 2001), in increase in total tumour $[Na^+]$ could also be due to an increase in the ratio of the extracellular fluid volume to intracellular fluid volume. There is little evidence explaining the location of this additional Na^+ in tumours, although two studies used xray dispersion to conclude that $[Na^+]_i$ is elevated in tumours (Cameron *et al.*, 1980; Hürter *et al.*, 1982). Supporting this, multiparametric diffusion-weighted and ^{23}Na MRI studies of tumours have indicated that $[Na^+]$ decreased upon successful chemotherapy treatment when apparent diffusion increased, indicating that the total $[Na^+]$ had decreased despite the fact that ratio of extracellular fluid to intracellular fluid had increased (Jacobs *et al.*, 2009; James *et al.*, 2021). Based on the evidence from these studies and the finding that $[Na^+]_e$ in these tumours was within the physiological range (Figure 3.4 B), it is likely that the elevation of total $[Na^+]$

in these xenograft tumours compared to normal mammary glands is due to an increased $[Na^+]_i$ in the tumours.

3.3.3.3 pH_e in MDA-MB-231 tumours

As previously reported in other types of tumour, the average pH_e of MDA-MB-231 xenografts was pH 6.9, which is below the normal physiological pH_e of pH 7.4 for healthy tissue (White *et al.*, 2017). This pH was not homogeneous but varied across the tumour, and low pH correlated with viable-appearing tissue towards the periphery of the tumour. Subsequent sectioning and staining indicated that the more acidic, peripheral region corresponded with areas with lower apoptosis and higher proliferation. H&E staining showed that subjectively, these areas had intact nuclei, and appeared more viable than the necrotic core. These findings are in agreement with other studies (Helmlinger *et al.*, 1997; Grillon *et al.*, 2011; Grillon *et al.*, 2015; Jardim-Perassi *et al.*, 2019) which show that invasive, more peripheral parts of tumours have an acidic pH_e. Thus, it is not appropriate to assume that low pH_e in tumours is due to hypoxia and poor vascularisation. This may help to explain why cancer treatments targeting angiogenesis have not been as successful as it was hoped (Zirlik & Duyster, 2018). It also fits with the large amount of evidence that tumours perform aerobic glycolysis, which will lead to acidification even in areas with adequate oxygen (Gatenby & Gillies, 2004; Vander Heiden *et al.*, 2009).

3.3.3.4 Effect of pH_e on VGSCs in tumours

The low pH_e found in tumours will increase the persistent Na^+ current through $Na_v1.5$, and therefore Na^+ influx into cancer cells expressing VGSCs. This will mean that Na^+ influx will be greater in regions of lower pH_e which may be partially responsible for the heterogeneity of $[Na^+]$ found in tumours by ^{23}Na MRI (Ouwerkerk *et al.*, 2007; James *et al.*, 2021). VGSCs are not the only transport mechanisms which may link pH_e and Na^+ influx: other Na^+ channels such as ENaC and ASIC channels are also more likely to pass an inward Na^+ current in low pH_e (Collier & Snyder, 2009; Boscardin *et al.*, 2016). These, along with pH

regulatory mechanisms powered by the Na^+ gradient such as NHE1 and NBCn1 will combine to increase Na^+ influx in regions of the tumour with low pH_e. The likely presence of these other Na^+ transporters in breast cancer cells may explain why VGSC currents did not correlate with $[Na^+]_i$ in the cell lines investigated.

To summarise this far, data from this chapter have shown that the pH_e of MDA-MB-231 breast cancer xenografts was relatively acidic, particularly in peripheral, highly proliferative regions. In turn, low pH_e leads to an increased influx of Na^+ into breast cancer cells expressing $Na_v1.5$. Taken together, activity of VGSCs may be higher in the more proliferative regions of the tumour. This chapter also showed that total tissue $[Na^+]$ is elevated in MDA-MB-231 breast cancer xenografts compared to normal mammary glands, and this is not due to an increase in $[Na^+]_e$. These findings point towards an elevation of $[Na^+]_i$ in these tumours compared to normal mammary glands, or an increase in volume of the extracellular compartment. Although previous work has shown that VGSC activity increases $[Na^+]_i$ by a small amount in cancer cell lines (Campbell *et al.*, 2013; Yang *et al.*, 2020), this did not lead to a correlation between VGSC current and $[Na^+]_i$ in breast cancer cell lines. It is likely therefore that other Na^+ transport mechanisms such as NKA are at least as important as VGSCs in regulating $[Na^+]_i$.

3.3.3.5 Mechanism of VGSC-induced extracellular acidification

Since expression of a VGSC current was not shown to greatly increase steady state $[Na^+]_i$ in breast cancer cell lines, it seemed likely that a more important effect of VGSCs was increasing the flux of Na^+ into cancer cells, leading to an increase in Na^+ efflux through NKA. The contribution of VGSCs to NKA-mediated acidosis was next investigated since there is already substantial evidence that NKA utilises glycolysis as its main ATP source (section 1.6.7), and NKA activity would therefore increase the rate of H^+ production. It was hypothesised that inhibiting NKA with ouabain would reduce intracellular acidification. This was not found to be the case, but it is likely that cells can maintain a stable intracellular pH

by removing excess H^+ through NHE1 and other pH regulatory mechanisms (Cardone *et al.*, 2005; Boedtkjer *et al.*, 2013; White *et al.*, 2017). A more reliable method of assessing glycolytic acid production would therefore be to measure changes in extracellular pH. In fact, extracellular acidification has already been assessed in the short term while treating MDA-MB-231 cells with ouabain, and ouabain treatment did decrease H^+ production (Epstein *et al.*, 2014). This fits with the hypothesis that NKA is powered by aerobic glycolysis in breast cancer cells. Further evidence provided by (Epstein *et al.*, 2014) supporting the theory that VGSCs increase the rate of glycolysis was that gramicidin treatment greatly increased H^+ production in breast cancer cells. Gramicidin is an ionophore which equilibrates extracellular and intracellular $[Na^+]_i$ (as well as other cations) so it would lead to Na^+ influx and be expected to increase the activity of NKA.

Another way of assessing the rate of glycolysis is by measurement of lactate (James *et al.*, 1996). Inhibition of NKA with ouabain was predicted to reduce lactate production, but instead lactate production was unchanged in MDA-MB-231 cells and it increased with ouabain treatment in MCF7 cells (Figure 3.17 F and J). There are many possible explanations for this. The dose and duration of ouabain treatment used was later shown to be toxic to MCF7 cells (Figure 3.18), so any of the processes associated with cell death may have contributed to an increase in lactate production. A common feature of apoptosis is a collapsed mitochondrial membrane potential, disabling mitochondrial ATP synthesis (Ly *et al.*, 2003). As when mitochondrial respiration was prevented with oligomycin in this study, inhibiting mitochondrial ATP production leads to an increase in glycolytic ATP synthesis and lactate production. This experiment highlighted the need to perform dose response and viability experiments in each cell line separately before choosing appropriate concentrations for physiological experiments. In addition, a much shorter-term experiment such as in (Epstein *et al.*, 2014) is preferable, since inhibiting NKA sufficiently to allow $[Na^+]_i$ to accumulate will always be toxic to the cell eventually.

It is likely that there was not enough statistical power to show significant effects of drugs in the MDA-MB-231 cells in the lactate assay study. However, clear non-significant trends were seen and were as expected with the positive controls – the GAPDH inhibitor iodoacetic acid reduced lactate production and the mitochondrial ATP synthase inhibitor oligomycin increased lactate production. Intriguingly, TTX also caused a non-significant decrease in lactate production by MDA-MB-231 cells in all three independent experiments but not in MCF7 cells which have no detectable VGSC current. This would fit with the hypothesis that VGSC activity leads to increased glycolysis, but further repeats of this experiment are required to test whether there truly is an effect of VGSC activity on lactate production.

From the experiments assessing intracellular Na^+ accumulation with metabolic inhibitors, it appeared that NKA in both MCF7 and MDA-MB-231 cell lines depended on glycolysis and could cope without oxidative phosphorylation. Cell viability followed the same pattern – cells were unable to survive without glycolysis but could manage without oxidative phosphorylation. These findings echo those where glycolysis was found to be the ATP source for another plasma membrane ion pump, the plasma membrane Ca^{2+} ATPase (PMCA) in pancreatic cancer cells (James *et al.*, 2015). From these results it is not possible to judge whether NKA is more reliant on glycolysis than other ATP-consuming processes, as in vascular smooth muscle (Paul *et al.*, 1979), but it does indicate that in our *in vitro* experimental conditions, NKA activity will mostly be powered by glycolysis. Our experimental conditions provide 25 mM glucose in the culture medium, far more than would be available *in vivo*, so cells cultured in DMEM will be trained to be particularly reliant on glucose as an energy source (James *et al.*, 2015). However, this experiment reflects the situation in most *in vitro* experiments including those in which the effect of VGSC activity on NHE1 extracellular acidification in MDA-MB-231 cells was elucidated (Gillet *et al.*, 2009; Brisson *et al.*, 2011; Brisson *et al.*, 2013). This means that the cells, and in particular NKA, in those experiments were likely to be highly reliant on glycolysis as an ATP source. Therefore, if NKA activity had been increased by VGSC activity in those experiments, it is

highly likely that this increased the rate of glycolytic H^+ production. This could explain the increase in H^+ extrusion through NHE1 which was reported.

3.3.4 Future work

As highlighted above, more lactate assays are necessary to test the effect of VGSC activity on rate of glycolysis. In addition, the effect of VGSC activity on extracellular acidification rate (as a proxy for glycolytic rate) should be tested in a Seahorse analyzer.

Part of the VGSC-induced glycolysis hypothesis which has not been tested in this thesis is the effect of Na^+ influx on NKA activity. It has been shown that NKA activity in astrocytes is increased by intracellular Na^+ binding (Pellerin & Magistretti, 1994), but it would be possible to test the effect of VGSC activity on NKA activity in cancer cells using radioactive tracer ions such as $^{86}Rb^+$ to replace K^+ entering the cell through NKA (Fujii *et al.*, 2021).

Another way to test the VGSC-induced glycolysis hypothesis would be to cause Na^+ influx independently of VGSCs, since VGSCs could act via a direct protein interaction with NHE1 as hypothesised in (Brisson *et al.*, 2013), rather than through an increase in $[Na^+]_i$. The Na^+ ionophore monensin has been used to increase $[Na^+]_i$ artificially in skeletal muscle and increase lactate production (James *et al.*, 1996), however monensin functions as a Na^+/H^+ antiporter (Huczyński *et al.*, 2012), so it may affect pH_i as well as $[Na^+]_i$. Gramicidin is another Na^+ ionophore which has been used to show an increase in extracellular acidification in breast cancer cells (Epstein *et al.*, 2014), however gramidicin also equilibrates other cations in addition to Na^+ which complicates the interpretation. There are no selective ligands which open ENaC or ASIC channels so Na^+ influx could be controlled via a genetically engineered cation channel which is gated selectively by a synthetic ligand, reducing the possibility of interactions of ligands with endogenous channels (Magnus *et al.*, 2011). In particular, the effect of activation of this channel on NKA activity and pericellular/extracellular acidification should be assessed to add further confidence to the

theory that VGSCs affect extracellular acidification through NKA activity and glycolytic respiration.

It would be useful to assess $[Na^+]_i$ in both normal glands and tumours to further explain why total tissue $[Na^+]$ is elevated in tumours. This is possible to perform using SBFI-AM in *ex-vivo* tissue slices as in (James *et al.*, 2021). In addition, $[Na^+]_e$ in tumours as measured by ISMEs in this study should be compared to that in normal mammary glands. Given the links between $[Na^+]_i$ and pH_e suggested by this work, it would be important to assess the distribution of $[Na^+]_i$ and pH_e within tumours, for example using ^{23}Na MRI and MRI-CEST pH imaging (Anemone *et al.*, 2021), or by co-registering ^{23}Na MRI images with histological sections of the same tumour, to assess pH_e using pimonidazole as in (Jardim-Perassi *et al.*, 2019).

3.3.5 Conclusion

MDA-MB-231 breast tumours have a lower pH_e than normal tissues, particularly in the peripheral, highly proliferative region. This decreased pH_e in turn increases persistent Na^+ current into cancer cells containing VGSCs. This may in part explain why elevated tissue $[Na^+]$ is higher in these tumours compared to normal mammary glands. Conversely, Na^+ entry into breast cancer cells through VGSCs is likely to increase the rate of glycolysis and extracellular acidification through upregulation of NKA activity, and some evidence for this was presented in this chapter. Together these mechanisms form a positive feedback loop linking Na^+ influx and H^+ efflux with aerobic glycolysis in breast cancer cells.

4 Gene networks associated with $Na_v1.5$ expression in MDA-MB-231 cells

4.1 Introduction

Several ion channels have been shown to affect gene transcription, for example VGCCs can affect activity of the transcription factors NFAT, CREB and calmodulin, thereby contributing to cancer progression (Tajada & Villalobos, 2020). The main function of VGSCs in cancer cells discovered by *in vitro* assays is to increase invasion (Grimes *et al.*, 1995; Laniado *et al.*, 1997; Roger *et al.*, 2003; Fraser *et al.*, 2005; House *et al.*, 2010). The mechanism by which VGSCs increase invasion of cancer cells is not fully understood. Previous work has implicated $Na_v1.5$ in transcriptional regulation of invasion-related genes. For example, in colon cancer cells, $Na_v1.5$ activity increased expression of a network of invasion-related genes by upregulating the PKA/ERK/c-JUN/ELK-1/ETS-1 transcriptional pathway (House *et al.*, 2010; House *et al.*, 2015). VGSCs may regulate this signalling cascade by interacting with the small GTPase Rap1, which is activated by depolarisation of the V_m (House *et al.*, 2015). In contrast, another study showed no robust transcriptional signature in differentially expressed genes from non small-cell lung cancer and neuroblastoma cells treated with VGSC inhibitors (Hompoonsup *et al.*, 2019). This second study examined a relatively small number of genes (44 genes chosen from a preliminary microarray analysis) to come to this conclusion and the function of the differentially expressed genes was not analysed, but instead global transcriptional changes were examined. Despite their main conclusion, the authors mentioned that there was a small gene set that was consistently perturbed with VGSC inhibition. It is therefore possible that this small gene set was important for cancer progression. In another study using the MDA-MB-231 cell line, shRNA knock-down of $Na_v1.5$ reduced EMT, characterised by an elongated cell shape and increased filopodia. EMT is an important precursor to invasion out of the primary tumour in carcinomas (Gradek *et al.*, 2019). In this study, $Na_v1.5$ knock-down reduced transcription of *SNAI1*, one of four genes involved in EMT which were assessed by qPCR in this project.

whereas overexpression of $Na_v1.5$ in MCF7 cells increased expression of the EMT genes *SNAI1* and *ZEB1*. This points towards a possible function of $Na_v1.5$ in transcriptional regulation of EMT genes.

In this chapter an unbiased transcriptomics experiment was performed using RNA sequencing to determine the gene expression changes caused by $Na_v1.5$ in breast cancer, since a transcriptomics analysis of the effect of VGSCs in breast cancer has not so far been reported. Transcriptional changes were assessed in xenograft tumours rather than in cell lines as in (House *et al.*, 2010; Gradek *et al.*, 2019; Hompoonsup *et al.*, 2019). This would allow assessment of the function of $Na_v1.5$ in its interactions with the tumour microenvironment, shown to be important in Chapter 3. In addition, gene expression in stromal cells could be investigated separately from that in cancer cells because the cancer cells were derived from a different species than the stromal cells. Although CRISPR knockout of $Na_v1.5$ was performed in MDA-MB-231 cells (Appendix III), in this experiment *SCN5A* was knocked down in MDA-MB-231 cells using shRNA and control cells were treated with scrambled shRNA. These cells were developed by Michaela Nelson who showed that $Na_v1.5$ knock-down MDA-MB-231 xenografts grew more slowly and showed less local invasion and metastasis less than control xenografts (Nelson *et al.*, 2015b). As in (Gradek *et al.*, 2019), $Na_v1.5$ knock-down increased the circularity of MDA-MB-231 cells but no protein expression changes were seen in the EMT markers investigated. In this same study, $Na_v1.5$ knock-down reduced CD44 expression *in vitro*, indicating that $Na_v1.5$ may act partly through the CD44-src-cortactin pathway as discussed in Section 1.6.1.

On the basis of these previous studies, shRNA knock-down of $Na_v1.5$ in MDA-MB-231 tumours was predicted to reduce expression of genes involved in invasion. In addition, metabolism and pH regulatory pathways were predicted to be affected by $Na_v1.5$ expression due to evidence presented in Chapter 3.

4.2 Results

4.2.1 RNA sequencing experiment

To assess gene expression differences due to the presence of $Na_v1.5$, previously characterised shRNA $Na_v1.5$ knock-down MDA-MB-231 cells (Nelson *et al.*, 2015b) were used in an RNA sequencing experiment. These cells or scrambled shRNA control cells were implanted in mice to produce xenograft tumours (Section 2.4).

4.2.1.1 Growth curve and $[Na^+]$ of $Na_v1.5$ knock-down tumours

Mice were weighed (Figure 4.1 A) and tumours were measured using callipers (Figure 4.1 B) after tumour implantation. The shRNA $Na_v1.5$ knock-down tumours grew slightly more slowly than control tumours as in (Nelson *et al.*, 2015b) but this was not significant at day 33 (Figure 4.1

Figure 4.1 B; P = 0.40; n = 6; unpaired *t* test). To test the hypothesis that total tissue $[Na^+]$ would be decreased in the absence of VGSCs, $[Na^+]$ was measured using ICP-MS (Section 2.22). There was no difference in the total tissue $[Na^+]$ with knock-down of $Na_v1.5$ (Figure 4.1 C; P = 0.58; n = 6 or 7; unpaired *t* test).

4.2.1.2 Quality control

First samples were checked for integrity and purity using agarose gel electrophoresis and an Agilent 2100 bioanalyzer. All samples had excellent integrity and purity (Section 2.15.1). Next the reads were mapped to the human or mouse genome (Section 2.15.2). Most of these reads were mapped to exons (Figure 4.2 A) and were evenly distributed between the chromosomes (Figure 4.2 B). The distribution of reads per gene was similar for all 12 samples, after controlling for the total number of reads per sample (Figure 4.3 A). Control and $Na_v1.5$ knock-down samples were well separated by cluster profiling based on gene expression level (Figure 4.3 B), and principal component analysis based on gene expression level (Figure 4.3 C).

It was important to check that the reads had been mapped to the genomes properly, since it is possible for a read to map to more than one location within a genome. The STAR aligner program produced BAM files for each read, and HTSeq generated the read count matrices, which indicated the number and percentage of reads which mapped to more than one gene in the human genome (multiple mapped reads). These reads comprised approximately 3% of the total reads for each sample (Table 4.1). Multiple mapped reads were ignored when generating the count matrix.

In a xenograft experiment, it is possible for reads to map to both human and mouse genomes. BBsplit was used to analyse which reads could be mapped to both genomes. It assigned 96-97% of the raw reads to human, mouse, or both and it labelled a very small percentage (0.45-0.55%) of reads as ambiguous to human or mouse genomes. To assess the likely impact of ambiguous reads on differentially expressed gene (DEG) analyses, the ambiguous reads were mapped back to the human and mouse genomes to show which gene read counts were affected. Very few genes in the significantly differentially expressed human gene set were affected, and in almost all of these genes the effect was negligible. In the case of only 9 out of 512 differentially expressed genes the ambiguous reads comprised over 1% of the total reads for that gene. These genes are shown in Table 4.2, along with the % ambiguous reads per gene. Even in these most affected genes, the proportion of ambiguous reads was never larger than 6.9%. All genes with over 5% ambiguous reads were removed from further analysis. Table 4.3 shows mouse DEGs with the most ambiguous reads. Again, all genes with over 5% ambiguous reads were removed from further analysis.

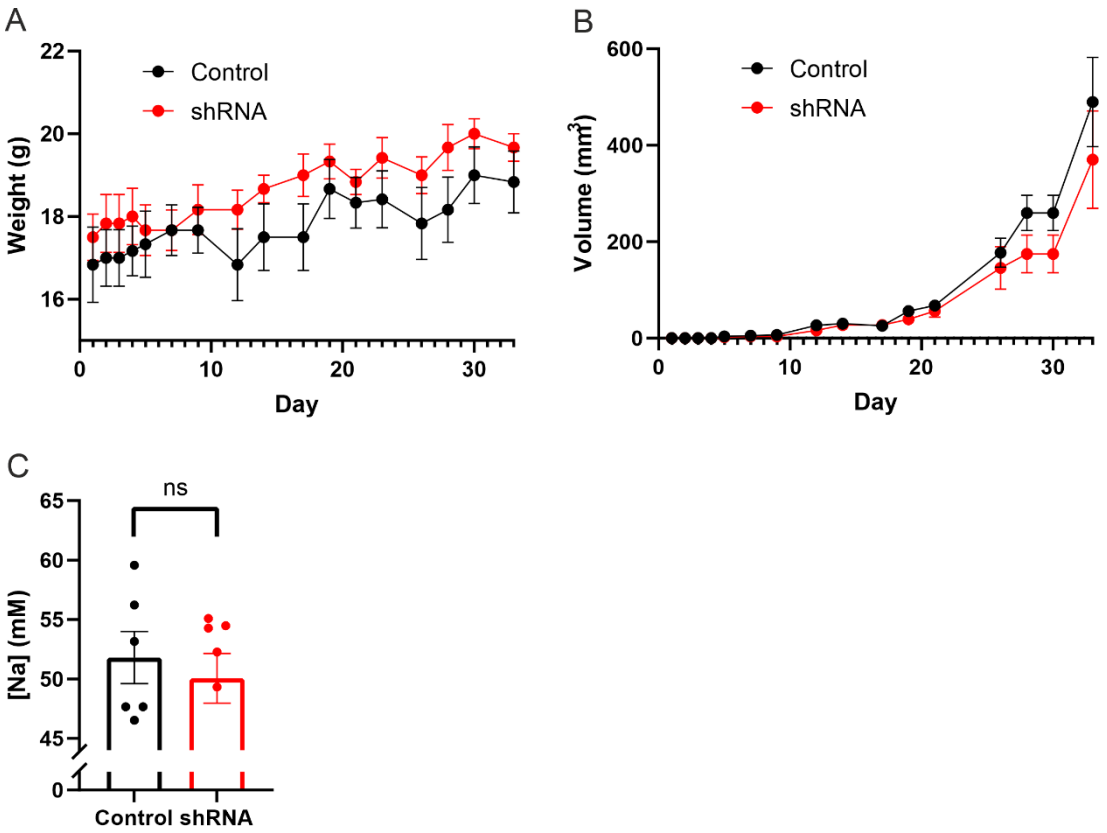

Figure 4.1 shRNA knock-down of *SCN5A* in MDA-MB-231 xenografts.
A. Mouse bodyweight during the period of the tumour growth. **B**. Growth of primary tumours. Tumours were measured with callipers every 2-3 days and tumour volume was calculated as 0.5 x length x width^2. **C**. Sodium content of tumours measured using ICP-MS after euthanasia (P = 0.58; n = 6 or 7; unpaired *t* test).

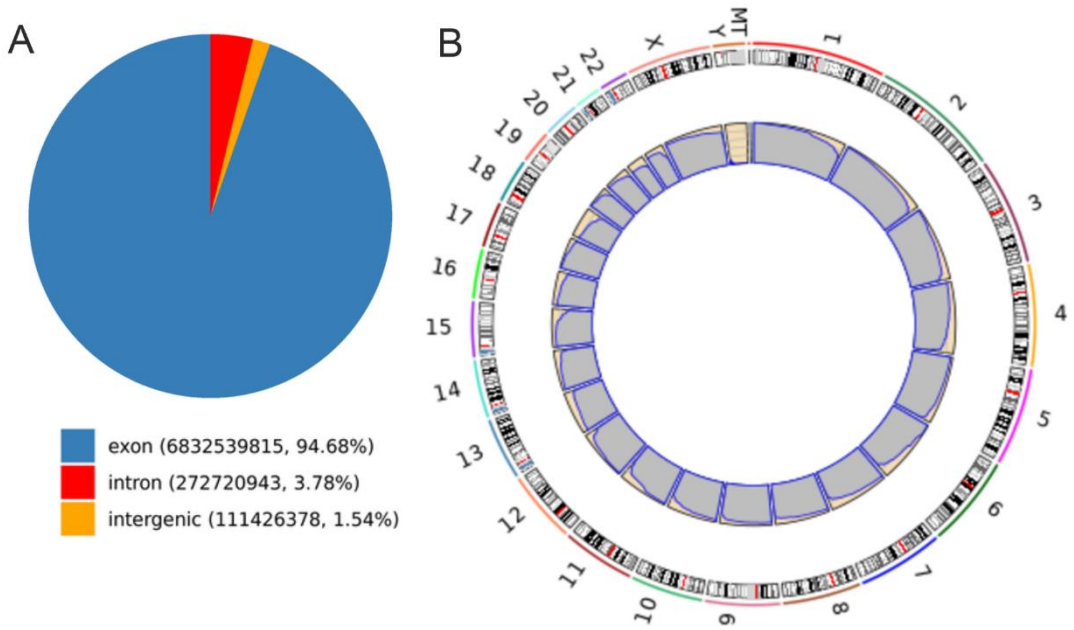

Figure 4.2 Mapping of reads to human genome.
A. Relative proportion of reads mapped to exons compared to other regions of the genome – example from one sample. **B**. Relative mapping of reads (inner circle, grey regions) to different chromosomes or mitochondrial DNA (MT).

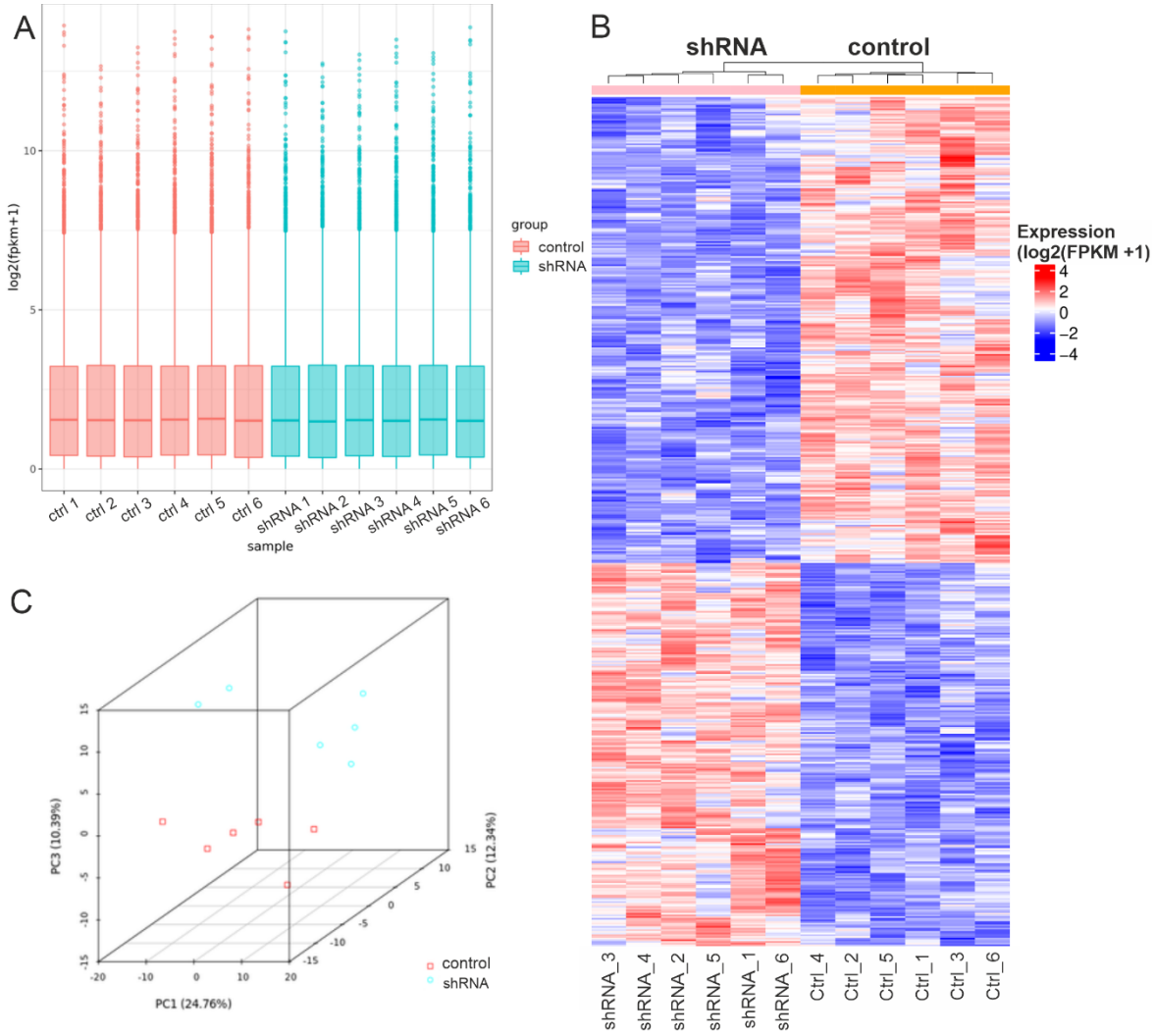

Figure 4.3 Read counts per human gene and clustering of genes by read count.
A. Distribution of the number of reads per gene (FPKM = fragments per kilobase of transcript per million) showing similar distribution for each sample. **B**. Cluster analysis heat map based on level of gene expression. This separates control and $Na_v1.5$ knock-down (shRNA) samples clearly. **C**. Principal component analysis of gene expression data showing good separation between control and $Na_v1.5$ knock-down (shRNA) samples. All graphs produced by Novogene.

Table 4.1 Quality of mapping of reads to genes within the human genome.
Multiple mapping indicates reads could be mapped to more than one location in the human genome.

Sample name	**ctrl_1**	**ctrl_2**	**ctrl_3**	**ctrl_4**	**ctrl_5**	**ctrl_6**
Total reads	47447712	55903982	41046486	49880146	41765272	45377990
Total mapped reads	42361264	48863164	37064946	44171910	36952552	40958354
Uniquely mapped reads	40724346	47440106	35784252	42613982	35890986	39822056
Multiple mapped reads	1636918	1423058	1280694	1557928	1061566	1136298
Total mapping rate	89.28%	87.41%	90.30%	88.56%	88.48%	90.26%
Uniquely mapping rate	85.83%	84.86%	87.18%	85.43%	85.93%	87.76%
Multiple mapping rate	3.45%	2.55%	3.12%	3.12%	2.54%	2.50%
Sample name	**shRNA_1**	**shRNA_2**	**shRNA_3**	**shRNA_4**	**shRNA_5**	**shRNA_6**
Total reads	47417128	49315918	45955460	44513906	42729202	44127662
Total mapped reads	43020532	44043534	38822678	38617972	38740742	39869482
Uniquely mapped reads	41391906	42729524	37312784	37509568	37512010	38738398
Multiple mapped reads	1628626	1314010	1509894	1108404	1228732	1131084
Total mapping rate	90.73%	89.31%	84.48%	86.75%	90.67%	90.35%
Uniquely mapping rate	87.29%	86.64%	81.19%	84.26%	87.79%	87.79%
Multiple mapping rate	3.43%	2.66%	3.29%	2.49%	2.88%	2.56%

Table 4.2 Ambiguous reads mapped to human genome.
All significantly differentially expressed genes for which over 1% of the reads mapped ambiguously to human and mouse genomes, showing ambiguously mapping reads as a % of total reads for each human gene.

Gene name	**padj**	**log2FC**	**Total Reads**	**Ambig Reads**	**% Ambig**
EPB41L4B	4.02E-07	0.659717	8634	264	3.1
SSBP2	0.0035522	-0.540957	1618	112	6.9
WDR20	0.0052997	0.3196335	6791	285	4.2
SOCS2	0.0056031	-0.464032	2676	56	2.1
ADD1	0.0158078	0.3143308	48915	1635	3.3
PCDH7	0.0288516	0.3507883	3123	36	1.2
LCP1	0.0398588	0.5235747	10511	167	1.6
GMFG	0.0426087	-0.453212	3127	189	6.0
FHL1	0.043432	-0.297429	16520	514	3.1

Table 4.3 Ambiguous reads mapped to mouse genome.
All significantly differentially expressed genes for which over 2% of the reads mapped ambiguously to human and mouse genomes, showing ambiguously mapping reads as a % of total reads for each mouse gene.

Gene name	padj	log2FC	Total Reads	Ambig Reads	% Ambig
Gm18194	4.02E-07	0.659717	8634	264	19.7
Zc3h14	0.0035522	-0.540957	1618	112	10.8
Rpl351-ps2	0.0052997	0.3196335	6791	285	5.6
Pdia3	0.0056031	-0.464032	2676	56	5.5
Mest	0.0158078	0.3143308	48915	1635	3.8
Pcdh7	0.0288516	0.3507883	3123	36	3.6
Wbp1l	0.0398588	0.5235747	10511	167	3.1
Epb41l4b	0.0426087	-0.453212	3127	189	2.3

4.2.1.3 Human gene differential expression analysis

The count matrices of reads per gene need to be normalised to the sequencing depth such as the number of reads per sample and to the gene lengths. Normalising to the total reads does not take account of the gene lengths, so the measure of read count shown in the quality assessments above is FPKM (fragments per kilobase of exon per million reads/fragments mapped). Using this type of normalisation for DEG analysis does not allow accurate comparison of gene expression between samples as required in this study, since extreme over or underexpression of a few genes can artificially affect the results. To avoid skewing of data by outlier genes, the counts were instead normalised to sample-specific size factors determined by the median ratio of gene counts between samples relative to the geometric mean per gene (Anders & Huber, 2010) in the algorithm used by DESeq2. An overview of the differentially expressed genes in the human and mouse genomes are shown in (Figure 4.4). For panel A (human DEGs) P values adjusted for false discovery rate were used. There were very few mouse DEGs once this adjustment had been made so DEGs with P values not adjusted for false discovery rate were plotted in panel B.

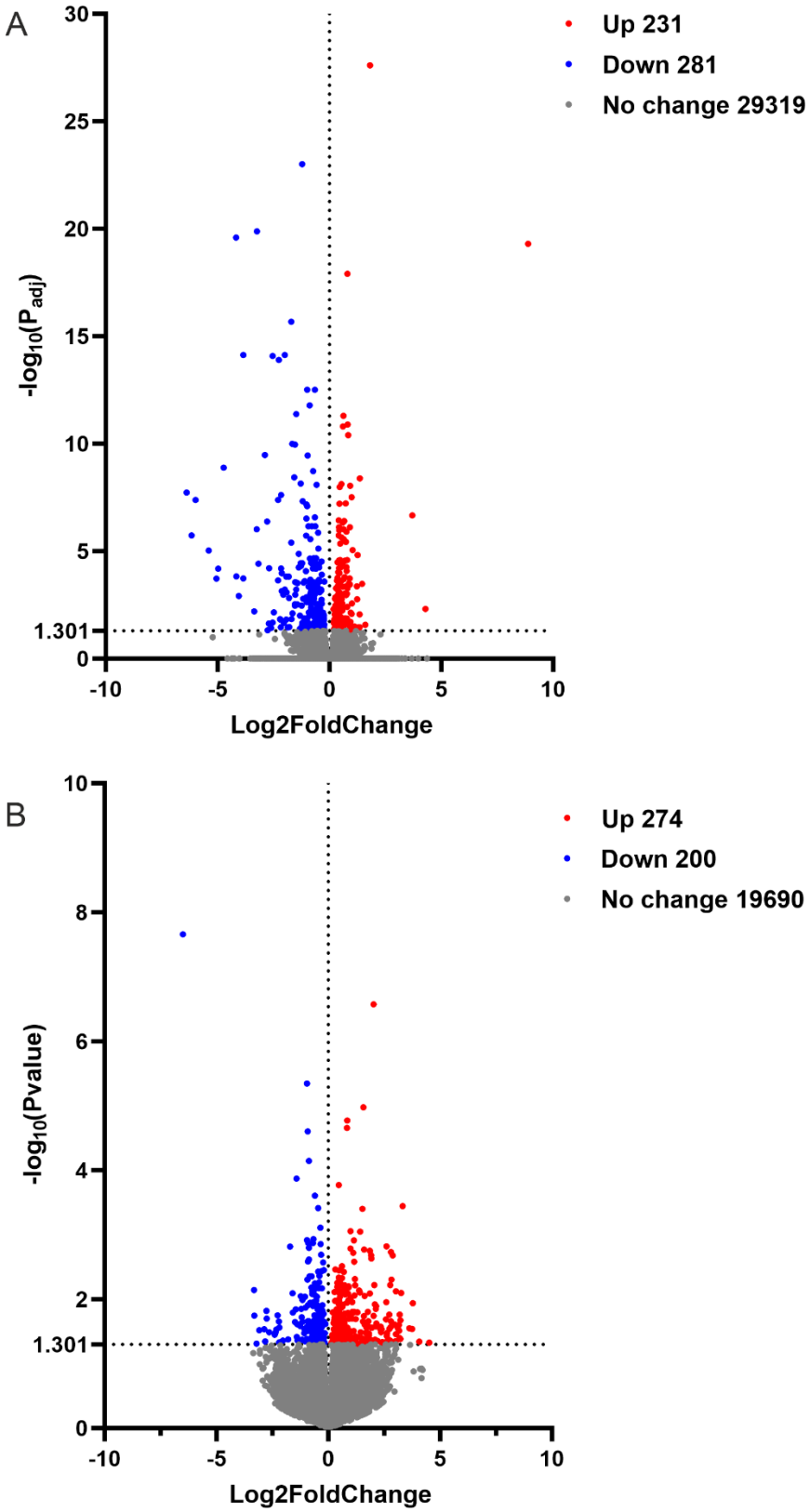

Figure 4.4 Volcano plots showing differentially expressed genes in human and mouse genomes following $Na_v1.5$ knockdown in MDA-MB-231 tumours.
A. Human DEGs (Padj < 0.05) **B**. Mouse DEGs using P values rather than Padj values (P < 0.05). Red symbols show significantly upregulated genes and blue symbols downregulated genes. Grey symbols are genes which were not significantly differentially expressed.

In the human genome there were more downregulated genes in the $Na_v1.5$ knock out tumours than upregulated genes. These downregulated genes were ordered by degree of differential expression (Log_2Fold change) and the functions of the most downregulated genes were investigated using Uniprot.org and Genecards.org (Stelzer *et al.*, 2016; Consortium, 2019). Brief descriptions of the most downregulated genes and categorisation of the descriptions are shown in Table 4.4. From this table it appeared that genes related to detoxification of ROS were strongly downregulated, with some important genes highlighted in Table 4.5. Many of the top downregulated genes in Table 4.4 had mitogenic activity and were associated with various cancers. In addition, there were many genes associated with antigen presentation which were downregulated, for example the HLA class II histocompatibility antigens *HLA-DPA1*, *HLA-DRA* and *CIITA*, and the HLA class I histocompatibility antigen *HCP5*. Other categories of downregulated genes that became apparent were Ca^{2+} regulatory genes (Table 4.6), genes associated with migration and invasion (Table 4.7) and genes associated with acid-base balance and metabolism (Table 4.8). The most downregulated genes associated with immune system function are shown in Table 4.9.

Genes involved in pH regulation were of particular interest because $Na_v1.5$ increases invasion through extracellular acidification via NHE1 in breast cancer (Brisson *et al.*, 2011). There were no expression changes in genes coding for NHE proteins, but an NHE3 inhibitory factor NHE-RF1, encoded by *SLC9A3R1*, was upregulated (L2FC = 0.40, Padj = 0.011). This gene is often mutated in breast cancer (Dai *et al.*, 2004). Another important pH regulatory protein, carbonic anhydrase IX, encoded by *CA9*, was downregulated with $Na_v1.5$ knock-down (L2FC = -0.87, Padj < 0.001). Acid-sensing ion channels (ASICs), which are part of the epithelial Na^+ channel (ENaC) family are also important in pH control as these open in low pH_e to allow Na^+ into cells (Gupta *et al.*, 2016). ASIC1 was downregulated in $Na_v1.5$ knock-down tumours (L2FC = -0.83, Padj = 0.003), indicating that as well as

Table 4.4 Most downregulated human genes in $Na_v1.5$ knockdown tumours.

	ROS detoxification
	Ca2+ release
	Invasion through ECM
	Migration/cytoskeleton
	Mitogen/oncogene
	Immune system

Gene name	L2FC	Padj	Gene name (long)	Function
GSTM1	-6.38	1.85E-08	Glutathione S transferase	Antioxidant
MAGEA6	-6.16	1.85E-06	Melanoma associated gene A6	Enhances ubiquitin ligase activity of TRIM28, leading to p53/TP53 ubiquitination
AC090809.1	-5.99	4.12E-08	lincRNA	Unknown function
BEX5	-5.39	9.48E-06	Brain expressed, X-linked, nerve growth factor receptor assoc.	Interacts with MAGE8A (a tumour specific antigen)
PRDM9	-5.05	0.0001913	PR domain zinc finger protein 9	Allows recombination during meiosis, double stranded DNA break repair
MAGEC1	-4.97	6.46E-05	Melanoma associated gene C1	Tumour specific antigen - unknown function
TSTD1	-4.73	1.29E-09	Thiosulfate:glutathione sulfurtransferase	Helps remove H_2S, which would otherwise inhibit cytochrome oxidase
MAGEA11	-4.17	2.56E-20	Melanoma associated gene A11	Aids proliferation in BCa. Linked to ER-beta and HER2 expression in Bca
SMIM31	-4.16	0.0001478	Small integral membrane protein 31	Unknown function
RYR2	-4.04	0.0012066	Ryanodine receptor 2	Ca^{2+} release from sarcoplasmic reticulum in heart
MAGEC2	-3.85	0.0001832	Melanoma assoc gene	Enhances ubiquitin ligase activity of TRIM28, leading to p53/TP53 ubiquitination
LYL1	-3.85	7.47E-15	Lymphoblastic leukemia-derived sequence 1	Transcriptional regulation
KIAA0040	-3.36	0.0063334	Uncharacterised	Unknown function
MPZL2	-3.26	9.43E-07	Myelin protein zero-like protein 2	Homophilic cell adhesion - important in inner ear
PRSS2	-3.24	1.31E-20	Serine protease 2 (trypsinogen)	Aids invasion and digestion of food
TNFSF18	-3.17	3.79E-05	Tumour necrosis factor ligand superfamily member 18	Aids activation of T-cells - triggers phosphorylation of STAT1
RHOD	-2.88	3.34E-10	Rho-related GTP-binding protein RhoD	Regulates cytoskeleton
MT1A	-2.78	4.19E-07	Metallotthionein 1A	Binds heavy metals
SERPINA5	-2.76	0.0476905	Serpin family A member 5 - plasma serine protease inhibitor	Pro-coagulant and pro-inflammatory
CD33	-2.71	0.0234668	Cluster of differentiation 33	Myeloid cell surface protein (particularly found in microglia)
EPHB6	-2.70	6.14E-05	Ephrin type-B receptor 6	Affects adhesion and migration, lost its tyrosine kinase activity
SAMSN1	-2.61	0.0375999	Same domain-containing protein SAMSN-1	Inhibits B-cell activation, promotes Rac1-dependent reorganization cytoskeleton
HLA-DPA1	-2.54	8.22E-15	HLA class II histocompatibility antigen DP alpha1	Antigen presentation
KIF21B	-2.54	0.0210948	Kinesin family member 21B	Oncogene, microtubule-associated motor protein, allows centrosome polarisation
HEPH	-2.49	0.0069617	Hephaestin	Ferroxidase (converts Fe^{2+} to Fe^{3+}), involved in iron and copper regulation

STRA6	-2.30	0.0002283	Receptor for retinol uptake	Oncogenic in gastric cancer - acts via wnt/beta catenin
INAVA	-2.30	4.16E-08	Innate immunity activator protein	Upregulated in breast cancer (GEO) and unfavourable in endometrial cancer
IFI27	-2.27	1.27E-14	Interferon alpha inducible protein 27 (mitchondrial)	Involved in typeI IFN-induced apoptosis (release of cyt C from mitochondria)
F2RL3	-2.21	0.014408	Thrombin receptor-like 3	Activated by trypsin and thrombin - involved in clotting and inflammation
AC068985.1	-2.20	0.0152657	lincRNA	Unknown function
JAK3	-2.17	0.0347521	Janus kinase 3 (TRK enzyme)	Found in NK and T cells, also in epithelium. Mediates IL-8 induced chemotaxis
VWA5A	-2.16	2.40E-08	von Willebrand factor A domain-containing protein 5A	Candidate breast cancer suppressor (aka BCSC1, LOH11CR2A)
GSTM2	-2.16	6.28E-05	Glutathione S-Transferase Mu 2	Detoxifies ROS and toxins including carcinogens
MAN1C1	-2.13	0.000105	Mannosyl-oligosaccharide 1,2-alpha-mannosidase IC	Involved in protein glycosylation
TRPV4	-2.12	0.0007072	Transient receptor potential cation channel subfam. V memb. 4	Ca^{2+} channel, activated by hypotonicity, motion, heat, low pH
ADORA1	-2.06	0.0010632	Adenosine receptor A1	Inhibits cAMP, increases proliferation in ER +ve BCa
LINC02253	-2.03	0.0215554	lincRNA	Unknown function
DRAXIN	-1.99	0.0006151	Dorsal inhibitory axon guidance protein	Chemo-repulsive agent in axon guidance. Antagonises wnt beta catenin pathway
TRIM22	-1.99	7.47E-15	Tripartite motif containing 22	IFN-induced ubiquitin ligase
LTK	-1.93	0.0151545	Leukocyte receptor tyrosine kinase	Promotes growth, neurite outgrowth, and cell survival. Involves PI3 kinase pathway
ADAMTS14	-1.93	0.0001532	ADAM metallopeptidase with thrombospondin type 1 motif 1	Has aminoprocollagen type I processing activity in the absence of ADAMTS2
HOOK1	-1.92	0.0008047	Hook microtubule tethering protein 1	Actin and microtubule binding
FBXO39	-1.86	0.0347521	F-box protein 39	Part of ubiquitin ligase pathway
MDFI	-1.82	0.0001531	MyoD family inhibitor	Inhibits muscle differentiation. Activates beta-catenin pathway

Table 4.5 Key human ROS detoxification genes significantly downregulated (Padj < 0.05) in $Na_v1.5$ knock-down tumours.

Gene name	Log2Fold Change	Description
Glutathione S transferase (*GSTM1*)	-6.38	Detoxifies ROS and toxins including carcinogens
Thiosulfate:glutathione sulfurtransferase (*TSTD1*)	-4.73	Helps remove H_2S, which would otherwise inhibit cytochrome oxidase
Glutathione S-Transferase Mu 2 (*GSTM2*)	-2.16	Detoxifies ROS and toxins including carcinogens
Carboxylesterase 3 (*CES3*)	-1.54	Detoxifies xenobiotics
Nicotinamide N-Methyltransferase (*NNMT*)	-1.19	Enzyme that uses SAMe donor to detoxify xenobiotics

Table 4.6 Key human genes involved in Ca^{2+} regulation, significantly downregulated (Padj < 0.05) in $Na_v1.5$ knock-down tumours.

Gene name	Log2Fold Change	Description
Ryanodine receptor 2 (*RYR2*)	-4.04	Ca2+ release from sarcoplasmic reticulum in heart
Transient receptor potential cation channel subfam.V memb. 4 (*TRPV4*)	-2.12	Ca2+ channel, activated by hypotonicity, motion, heat, low pH
Voltage-dependent calcium channel subunit alpha-2/delta-4 (*CACNA2D4*)	-0.80	Voltage dependent plasma membrane Ca2+ channel
cAMP-specific 3',5'-cyclic phosphodiesterase 4B (*PDE4B*)	-0.55	Hydrolyzes cAMP - involved in Ca2+ handling in heart, chemotaxis and migration
Calcium/calmodulin-dependent protein kinase type IV (*CAMK4*)	-0.51	Ca2+/calmodulin dependent kinase
Calsenilin (*CKNIP3*)	-0.48	Calcium-dependent transcriptional repressor that binds to the DRE element of genes
Sodium/potassium/calcium exchanger 1 (*SLC24A1*)	-0.42	Transports 1 Ca2+ and 1 K+ in exchange for 4 Na+ in visual transduction cascade

Table 4.7 Key human genes involved in migration and invasion, significantly downregulated (Padj < 0.05) in $Na_v1.5$ knock-down tumours.

Gene name	Log2Fold Change	Description
Serine protease 2/Trypsinogen (*PRSS2*)	-3.24	Aids invasion through ECM
Rho-related GTP-binding protein RhoD (*RHOD*)	-2.88	Regulates cytoskeleton
Ephrin type-B receptor 6 (*EPHB6*)	-2.7	Affects adhesion and migration, lost its tyrosine kinase activity
Same domain-containing protein (*SAMSN1*)	-2.61	Promotes Rac1-dependent reorganization cytoskeleton
Leukocyte receptor tyrosine kinase (*LTK*)	-1.93	Promotes growth, neurite outgrowth, and cell survival
Metalloproteinase with thrombospondin type 1 motif 1 (*ADAMTS14*)	-1.93	Has aminoprocollagen type I processing activity in the absence of *ADAMTS2*
Hook microtubule tethering protein 1 (*HOOK1*)	-1.92	Actin and microtubule binding

Table 4.8 Key human genes involved in metabolism and acid-base balance, significantly downregulated (Padj < 0.05) in $Na_v1.5$ knock-down tumours.

Gene name	Log2Fold Change	Description
Carbonic anhydrase 11 (*CA11*)	-1.28	Unlikely to have catalytic activity
Serine Incorporator 2 (*SERINC2*)	-1.21	Amino acid synthesis
Solute Carrier Family 45 Member 1 (*SLC45A1*)	-1.21	glycoside-pentoside-hexuronide cation symporter transporter family and may play a role in glucose uptake
Choline dehydrogenase, mitochondrial (*CHDH*)	-1.09	Amino acid synthesis
Hydroxycarboxylic acid receptor 1 (*HCAR1*)	-0.88	Receptor for L-lactate - anti lipolytic
Carbonic anhydrase 9 (*CA9*)	-0.87	pH regulation and control of cell proliferation and transformation
Acid-sensing ion channel 1 (*ASIC1*)	-0.83	Isoform 1 does not show proton gated ion channel activity
P2X purinoceptor 5 (*P2RX5*)	-0.81	Purinergic-gated cation channel
Enoyl-CoA hydratase domain-containing protein 2, mitochondrial (*ECHDC2*)	-0.81	Fatty acid oxidation

Table 4.9 Key human genes involved in immune system function, significantly downregulated (Padj < 0.05) in $Na_v1.5$ knock-down tumours.

Gene name	Log2Fold Change	Description
Tumour necrosis factor ligand superfamily member 18 (*TNFSF18*)	-3.17	Aids activation of T-cells - triggers phosphorylation of STAT1
Serpin family A member 5 (*SERPINA5*)	-2.76	Pro-coagulant and pro-inflammatory
Cluster of differentiation 33 (*CD33*)	-2.71	Myeloid cell surface protein (particularly found in microglia)
HLA class II histocompatibility antigen DP alpha1 (*HLA-DPA1*)	-2.54	Antigen presentation
Innate immunity activator protein (*INAVA*)	-2.30	Upregulated in breast cancer and unfavourable in endometrial cancer
Janus kinase 3 (*JAK3*)	-2.17	Found in NK and T cells, also in epithelium. Mediates IL-8 induced chemotaxis
Tripartite motif containing 22 (*TRIM22*)	-1.99	IFN-induced ubiquitin ligase
TNF Receptor Superfamily Member 18 (*TNFRSF18*)	-1.70	Involved in interactions between activated T-lymphocytes and endothelial cells
HLA class II histocompatibility antigen, DR alpha chain (*HLA-DRA*)	-1.54	Antigen presentation
Caspase 1 (*CASP1*)	-1.53	Reduces anti-tumour immunity by inhibiting cGAS-STING. Initiates pyroptosis

Table 4.10 Most upregulated human genes in $Na_v1.5$ knockdown tumours.

Gene name	L2FC	padj	Gene name (long)	Function
KCTD15	8.88	4.51E-20	Potassium channel tetramerization domain containing 15	Inhibits AP2A (transcription factor) - tumour suppressor
MAGEA10	4.29	4.79E-03	Melanoma associated gene A10	Expressed in spermatogonia, tumour specific antigen
GPR158	3.71	2.14E-07	G protein-coupled receptor 158	Aids proliferation in prostate cancer
FAM133A	1.81	2.59E-28	Family with sequence similarity 133 member A	Unknown function
SPINK1	1.60	2.61E-02	Serine peptidase inhibitor, Kazal type 1	Inhibits trypsin before exit from the pancreas
INHBB	1.46	3.31E-04	Inhibin subunit beta B	Inhibits FSH secretion from pituitary
AP003555.2	1.36	4.06E-09	Novel transcript	Unknown function
PAGE5	1.36	8.75E-03	Prostate-associated gene 5	Unknown function

increasing Na^+ influx in low pH_e conditions itself (section 3.2.6), $Na_v1.5$ increases expression of another Na^+ channel which performs this same action.

There were no clear patterns in the most upregulated human genes in $Na_v1.5$ knock-down tumours, and the significantly upregulated genes were not changed by as great a degree as the downregulated genes. The most changed genes are shown in Table 4.10.

4.2.1.4 Human gene overrepresentation analysis

Overrepresentation analysis was performed to look for enrichment of the differentially expressed gene set for certain cell compartments, biological processes or molecular functions. Using the Gene Ontology (GO) database (http://www.geneontology.org/) there were 102 significantly enriched GO terms in the set of genes which were downregulated in $Na_v1.5$ knock-down tumours. In contrast, there were no significantly enriched GO terms in the set of genes which were upregulated in $Na_v1.5$ knock-down tumours. The 102 significantly enriched GO terms in the downregulated gene set fell into distinct categories, the largest of which was terms associated with immune system function, in particular antigen presentation. (Figure 4.5). Another category of significantly enriched GO terms was terms associated with invasion and migration; in particular many terms involving peptidase function (Figure 4.6 A). A third category of enriched GO terms was kinases, particularly tyrosine kinases (Figure 4.6 B). A fourth, large category was GO terms involved with ion channels, mostly Ca^{2+} ion transport (Figure 4.7 A). The final category was GO terms involved in detoxification of ROS (Figure 4.7 B). Only eleven significantly enriched GO terms remained which did not fall into one of these categories.

Although there were no significantly enriched GO terms in the upregulated human genes, there were some interesting findings when the GO terms with lowest Padj values were examined. These were separated into biological process (BP), cell component (CC) and molecular function (MF) (Figure 4.8). Categories of GO terms which were enriched in the

upregulated gene set in $Na_v1.5$ knock out tumours included cell adhesion regulation (particularly in BP), plasma membrane processes including those involved in migration (particularly in CC) and redox genes (MF).

4.2.1.5 Human disease ontology

It is helpful to assess whether the differentially expressed genes are likely to be relevant to the disease process in question. The disease ontology (DO) database http://www.disease-ontology.org is an ontology database which links biomedical datasets, for example transcriptomics datasets, with various diseases. When the DEG set from this study was analysed against the DO database, there were no significantly enriched terms at the Padj < 0.05 level. The 16 DO terms with Padj values < 0.3 are displayed in Figure 4.9 A. The majority of these DO terms are cancers, including breast cancer.

4.2.1.6 Human DEG analysis with Reactome

The Reactome database contains information about which genes are associated with certain reactions or pathways. When the downregulated set from this study was analysed against the Reactome database, there was only one significantly enriched Reactome term, "interferon signalling". The 16 terms most enriched terms with Padj values < 0.5 are shown in Figure 4.9 B. The terms from this analysis match some findings from the GO analysis, particularly in interferon signalling and antigen presentation. An interesting addition to this group of terms was "PD-1 signalling" since this pathway is a major way in which cancer cells negatively regulate the adaptive immune response (Ahmadzadeh *et al.*, 2009). Again, in agreement with the GO analysis, redox reactions were affected by $Na_v1.5$ knock down. An interesting category of terms which appeared from this analysis was VEGF signalling and reversible hydration of CO_2. These terms indicate that $Na_v1.5$ knock down might interfere with hypoxia signalling and pH regulation, both of which are disrupted in cancer and are associated with upregulation of glycolysis.

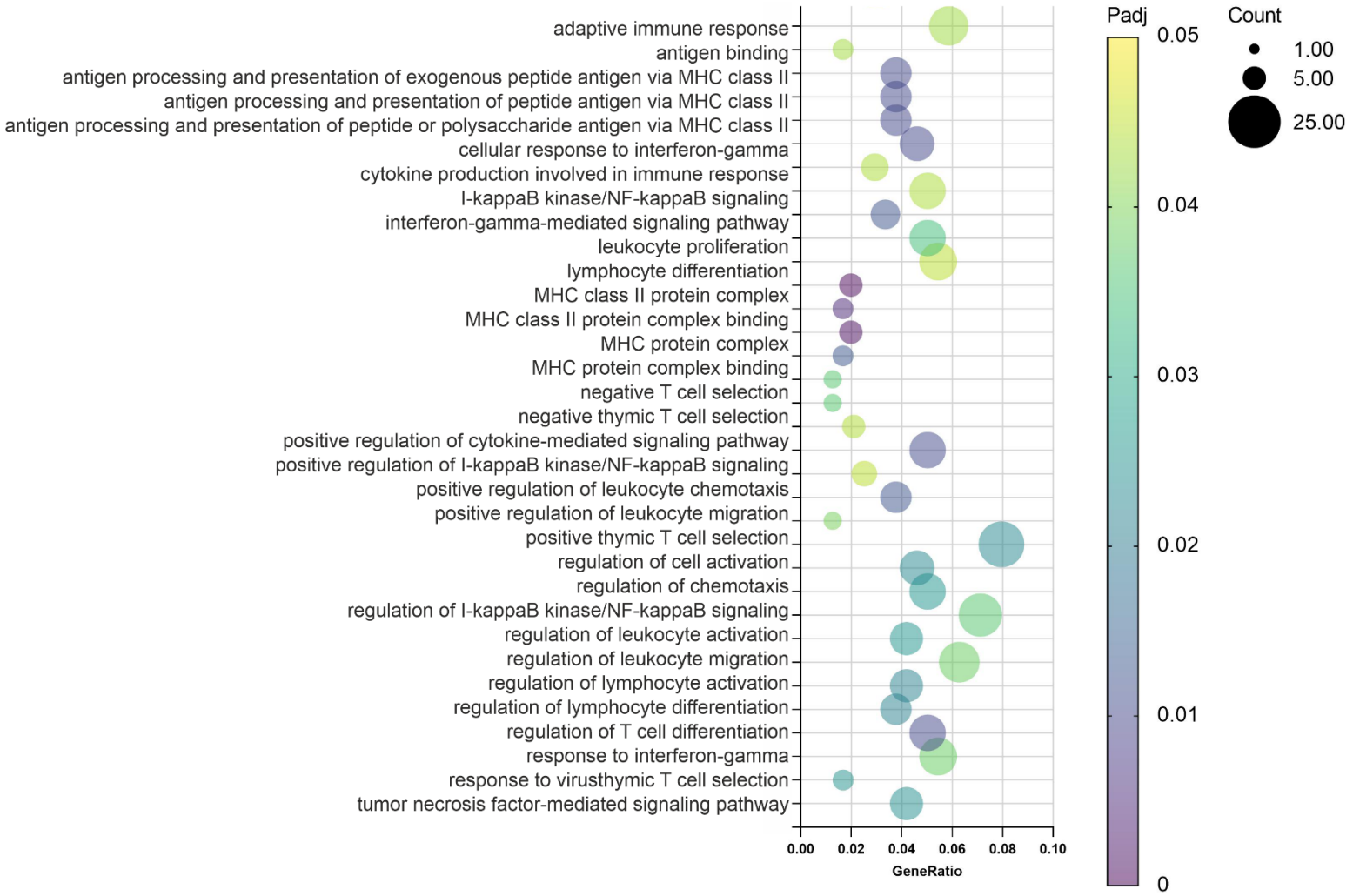

Figure 4.5 Enriched GO terms associated with the immune system in human DEGs from $Na_v1.5$ knock-down tumours.
These GO terms are particularly associated with antigen presentation and response to interferon-gamma. Produced using the Gene Ontology database.

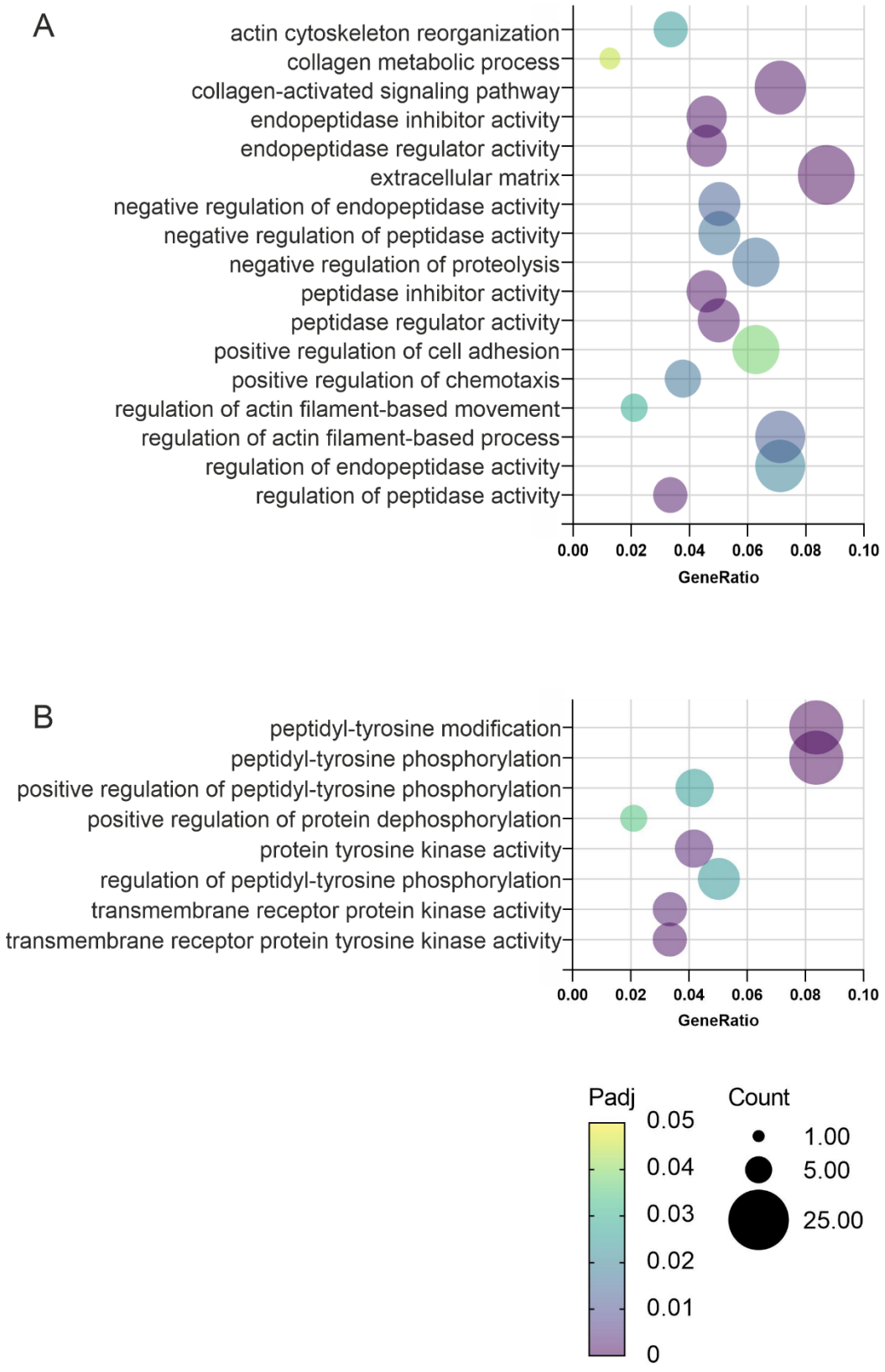

Figure 4.6 Enriched invasion, migration and kinase GO terms in human DEGs from $Na_v1.5$ knock-down tumours.
A. Enriched invasion and migration-related GO terms **B**. Enriched kinase-related GO terms. Produced using the Gene Ontology database.

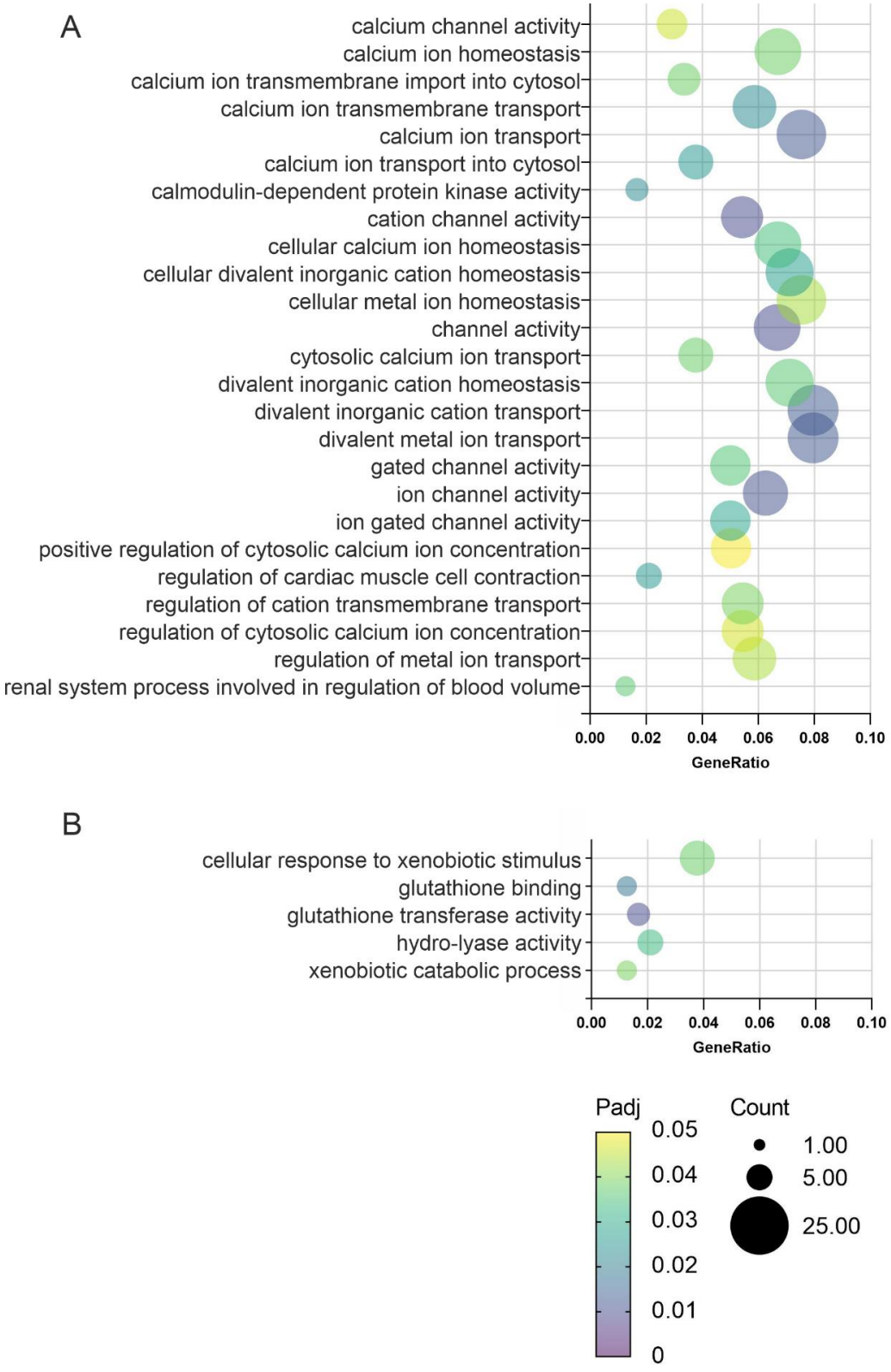

Figure 4.7 Enriched ion transport and ROS detoxification GO terms in human DEGs from $Na_v1.5$ knock-down tumours.
A. Enriched ion transport-related GO terms **B**. Enriched ROS detoxification-related GO terms. Produced using the Gene Ontology database.

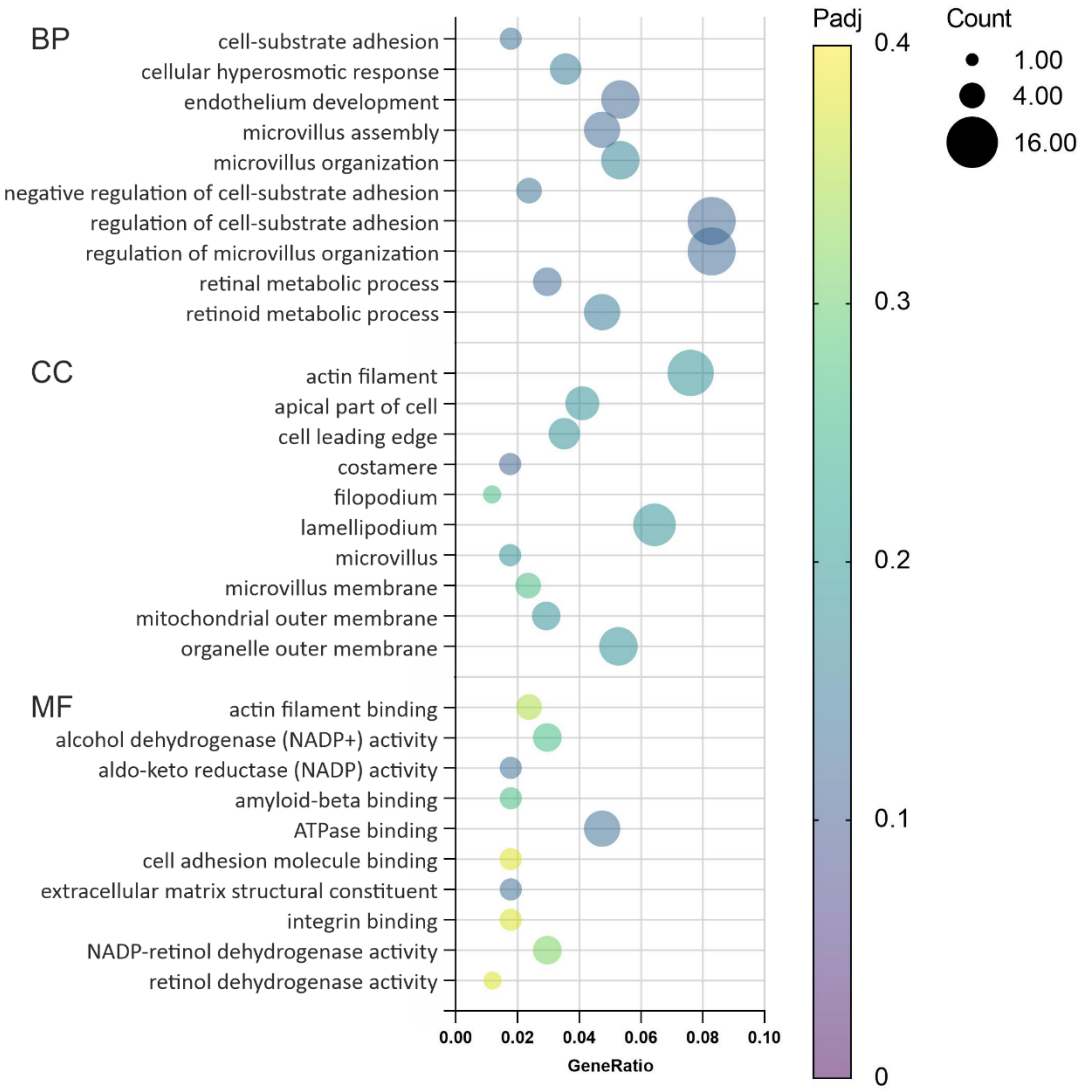

Figure 4.8 Enrichment of GO terms in upregulated human DEGs in $Na_v1.5$ knock-down tumours.
BP. 10 Most significant biological process GO terms **CC**. 10 Most significant cell component GO terms. **MF**. 10 Most significant molecular function GO terms. Produced using the Gene Ontology database.

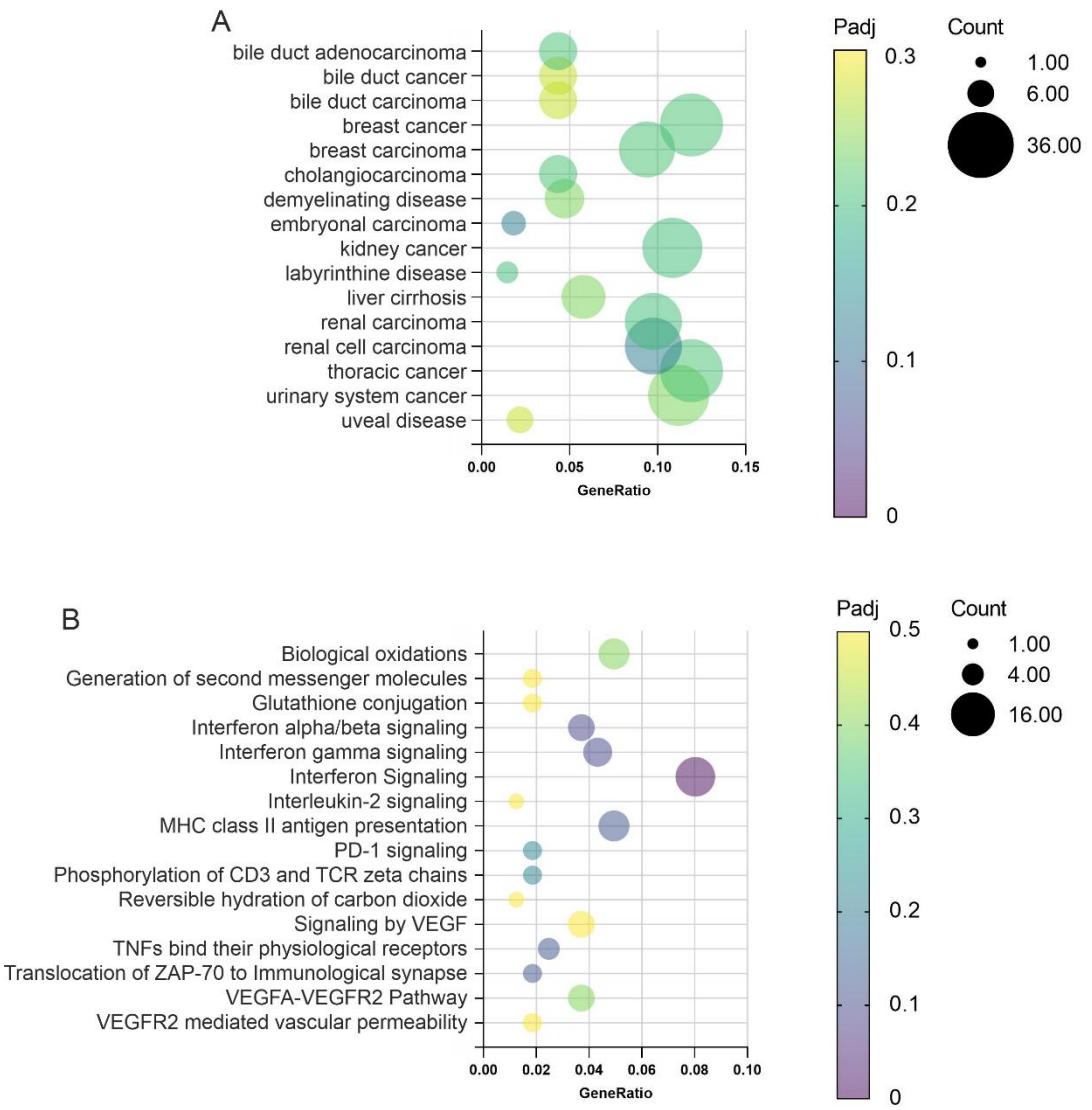

Figure 4.9 Disease Ontology and Reactome analyses.
A. Enrichment of Disease Ontology terms in both upregulated and downregulated DEGs from $Na_v1.5$ knock-down tumours. **B**. Enrichment of Reactome biological pathways in downregulated DEGs from $Na_v1.5$ knock-down tumours. Note Padj scaling is different from GO analyses in previous figures. Produced using the Disease Ontology database and the Reactome database.

4.2.1.7 Mouse gene differential expression analysis

In MDA-MB-231 xenograft tumours there appears to be little stromal tissue compared to patient breast tumours. Closely packed round cells with large nuclei are seen in H&E stained sections of MDA-MB-231 xenografts for example in Figure 3.7 A and in (Nelson *et al.*, 2014). Therefore as expected, most RNA sequencing reads (~ 90 % of reads, see Table 4.1) mapped to the human genome. The stromal component of these tumours is very small so only around 6-11 % of reads per sample mapped to the mouse genome. This provided an order of magnitude fewer reads per gene for the mouse genome than for the human genome, reducing the statistical power to detect DEGs. Despite this, the volcano plot in Figure 4.4 shows 474 mouse genes which were differentially expressed in $Na_v1.5$ knock-down tumours. The P values for all of these genes were < 0.05 but the Padj values were not. In fact, there was only one significantly downregulated gene (Hbb-bs) and only one significantly upregulated gene (Chil1) with Padj values < 0.05. The most significantly downregulated genes in $Na_v1.5$ knock-down tumours are displayed in Table 4.11. The main category which appeared here was oxygen carrying function. The most significantly upregulated mouse genes in $Na_v1.5$ knock-down tumours, displayed in Table 4.12 are mostly associated with immune system function. Of particular interest were the genes Ido1 (L2FC = 2.73, P = 0.028, Padj = 0.999) and Kyat1 (L2FC = 0.89, P = 0.045, Padj = 0.999). Both Ido1 and Kyat1 which codes for Kynurenine Aminotransferase 1 are involved in the IDO1 pathway which cancers utilise to suppress the immune system (Liu *et al.*, 2018).

Table 4.11 Most significantly downregulated mouse genes in $Na_v1.5$ knock-down tumours. Inclusion in this table was determined by lowest Padj values, but genes are ordered by L2FC.

	Oxygen carrying
	Immune system

Gene name	L2FC	Padj	Gene name (long)	Description
Alas2	-1.42	0.30277	aminolevulinic acid synthase	For synthesizing heme
Hbb-bs	-0.95	0.03049	Beta-globin	Binds heme
Ifitm1	-0.91	0.07232	Interferon-induced transmembrane protein 1	IFN-induced antiviral protein - stops virus fusing with endosome
Hba-a1	-0.86	0.18048	Haemoglobin alpha	Binds heme
Nrep	-0.60	0.45684	Neuronal regeneration-related protein	Promotes axonal regeneration and augments motility of gliomas.
Fbln1	-0.45	0.57032	Fibulin 1	ECM component - controls formation of basement membrane

Table 4.12 Most significantly upregulated mouse genes in $Na_v1.5$ knock-down tumours. Inclusion in this table was determined by lowest Padj values, but genes are ordered by L2FC.

	Immune system

Gene name	L2FC	Padj	Gene name (long)	Description
Thrsp	3.33	0.57032	Thyroid hormone-inducible hepatic protein	Lipogenesis in lactating mammary gland
Chil1	2.03	0.00269	Chitinase-3-like protein 1	Involved in Th2 response, macrophages, regulates apoptosis in response to ROS
Krt7	1.58	0.05336	Keratin Type II cytoskeletal 7	Blocks interferon-dependent interphase and stimulates DNA synthesis in cells
Krt19	1.53	0.57032	Keratin Type I cytoskeletal 19	Cytoskeletal organisation in myocytes
Ccl5	0.84	0.06859	C-C motif chemokine 5	Chemoattractant for blood monocytes, memory T-helper cells and eosinophils.
Anxa8	0.84	0.07232	Annexin A8	Anticoagulant, Ca2+ binding, IP3 binding
Xdh	0.47	0.34199	Xanthine dehydrogenase	Purine degradation - contributes to generation of ROS

4.2.1.8 Mouse gene ontology

In the mouse GO analysis very few Padj values were < 0.05, but when the terms with lowest Padj values were listed some interesting categories appeared. When $Na_v1.5$ was knocked-down in tumours, the mouse GO terms which were most enriched in the downregulated genes were associated with cell division (Figure 4.10). This indicates that stromal cell division may have been slower in $Na_v1.5$ knock-down tumours than in control tumours. Other mouse GO term categories which were enriched in the downregulated gene set were oxygen binding and ROS detoxification.

Next the upregulated mouse genes were assessed for GO term enrichment. When $Na_v1.5$ was knocked-down in tumours, GO terms which were significantly enriched (Padj < 0.05) were associated with ECM and epithelial membrane polarity (Figure 4.11 A). The molecular function GO terms which were enriched included many associated with ROS detoxification.

4.2.1.9 Protein-protein interactions

Protein-protein interactions (PPIs) were assessed for human DEGs using the STRING database (http://string-db.org/). The network of downregulated human genes is shown in Figure 4.12 A. For this number of networked genes, the clusters of genes were not particularly useful in comparison to the overrepresentation analysis, although some clusters were seen, such as the genes involved in Ca^{2+} signalling just below the *SCN5A* gene in Figure 4.12, and the cluster of cancer-associated genes in the bottom left. A larger, mixed-function network including many immune-system genes was seen at the top of the network diagram. A separate, network of three glutathione S-transferase genes was also seen (Figure 4.12 B). The genes with direct PPIs with $Na_v1.5$ were *SPTBN2* (a membrane cytoskeletal protein) and *GJA3* (a connexin), *SNTB1* (a cytoskeleton interacting protein), *JUP* (a desmosomal protein) and *RYR2* (the ryanodine receptor). A similar diagram displaying the significantly upregulated human genes is shown in Figure 4.13. Like the overrepresentation

analysis for the upregulated genes, there was no obvious pattern to the gene clusters in this analysis.

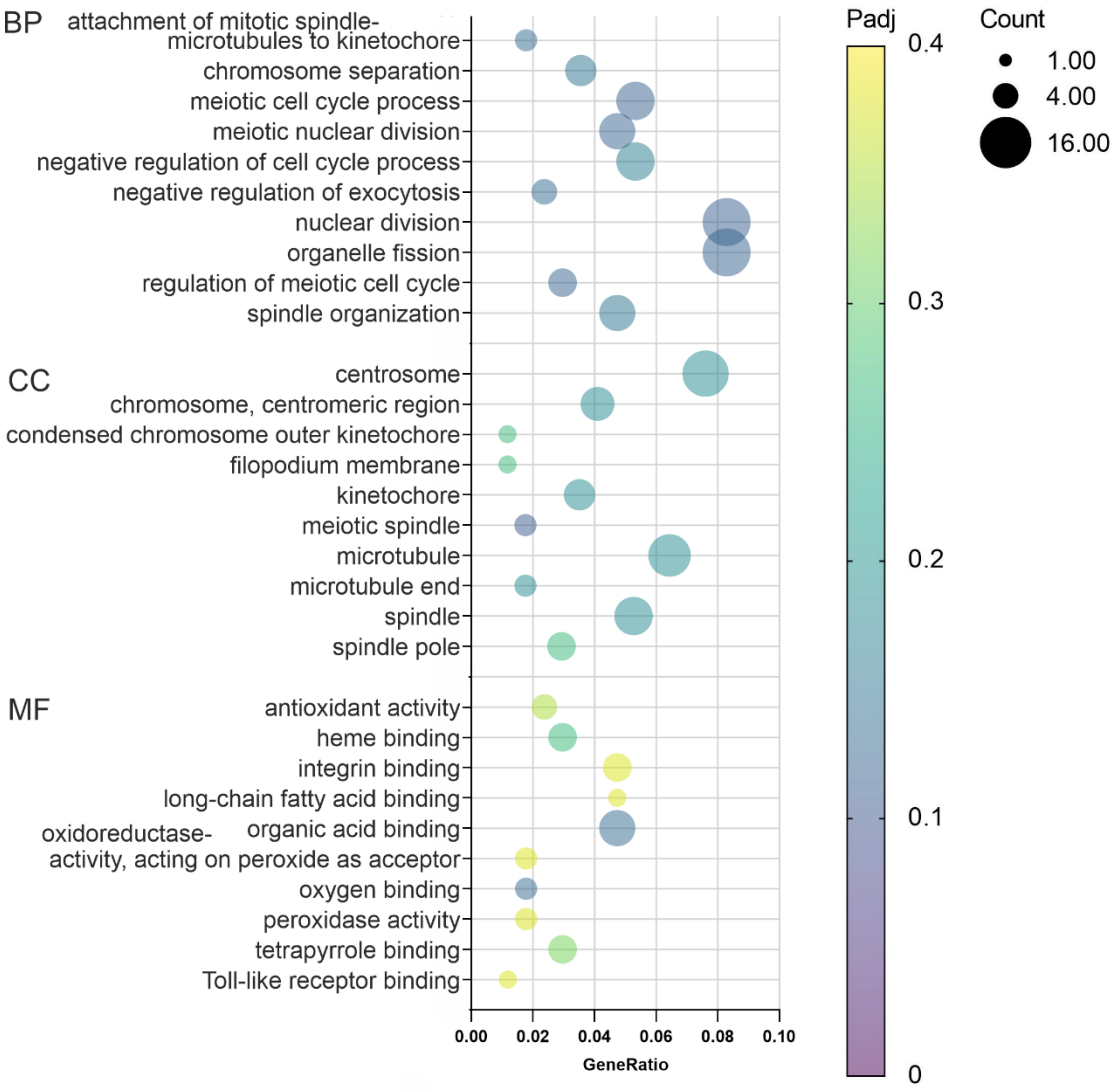

Figure 4.10 Enrichment of GO terms in downregulated mouse DEGs in $Na_v1.5$ knock-down tumours.
BP. 10 Most significant biological process GO terms. **CC**. 10 Most significant cell component GO terms. **MF**. 10 Most significant molecular function GO terms. Produced using the Gene Ontology database.

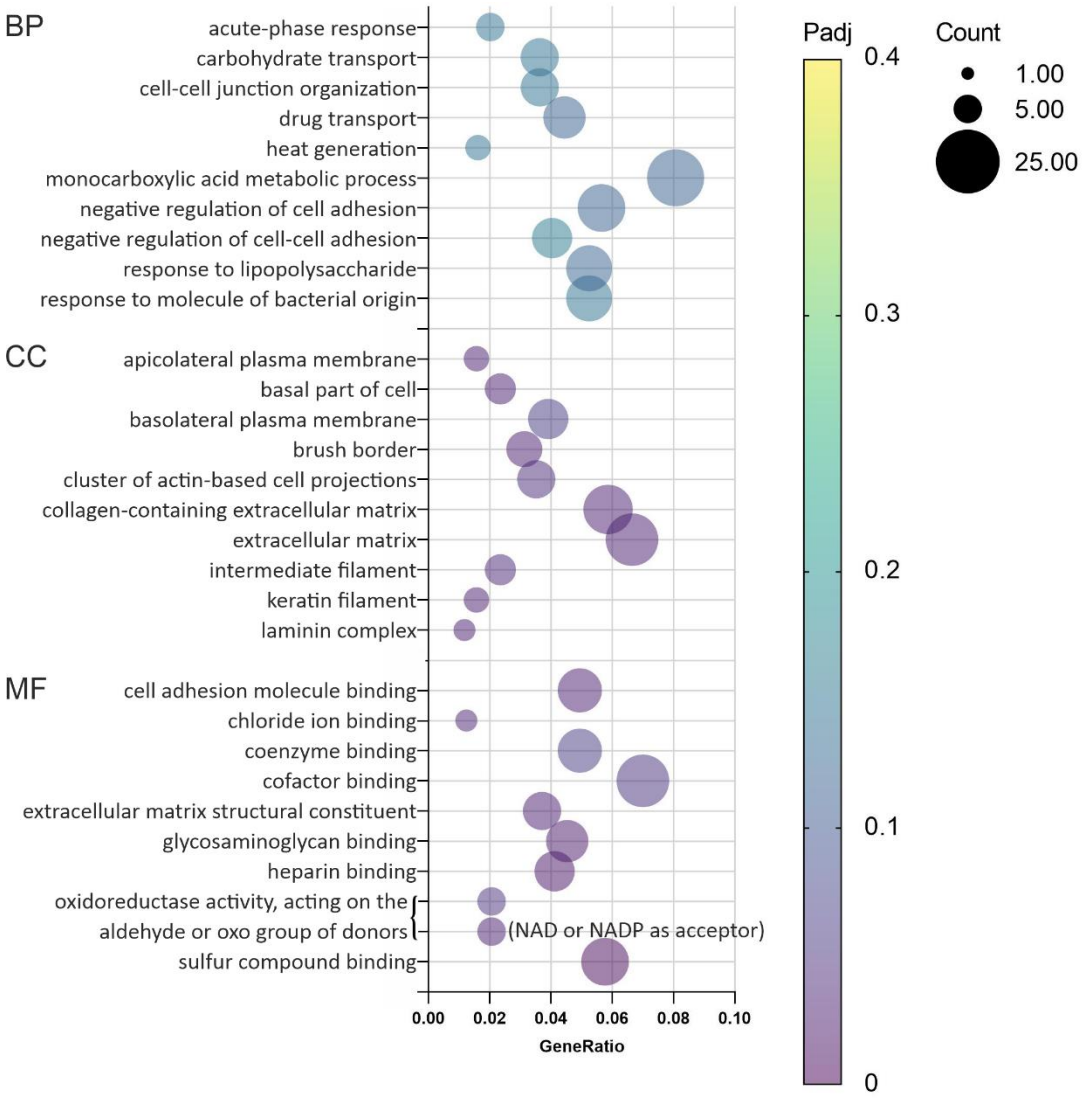

Figure 4.11 Enrichment of GO terms in upregulated mouse DEGs in $Na_v1.5$ knock-down tumours.
BP. 10 Most significant biological process terms. **CC**. 10 Most significant cell component GO terms (Padj all < 0.05). **MF**. 10 Most significant molecular function GO terms (Padj all < 0.07). Produced using the Gene Ontology database.

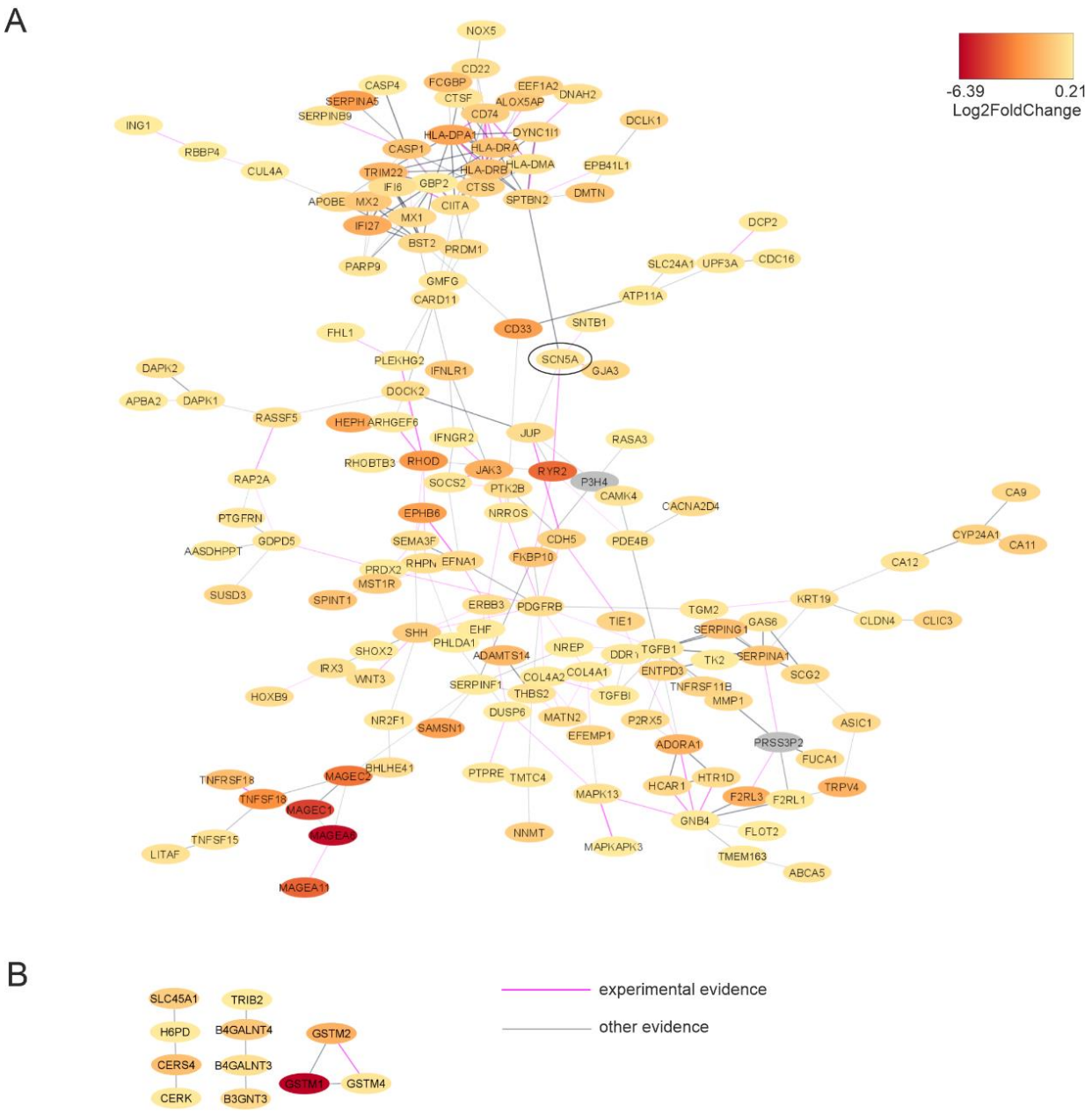

Figure 4.12 Downregulated human gene PPIs from the STRING database.
Darker coloured ovals indicate a greater degree of downregulation of the gene. Pink linker lines indicate there is experimental evidence for a PPI between two gene products and grey lines indicate any other kind of evidence for a PPI.

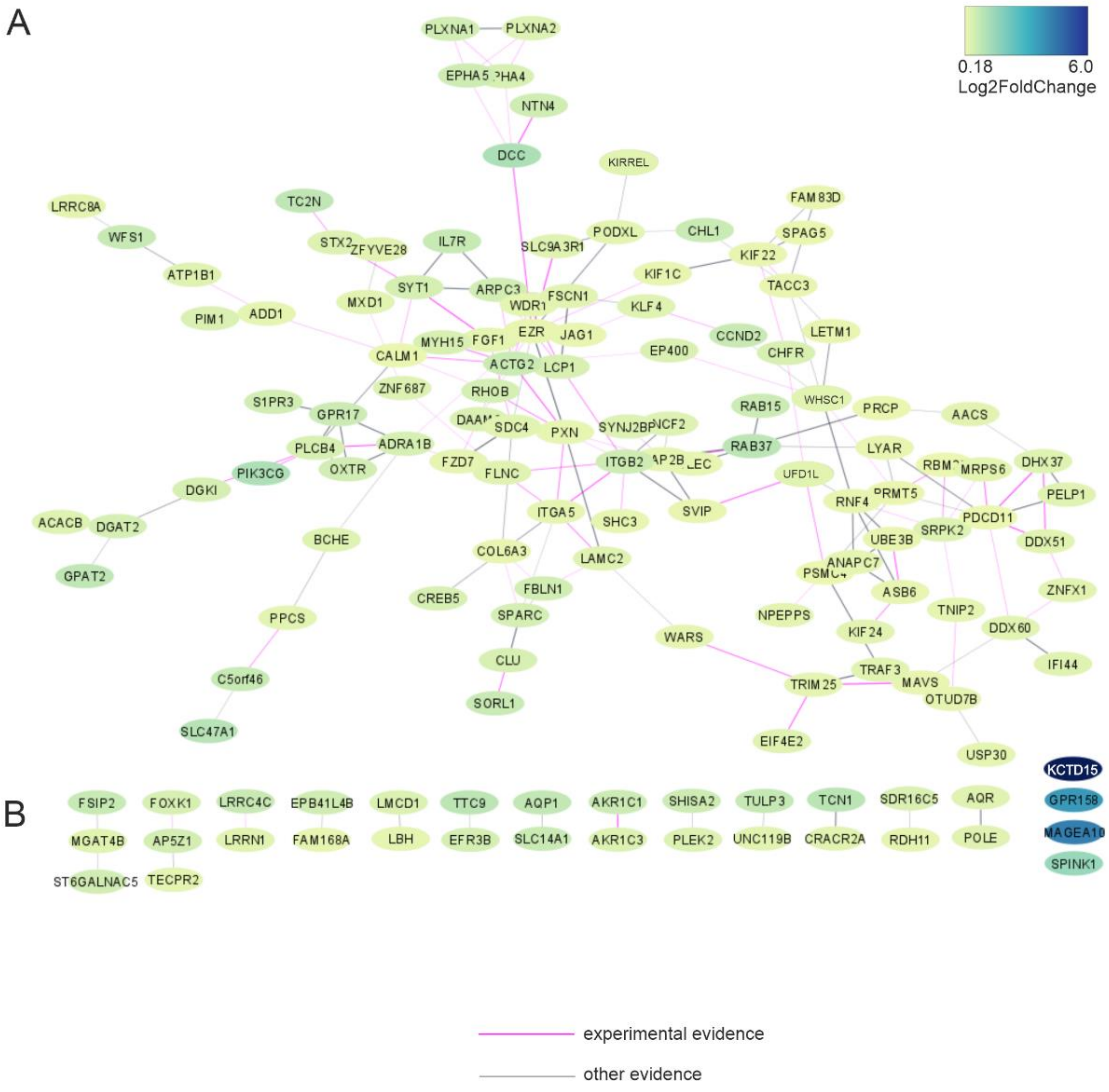

Figure 4.13 Upregulated human gene PPIs from the STRING database.
Darker coloured ovals indicate a greater degree of downregulation of the gene. Pink linker lines indicate there is experimental evidence for a PPI between two gene products and grey lines indicate any other kind of evidence for a PPI.

To summarise, the RNAseq data showed that knock-down of $Na_v1.5$ in MDA-MB-231 xenograft tumours caused expression changes in both human and mouse genes. The human DEGs were associated with cancer. The main findings from overrepresentation analysis of human genes were downregulation of genes involved in Ca^{2+} signalling, antigen presentation, ROS detoxification and invasion and migration.

4.3 Discussion

4.3.1 Summary of main findings:

Knocking down *SCN5A*/$Na_v1.5$ with shRNA in MDA-MB-231 xenografts led to changes in expression of genes that are important in cancer. The main changes that were seen in the cancer cells were decreased expression of genes involved in invasion and migration, interferon signalling, antigen presentation, ROS detoxification and Ca^{2+} signalling. The main changes that were seen in the stromal cells were a decrease in oxygen carrying and mitosis-associated genes and an increase in ECM modifying and redox-related genes.

4.3.2 Effects of $Na_v1.5$ knock-down on the immune system

There were several indications that $Na_v1.5$ knock down had implications for the immune system in MDA-MB-231 tumours, for example changes in IFN and NF-κB signalling. The $GC^{-/-}Rag2^{-/-}$ mice which hosted these tumours exhibit T cell, B cell and NK cell immunodeficiencies, but still have functioning innate immune system components such as macrophages and neutrophils. Bearing this in mind, gene expression changes relating to immune interactions may still be explored in the cancer cells in this model. The RNAseq data showed that $Na_v1.5$ knock-down decreased the expression of many genes involved in the immune system, particularly several genes involved in antigen presentation. This is apparently in conflict with the findings of (Murtadha *et al.*, 2021) who showed that $Na_v1.5$ downregulation in MDA-MB-231 cells by siRNA increased MHC class I mRNA expression. This difference may be explained by the fact that one study was performed in MDA-MB-231 cells *in vitro* whereas this project used the same cells but in an *in vivo* experiment

model. Alternatively, there may be a change in MHC class with $Na_v1.5$ knock-down, since most of the downregulated HLA genes were class II in this study. Class II MHC molecules mostly present peptides deriving from the endolysosomal system whereas class I MHC mostly presents endogenously expressed proteins. Decreased expression of MHC class I is a common method of immune evasion in cancer cells (Maleno *et al.*, 2002; McGranahan *et al.*, 2017), since it prevents activation of cytotoxic T-cells. Another important means of evading the adaptive immune system is by PD1 signalling, reducing activation of CD8 +ve T lymphocytes (Iwai *et al.*, 2002). The Reactome analysis showed that this pathway might have been affected by knock-down of $Na_v1.5$ (Figure 4.9 B).

The IDO1/kynurenine pathway is a third immunosuppressive mechanism important in immune evasion by cancers. IDO1 and kynurenine aminotransferase 1 (encoded by Kyat1) both convert tryptophan to kynurenine, starving immune cells of tryptophan. IDO1 is often upregulated in cancer cells but it can also be produced by tumour stromal cells in response to inflammatory mediators such as interferon-γ and TNF-α (Liu *et al.*, 2018). The upregulation of mouse Ido1 and Kyat1 in the $Na_v1.5$ knock-down tumours could be due to an increase in IFN signalling, as this appears to be changed in cancer cells upon knock-down of $Na_v1.5$ (Figure 4.55 and Figure 4.9 B). There was no evidence of changed *IDO1* expression in the cancer cells however.

4.3.3 Effects of $Na_v1.5$ knock-down on ROS signalling

The downregulation of human (Figure 4.7 B) and mouse (Figure 4.10) ROS detoxification genes when $Na_v1.5$ was knocked down was particularly interesting since ROS signalling is disrupted in cancer and is important in regulating cell survival, angiogenesis and EMT (Aggarwal *et al.*, 2019; Lee *et al.*, 2019b). ROS regulates VGSC function by increasing persistent Na^+ current through $Na_v1.5$ in cardiomyocytes (Avula *et al.*, 2021). Similarly, ROS increases VGSC current in dorsal root ganglion neurons (Wang *et al.*, 2011a). In HEK-293 cells expressing $Na_v1.5$ however, *acute* ROS treatment decreased Na^+ currents by

approximately half, so the effect of ROS on VGSCs may be timing- or context-dependent (Liu *et al.*, 2010). It is likely that ROS-dependent increase in $Na_v1.5$ current may require changes in transcription if this effect only happens with longer term ROS treatment.

There is little known about the effect of VGSCs on ROS homeostasis, so the finding that $Na_v1.5$ knock-down affects ROS-related genes opens a new avenue for research. Recently high mitochondrial [Na^+] has been shown to increase ROS production in mitochondria by increasing inner membrane fluidity and therefore preventing ubiquinone from moving to complex III of the electron transport chain (Hernansanz-Agustín *et al.*, 2020). Increase in cytosolic [Na^+] mediated by VGSCs might be expected to increase mitochondrial [Na^+] through NCLX, and VGSCs may therefore lead to ROS production in this way.

Superoxide anions and hydrogen peroxide regulate the activity of transcription factors, including AP-1 and NF-κB in breast cancer cells (Li *et al.*, 1998). In the overrepresentation analysis, several gene ontology terms related to NF-κB signalling were enriched in the downregulated gene set (Figure 4.5) so it is possible that VGSCs affect NF-κB signalling via ROS intermediates.

4.3.4 Effects of $Na_v1.5$ knock-down on invasion and migration

Metastasis is associated with EMT which includes an increase in expression of ECM components collagens and fibronectin, and matrix metalloproteases (MMPs) (Park & Schwarzbauer, 2014). It is therefore unsurprising that VGSC downregulation, which decreases metastasis (Nelson *et al.*, 2015b) also decreases expression of genes associated with the extracellular compartment (Figure 4.6 A). Interestingly, this category of genes was also enriched in the upregulated mouse genes (Figure 4.11), suggesting that stromal cells may resume control of extracellular matrix production when $Na_v1.5$ is knocked down in the cancer cells.

After showing that $Na_v1.5$ was involved in a network of invasion genes in colon cancer cells, House *et al.* performed qPCR to look for changes of expression of certain invasion-related genes after veratridine treatment to open VGSCs (House *et al.*, 2015). The invasion genes upregulated with increased VGSC activity were *CD44, CLIC4, ITGB1, SEMA6A, VEGFC, WNT9A* and *HIF1A*. It might be expected that these same genes would have decreased expression with reduction in VGSC expression, however, none of these genes were downregulated in $Na_v1.5$ knock-down tumours. The following similar genes were downregulated: *CLIC3*, *SEMA3F* and *WNT3*. In addition, several genes involved in degradation of ECM proteins were downregulated (Table 4.7 and Figure 4.6 A). These results are consistent with the findings from (Gillet *et al.*, 2009) showing that VGSC activity in cancer cells aids degradation of the ECM.

Several Ca^{2+} signalling terms were enriched in the overrepresentation analysis of $Na_v1.5$ knock-down tumours, although the particular cancer cell functions which would be likely to occur based on these changes are unclear. The gene coding for the transient receptor potential cation channel subfamily member V4, *TRPV4*, was downregulated, and this gene increases migration via the RhoA/ROCK1 pathway in endometrial cancer (Li *et al.*, 2020), so could potentially be important for migration in breast cancer cells. This would fit with the findings that $Na_v1.5$ promotes migration in cancer cells (Fraser *et al.*, 2003; Brackenbury & Djamgoz, 2006). Other Ca^{2+} signalling genes which were downregulated were *CACNA2D4* which codes for the $\alpha_2\delta4$ subunit of VGCCs. $\alpha_2\delta$ subunits increase VGCC currents at the plasma membrane (Dolphin, 2018) and are associated with a poor prognosis in gastric cancer (Wanajo *et al.*, 2008). Also the gene coding for the ryanodine receptor 2 (*RYR2)* and *CAMK4* were downregulated. In breast cancer RyR2 protein expression correlates with higher tumour grade and blocking RyR2 reduced proliferation in MCF7 and MDA-MB-231 cells (Abdul *et al.*, 2008). Thus it is possible that $Na_v1.5$ regulation of RyR2 expression may be important for its function in cancer.

4.3.5 Effects of $Na_v1.5$ knock-down on hypoxia and pH homeostasis

To address the possibility that VGSC activity may increase glycolytic respiration it was important to look at enzymes involved in respiration, hypoxia and acid-base regulation (Table 4.8). The hypoxia biomarker and pH regulator *CA9* (carbonic anhydrase IX) was downregulated when $Na_v1.5$ was knocked down. It is possible that hypoxia is more prevalent in $Na_v1.5$-expressing tumours, but another explanation is that in $Na_v1.5$-expressing tumours carbonic anhydrase IX is required to mitigate a greater production of acidic metabolites even in normoxic conditions. Other evidence for changes to metabolism are shown by the redox regulatory genes discussed earlier. In addition, VEGF signalling was slightly enriched in the Reactome analysis when $Na_v1.5$ was knocked down (Figure 4.9 B). In a similar vein, in the mouse genome analysis, oxygen delivery genes were downregulated in the $Na_v1.5$ knock-down tumours (Table 4.11). It is likely that these genes were present in reticulocytes (premature erythrocytes which still contain some DNA) since these comprise up to 6% of the red blood cells in mice (O'Connell *et al.*, 2015). These findings indicate that oxygen delivery might be better in $Na_v1.5$-expressing tumours, despite a higher expression of carbonic anhydrase IX in the cancer cells. This indicates that $Na_v1.5$ may be involved in generating a Warburg phenotype.

4.3.6 Conclusions and further work

The key findings from the RNAseq experiment (Figure 4.14) go some way to support the hypothesis that VGSC activity increases the rate of glycolysis and H^+ production. Particular evidence which supports this theory is the positive regulation of CAIX by $Na_v1.5$. An increase in expression of CAIX indicates a greater need for H^+ removal from the cell. If the previous hypothesis is true, that $Na_v1.5$ activity allosterically modulates NHE1 to promote H^+ extrusion (Brisson *et al.*, 2013), there would be less requirement for CAIX when $Na_v1.5$ is active. Other evidence of a change in metabolism was shown by changes in ROS regulation in both cancer and stromal cells, since ROS is produced by mitochondria instead of ATP in certain states such as hypoxia (Kim *et al.*, 2007b). $Na_v1.5$ promotion of VEGF

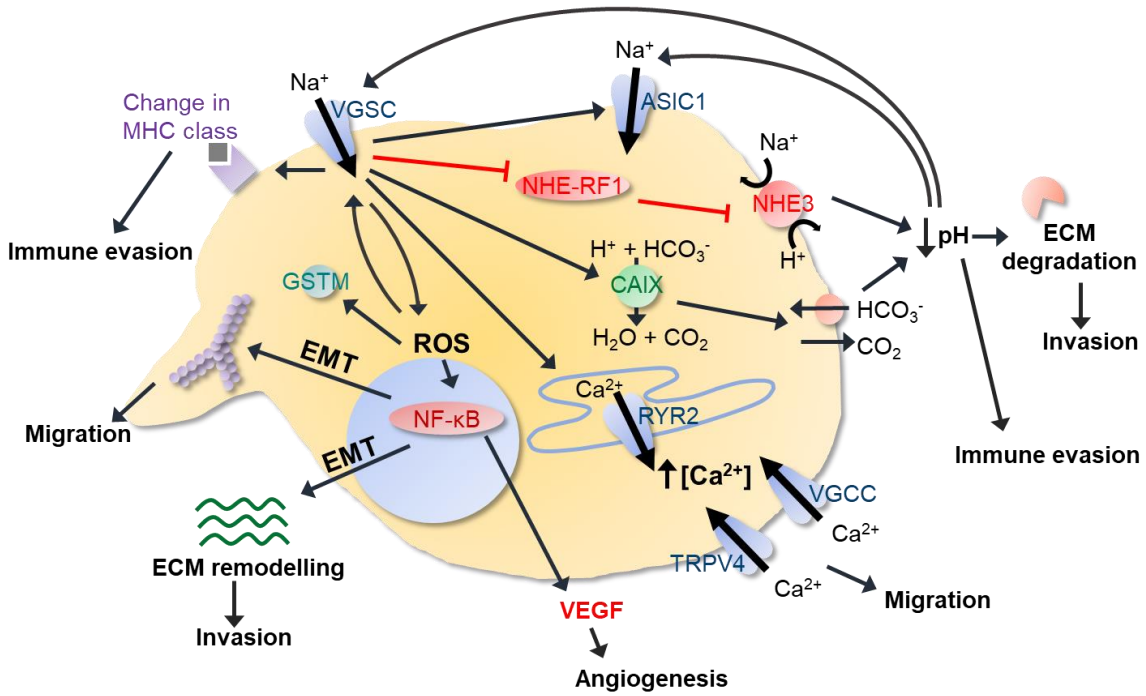

Figure 4.14 RNAseq findings: possible oncogenic actions of $Na_v1.5$ in MDA-MB-231 cells. 1. Extracellular acidification through reduced NHE-RF1 inhibition of NHE3 as well as upregulation of CAIX. Others have shown that this increases ECM degradation and invasion. 2.Immune evasion via a change from MHC class I to MHC class II, as well as via extracellular acidification via NHE3 and CAIX. 3. Upregulation of ASIC1 which, like $Na_v1.5$ allows Na^+ into the cell in low pH_e. 4. Upregulation of ROS signalling with positive feedback on persistent Na^+ current through VGSCs. 4. Upregulation of NF-κB signalling (possibly via ROS signalling) which promotes EMT. EMT increases migration and production of ECM components which promotes cancer cell invasion. 5. Upregulation of VEGF signalling and angiogenesis, perhaps via ROS and/or NF-κB. 6. Increased Ca^{2+} signalling via RYR2, TRPV4 and the $\alpha_2\delta$ subunit of VGCCs which might increase migration.

signalling and angiogenesis was another indicator that hypoxia may be more prevalent when $Na_v1.5$ is active, necessitating an upregulation of glycolysis. These new findings show that there may be additional metabolic changes driven by $Na_v1.5$ on top of those caused by an increase in NKA activity.

The effect of $Na_v1.5$ on ROS detoxification genes was particularly interesting, considering that high mitochondrial [Na^+] disrupts the electron transport chain (Hernansanz-Agustín *et al.*, 2020). Since several glutathione-S-transferase genes were downregulated when $Na_v1.5$ was knocked down, this should be confirmed by qPCR. A glutathione functional assay would then be useful to indicate whether glutathione antioxidant function is reduced in $Na_v1.5$ knock-down cells. Since glutathione is likely to be produced to counteract an increase in cellular ROS, assays of ROS could be performed in cancer cells expressing VGSCs and compared to those in which VGSCs are genetically or pharmacologically inhibited. Linked to the ROS studies, immunohistochemical investigations into vascularisation, oxygenation and pH status of tumours may show differences with VGSC activity, even though no difference in protein expression of the endothelial marker CD31 was seen in $Na_v1.5$ knock-down tumours (Nelson *et al.*, 2015b). There were however indications of $Na_v1.5$-dependent changes to VEGF signalling in the human Reactome analysis and changes to oxygen carrying genes in the mouse genome analysis of the RNAseq data.

There is evidence that high extracellular NaCl may affect NFAT-5 signalling via ROS intermediates (Zhou *et al.*, 2005). The transcription factor NFAT-5 is important in regulating the immune system and promotes VEGF signalling in response to hyperosmolar conditions in breast cancer (Amara *et al.*, 2016). Given that there are indications that VGSCs might be involved in VEGF signalling and immune system modulation from this RNAseq data, involvement of VGSCs or other Na^+ channels in the NFAT-5 pathway should be explored.

Performing an RNAseq experiment in a xenograft model of breast cancer does not allow a proper examination of the anti-tumour immune response. Given several indications from this study that $Na_v1.5$ expression affects antigen presentation and immune modulation, it would be helpful to perform a similar study in an immunocompetent host. A benefit of using a xenograft model in this study was that gene expression in stromal cells could be examined separately from gene expression in cancer cells, whereas in a syngeneic allograft (e.g. 4T1 cells in BALB/c mice) or spontaneous model of breast cancer (e.g. MMTV-PyMT transgenic mice) (Liu *et al.*, 2021) it would be impossible to know whether any gene expression changes were in cancer cells or other cell populations. To be able to study the activity of $Na_v1.5$, this protein would need to be expressed in the cancer cells of whichever model was chosen, and $Na_v1.5$ has been shown to be present in 4T1 cells by immunofluorescence (Mokhtar *et al.*, 2019).

5 $Na_v1.5$ expression and functional activity in breast tumours

5.1 Introduction

Functional $Na_v1.5$ has been found in the highly metastatic MDA-MB-231 breast cancer cell line, and several experiments have been performed with this cell line to show that activity of this channel is important for tumour growth and metastasis in mice (Driffort *et al.*, 2014; Nelson *et al.*, 2015a; Nelson *et al.*, 2015b). At the mRNA level, expression of $Na_v1.5$ was upregulated in breast cancer compared to normal breast in three datasets, and it correlated with worse prognosis (Yang *et al.*, 2012). Less is known about protein expression of $Na_v1.5$, but in subjective analysis of six breast cancer biopsies, protein expression of neonatal $Na_v1.5$ was upregulated compared to four normal breast tissue specimens (Fraser *et al.*, 2005). A larger study of protein expression of $Na_v1.5$ in 36 breast cancer biopsies also revealed that $Na_v1.5$ was upregulated in cancer tissue compared to adjacent healthy breast tissue (Nelson *et al.*, 2015b). Similarly, neonatal $Na_v1.5$ protein expression was higher in breast cancer tissue than in normal specimens (Yamaci *et al.*, 2017).

The predominantly expressed β-subunit in MCF7 cells is β1 (Chioni *et al.*, 2009), and artificial β1 expression in MDA-MB-231 cells increased tumour growth and metastasis (Nelson *et al.*, 2014). There is less information on β1 than on $Na_v1.5$ in breast cancer patients, but β1 mRNA expression was upregulated in breast cancer in two out of eight datasets (Nelson *et al.*, 2014). At the protein level, β1 protein was upregulated in breast cancer compared to adjacent healthy breast tissue in a sample size of 66 tumours, but it did not correlate with ER status, lymph node invasion or grade (Nelson *et al.*, 2014). Given the role that β1 has been shown to have in breast cancer invasion and metastasis (Chioni *et al.*, 2009; Nelson *et al.*, 2014), it would be desirable to know more about the relationship of β1 with breast cancer prognosis.

Although there were indications that $Na_v1.5$ expression might correlate with lymph node invasion (Nelson *et al.*, 2015b) and ER -ve status (Yamaci *et al.*, 2017) in breast cancer, no previous protein expression studies were able to find any statistically significant relationships between $Na_v1.5$ or β1 expression and survival, receptor status or other prognostic indicators so there was a clear need for a larger study to address these questions.

VGSC currents have been reported in the MDA-MB-231 and MDA-MB-468 breast cancer cell lines (Roger *et al.*, 2003; Fraser *et al.*, 2005; Fraser *et al.*, 2016). However, to establish clinical relevance, it is also important to evaluate whether VGSC are functionally active in breast cancer tissue/cells direct from patients. The only VGSC currents reported thus far in any primary cancer cells were in long-term primary cultures of cervical cancer cells from two patients, out of an unknown number of samples tested (Farias *et al.*, 2004; Hernandez-Plata *et al.*, 2012). There are no reported recordings of VGSC currents in cancer tissue slices of any cancer type. In fact, patch clamp recording in tissue slices is uncommonly performed other than in brain slices. There is one example of patch clamp recordings from cancer cells in brain slices (Bordey & Sontheimer, 1998). It is therefore relevant to try to measure VGSC currents in breast cancer tissue and/or near patient primary breast cancer cells. Therefore, the aims of this chapter were to assess VGSC currents in breast cancer tissue slices and primary cells using whole cell patch clamp recording.

5.2 Results

5.2.1 Protein expression of $Na_v1.5$ and β1 in breast tumours

A TMA containing sections from 1481 patients was obtained from the Breast Cancer Now Tissue Bank (Figure 5.1 B), and the slides were stained with anti-$Na_v1.5$ or anti-β1 antibody (see Section 2.8). The anti-$Na_v1.5$ antibody used recognizes both adult and neonatal splice variants (House *et al.*, 2010). Scoring of staining intensity in carcinoma cells was performed using a modified Allred scoring system (Allred *et al.*, 1998). Examples of scored sections for both antibodies are shown in Figure 5.1 A and negative controls in Figure 5.1 B. These

negative controls were sections stained with antibody which had been pre-incubated with the immunising peptide to inhibit its activity. $Na_v1.5$ was seen mostly in the cytoplasm whereas β1 was sometimes seen in the nucleus, but other times as cytoplasmic granules (likely organelles) or diffusely present in the cytoplasm (Figure 5.1 C). For this reason, the distribution of β1 staining was also scored as nuclear, mixed or cytoplasmic. Previously β1 has been found mainly in the cytoplasm and less often at the plasma membrane in breast cancer biopsies (Nelson *et al.*, 2014).

5.2.1.1 Concordance between observers

The reliability of scoring was assessed in a sample of ~ 10 % of the anti-$Na_v1.5$-stained sections by a qualified histopathologist, Dr Wakkas Fadhil. The concordance between the two observers was assessed in this subset of sections. For these two scorers, the Intraclass Correlation Coefficient was 0.954 (95% CI 0.938-0.966, P <0.0001). Another measure of concordance, Cohen's weighted kappa was 0.814 (95% CI 0.766- 0.865, P < 0.0001). Both of these statistical tests show excellent agreement of the two scorers.

Since both $Na_v1.5$ and β1 were assessed in serial sections from the same cores, the relationship between $Na_v1.5$- and β1- staining could be investigated in the tumour cores. There was no correlation between $Na_v1.5$ and β1 scores (Spearman test P = 0.30).

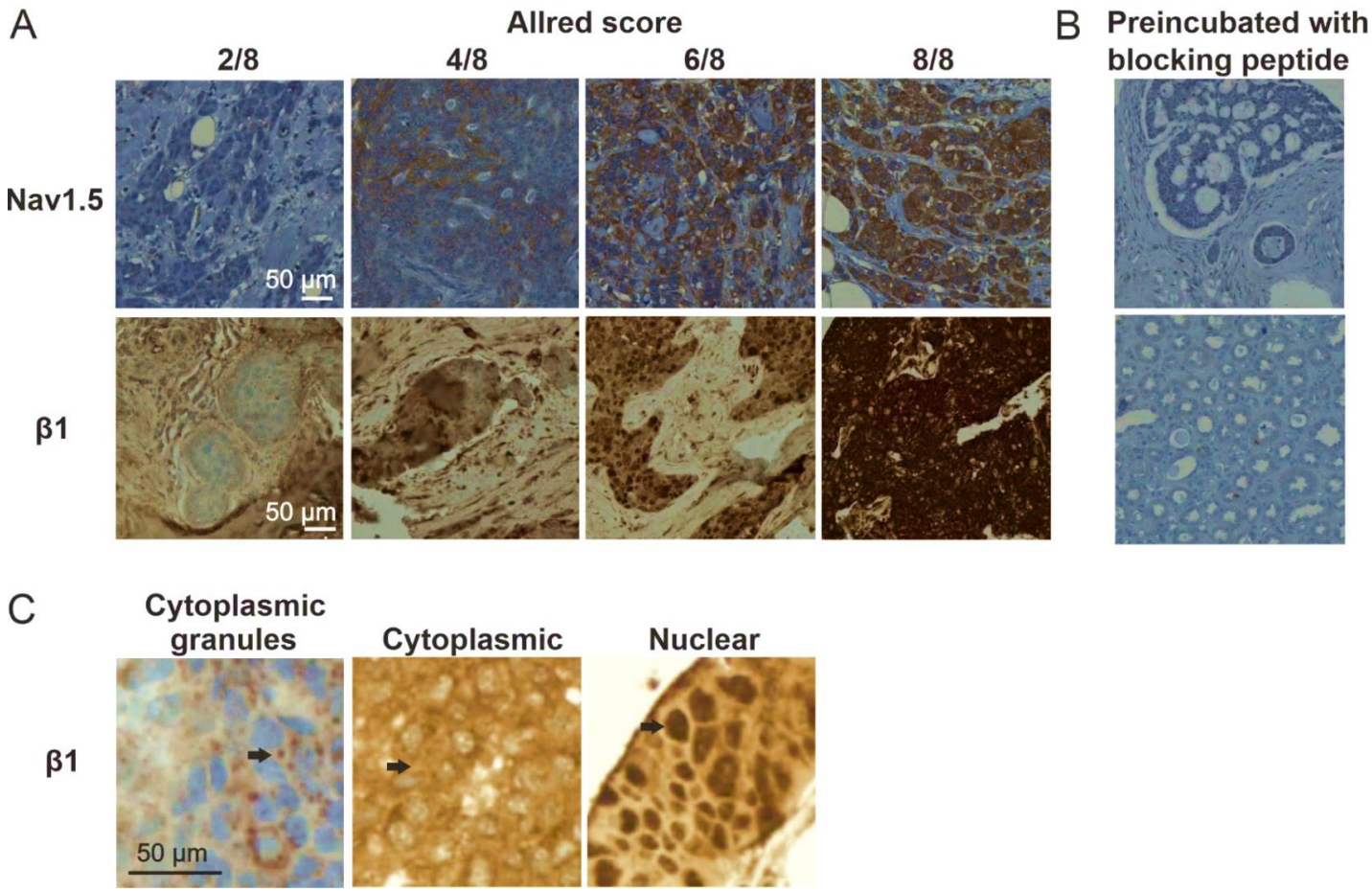

Figure 5.1 Breast tumour TMA staining.
A. Example TMA slide showing sections from many different tumours. **B**. Examples of each score of staining for both anti-$Na_v1.5$ and anti-β1 antibodies. **C**. Example sections which had been stained with anti-$Na_v1.5$ or anti-β1 antibody, each of which had been pre-incubated with the immunising peptide to block its activity. **D**. Examples of TMA sections showing a variety of distributions of β1 staining.

5.2.1.2 Association between $Na_v1.5$ or β1 and survival

Next, anonymised patient data were obtained from the Breast Cancer Now Tissue Bank, allowing investigation into the prognostic potential of $Na_v1.5$ and β1. Kaplan Meier plots were generated and log-rank (Mantel-Cox) tests were performed to compare survival in low and high scoring tumours. For $Na_v1.5$, low scores were considered to be 0-3 and high scores were 4-8. For β1 in which most sections scored highly, low scores were considered to be 0-4 and high scores were 5-8. High $Na_v1.5$ scoring was associated with significantly poorer outcomes with all surrogate measures of survival as well as overall survival. Metastasis was the outcome which was most associated with $Na_v1.5$, both in size and significance of the effect, with a hazard ratio of 2.18 (95 % CI 1.62-2.92) and $P < 0.0001$ (Table 5.1; Figure 5.2 A-E). In contrast, there was no relationship of β1 with any survival outcome, or nuclear β1 with overall survival (Table 5.1; Figure 5.3).

5.2.1.3 Association of $Na_v1.5$ and β1 with common prognostic indicators

Next the relationship between receptor status and $Na_v1.5$ or β1 presence was investigated. As in survival analyses, β1 was not associated with any receptor status (Fisher's exact tests; Table 5.2; Figure 5.5 A-D). $Na_v1.5$ was negatively correlated with the oestrogen receptor (ER; $P < 0.05$; Fisher's exact test; Table 5.2) and progesterone receptor (PgR; $P < 0.001$; Fisher's exact test, Table 5.2). $Na_v1.5$ was positively correlated with human epidermal growth factor receptor 2 (HER2; $P < 0.01$; Fisher's exact test, Table 5.2). There was no association between $Na_v1.5$ score and triple negative breast cancer (TNBC) status ($P = 0.12$; Fisher's exact test, Table 5.2). These relationships are displayed as violin plots with Mann-Whitney tests in Figure 5.4 A-D. Since there was a strong correlation between $Na_v1.5$ and HER2, the effect of $Na_v1.5$ on survival was assessed in the subset of HER2 +ve patients. There were only 7 patients with HER2 +ve and low $Na_v1.5$ tumours, compared to 170 patients with HER2 +ve and high $Na_v1.5$ tumours, so despite a large apparent hazard ratio of 2.71 (95 % CI 1.12-6.52), there was no significant association of $Na_v1.5$ with survival in the HER2 +ve subset ($P = 0.14$; Figure 5.2 F).

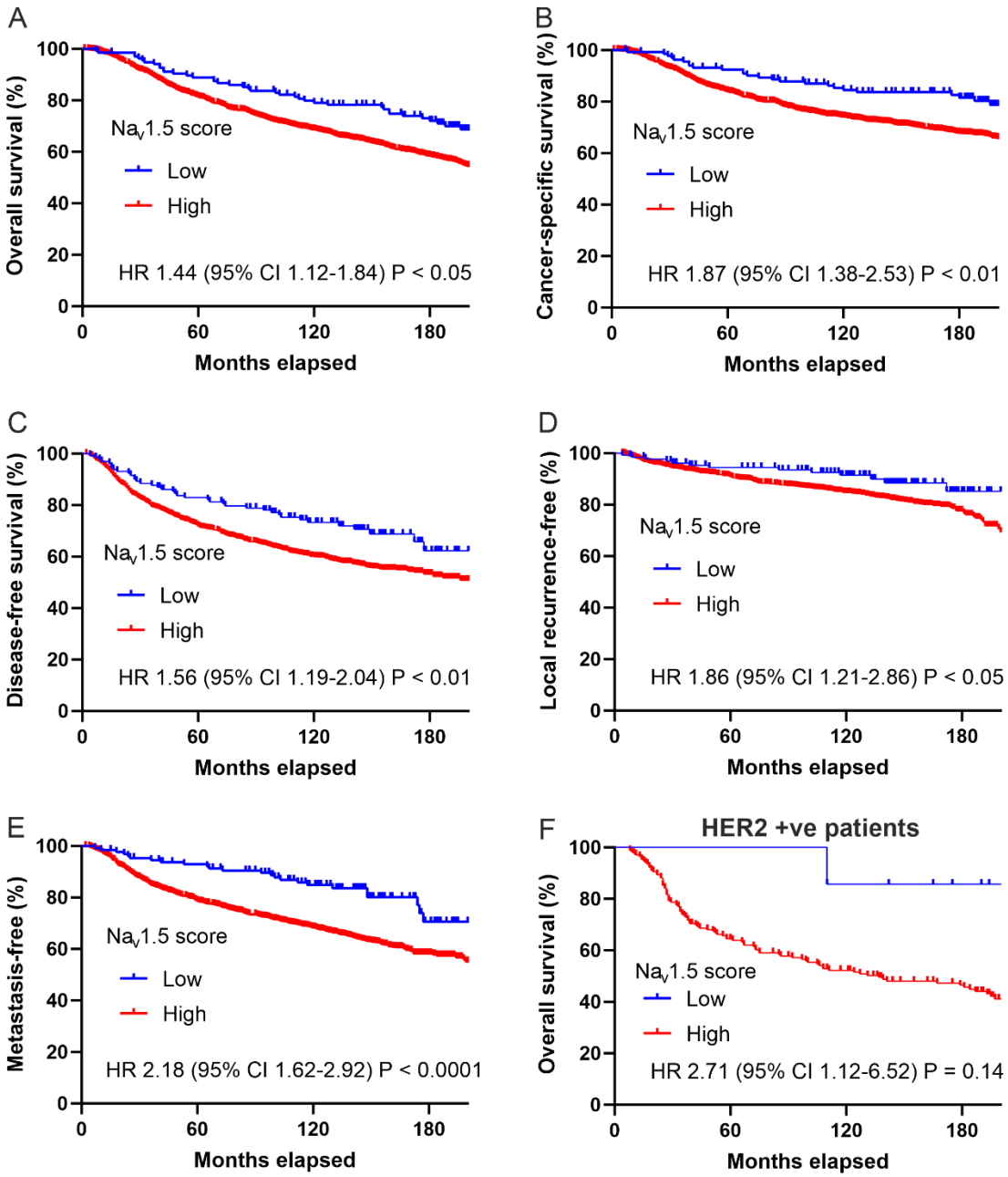

Figure 5.2 Relationship between $Na_v1.5$ expression and survival.
A. Overall survival of patients with tumours of low or high $Na_v1.5$ score ($P < 0.05$; log-rank test). **B**. Cancer-specific survival of patients with tumours of low or high $Na_v1.5$ score ($P < 0.01$; log-rank test). **C**. Disease-free interval of patients with tumours of low or high $Na_v1.5$ score ($P < 0.01$; log-rank test). **D**. Interval until local recurrence of cancer in patients with tumours of low or high $Na_v1.5$ score ($P < 0.05$; log-rank test). **E**. Interval until metastasis in patients with tumours of low or high $Na_v1.5$ score ($P < 0.0001$; log-rank test). **F**. Overall survival of a subset of patients with HER2 +ve positive tumours, showing association with $Na_v1.5$ score ($P = 0.14$; log-rank test).

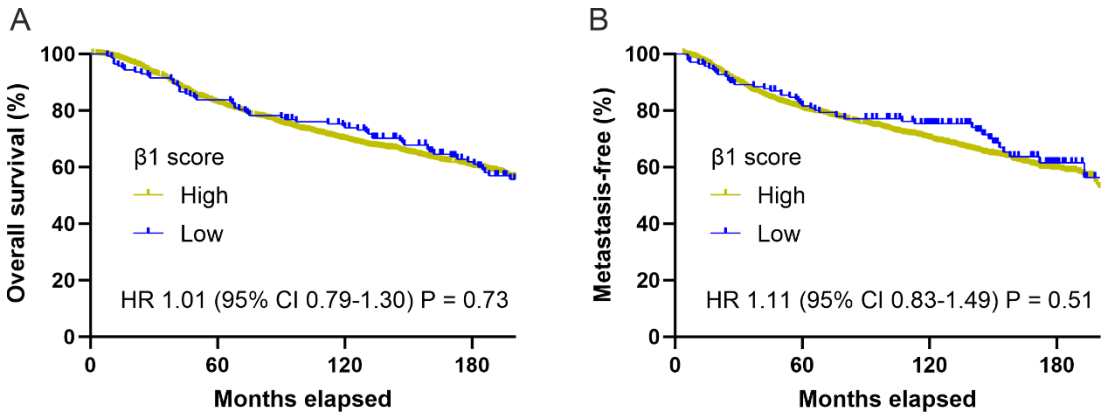

Figure 5.3 Relationship between β1 expression and survival.
A. Overall survival of patients with tumours of low or high β1 score (P = 0.73; log-rank test). **B**. Interval until metastasis in patients with tumours of low or high β1 score (P = 0.51; log-rank test).

Table 5.1 Hazard ratios and log-rank tests of significance of effect of $Na_v1.5$ or β1 on survival outcomes.
Lack of effect of nuclear β1 score (β1 Allred score x nuclear distribution score) on overall survival is also shown.

TMA	Hazard Ratio (95 % CI)		Hazard Ratio (95 % CI)	
	High $Na_v1.5$	P	High β1	P
Overall survival	1.44 (1.12-1.84)	<0.05	1.01 (0.79-1.20)	0.93
Breast cancer specific survival	1.87 (1.38-2.53)	<0.01	1.05 (0.77-1.43)	0.76
Recurrence-free survival	1.56 (1.19-2.04)	<0.01	1.15 (0.88-1.51)	0.33
Metastasis-free survival	2.18 (1.63-2.92)	<0.001	1.11 (0.83-1.49)	0.51
			High nuclear β1	**P**
Breast cancer specific survival			0.92 (0.71-1.19)	0.51

Table 5.2 Contingency tables and Fishers exact tests showing relationships between prognostic indicators and $Na_v1.5$ or β1 score.
Odds ratios > 1 indicate a positive correlation, and < 1 indicate a negative correlation.

TMA	$Na_v1.5$ expression		Odds ratio (95 % CI)	
	Low (%)	High (%)	High $Na_v1.5$	P
ER -ve	24 (1.6)	348 (23.7)	1	
ER +ve	134 (7.5)	983 (6.71)	0.62 (0.39-0.97)	<0.05
PgR -ve	34 (2.4)	539 (38.2)	1	
PgR +ve	94 (6.7)	744 (52.7)	0.50 (0.33-0.75)	<0.001
HER2 -ve	123 (8.8)	1106 (78.7)	1	
HER2 +ve	7 (0.5)	170 (12.1)	2.71 (1.28-5.93)	<0.01
Non-TNBC	113 (7.9)	1065 (74.4)	1	
TNBC	16 (1.1)	238 (16.6)	1.58 (0.92-2.79)	0.12
LN -ve	95 (6.5)	807 (54.9)	1	
LN +ve	42 (2.9)	527 (35.8)	1.48 (1.02-2.17)	< 0.05
Grade 1	42 (2.9)	209 (14.3)	1	
Grade 2 cf 1	39.(2.7)	447 (30.5)	2.30 (1.46-3.65)	<0.001
Grade 3 cf 1	54 (3.7)	674 (46.0)	2.51 (1.64-3.87)	<0.001
Age ≤ 50 years	58 (3.9)	530 (35.9)	1	
Age > 50 years	78 (5.3)	811 (54.9)	1.14 (0.79-1.63)	0.52

TMA	β1 expression		Odds ratio (95 % CI)	
	Low (%)	High (%)	High β1	P
ER -ve	39 (2.7)	306 (21.3)	1	
ER +ve	104 (7.2)	987 (68.7)	1.21 (0.82-1.78)	0.35
PgR -ve	65 (4.7)	483 (35.2)	1	
PgR +ve	72 (5.3)	751 (54.8)	1.40 (0.99-2.01)	0.07
HER2 -ve	122 (8.9)	1085 (78.9)	1	
HER2 +ve	15 (1.1)	154 (11.2)	1.15 (0.67-2.00)	0.68
Non-TNBC	111 (7.9)	1062 (75.6)	1	
TNBC	26 (1.9)	205 (14.6)	0.82 (0.52-1.30)	0.40
LN -ve	86 (5.9)	815 (56.2)	1	
LN +ve	57 (3.9)	492 (33.9)	0.91 (0.64-1.30)	0.65
Grade 1	23 (1.6)	232 (16.1)	1	
Grade 2 cf 1	46 (3.2)	447 (31.0)	0.96 (0.58-1.60)	0.89
Grade 3 cf 1	74 (5.1)	622 (43.1)	0.83 (0.50-1.35)	0.47
Age ≤ 50 years	43 (2.9)	456 (31.3)	1	
Age > 50 years	101 (6.9)	858 (58.8)	0.80 (0.55-1.17)	0.27

ER = oestrogen receptor, PgR = progesterone receptor, HER2 = human epidermal growth factor receptor 2, TNBC = triple negative breast cancer, LN +ve = cancer found in at least one lymph node at diagnosis.

The relationships between $Na_v1.5$ or β1 and other prognostic indicators such as tumour size, grade and lymph node involvement were next investigated. In these, $Na_v1.5$ was associated with worse prognostic indication in every case, whereas β1 had no association with any of these features (Table 5.2 and Figure 5.5). Specifically, $Na_v1.5$ was associated with positive lymph node status ($P < 0.05$; Fisher's exact test; Table 5.2; Figure 5.4 F). $Na_v1.5$ was also positively associated with lymphovascular invasion ($P < 0.01$; Kruskal-Wallis test; Figure 5.4 G), with tumour grade ($P < 0.001$; Fisher's exact tests; Table 5.2; Figure 5.4 H), and with tumour size ($P < 0.001$; Mann-Whitney test; Figure 5.4 I). Unsurprisingly, $Na_v1.5$ was also positively associated with Nottingham Prognostic Index (NPI; $P < 0.001$; Mann-Whitney test; Figure 5.4 J). NPI is a measure which combines tumour size, grade and lymph node involvement in the following formula: NPI = maximum invasive cancer size (S) × 0.2 + lymph node stage (LN = 1, 2, or 3) + histological grade (H = 1, 2, or 3) (Fong *et al.*, 2015).

When the prognostic value of $Na_v1.5$ was compared to that of several commonly used prognostic indicators in breast cancer using a Cox proportional hazards analysis, it was found to perform similarly well to other prognostic indicators (Table 5.3).

In summary, high $Na_v1.5$ protein expression was shown to correlate with worse prognosis, high tumour grade and with lymph node and distant metastasis in breast cancer. No correlation was found between β1 and outcome or tumour characteristics. The presence of functional $Na_v1.5$ in patient tumour tissue and primary cells was next explored.

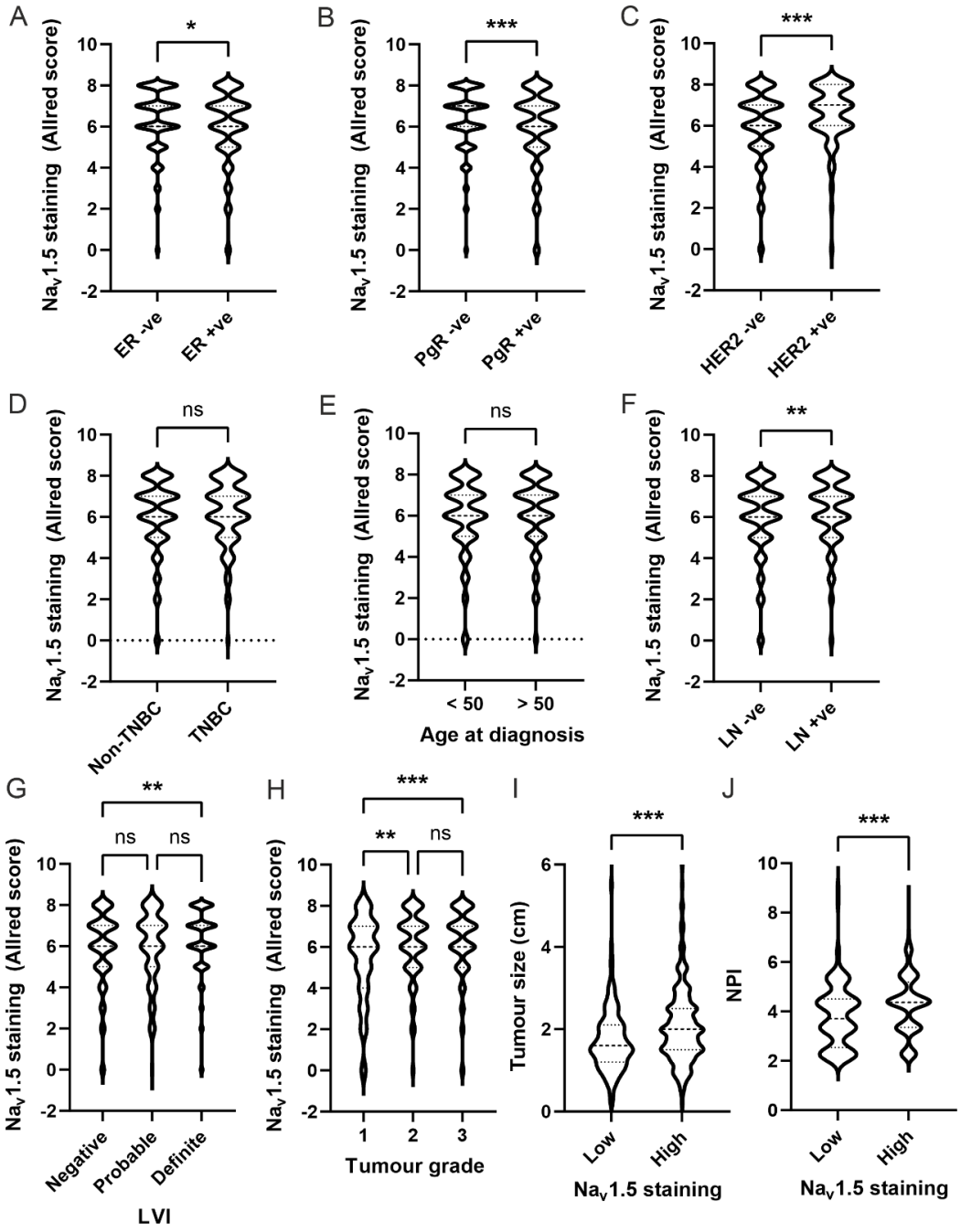

Figure 5.4 Relationship between $Na_v1.5$ score and other prognostic indicators of tumours. **A**. Effect of ER status on $Na_v1.5$ score ($P < 0.05$). **B**. Effect of PgR status on $Na_v1.5$ score ($P < 0.001$). **C**. Effect of HER2 status on $Na_v1.5$ score ($P < 0.001$). **D**. Effect of TNBC status on $Na_v1.5$ score ($P = 0.44$). **E**. Effect of age at diagnosis on status on $Na_v1.5$ score ($P = 0.07$). **F**. Effect of lymph node status on $Na_v1.5$ score ($P < 0.01$). **G**. Effect of lymphovascular invasion status on $Na_v1.5$ score ($P < 0.01$ between negative and definite). **H**. Effect of tumour grade on $Na_v1.5$ score ($P < 0.001$ between grades 1 and 3). **I**. Effect of $Na_v1.5$ score on tumour size ($P < 0.001$). **J**. Effect of $Na_v1.5$ score on Nottingham Prognostic Index (NPI) ($P < 0.001$). Results are Median + quartiles, Mann-Whitney tests (2 groups) or Kruskal - Wallis (3 groups).

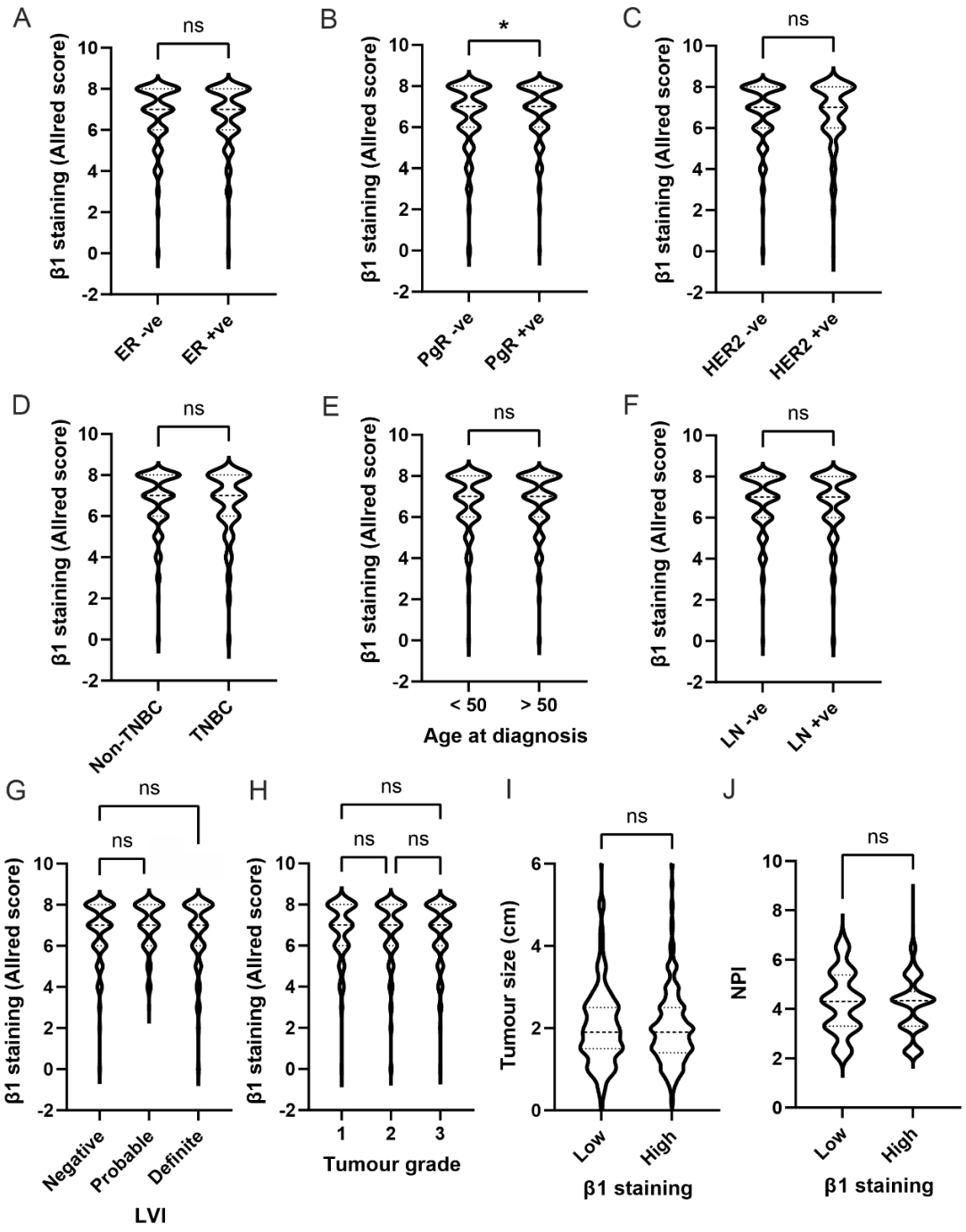

Figure 5.5 Relationship between β1 score and other prognostic indicators of tumours. **A**. Effect of ER status on β1 score (P = 0.71). **B**. Effect of PgR status on β1 score (P < 0.05). **C**. Effect of HER2 status on β1 score (P = 0.74). **D**. Effect of TNBC status on β1 score (P = 0.31). **E**. Effect of age at diagnosis on status on β1 score (P = 0.61). **F**. Effect of lymph node status on β1 score (P = 0.66). **G**. Effect of lymphovascular invasion status on β1 score (P = 0.15 between negative and definite). **H**. Effect of tumour grade on β1 score (P = 0.74 between grades 1 and 3). **I**. Effect of β1 score on tumour size (P = 0.63). **J**. Effect of β1 score on Nottingham Prognostic Index (NPI) (P = 0.49). Results are Median + quartiles, Mann-Whitney tests (2 groups) or Kruskal -Wallis (3 groups).

Table 5.3 Cox proportional hazards analysis of common prognostic indicators compared to $Na_v1.5$ score.

Feature	value	Hazard ratio (95 % CI)	P
$Na_v1.5$ score	**low**	1	
	high	1.58 (1.05-2.37)	<0.05
LN status	**negative**	1	
	positive	1.65 (1.36-2.00)	<0.001
Grade	**1**	1	
	2	1.46 (1.01-2.11)	<0.05
	3	2.62 (1.86-3.70)	<0.001
Size (cm)	**Per increase of 1 cm**	1.16 (1.10-1.22)	<0.001

5.2.2 Electrophysiological recordings from human breast cancer tissue and primary cells

5.2.2.1 Samples used for electrophysiological recordings

As a pilot study, samples from four patient breast tumours that were excess to pathology requirements were acquired via the Breast Cancer Now Tissue Bank (BCNTB). The samples were kept as viable as possible since they were transported in culture medium on ice and arrived on within hours of surgical removal from the patients. The aim of this study was to ascertain whether ion channel currents, in particular VGSC currents, could be recorded from fresh tissue specimens. In tissue slices of the biopsies, there were few cellular areas and most of the slices were composed of connective tissue or fat. Patch clamp recordings were made from small pockets of small, round cells within the connective tissue and were only possible when cells were at the top surface of the slice. Lipocytes were identified by size and avoided. In one of three specimens from which recordings were taken, cells could only be patched successfully after slices had been kept in culture at least overnight, and in one of four specimens received, no cells were seen in any of the slices; instead the slices were composed only of connective tissue. Portions of each tumour were dissociated into individual cells, which were seeded onto coverslips for patch clamp recording. No cells were retrieved from the acellular-appearing specimen in this process.

5.2.2.2 Outward and inward currents in tumour slices

Initially intracellular pipette solution was used which did not contain Cs^+, so K^+ channels were not inhibited. Figure 5.6 A shows example currents measured from using a typical VGSC IV protocol in specimen T2. Obvious outward currents could be seen, but the presence of inward currents was less clear since they can be confused with incompletely compensated capacitance transients. Average current-voltage relationships of the inward currents (Figure 5.6 B), although noisy, show a possible activation at around -50 mV, as expected in VGSC currents. The current-voltage relationships of the outward currents (Figure 5.6 C) are in accordance with many voltage-gated K^+ channels, with activation at around -50 mV.

Comparisons were made between cells in slices of the patient tumours, and cells dissociated from the tumours (Figure 5.7). Patch clamp recordings were challenging in the tumour slices due to the large connective tissue component. This made visualisation, access to the cells and physical stabilisation of the cells difficult. In contrast, it was easier to record from dissociated cells and therefore it was useful to determine whether this was a good alternative to recording from tissue slices. Ion channel currents had similar appearances in slices and on coverslips and they had similar current voltage relationships (Figure 5.7 C and D). The size of the cells, determined by whole cell capacitance did differ between cells in slices and on coverslips, with cells in slices being larger than dissociated cells (Figure 5.7 E).

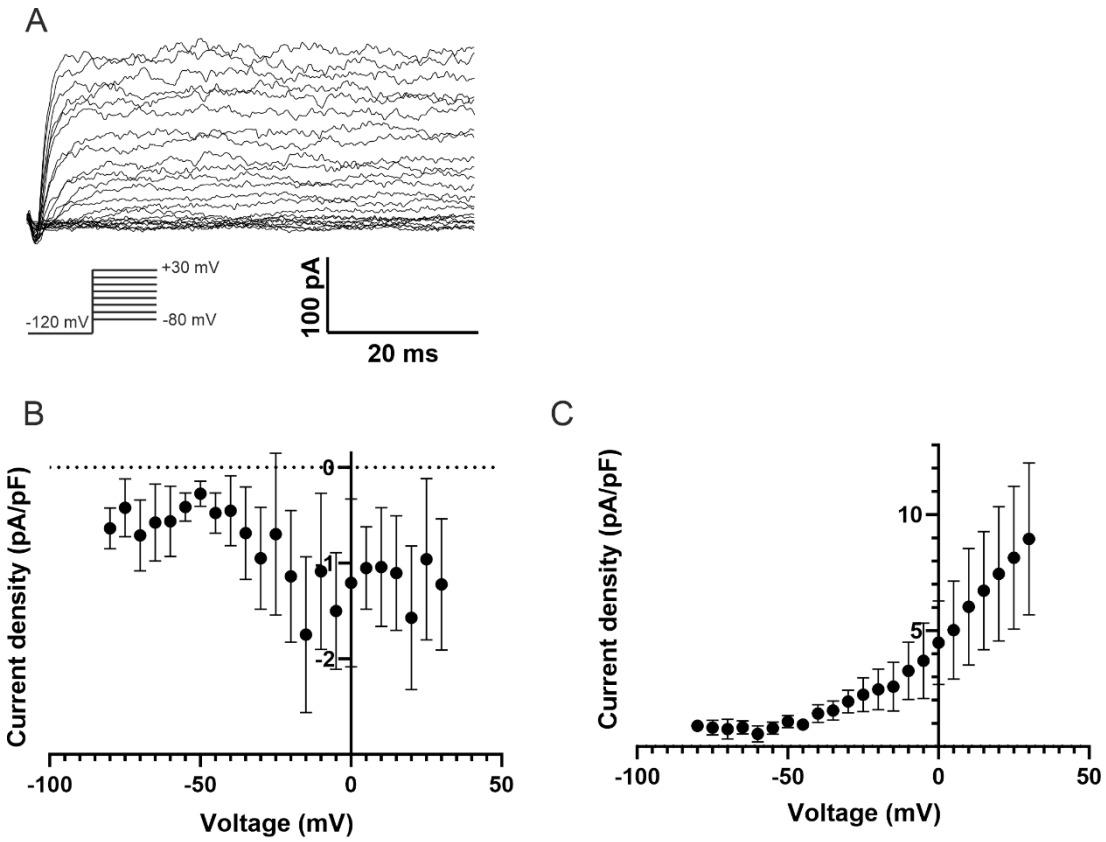

Figure 5.6 Ion channel currents in *ex-vivo* slices of three patient breast cancer tumours. **A**. Family of currents elicited by depolarisation from a V_h of -120 mV to between -80 mV and +30 mV, showing inward and outward currents in specimen T2. **B**. Current-voltage relationship of possible inward currents in tissue slices from specimens T1 and T2 (n = 5 cells from 2 tumours). **C**. Current-voltage relationship of outward currents in tissue slices from specimens T1, T2 and T3 (n = 9 cells from 3 tumours).

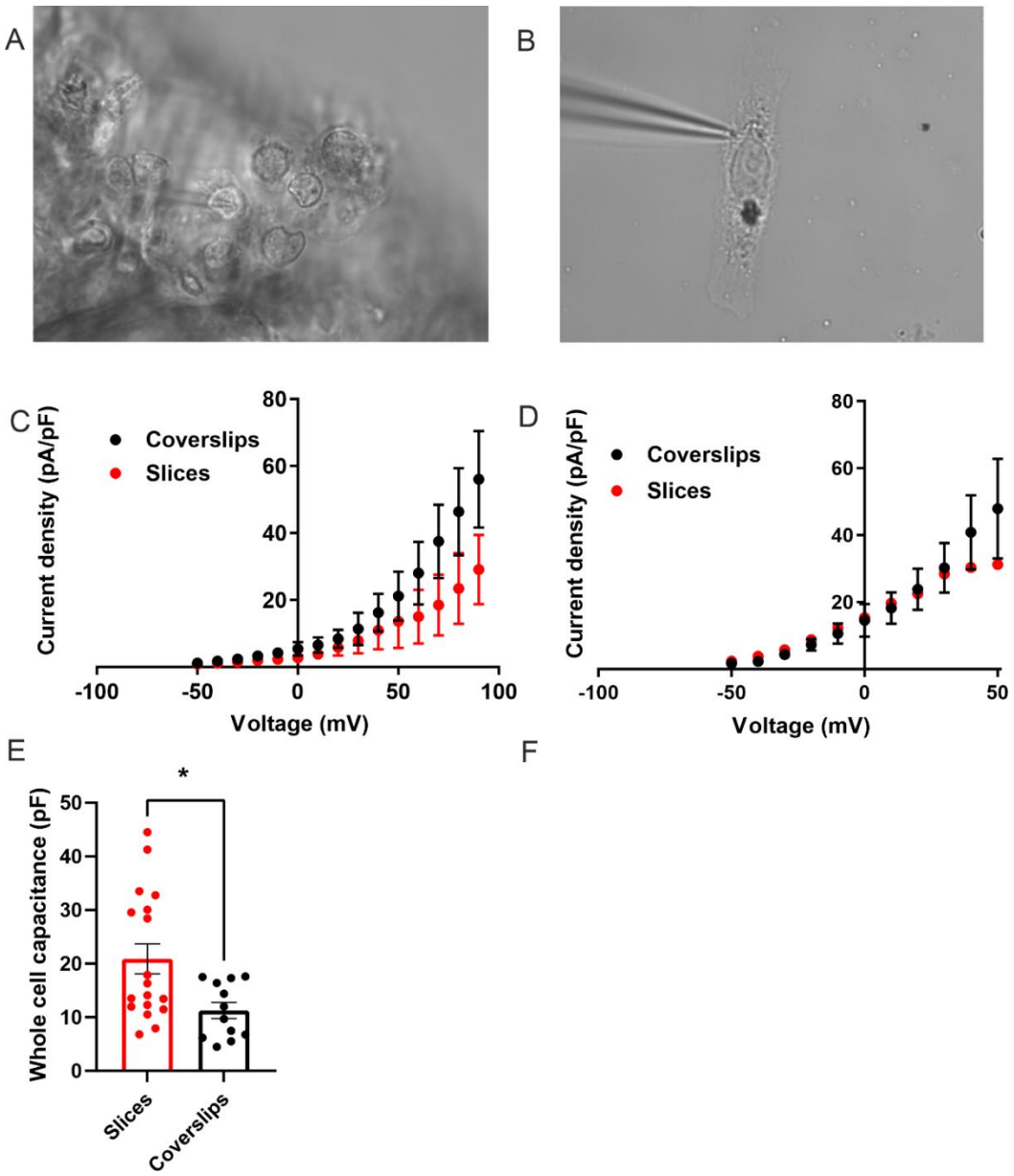

Figure 5.7 Comparison between electrophysiological recordings from cells in tissue slices and cells dissociated from the same tissue.
A. Micrograph of patch clamp recording in a cell in a tumour tissue slice. **B**. Micrograph of patch clamp recording in a cell on a coverslip after its dissociation from a tumour. **C**. Outward current density comparison between coverslips and slices from specimen T1 (n = 2 coverslip cells and 3 slice cells). **D**. Outward current density comparison between coverslips and slices from specimen T2 (n = 3 coverslip cells and 1 slice cell). **E**. Whole cell capacitance measurements from cells in slices and on coverslips from specimens T1 and T2. n = 12 cells on coverslips and 18 cells in slices. Results are mean ± SEM, Students' *t* test.

5.2.2.3 Assessment of cell type in primary cells

Because ion channel recordings did not differ significantly between dissociated cells and cells in slices, dissociated cells were chosen for further investigation. Samples of primary cultures of breast cancer cells and normal breast epithelial cells were obtained from the BCNTB. One sample of primary breast cancer cells (BC2) was examined by immunocytochemistry to assess whether cells were of epithelial or stromal origin. ERα and HER2 antibodies were used as markers of epithelial cells since the tumour of origin was classed as positive for both of these markers by a histopathologist. In this sample, 57/57 cells stained positively for ER (Figure 5.8 A) and 51/52 cells stained as positive for HER2 (Figure 5.8 B). These findings indicate that the vast majority of the primary cells adherent to coverslips were of epithelial origin.

5.2.2.4 Outward and inward currents in primary cells

Out of 14 BC2 cells (a ER+/HER2+ sample) in which patch clamp recordings were made, three had small inward currents (Figure 5.8 C and D). Again, these are not very clear, as they are superimposed on outward currents, but the current-voltage relationships of these inward currents are suggestive of VGSC currents, with activation at -50 mV (Figure 5.8 E-G). In sample BC3 (also ER+/HER2+), one cell out of four had a small inward current, and in sample BC1 (which was triple negative) no inward currents were detected. Voltage-dependent outward currents were found in all three breast cancer samples (BC1-3) (Figure 5.9 A and B). In neither of the two normal breast epithelial cell samples (N1 and N2) were any inward currents found. In the single sample of normal breast epithelial primary cells in which Cs^+-free intracellular solution was used (N1), small voltage-dependent outward currents were seen (Figure 5.9 A and B).

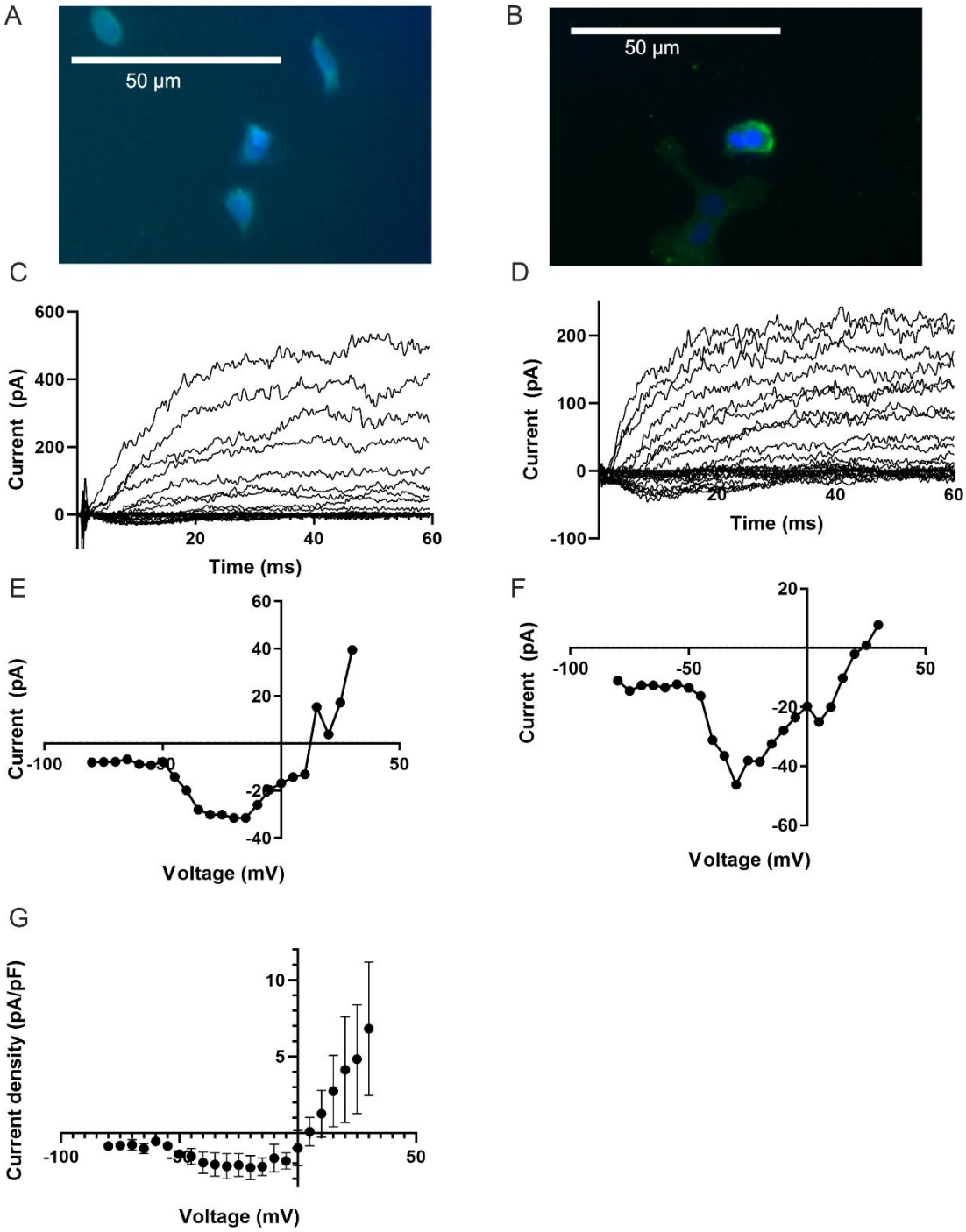

Figure 5.8 Primary breast cancer cells from ER+/ HER2+ tumours.
A. Immunocytochemical staining for ERα in sample BC2. **B**. Immunocytochemical staining for HER2 in sample BC2. **C**. Family of currents elicited by depolarisation from a V_h of -120 mV to between -80 mV and +30 mV in one cell from sample BC2, showing inward and outward currents. **D**. Family of currents as in **C**, from another BC2 cell. **E**. Current-voltage relationships of inward currents in **C**. **F**. Current-voltage relationships of inward currents in **D**. **G**. Average current-voltage relationship of inward currents (n = 4 cells from samples BC2 and BC3).

5.2.2.5 TEA sensitivity of outward currents

To assess whether the outward currents were due to K^+ flux or were instead Cl^- currents or recording artefacts, tetraethylammonium (TEA) was used to inhibit K^+ channels. A reduction in the outward current was seen with application of 5 mM TEA onto a dissociated tumour cell from sample T2 (Figure 5.9 C and D), and the current increased on washout of TEA. However, the current did not reduce to zero with TEA in this cell. In the BC2 cancer cells (Figure 5.9 E) and in the normal breast epithelial cells, TEA had a large inhibitory effect on outward currents (Figure 5.9 F). It therefore appears that most of each of the recorded outward currents can be attributed to K^+ channels. Where the outward current was not fully inhibited with TEA, it is possible that the K^+ channels were not fully sensitive to TEA (Al-Sabi *et al.*, 2010).

5.2.2.6 Assessment of inactivation of outward currents

Perfusing inhibitors onto weakly adherent cells is problematic, as it can alter the seal resistance between the microelectrode and cell. Another method of differentiating between K^+ channels was therefore attempted. Clamping the voltage to -50 mV before the test pulse depolarisations will cause any inactivating voltage-gated K^+ channels to inactivate, whereas holding at a much more negative prepulse voltage (V_h) will make these channels available. Cells were held at either -50 mV or -90 mV for 250 ms before each depolarisation step. In one normal and one of three cancer cells there was a small reduction in outward current with a V_h of -50 mV compared to -90 mV (Figure 5.10 A-D), and one family of traces from a cell in specimen BC1 had evidence of a partially inactivating outward current (Figure 5.10 F) but most currents appeared to be non-inactivating as in Figure 5.10 E.

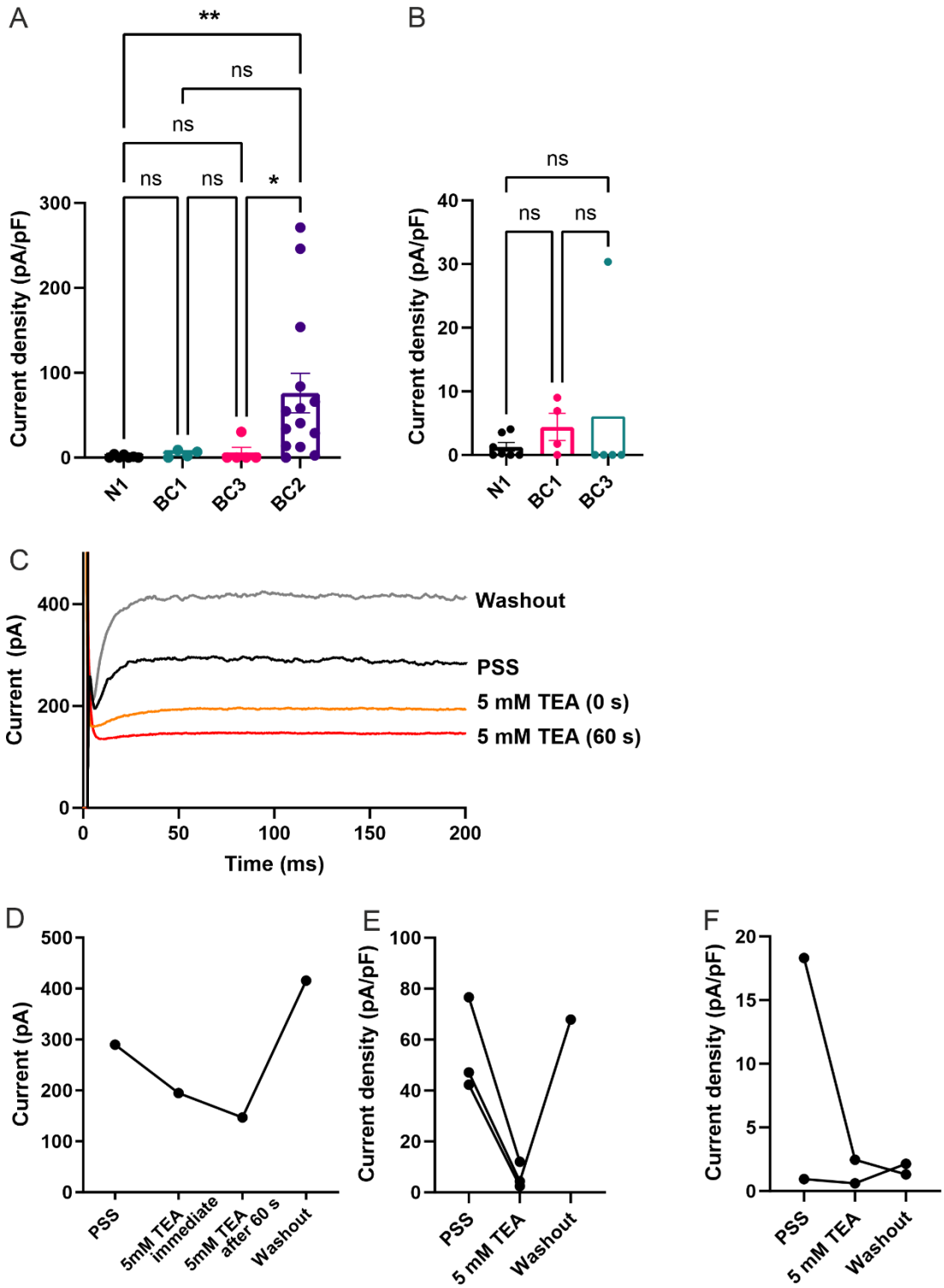

Figure 5.9 Voltage-dependent outward currents in primary cells.
A. Outward current density in primary cells (N1 = normal epithelial cells, BC2 and BC3 = ER+/HER2+ breast cancer and BC1 = triple negative breast cancer). **B**. Graph from **A**, missing sample BC2 so that the Y axis can be expanded. **C**. Example currents elicited by a depolarisation from -60 mV to +50 mV in a cell dissociated from T2, showing reduction with perfusion of 5 mM TEA and increase after washout. **D**. Quantification of currents in **C**. **E**. Effect of 5 mM TEA on outward currents in three BC2 cells. **F**. Effect of 5 mM TEA on outward currents in two N1 cells.

5.2.2.7 RT-PCR detection of K^+ channel mRNA

Likely candidate channels were sought which matched the criteria of non-inactivating, voltage-sensitive K^+ channels with current/voltage relationships like those found in the primary breast cancer cells. Channels matching this description which have been reported to be present in breast cancer cells were K_v10.1 (*KCNH1*) (Borowiec *et al.*, 2007; Ouadid-Ahidouch *et al.*, 2016), K_v11.1 (*KCNH2*) (Arcangeli & Becchetti, 2017; Breuer *et al.*, 2019), K_{Ca}1.1 (*KCNMA1*) (Khaitan *et al.*, 2009; Schickling *et al.*, 2015) and K_{Ca}3.1 (*KCNN4*) (Ouadid-Ahidouch *et al.*, 2004; Thurber *et al.*, 2017). Another candidate K^+ channel found in breast cancer is K_v1.3 (*KCNA3*), although this channel shows inactivation so does not match the majority of currents found in the primary cells (Abdul *et al.*, 2003; Jang *et al.*, 2009; Jang *et al.*, 2011). Expression of these genes was determined by RT-PCR in two tumour and two normal primary cell samples, as well as in the MCF7 cell line (Figure 5.11). Primers used in this analysis are in Appendix II. K_{Ca}1.1 (*KCNMA1*) was only present in the three cancer samples, and not in the two normal samples. K_v1.3 (*KCNA3*) was also present in all three cancer samples but also detectable in one of the normal samples. K_{Ca}3.1 (*KCNN4*) was present in all samples. K_v11.1 (*KCNH2*) was present in one tumour and one normal sample, as well as in MCF7. K_v10.1 (*KCNH1*) was only present in one tumour sample and MCF7 cells.

In summary, this section showed that it is possible to make patch clamp recordings from breast tumour tissue slices, but recording from dissociated cells is an easier alternative. While voltage-gated outward currents were common in breast cancer tissue and primary cell culture samples, voltage-gated inward currents were rarer, and were very small. Outward currents, likely to be through non-inactivating, voltage-sensitive K^+ channels were seen in both cancer and normal breast epithelial cells, but further work is required if these channels are to be identified.

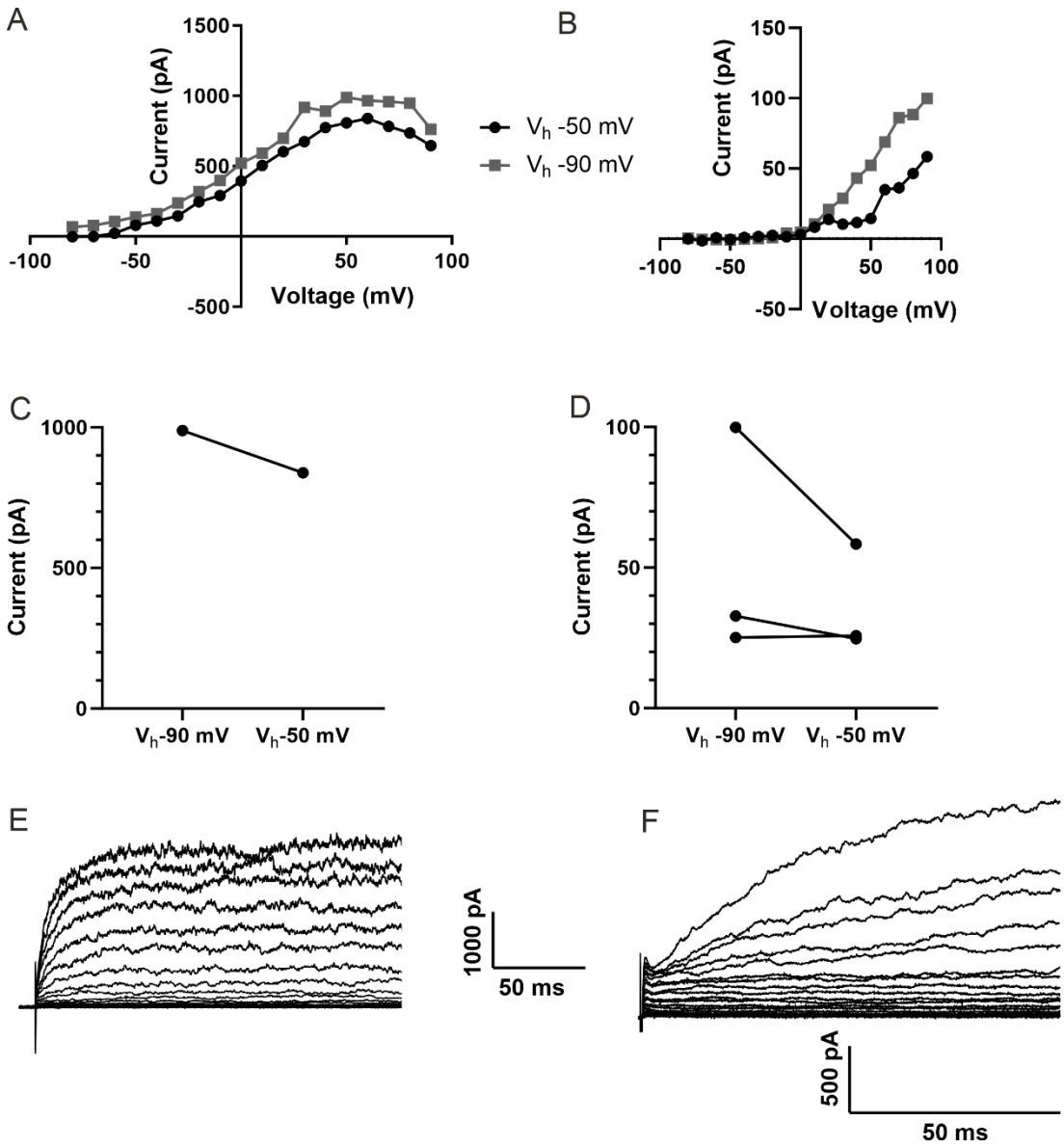

Figure 5.10 Characterising outward currents in primary breast cancer and non-cancer cells. **A**. Current-voltage relationship of outward currents in a N1 normal breast epithelial cell with different V_h before depolarisation. **B**. Current-voltage relationship of outward currents in a BC3 (HER2+/ER+) breast cancer cell with different V_h before depolarisation. **C**. Quantification of outward current in a N1 normal breast epithelial cell after depolarisation to +90 mV from a V_h of -90 mV or +50 mV. **D**. Quantification of outward current in three BC3 cells after depolarisation to +90 mV from a V_h of -90 mV or +50 mV. **E**. Example of non-inactivating outward currents: a family of currents elicited by depolarisation from -50 mV to between -80 and +90 mV in a BC2 (ER+ /HER2+) breast cancer cell. **F**. Example of partially inactivating outward currents: a family of currents elicited by depolarisation from -90 mV to between -80 and +90 mV in a BC1 (triple negative) breast cancer cell.

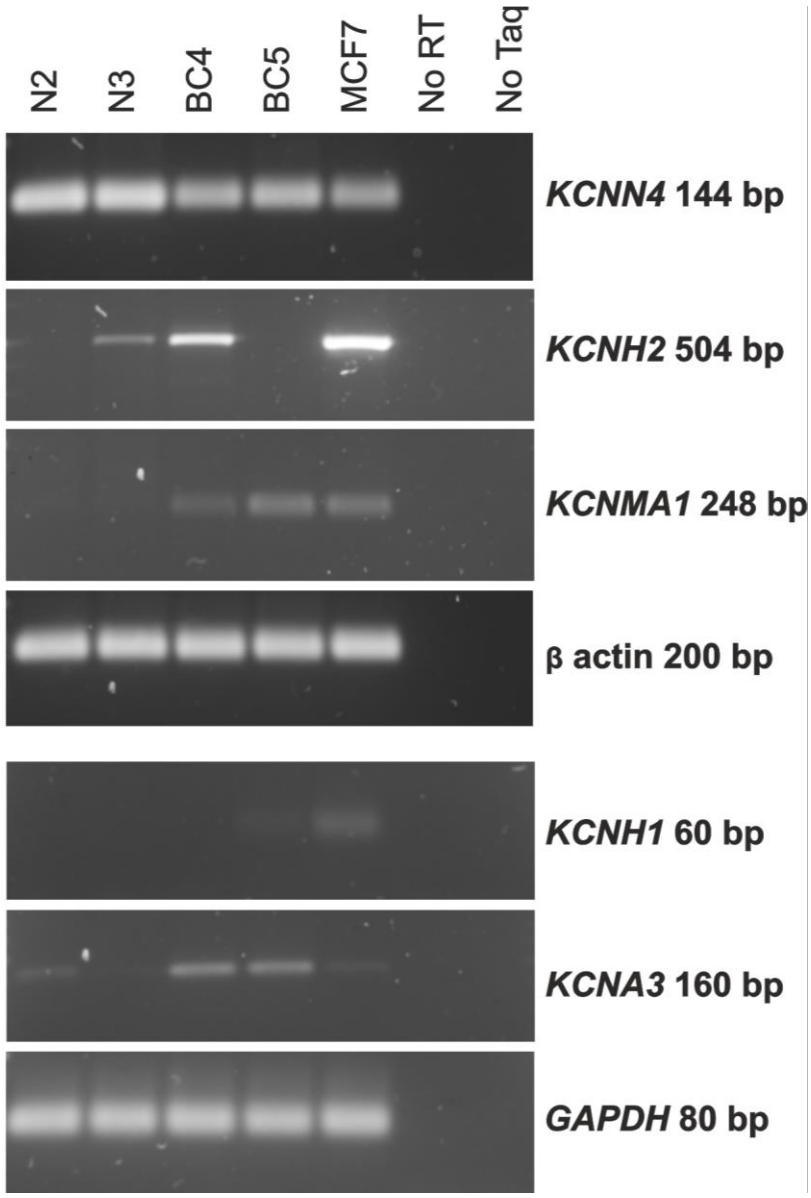

Figure 5.11 RT-PCR detection of K^+ channel mRNA in breast cancer and normal breast epithelial cells.
Agarose gels showing RT-PCR amplification of the K^+ channel genes *KCNN4* ($K_{Ca}3.1$), *KCNH2* ($K_v11.1$), *KCNMA1* ($K_{Ca}1.1$), (*KCNH1* ($K_v10.1$) and *KCNA3* ($K_v1.3$). Breast cancer cells: BC4, BC5 and MCF7; Normal breast cells: N2 and N3. Primers were chosen by the author and RT-PCR and gel electrophoresis were performed by Michaela Nelson.

5.3 Discussion

5.3.1 Summary of main findings:

$Na_v1.5$ protein expression correlates with reduced survival, increased metastasis, higher tumour grade, positive lymph node status, ER -ve status and HER2 +ve status. The prognostic predictive potential of $Na_v1.5$ was comparable to that of LN status, tumour grade and tumour size. In contrast, β1 protein expression did not correlate with any survival or histoclinical characteristics, nor with $Na_v1.5$ expression. Voltage-gated K^+ currents are common in primary cultures of breast cancer cells, but voltage-gated Na^+ currents are small and rare.

5.3.2 VGSC expression in clinical specimens

The strong correlations between $Na_v1.5$ and poor clinical outcomes fit with the other findings from this study that high $Na_v1.5$ expression is associated with higher grade, lymphovascular invasion and lymph node involvement. This confirms trends seen in previous studies with smaller sample sizes (Nelson *et al.*, 2015b; Yamaci *et al.*, 2017). All survival data and histoclinical characteristics point towards $Na_v1.5$ having breast cancer-promoting properties. This is in keeping with many studies showing the effect of $Na_v1.5$ on invasion and migration *in vitro* (Fraser *et al.*, 2003; Roger *et al.*, 2003; Fraser *et al.*, 2005; Brackenbury *et al.*, 2007; Ding *et al.*, 2008; Gillet *et al.*, 2009; Brisson *et al.*, 2011; Driffort *et al.*, 2014; Yang *et al.*, 2020) and tumour growth and metastasis *in vivo* (Yildirim *et al.*, 2012; Driffort *et al.*, 2014; Nelson *et al.*, 2015a; Nelson *et al.*, 2015b). Given the main effect of $Na_v1.5$ in the above studies was increased invasion *in vitro* and metastasis *in vivo*, it makes sense that metastasis was the survival outcome most associated with $Na_v1.5$ in this study.

In this study, high $Na_v1.5$ protein expression associated with ER -ve status. This agrees with studies on cell lines which have shown that the ER +ve cell line MCF7 has low expression of VGSCs, whereas the ER -ve cell line MDA-MB-231 has high VGSC expression (Fraser

et al., 2005). It is also consistent with the findings in (Mohammed *et al.*, 2016) which showed that ER knock down in MCF7 cells increased VGSC current and VGSC-dependent invasion. Similarly, the finding that high $Na_v1.5$ protein expression associated with ER -ve status agrees with the non-significant trend seen in (Yamaci *et al.*, 2017). The implications of these findings together suggest a functional link between ER and $Na_v1.5$, meaning that anti-oestrogen therapies may act partly through decreasing $Na_v1.5$ activity but also loss of ER during breast cancer progression may increase $Na_v1.5$ activity. The intracellular ERα receptor referred to in the above studies is not the only type of oestrogen receptor. The G-protein coupled oestrogen receptor GPR30 (also referred to as ERβ) is present in MDA-MB-231 cells and acute activation of this receptor by oestrogen leads to an increase in Na^+ current (Fraser *et al.*, 2010). Thus it appears that oestrogen has opposite effects on Na^+ current when activating ERβ or ERα. It is likely that ERα acts by changing transcription of $Na_v1.5$ or another protein that regulates $Na_v1.5$ so it may be possible to find an oestrogen response element regulating one of these genes. In contrast, ERβ which acts through a G-protein and PKA has immediate effects on Na^+ current (Fraser *et al.*, 2010).

$Na_v1.5$ expression correlated with HER2 +ve status in this study. There were so few patients with HER2 +ve and low $Na_v1.5$ expression in their tumours that it was not possible to assess the association of $Na_v1.5$ expression with survival in HER2 +ve patients. Given that HER2 +ve status is associated with higher risk of metastasis (Ahmed, 2016), further investigation into the link between HER2 and $Na_v1.5$ is warranted. HER2 is a tyrosine kinase with similarity to EGFR but it does not require EGF to bind to activate mitogenic signalling. HER2 can also dimerise with EGFR instead of another HER2 molecule (Pollock & Grandis, 2015). Given that the growth factor receptors EGFR, VEGFR and IGF-1R increase VGSC transcription via PI3K or MAPK signalling (Fraser *et al.*, 2014), HER2 may have a similar action. This could explain the strong correlation between HER2 and $Na_v1.5$ expression in the breast cancer TMA.

Since the only breast cancer cell lines to exhibit obvious VGSC currents are MDA-MB-231 and MDA-MB-468, two TNBC cell lines (Fraser *et al.*, 2005; Fraser *et al.*, 2016), it could be hypothesised that $Na_v1.5$ correlates with TNBC status. This was not supported by data from the TMA. It is possible that VGSCs are negatively regulated by ERα and positively regulated by HER2 in breast cancer as discussed earlier, but further work is required to determine how these receptors and others regulate $Na_v1.5$ in breast cancer.

The lack of relationship between β1 and $Na_v1.5$ was not as expected since there was a positive correlation reported previously (Nelson *et al.*, 2015b). In addition, since β1 has striking effects on MDA-MB-231 cell morphology and invasion *in vitro* (Chioni *et al.*, 2009; Nelson *et al.*, 2014) and on tumour growth and metastasis *in vivo* (Nelson *et al.*, 2014), it is notable that β1 had no relationship with any histoclinical characteristics or survival in breast cancer patients. The antibody staining for β1 was very strong in almost all tumour sections in the TMA, and it is possible that despite choosing the same antibody and concentration as in (Nelson *et al.*, 2014), the staining was too strong to allow subtle differences in β1 concentration to be resolved. Before any future studies are carried out, careful titration of anti-β1 antibody concentration, or development/selection of a more specific antibody, is needed.

In summary, A much larger cohort of patients was available in this thesis than in previous studies (Fraser *et al.*, 2005; Nelson *et al.*, 2015b; Yamaci *et al.*, 2017). This allowed for better statistical power and confirmed previously non-significant trends seen between $Na_v1.5$ and lymph node status or ER status. It also highlighted novel positive correlations between $Na_v1.5$ and tumour size, grade, lymphovascular invasion and HER2 status.

5.3.2.1 Ion channel activity in tumour slices and primary cells

Given the high proportion of $Na_v1.5$ positive cells in the TMA, it was notable that voltage-gated inward currents were so rare and so small in breast cancer tissues and primary cells.

There are several possible explanations for this apparent contradiction. In the TMA, $Na_v1.5$ staining was visible in the cytoplasm, so plasma membrane staining was difficult to assess. It is possible that VGSCs are usually present on membranes of organelles, and therefore unavailable to carry Na^+ currents at the plasma membrane. It is also possible that the tissue and cell culture conditions led to transport of VGSCs away from the plasma membrane, as $K_{Ca}3.1$ currents in microglia and glioblastoma cells are present in cultured cells but not in tissue slices, discussed in (Catacuzzeno *et al.*, 2012). Increasing the concentration of serum from 5 % to 10 % in culture medium reduced Na^+ current in prostate cancer cells (Ding & Djamgoz, 2004; Ding *et al.*, 2008). Slices and primary cells were cultured in 10 % FBS so this may have reduced their Na^+ current. Both breast cancer cell lines which exhibit large Na^+ currents, MDA-MB-231 and MDA-MB-468 are derived from pleural effusions, and it is possible that Na^+ currents are therefore increased as cells metastasise. More evidence supporting this is the fact that $Na_v1.5$ promotes EMT in MDA-MB-231 and MCF7 cells *in vitro* (Gradek *et al.*, 2019). It would therefore be desirable to assess primary cultures derived from breast cancer metastases for the presence of Na^+ currents. Given the links between ER status and $Na_v1.5$ expression seen in the TMA experiment, Na^+ currents may be more common in ER-ve tumours. The data from these primary cells did not support this theory since the 2/5 specimens which exhibited small Na^+ currents were both ER+ve and the two ER-ve specimens showed no Na^+ currents.

The main evidence for the inward currents being VGSC currents was from IV relationships which showed activation at around -50 mV. This does not however exclude the possibility that these are VGCC currents (Blesneac *et al.*, 2015; Buchanan & McCloskey, 2016). The IV relationships of the inward currents showed a reversal potential closer to zero than would be expected for Na^+ in these recording conditions (+85 mV), but this was an artefact, since inward currents were superimposed by voltage-sensitive outward currents, particularly as the

voltage become positive. Future work is required to fully characterise the identity of these inward currents using pharmacological inhibitors, e.g. TTX.

Several K^+ channels are of importance in cancer development (Pardo & Stuhmer, 2014). The outward current I/V relationships found in breast tumours and primary cells could fit both voltage-gated K^+ or Cl^- channels (Pusch *et al.*, 1995; An *et al.*, 2000; Borowiec *et al.*, 2007). At least some of the outward currents measured were due to K^+ conductance since there was a reduction in current with addition of 5 mM TEA (Hille, 2001). Pre-pulsing at different potentials before depolarising the cell should be able to distinguish between K^+ channels which show inactivation and those that do not. In this study, there was very little evidence of the presence of inactivating currents (Section 5.2.2.5). In agreement with this, there was only one visible example of fast-inactivation of an outward current and this was only partial (Figure 5.10 F). Of the likely K^+ channels fitting the profile of the outward currents measured, there were some ($K_{Ca}1.1$ and $K_v10.1$) which were only expressed in the tumour samples, based on the RT-PCR study (Section 5.2.2.7). The RT-PCR experiment had too small a sample size (n = 2 patients) to make any general conclusions about K^+ channel expression in breast cancer, however.

Notably, the only published recordings of VGSC currents in any cancer cells other than cell lines were from two samples of cells dissociated from cervical cancer tissue, which had been kept in long-term culture (Farias *et al.*, 2004; Hernandez-Plata *et al.*, 2012). This was therefore the first published attempt at recording VGSC currents from primary cancer cells or tumour tissue samples. Although it was possible to make whole cell patch clamp recordings from breast cancer tissue slices, it is a low through-put technique and technically demanding. The main issue is the difficulty in navigating the microelectrode to the cell without first contacting connective tissue. Cleaning the cells by fluid flow and then suction over cell of interest in slices as in brain slices (Edwards & Konnerth, 1992) is not an option due to the poor attachment of cells to the slice. Another issue is the difficulty in obtaining

fresh tissue which is still viable. In future work, in addition to addressing these challenges, it would be important to confirm cell type (e.g. carcinoma vs. stromal) following recordings. One option may be to perform patch-Seq/single-cell RNA sequencing to determine the cell type (Haque *et al.*, 2017).

Although outward current recordings were similar from cells in slices and cells dissociated from the same tumour sample, cells in slices had a larger mean whole-cell capacitance than dissociated cells. It is possible that measurements of larger than normal whole cell capacitance in tissue slices indicated electrical connectivity between cells via gap junctions (Banerjee, 2016). Indeed, whole cell capacitance measurements were used to estimate gap junctional connectivity between cochlear cells (Santos-Sacchi, 1991). Other explanations for the difference in whole cell capacitance could be endocytosis reducing the area of the plasma membrane upon cell dissociation or recording from different cell types in the different situations.

5.3.3 Conclusion

$Na_v1.5$ was associated with poor prognosis and increased metastasis in breast cancer. In addition, $Na_v1.5$ correlated with increased grade, lymph node involvement and lymphovascular invasion. $Na_v1.5$ expression correlated positively with HER2+ve status and negatively with ER+ve status. Ion channel currents could be recorded in human breast tumour tissue slices and primary cells, and primary cells are a useful alternative to slice recording for channel detection. Inward currents were difficult to detect but there were some small currents consistent with VGSCs. The reason for the paucity of inwards currents is unclear, but it is possible that large VGSC currents only appear in metastatic cells.

6 Effect of eslicarbazepine on $Na_v1.5$ in MDA-MB-231 and HEK-293 cells

6.1 Introduction

Preclinical studies have been performed with the VGSC inhibitors ranolazine and phenytoin to assess the effect of these drugs on the MDA-MB-231 xenograft model of breast cancer, and both have shown some promise as anti-cancer drugs (Driffort *et al.*, 2014; Nelson *et al.*, 2015a). Rather unexpectedly given these findings, a retrospective study of cancer patients prescribed VGSC-inhibiting drugs showed that exposure to VGSC inhibitors associated significantly with poorer survival (Fairhurst *et al.*, 2015). The results of this study were skewed by the presence of comorbidities in the treated group since VGSC inhibitors are prescribed for life-shortening conditions such as epilepsy and cardiac arrhythmia. It would therefore be necessary to test the effectiveness of VGSC inhibitors in a randomised controlled trial. Unfortunately, phenytoin, the anti-epileptic drug which showed anti-cancer activity in preclinical models has complicated pharmacokinetics. It takes around three weeks to reach a steady state plasma concentration, partly due to induction of cytochrome P450 (Riva *et al.*, 1996). In addition, induction of cytochrome P450 contributes to multidrug resistance which would be detrimental to cancer patients embarking on chemotherapy. Because of this we wished to investigate the potential of using another antiepileptic VGSC-inhibiting drug in a clinical trial. Eslicarbazepine acetate (ESL) is a member of the dibenzazepine anticonvulsant family of compounds which also includes oxcarbazepine and carbamazepine. It has an improved safety profile and pharmacokinetics compared to older members of the family, taking around one week to reach steady state plasma concentration (Bialer & Soares-da-Silva, 2012; Falcao *et al.*, 2012; Hebeisen *et al.*, 2015). In addition, it does not cause as much induction of cytochrome P450 (Galiana *et al.*, 2017) and has limited drug-drug interactions (Falcao *et al.*, 2012; Zaccara *et al.*, 2015). ESL is taken orally and undergoes first pass hydrolysis to form the stereoisomeric metabolites R-licarbazepine and S-licarbazepine (S-Lic; also known as eslicarbazepine) (Figure 6.1). S-licarbazepine is the

active metabolite and 95% of the circulating drug is in this form in humans (Almeida *et al.*, 2005; Falcão *et al.*, 2007; Maia *et al.*, 2008; Perucca *et al.*, 2011).

Since ESL is an anticonvulsant drug, its effects have mostly been studied on the VGSC isoforms found in the CNS, $Na_v1.1$, $Na_v1.2$ and $Na_v1.6$. These isoforms plus $Na_v1.3$ and $Na_v1.7$ are present in the neuroblastoma cell line N1E-115. In this cell line, both ESL and S-licarbazepine inhibit the transient VGSC Na^+ current (Bonifacio *et al.*, 2001; Hebeisen *et al.*, 2015) and S-licarbazepine significantly hyperpolarises the voltage-dependence of slow inactivation, which would reduce the persistent current through VGSCs (Hebeisen *et al.*, 2015). A reduction in persistent current through VGSCs is also seen with S-licarbazepine treatment of murine hippocampal CA1 neurons (Saint, 2008; Doeser *et al.*, 2014), which express $Na_v1.1$, $Na_v1.2$ and $Na_v1.6$. Surprisingly, if the VGSC β1 subunit is not functional, carbamazepine can have the paradoxical effect of increasing the persistent Na^+ current (Uebachs *et al.*, 2010), but S-licarbazepine still reduces the persistent current even in the absence of β1 (Doeser *et al.*, 2014). This may be of importance for cancer cells which may or may not express the VGSC β1 subunit. The effect of ESL and S-licarbazepine on the cardiac isoform $Na_v1.5$ has not been studied, but since ESL prolongs the cardiac PR interval in patients (Vaz-Da-Silva *et al.*, 2012), it might inhibit $Na_v1.5$ in a similar way to the other VGSC isoforms. The rationale for performing these experiments was to assess in breast cancer cells a VGSC inhibitor with an improved safety profile compared to phenytoin before using it in *in vivo* experiments to assess anti-breast cancer properties, similar to those in (Nelson *et al.*, 2015a).

6.2 Results

ESL is used clinically to inhibit VGSCs in the CNS, but detailed electrophysiological effects of this drug on the $Na_v1.5$ isoform have not been studied. In this project, the effect of ESL and S-Lic on the neonatal splice variant of $Na_v1.5$ was assessed in MDA-MB-231 cells which express neonatal $Na_v1.5$ endogenously. The adult variant of $Na_v1.5$ was assessed in

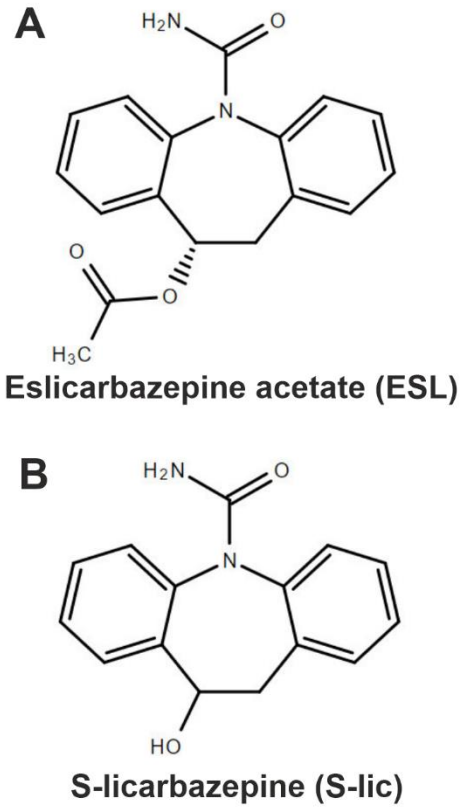

Figure 6.1 Chemical structures of eslicarbazepine acetate and S-licarbazepine.
A. eslicarbazepine acetate; (9S)-2-carbamoyl-2-azatricyclo[9.4.0.0^{3},^{8}]pentadeca-1(15),3,5,7,11,13-hexaen-9-yl acetate. **B**. S-licarbazepine; (10R)-10-hydroxy-2-azatricyclo[9.4.0.03,8]pentadeca-1(11),3,5,7,12,14-hexaene-2-carboxamide. Structures are from Chemspider.

HEK-293 cells overexpressing $Na_v1.5$ (Patino *et al.*, 2011). A concentration of 300 μM ESL or S-Lic was chosen for initial experiments so that results would be comparable to those in other *in vitro* studies (Bonifacio *et al.*, 2001; Doeser *et al.*, 2014; Doeser *et al.*, 2015). Experiments were also performed with 100 μM ESL since this was close to the peak plasma concentration of ESL in patients taking 1200 mg ESL orally once daily (90 μM) (Hebeisen *et al.*, 2015). The highest final concentration of DMSO in these experiments was 0.45% and this was shown to have no effect on peak transient Na^+ current or voltage dependence of activation or inactivation (Appendix figure VII).

6.2.1.1 Transient Na^+ current

First, the peak transient Na^+ current was assessed in the presence or absence of the prodrug ESL at a concentration of 300 μM. In MDA-MB-231 cells, the peak current was reversibly inhibited by 49.6 ± 3.2 % when the V_h was -120 mV (Figure 6.2 A and D, Table 6.1). When V_h was changed to -80 mV which would put some of the channels into the inactivated state, ESL reversibly inhibited the peak Na^+ current by a greater proportion (79.5 ± 4.5 %) (Figure 6.2 C and E, Table 6.1). This showed that ESL preferentially inhibits channels in the open or inactivated state. A similar result was obtained when recording from HEK-$Na_v1.5$ cells; ESL inhibited $Na_v1.5$ current by 74.7 ± 4.3 % when the V_h was -120 mV (Figure 6.2 F and I, Table 6.1) and by 90.5 ± 2.8 % when the V_h was -80 mV (Figure 6.2 H and J, Table 6.1). Similar preferential inhibition of channels in the open or inactivated state was seen when a concentration of 100 μM ESL was used (Figure 6.3, Table 6.3). Briefly, in MDA-MB-231 cells, 100 μM ESL inhibited Na^+ current by 47.5 ± 35.7 % when the V_h was -120 mV but by 70.4 ± 28.2 % when the V_h was -80 mV. In HEK-$Na_v1.5$ cells, 100 μM ESL inhibited Na^+ current by 50.9 ± 32.4% when the V_h was -120 mV but by 79.3 ± 20.2 % when the V_h was -80 mV. Notably, the inhibition of peak transient Na^+ current by ESL appeared fully reversible in MDA-MB-231 cells (Figure 6.2 D and E) but was only partially reversible in HEK-$Na_v1.5$ cells (Figure 6.2 I and J).

Next, the active metabolite s-licarbazepine (S-Lic) was assessed at a concentration of 300 μM. S-Lic inhibited the transient Na^+ current in MDA-MB-231 cells by 44.4 ± 6.1 % when the V_h was -120 mV (Figure 6.4 A and D, Table 6.2), but by 73.6 ± 4.1 % when the V_h was -80 mV (Figure 6.4 C and E, Table 6.2). In HEK-Na_v1.5 cells, S-lic inhibited Na_v1.5 current by 46.4 ± 3.9 % when V_h was -120 mV (Figure 6.4 F and I, Table 6.2) and by 74.0 ± 4.2 % when V_h was -80 mV (Figure 6.4 H and J, Table 6.2). Similar preferential inhibition of channels in the open or inactivated state was seen when a concentration of 100 μM S-lic was used (Figure 6.5, Table 6.4). Briefly, in MDA-MB-231 cells, 100 μM S-lic inhibited Na^+ current by 28.5 ± 43.0 % when the V_h was -120 mV but by 55.1 ± 33.3% when the V_h was -80 mV. In HEK-Na_v1.5 cells, 100 μM S-lic inhibited Na^+ current by 30.3 ± 28.5 % when the V_h was -120 mV but by 60.9 ± 4.3 % when the V_h was -80 mV. S-lic inhibition of the transient Na^+ current was less reversible than ESL inhibition, with only partial reversibility in MDA-MB-231 cells (Figure 6.4 D and E) and no reversibility in HEK- Na_v1.5 cells over the time of the experiment (Figure 6.4 I and J).

6.2.1.2 Persistent Na^+ current

The persistent Na^+ current was measured 20-25 ms after depolarisation to -10 mV from a V_h of -120 mV and the effect on this of 300 μM ESL or S-lic was assessed. In MDA-MB-231 cells, ESL inhibited the persistent Na^+ current by 77 ± 34 % although the reduction was not statistically significant (Figure 6.2 B, Table 6.1). In HEK-Na_v1.5 cells, ESL inhibited persistent current by 76 ± 10 % (Figure 6.2 G, Table 6.1). S-Lic inhibited the persistent Na^+ current in MDA-MB-231 cells by 66 ± 16 % (Figure 6.4, Table 6.2). In HEK-Na_v1.5 cells, S-Lic inhibited persistent current by 35 ± 16 % (Figure 6.4 G, Table 6.2).

Similar results were seen with 100 μM ESL or S-lic. In MDA-MB-231 cells, 100 μM ESL inhibited the persistent Na^+ current by 20 ± 40 % although the reduction was not statistically significant, however in HEK-Na_v1.5 cells, 100 μM ESL inhibited persistent current significantly by 60 ± 10 %. (Figure 6.3, Table 6.3). 100 μM S-Lic inhibited the persistent

Na^+ current in MDA-MB-231 cells by 33 ± 33 % and in HEK-Na_v1.5 cells, 100 μM S-Lic inhibited persistent current by 40 ± 20 % (Figure 6.5, Table 6.4). In summary, both ESL and S-Lic inhibited the persistent Na^+ current through Na_v1.5 at doses of 100-300 μM.

6.2.1.3 Voltage dependence of activation and inactivation

The effect of 300 μM ESL or S-Lic on the current-voltage relationship of Na_v1.5 was next assessed. Neither ESL nor S-Lic had affected the threshold voltage for activation in either MDA-MB-231 or HEK-Na_v1.5 cells (Figure 6.6, Table 6.1 and Table 6.2). When examining the activation (conductance) curves, ESL had no significant effect on the half-activation voltage (V½) or slope factor (k) for activation in MDA-MB-231 cells (Figure 6.7 A, Table 6.1). The activation k in HEK-Na_v1.5 cells was also unchanged but the activation V½ was significantly hyperpolarised by ESL from -39.4 ± 1.3 to -44.2 ± 1.8 mV (Figure 6.7 B, Table 6.1). S-Lic also had no significant effect on the activation V½ or k in MDA-MB-231 cells (Figure 6.7 C, Table 6.2). However, the V½ of activation in HEK-Na_v1.5 cells was significantly hyperpolarised from -32.8 ± 3.1 mV to -40.5 ± 3.4 mV and k changed from 5.9 ± 0.9 mV to 4.5 ± 1.1 mV (Figure 6.7 D, Table 6.2).

When examining steady-state inactivation, in MDA-MB-231 cells, ESL significantly hyperpolarised the inactivation V½ from -80.6 ± 0.7 mV to -86.7 ± 1.2 mV without affecting inactivation k (Figure 6.7 A, Table 6.1). ESL also hyperpolarised the inactivation V½ in HEK-Na_v1.5 cells from -78.2 ± 2.5 mV to -88.3 ± 2.7 mV and changed the inactivation k from -6.9 ± 0.4 mV to -9.8 ± 0.7 mV (Figure 6.7 B; Table 6.1). S-Lic also significantly hyperpolarised the inactivation V½ in MDA-MB-231 cells from -71.8 ± 2.5 mV to -76.8 ± 2.2 mV without affecting inactivation k (Figure 6.7 C, Table 6.2). The inactivation V½ in HEK-Na_v1.5 cells was not significantly altered by S-Lic, although the inactivation k significantly changed from -6.5 ± 0.4 mV to -8.1 ± 0.5 mV (Figure 6.7 D, Table 6.2).

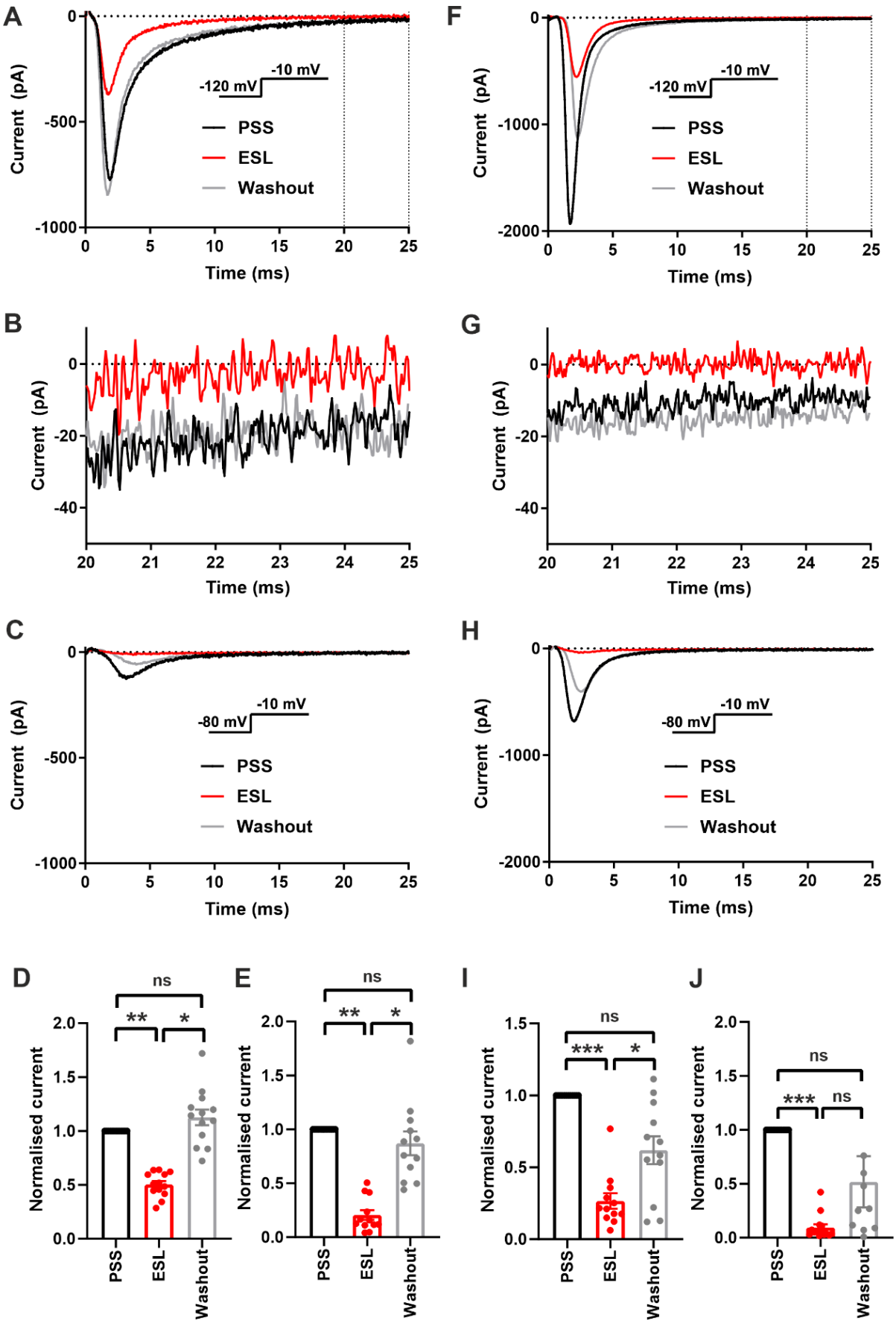
A
F
B
G
C
H
D
E
I
J
Current (pA)
Time (ms)
-120 mV
-10 mV
-80 mV
PSS
ESL
Washout
Normalised current
ns
**
*
***

Figure 6.2 Effect of 300 μM eslicarbazepine acetate (ESL) on $Na_v1.5$ currents.
A. Representative Na^+ currents in an MDA-MB-231 cell elicited by a depolarisation from -120 mV to -10 mV in physiological saline solution (PSS; black), in 300 μM ESL (red) and after washout (grey). Dotted vertical lines define the time period magnified in **B**. **B**. Representative persistent Na^+ currents in an MDA-MB-231 cell elicited by a depolarisation from -120 mV to -10 mV. **C**. Representative Na^+ currents in an MDA-MB-231 cell elicited by a depolarisation from -80 mV to -10 mV. **D**. Normalised Na^+ currents in MDA-MB-231 cells elicited by a depolarisation from -120 mV to -10 mV. **E**. Normalised Na^+ currents in MDA-MB-231 cells elicited by a depolarisation from -80 mV to -10 mV. **F**. Representative Na^+ currents in a HEK-$Na_v1.5$ cell elicited by a depolarisation from -120 mV to -10 mV in PSS (black), 300 μM ESL (red) and after washout (grey). Dotted vertical lines define the time period magnified in **G**. **G**. Representative persistent Na^+ currents in a HEK-$Na_v1.5$ cell elicited by a depolarisation from -120 mV to -10 mV. **H**. Representative Na^+ currents in a HEK-$Na_v1.5$ cell elicited by a depolarisation from -80 mV to -10 mV. **I**. Normalised Na^+ currents in HEK-$Na_v1.5$ cells elicited by a depolarisation from -120 mV to -10 mV. **J**. Normalised Na^+ currents in HEK-$Na_v1.5$ cells elicited by a depolarisation from -80 mV to -10 mV. Results are mean + SEM. one-way ANOVA with Tukey tests (n = 12-14 cells). Data from HEK-$Na_v1.5$ cells was collected by Lotte Brückner.

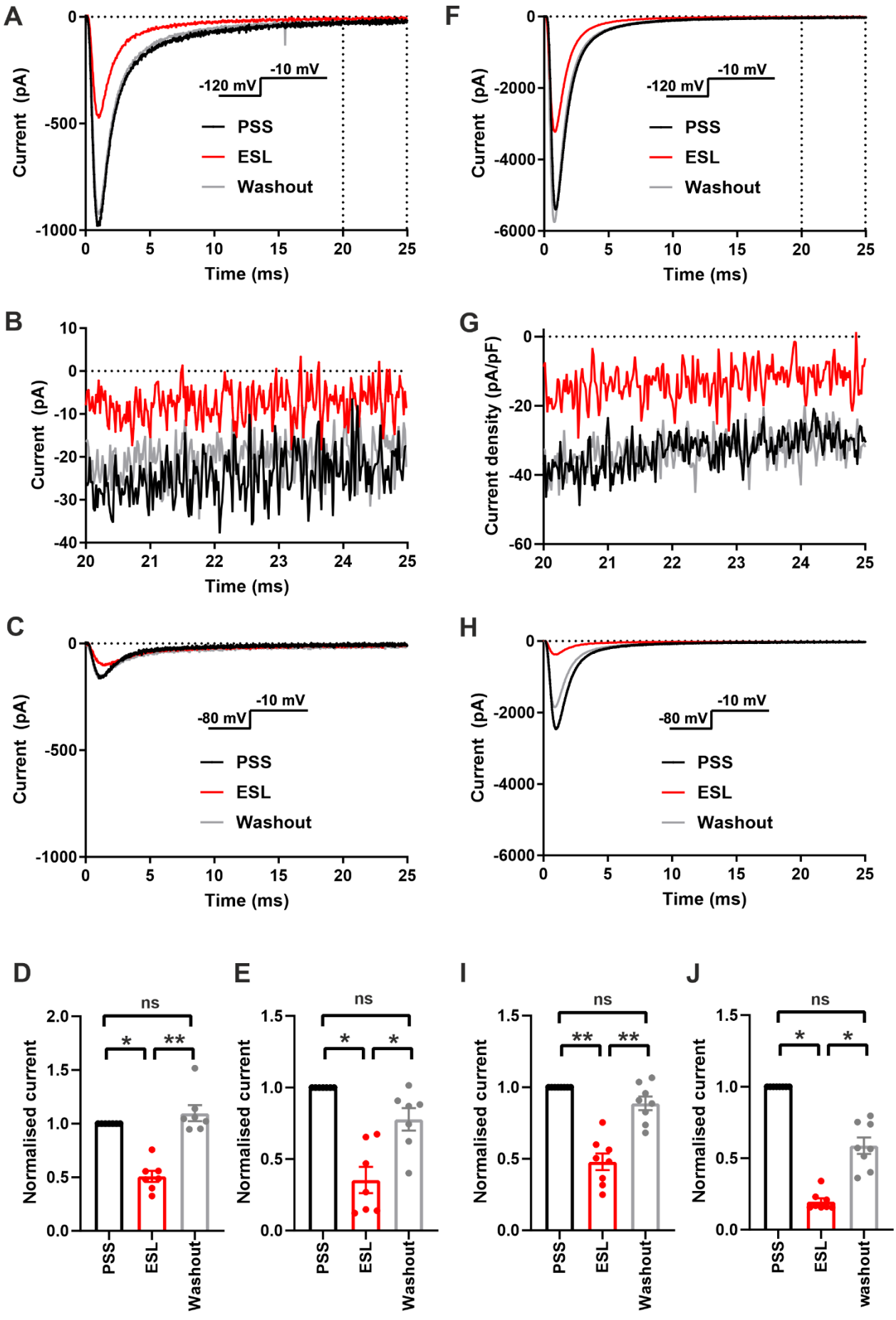
A
Current (pA)
Time (ms)
-120 mV
-10 mV
PSS
ESL
Washout
F
Current (pA)
Time (ms)
-120 mV
-10 mV
PSS
ESL
Washout
B
Current (pA)
Time (ms)
G
Current density (pA/pF)
C
Current (pA)
Time (ms)
-80 mV
-10 mV
PSS
ESL
Washout
H
Current (pA)
Time (ms)
-80 mV
-10 mV
PSS
ESL
Washout
D
Normalised current
ns
*
**
PSS
ESL
Washout
E
Normalised current
ns
*
*
PSS
ESL
Washout
I
Normalised current
ns
**
**
PSS
ESL
Washout
J
Normalised current
ns
*
*
PSS
ESL
washout

Figure 6.3 Effect of 100 μM eslicarbazepine acetate on $Na_v1.5$ currents.
A. Representative Na^+ currents in an MDA-MB-231 cell elicited by a depolarisation from -120 mV to -10 mV in physiological saline solution (PSS; black), eslicarbazepine acetate (ESL; 100 μM; red) and after washout (grey). Dotted vertical lines define the time period magnified in **B**. **B**. Representative persistent Na^+ currents in an MDA-MB-231 cell elicited by a depolarisation from -120 mV to -10 mV. **C**. Representative Na^+ currents in an MDA-MB-231 cell elicited by a depolarisation from -80 mV to -10 mV. **D**. Normalised Na^+ currents in MDA-MB-231 cells elicited by a depolarisation from -120 mV to -10 mV. **E**. Normalised Na^+ currents in MDA-MB-231 cells elicited by a depolarisation from -80 mV to -10 mV. **F**. Representative Na^+ currents in a HEK-$Na_v1.5$ cell elicited by a depolarisation from -120 mV to -10 mV in PSS (black), ESL (100 μM; red) and after washout (grey). Dotted vertical lines define the time period magnified in **G**. **G**. Representative persistent Na^+ currents in a HEK-$Na_v1.5$ cell elicited by a depolarisation from -120 mV to -10 mV. **H**. Representative Na^+ currents in a HEK-$Na_v1.5$ cell elicited by a depolarisation from -80 mV to -10 mV. **I**. Normalised Na^+ currents in HEK-$Na_v1.5$ cells elicited by a depolarisation from -120 mV to -10 mV. **J**. Normalised Na^+ currents in HEK-$Na_v1.5$ cells elicited by a depolarisation from -80 mV to -10 mV. Results are mean + SEM. *$P \leq 0.05$; **$P \leq 0.01$; one-way ANOVA with Tukey tests (n = 7-8). NS, not significant.

In summary, both ESL and S-Lic affected the voltage dependence characteristics of $Na_v1.5$ in MDA-MB-231 and HEK-$Na_v1.5$ cells, predominantly hyperpolarising the voltage dependence of inactivation.

6.2.1.4 Activation and inactivation kinetics

The effect of 300 μM ESL or S-lic on kinetics of activation and inactivation were next studied. Cells were depolarised from -120 mV to -10 mV and the time to peak current (T_p) was measured. In MDA-MB-231 cells, ESL significantly accelerated the T_p from 2.1 ± 0.2 ms to 1.9 ± 0.2 ms (Table 6.1). However, in HEK-$Na_v1.5$ cells, ESL significantly slowed T_p from 1.4 ± 0.2 ms to 1.9 ± 0.2 ms (Table 6.1). S-Lic (300 μM) had no significant effect on T_p in MDA-MB-231 cells but significantly slowed T_p in HEK-$Na_v1.5$ cells from 1.8 ± 0.5 ms to 2.3 ± 0.6 ms (Table 6.2).

To study effects on inactivation kinetics, the current decay following depolarisation from -120 mV to -10 mV was fitted to a double exponential function to derive fast and slow time constants of inactivation (τ_f and τ_s). Neither ESL nor S-Lic had any significant effect on τ_f or τ_s in MDA-MB-231 cells (Table 6.1 and Table 6.2). However, in HEK-$Na_v1.5$ cells, ESL significantly slowed τ_f from 0.9 ± 0.1 ms to 1.2 ± 0.1 ms (Table 6.1) and slowed τ_s from 6.6 ± 0.8 ms to 20.8 ± 8.5 ms, although this was not statistically significant. S-Lic significantly slowed τ_f from 1.0 ± 0.04 ms to 1.3 ± 0.06 ms and τ_s from 6.3 ± 0.5 ms to 7.3 ± 0.5 ms (Table 6.2). In summary, both ESL and S-lic elicited various effects on kinetics in MDA-MB-231 and HEK-$Na_v1.5$ cells, predominantly slowing activation and inactivation.

6.2.1.5 Recovery from fast inactivation

To investigate the effect of ESL and S-lic on channel recovery from fast inactivation, cells were subjected to two depolarisations from V_h of -120 mV to 0 mV, changing the interval between these in which the channels were held at -120 mV to facilitate recovery. Significance was determined by fitting a single exponential curve to the normalised

current/time relationship and calculating the time constant (τ_r). In MDA-MB-231 cells, ESL (300 μM) significantly slowed τ_r from 6.0 ± 0.5 ms to 8.7 ± 0.7 ms (Figure 6.8 A, Table 6.1). Similarly, in HEK-$Na_v1.5$ cells, ESL significantly slowed τ_r from 4.5 ± 0.4 ms to 7.1 ± 0.6 ms (Figure 6.8 B, Table 6.1). S-Lic (300 μM) also significantly slowed τ_r in MDA-MB-231 cells from 6.8 ± 0.4 ms to 13.5 ± 1.0 ms (Figure 6.8 C, Table 6.2). Finally, S-Lic also significantly slowed τ_r in HEK-$Na_v1.5$ cells from 5.7 ± 0.7 ms to 8.0 ± 1.2 ms (Figure 6.8 D, Table 6.2). In summary, both ESL and S-Lic slowed recovery from fast inactivation of $Na_v1.5$.

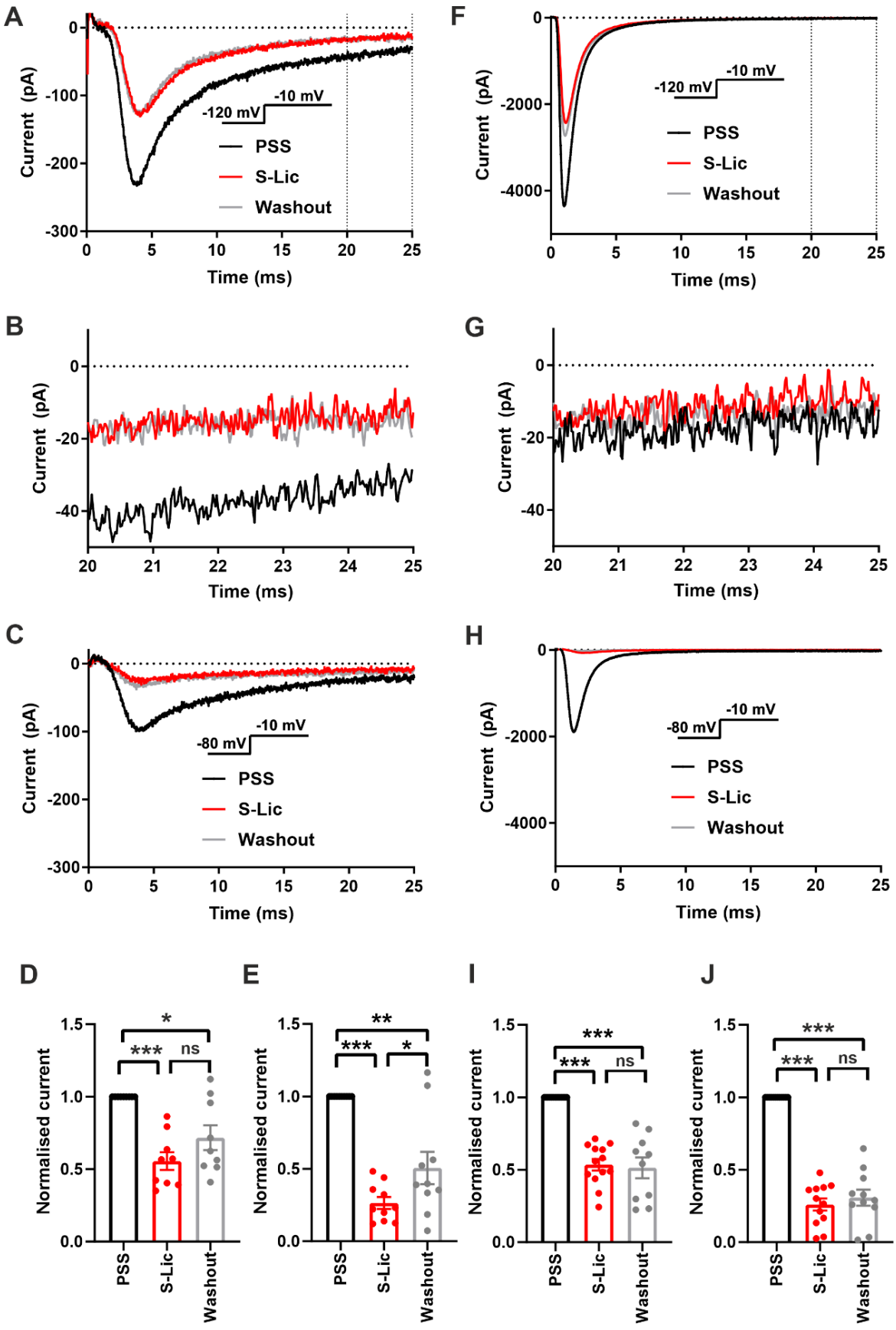
A
Current (pA)
Time (ms)
-120 mV
-10 mV
PSS
S-Lic
Washout
F
B
G
C
-80 mV
H
D
E
I
J
Normalised current
*
**
***
ns

Figure 6.4 Effect of 300 μM S-licarbazepine on $Na_v1.5$ currents.
A. Representative Na^+ currents in an MDA-MB-231 cell elicited by a depolarisation from -120 mV to -10 mV in physiological saline solution (PSS; black), in 300 μM S-lic (red) and after washout (grey). Dotted vertical lines define the time period magnified in **B**. **B**. Representative persistent Na^+ currents in an MDA-MB-231 cell elicited by a depolarisation from -120 mV to -10 mV. **C**. Representative Na^+ currents in an MDA-MB-231 cell elicited by a depolarisation from -80 mV to -10 mV. **D**. Normalised Na^+ currents in MDA-MB-231 cells elicited by a depolarisation from -120 mV to -10 mV. **E**. Normalised Na^+ currents in MDA-MB-231 cells elicited by a depolarisation from -80 mV to -10 mV. **F**. Representative Na^+ currents in a HEK-$Na_v1.5$ cell elicited by a depolarisation from -120 mV to -10 mV in PSS (black), 300 μM S-lic (red) and after washout (grey). Dotted vertical lines define the time period magnified in **G**. **G**. Representative persistent Na^+ currents in a HEK-$Na_v1.5$ cell elicited by a depolarisation from -120 mV to -10 mV. **H**. Representative Na^+ currents in a HEK-$Na_v1.5$ cell elicited by a depolarisation from -80 mV to -10 mV. **I**. Normalised Na^+ currents in HEK-$Na_v1.5$ cells elicited by a depolarisation from -120 mV to -10 mV. **J**. Normalised Na^+ currents in HEK-$Na_v1.5$ cells elicited by a depolarisation from -80 mV to -10 mV. Results are mean + SEM. one-way ANOVA with Tukey tests (n = 9-13 cells). Data was collected by Lotte Brückner.

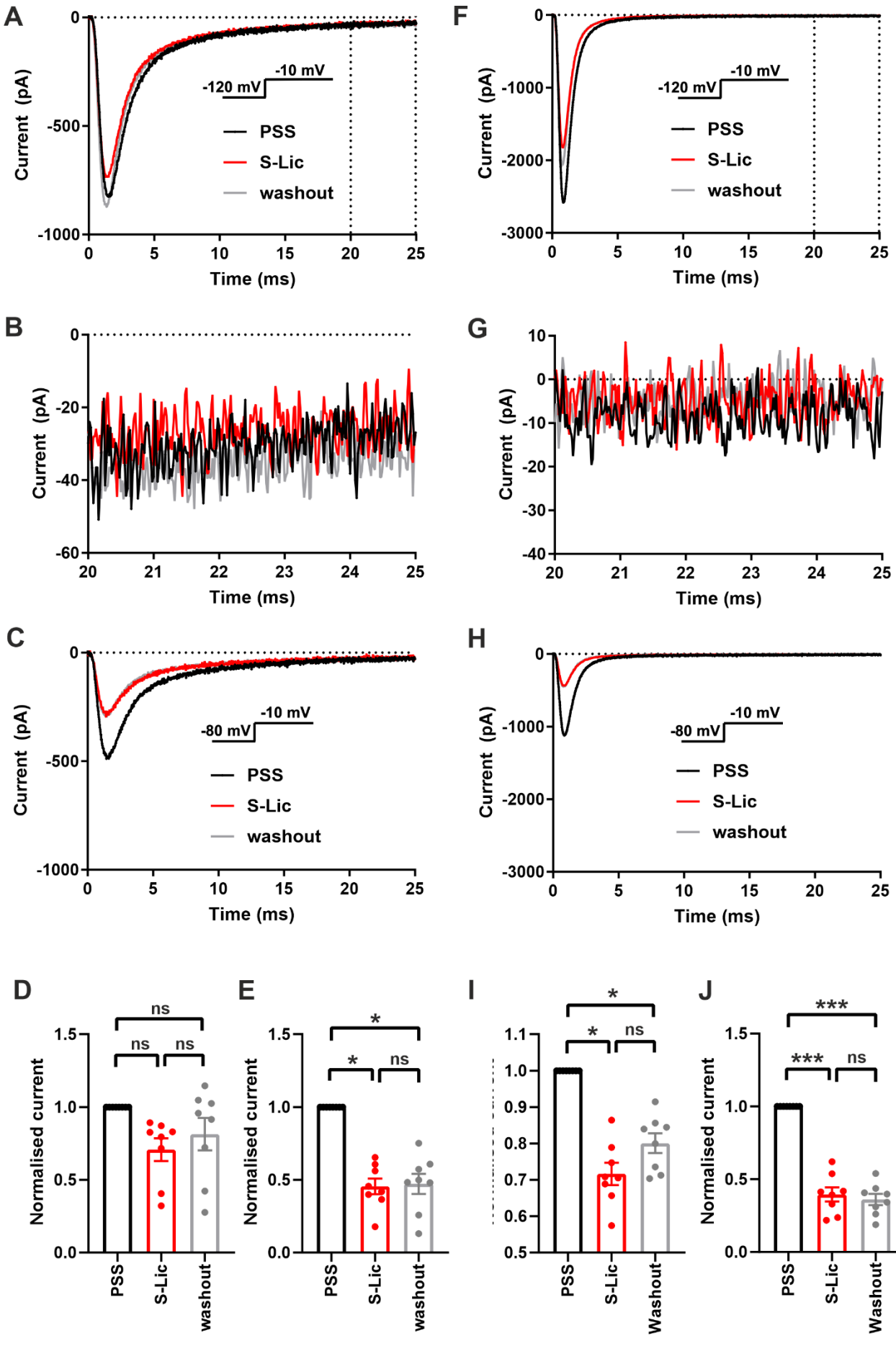
A
Current (pA)
Time (ms)
-120 mV
-10 mV
PSS
S-Lic
washout
F
B
G
C
-80 mV
H
D
Normalised current
ns
E
*
I
J
***
PSS
S-Lic
washout
Washout

Figure 6.5 Effect of 100 μM S-licarbazepine on $Na_v1.5$ currents.
A. Representative Na^+ currents in an MDA-MB-231 cell elicited by a depolarisation from -120 mV to -10 mV in physiological saline solution (PSS; black), S-licarbazepine (S-Lic; 100 μM; red) and after washout (grey). Dotted vertical lines define the time period magnified in **B**. **B**. Representative persistent Na^+ currents in an MDA-MB-231 cell elicited by a depolarisation from -120 mV to -10 mV. **C**. Representative Na^+ currents in an MDA-MB-231 cell elicited by a depolarisation from -80 mV to -10 mV. **D**. Normalised Na^+ currents in MDA-MB-231 cells elicited by a depolarisation from -120 mV to -10 mV. **E**. Normalised Na^+ currents in MDA-MB-231 cells elicited by a depolarisation from -80 mV to -10 mV. **F**. Representative Na^+ currents in a HEK-$Na_v1.5$ cell elicited by a depolarisation from -120 mV to -10 mV in PSS (black), S-Lic (100 μM; red) and after washout (grey). Dotted vertical lines define the time period magnified in **G**. **G**. Representative persistent Na^+ currents in a HEK-$Na_v1.5$ cell elicited by a depolarisation from -120 mV to -10 mV. **H**. Representative Na^+ currents in a HEK-$Na_v1.5$ cell elicited by a depolarisation from -80 mV to -10 mV. **I**. Normalised Na^+ currents in HEK-$Na_v1.5$ cells elicited by a depolarisation from -120 mV to -10 mV. **J**. Normalised Na^+ currents in HEK-$Na_v1.5$ cells elicited by a depolarisation from -80 mV to -10 mV. Results are mean + SEM. *$P \leq 0.05$; ***$P \leq 0.001$; one-way ANOVA with Tukey tests (n = 7-8). NS, not significant.

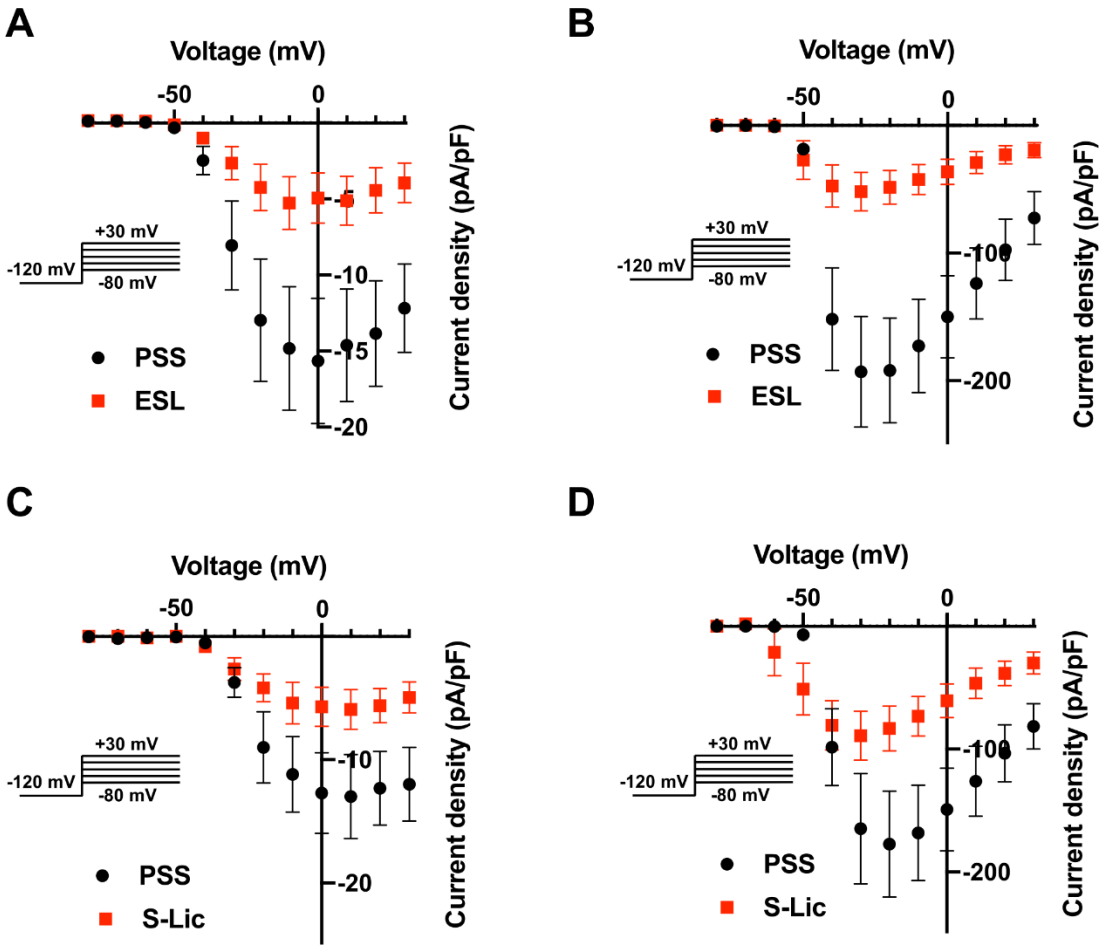

Figure 6.6 Effect of eslicarbazepine acetate (ESL) and S-licarbazepine (S-lic) on the current-voltage relationship of $Na_v1.5$.
A. Current-voltage (I-V) plots of Na^+ currents in MDA-MB-231 cells in physiological saline solution (PSS; black circles) and in 300 µM ESL (red squares). **B**. (I-V) plots of Na^+ currents in HEK-$Na_v1.5$ cells in PSS (black circles) and 300 µM ESL (red squares). **C**. I-V plots of Na^+ currents in MDA-MB-231 cells in PSS (black circles) and 300 µM S-lic (red squares). **D**. I-V plots of Na^+ currents in HEK-$Na_v1.5$ cells in PSS (black circles) and 300 µM S-lic (red squares). Currents were elicited using 10 mV depolarising steps from -80 to +30 mV for 30 ms, from a holding potential of -120 mV. Results are mean ± SEM (n = 7-13). Data in HEK-$Na_v1.5$ cells was collected by Lotte Brückner.

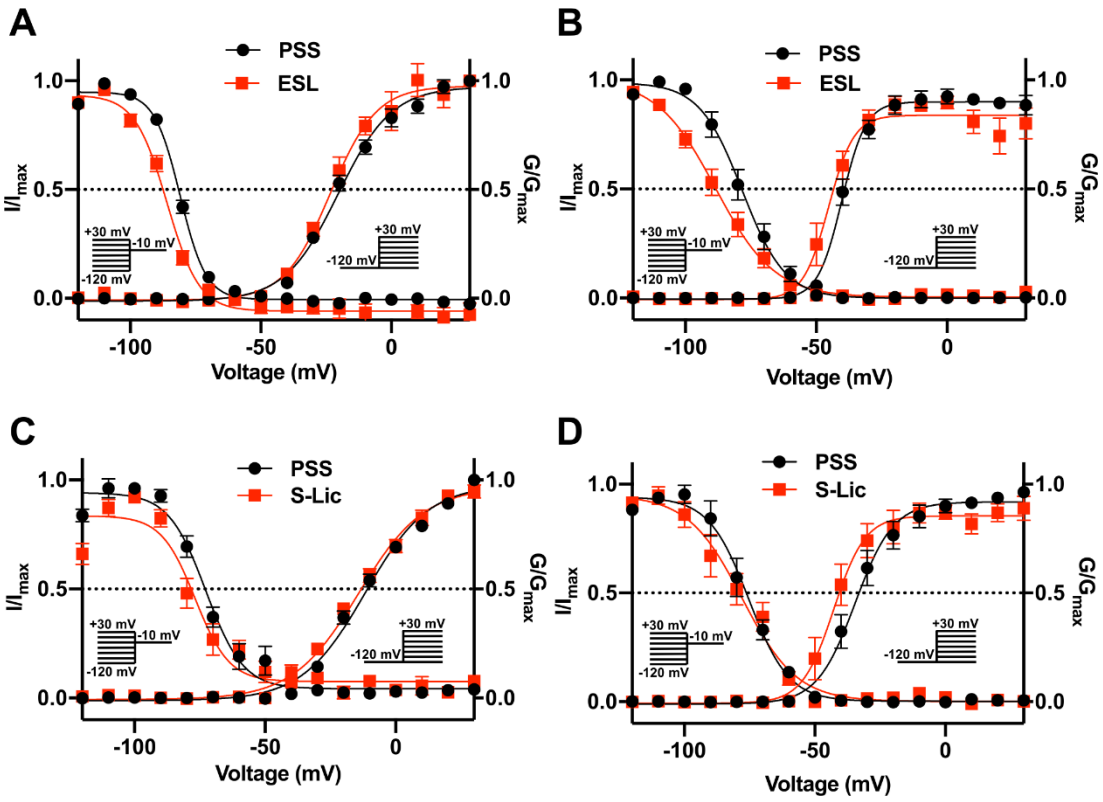

Figure 6.7 Effect of eslicarbazepine acetate (ESL) and S-licarbazepine (S-lic) on activation and steady-state inactivation of $Na_v1.5$.
A. Activation and steady-state inactivation in MDA-MB-231 cells in physiological saline solution (PSS; black circles) and in 300 µM ESL (red squares). **B**. Activation and steady-state inactivation in HEK-$Na_v1.5$ cells in PSS (black circles) and 300 µM ESL (red squares). **C**. Activation and steady-state inactivation in MDA-MB-231 cells in PSS (black circles) and 300 µM S-lic (red squares). **D**. Activation and steady-state inactivation in HEK-$Na_v1.5$ cells in PSS (black circles) and 300 µM S-lic (red squares). For activation, normalised conductance (G/Gmax) was calculated from the current data and plotted as a function of voltage. For steady-state inactivation, normalised current (I/Imax), elicited by 50 ms test pulses at -10 mV following 250 ms conditioning voltage pulses between -120 mV and +30 mV, applied from a holding potential of -120 mV, was plotted as a function of the prepulse voltage. Results are mean ± SEM (n = 7-13). Activation and inactivation curves are fitted with Boltzmann functions. Data in HEK-$Na_v1.5$ cells and with S-Lic on MDA-MB-231 cells was collected by Lotte Brückner.

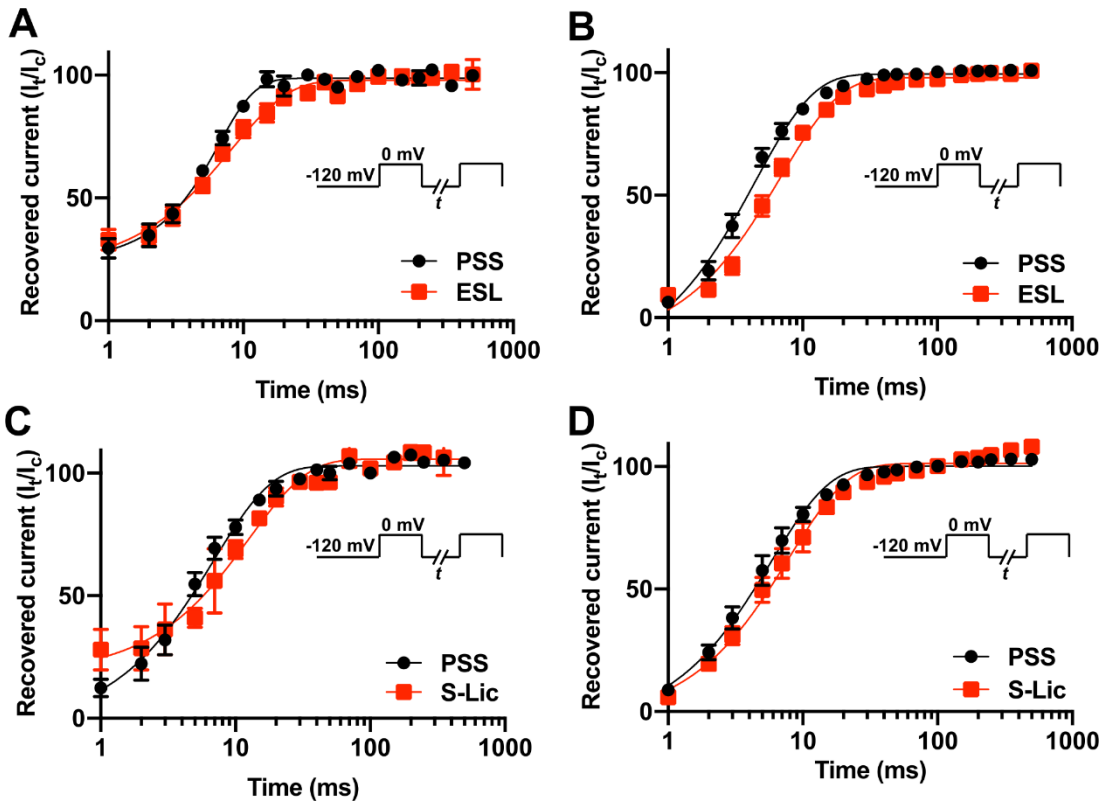

Figure 6.8 Effect of eslicarbazepine acetate (ESL) and S-licarbazepine (S-lic) on recovery from inactivation.
A. Recovery from inactivation in MDA-MB-231 cells in physiological saline solution (PSS; black circles) and in 300 µM ESL (red squares). **B**. Recovery from inactivation in HEK-$Na_v1.5$ cells in PSS (black circles) and 300 µM ESL (red squares). **C**. Recovery from inactivation in MDA-MB-231 cells in PSS (black circles) and S-licarbazepine 300 µM S-lic (red squares). **D**. Recovery from inactivation in HEK-$Na_v1.5$ cells in PSS (black circles) and 300 µM S-lic (red squares). The fraction recovered (I_t/I_c) was determined by a 25 ms pulse to 0 mV (I_c), followed by a recovery pulse to -120 mV for 1-500 ms, and a subsequent 25 ms test pulse to 0 mV (I_t), applied from a V_h of -120 mV, and plotted as a function of the recovery interval. Data are fitted with single exponential functions which are statistically different between control and drug treatments in all cases. Results are mean ± SEM (n = 7-10). Data was collected by Lotte Brückner.

Table 6.1 Effect of eslicarbazepine acetate (ESL, 300 μM) on Na^+ current characteristics in MDA-MB-231 and HEK-$Na_v1.5$ cells.

A. MDA-MB-231 cells				
Parameter	**Control**	**ESL**	**P**	**N**
V_{thres} (mV)	-45.7 ± 1.7	-45.0 ± 1.4	0.58	13
V_{peak} (mV)	3.1 ± 2.1	-3.9 ± 2.7	0.056	13
Activation V½ (mV)	-19.3 ± 1.4	-22.0 ± 1.5	0.095	12
Activation k (mV)	10.6 ± 0.7	9.3 ± 0.8	0.076	12
Inactivation V½ (mV)	-80.6 ± 0.7	-86.7 ± 1.2	<0.001	13
Inactivation k (mV)	-4.8 ± 0.4	-7.4 ± 1.7	0.139	13
Peak current density at -10 mV (pA/pF)	-14.8 ± 3.9	-8.0 ± 2.5	<0.001	13
Persistent current density at -10 mV (pA/pF)	-0.15 ± 0.05	-0.02 ± 0.07	0.13	12
T_p at -10 mV (ms)	2.1 ± 0.2	1.9 ± 0.2	<0.01	13
τ_f at -10 mV (ms)	1.3 ± 0.1	1.3 ± 0.2	0.954	13
τ_s at -10 mV) (ms)	10.0 ± 2.3	6.9 ± 2.0	0.289	13
τ_r (ms)	6.0 ± 0.5	8.7 ± 0.7	<0.05	10
B. HEK-$Na_v1.5$ cells				
Parameter	**Control**	**ESL**	**P**	**N**
V_{thres} (mV)	-55.0 ± 1.7	-54.0 ± 2.2	0.758	10
V_{peak} (mV)	-26.0 ± 2.2	-24.0 ± 4.3	0.591	10
Activation V½ (mV)	-39.4 ± 1.3	-44.2 ± 1.8	<0.05	10
Activation k (mV)	5.3 ± 1.3	3.8 ± 0.7	0.361	10
Inactivation V½ (mV)	-78.2 ± 2.5	-88.3 ± 2.7	<0.001	10
Inactivation k (mV)	-6.9 ± 0.4	-9.8 ± 0.7	<0.001	10
Peak current density at -10 mV (pA/pF)	-154.4 ± 24.0	-33.1 ± 4.7	<0.001	12
Persistent current density at -10 mV (pA/pF)	-0.61 ± 0.15	-0.12 ± 0.05	<0.01	12
T_p at -10 mV (ms)	1.4 ± 0.2	1.9 ± 0.2	<0.001	14
τ_f at -10 mV (ms)	0.9 ± 0.1	1.2 ± 0.1	<0.001	12
τ_s at -10 mV (ms)	6.6 ± 0.8	20.8 ± 8.5	0.128	12
τ_r (ms)	4.5 ± 0.4	7.1 ± 0.6	<0.001	10

ESL: eslicarbazepine acetate (300 μM); V_{thres}: threshold voltage for activation; V_{peak}: voltage at which current was maximal; V½: half (in)activation voltage; k: slope factor for (in)activation; T_p: time to peak current; τ_f: fast time constant of inactivation; τ_s: slow time constant of inactivation; τ_r: time constant of recovery from inactivation. The holding potential was -120 mV. Results are mean ± SEM. Statistical comparisons were made with paired *t*-tests on non-normalised data.

Table 6.2 Effect of S-licarbazepine (S-lic, 300 μM) on Na^+ current characteristics in MDA-MB-231 and HEK-$Na_v1.5$ cells.

A. MDA-MB-231 cells				
Parameter	**Control**	**S-Lic**	**P**	**N**
V_{thres} (mV)	-34.4 ± 2.0	-35.7 ± 2.0	0.603	7
V_{peak} (mV)	11.43 ± 4.4	10.0 ± 4.9	0.818	7
Activation V½ (mV)	-12.9 ± 1.3	-13.7 ± 1.4	0.371	7
Activation k (mV)	11.0 ± 0.5	11.9 ± 0.8	0.520	7
Inactivation V½ (mV)	-71.8 ± 2.5	-76.8 ± 2.2	<0.05	7
Inactivation k (mV)	-6.8 ± 0.9	-6.0 ± 1.2	0.302	7
Peak current density at -10 mV (pA/pF)	-12.0 ± 3.1	-6.9 ± 2.5	<0.001	9
Persistent current density at -10 mV	-1.3 ± 0.4	-0.6 ± 0.2	<0.05	9
T_p at -10 mV (ms)	4.5 ± 0.4	5.1 ± 0.7	0.103	9
τ_f at -10 mV (ms)	3.8 ± 1.1	3.2 ± 0.4	0.553	7
τ_s at -10 mV (ms)	25.7 ± 7.0	27.1 ± 12.0	0.920	7
τ_r (ms)	6.8 ± 0.4	13.5 ± 1.0	<0.01	7
B. HEK-$Na_v1.5$ cells				
Parameter	**Control**	**S-Lic**	**P**	**N**
V_{thres} (mV)	-50.0 ± 1.9	-51.3 ± 3.5	0.598	9
V_{peak} (mV)	-18.0 ± 4.2	-30.0 ± 5.6	<0.001	9
Activation V½ (mV)	-32.8 ± 3.1	-40.5 ± 3.4	<0.01	9
Activation k (mV)	5.9 ± 0.9	4.5 ± 1.1	<0.05	9
Inactivation V½ (mV)	-75.9 ± 2.6	-79.3 ± 4.1	0.116	9
Inactivation k (mV)	-6.5 ± 0.4	-8.1 ± 0.5	<0.05	9
Peak current density at -10 mV (pA/pF)	-140.9 ± 26.8	-77.2 ± 17.0	<0.001	13
Persistent current density at -10 mV	-0.9 ± 0.2	-0.5 ± 0.2	<0.05	11
T_p at -10 mV (ms)	1.8 ± 0.5	2.3 ± 0.6	<0.01	13
τ_f at -10 mV (ms)	1.0 ± 0.04	1.3 ± 0.06	<0.001	11
τ_s at -10 mV (ms)	6.3 ± 0.5	7.3 ± 0.5	<0.05	11
τ_r (ms)	5.7 ± 0.7	8.0 ± 1.2	<0.01	10

S-Lic: S-licarbazepine (300 μM); V_{thres}: threshold voltage for activation; V_{peak}: voltage at which current was maximal; V½: half (in)activation voltage; k: slope factor for (in)activation; T_p: time to peak current; τ_f: fast time constant of inactivation; τ_s: slow time constant of inactivation; τ_r: time constant of recovery from inactivation. The holding potential was -120 mV. Results are mean ± SEM. Statistical comparisons were made with paired *t*-tests on non-normalised data.

Table 6.3 Effect of eslicarbazepine acetate (100 μM) on Na^+ current characteristics in MDA-MB-231 and HEK-Na_v1.5 cells.

A. MDA-MB-231 cells				
Parameter	**Control**	**ESL**	**P**	**N**
Peak current density at -10 mV, Vh -120 mV (pA/pF)	-22.1 ± 13.5	-11.6 ± 7.9	<0.05	7
Peak current density at -10 mV, Vh -80 mV (pA/pF)	-7.1 ± 4.1	-2.1 ± 2.0	<0.05	7
Persistent current density at -10 mV (pA/pF)	-0.5 ± 0.3	-0.4 ± 0.2	0.277	7
B. HEK-Na_v1.5 cells				
Parameter	**Control**	**ESL**	**P**	**N**
Peak current density at -10 mV, Vh -120 mV (pA/pF)	-158.4 ± 85.7	-77.7 ± 51.3	<0.01	8
Peak current density at -10 mV, Vh -80 mV (pA/pF)	-59.0 ± 50.7	-12.2 ± 11.9	<0.05	8
Persistent current density at -10 mV (pA/pF)	-1.0 ± 0.3	-0.4 ± 0.1	<0.001	8

ESL: eslicarbazepine acetate (100 μM). Results are mean ± SEM. Statistical comparisons were made with paired *t*-tests on non-normalised data.

Table 6.4 Effect of S-licarbazepine (100 μM) on Na^+ current characteristics in MDA-MB-231 and HEK-Na_v1.5 cells.

A. MDA-MB-231 cells				
Parameter	**Control**	**S-Lic**	**P**	**N**
Peak current density at -10 mV, Vh -120 mV (pA/pF)	-17.2 ± 8.7	-12.3 ± 7.4	0.084	8
Peak current density at -10 mV, Vh -80 mV (pA/pF)	-7.8 ± 4.7	-3.5 ± 2.6	<0.05	8
Persistent current density at -10 mV (pA/pF)	-0.6 ± 0.3	-0.4 ± 0.2	<0.01	8
B. HEK-Na_v1.5 cells				
Parameter	**Control**	**S-Lic**	**P**	**N**
Peak current density at -10 mV, Vh -120 mV (pA/pF)	-108.5 ± 20.3	-75.6 ± 30.9	<0.05	8
Peak current density at -10 mV, Vh -80 mV (pA/pF)	-30.2 ± 0.9	-11.8 ± 1.3	<0.001	8
Persistent current density at -10 mV (pA/pF)	-0.5 ± 0.1	-0.3 ± 0.1	<0.05	7

S-Lic: S-licarbazepine (100 μM). Results are mean ± SEM. Statistical comparisons were made with paired *t*-tests on non-normalised data.

6.3 Discussion

6.4 Summary of main findings

Both ESL and the active metabolite S-Lic reduce transient and persistent currents through $Na_v1.5$. Both drugs preferentially inhibit channels in the open/inactivated state, and both hyperpolarise the voltage dependence of inactivation. Similar effects of the drugs were seen in adult and in neonatal isoforms of $Na_v1.5$.

The inhibitory effects of ESL and S-Lic on transient current through $Na_v1.5$ are similar to those seen in neuronal VGSC isoforms ($Na_v1.1$, $Na_v1.2$, $Na_v1.3$ $Na_v1.6$ and $Na_v1.7$) expressed in the N1E-115 neuroblastoma cell line (Bonifacio *et al.*, 2001; Hebeisen *et al.*, 2015). In addition, the inhibitory effect on persistent current through $Na_v1.5$ is similar to that seen in hippocampal CA1 neurons (Doeser *et al.*, 2014) which express the neuronal VGSC isoforms $Na_v1.1$, $Na_v1.2$ and $Na_v1.6$ (Westenbroek *et al.*, 1989; Yu *et al.*, 2006; Royeck *et al.*, 2008). The similarity of effect of ESL and S-Lic on the different isoforms is unsurprising, given that the amino acids in $Na_v1.2$ proposed to interact with ESL (Shaikh *et al.*, 2014) are conserved in $Na_v1.5$ (Figure 6.9).

Na^+ currents were far larger in HEK-$Na_v1.5$ cells than in MDA-MB-231 cells which increased the signal to noise ratio and may account for the greater apparent inhibition of $Na_v1.5$ in HEK-$Na_v1.5$ cells. The inhibitory effect of ESL only appeared to be only partially reversible in HEK cells, which could be due to differences in drug clearance from cells; drug clearance might be much faster from MDA-MB-231 cells since these are cancer cells exhibiting resistance to multiple chemotherapy drugs (Chen *et al.*, 2011). One of the mechanisms of cancer cell drug resistance is via upregulation of ATPase binding cassette (ABC) transporters which pump chemicals out of cells (Leslie *et al.*, 2005). P-glycoprotein (Pgp) is an example of one of these transporters which is important for transport of drugs across the blood-brain barrier, and therefore this transporter is of interest in the context of anti-epileptic drug development. There are conflicting reports about the role that Pgp plays

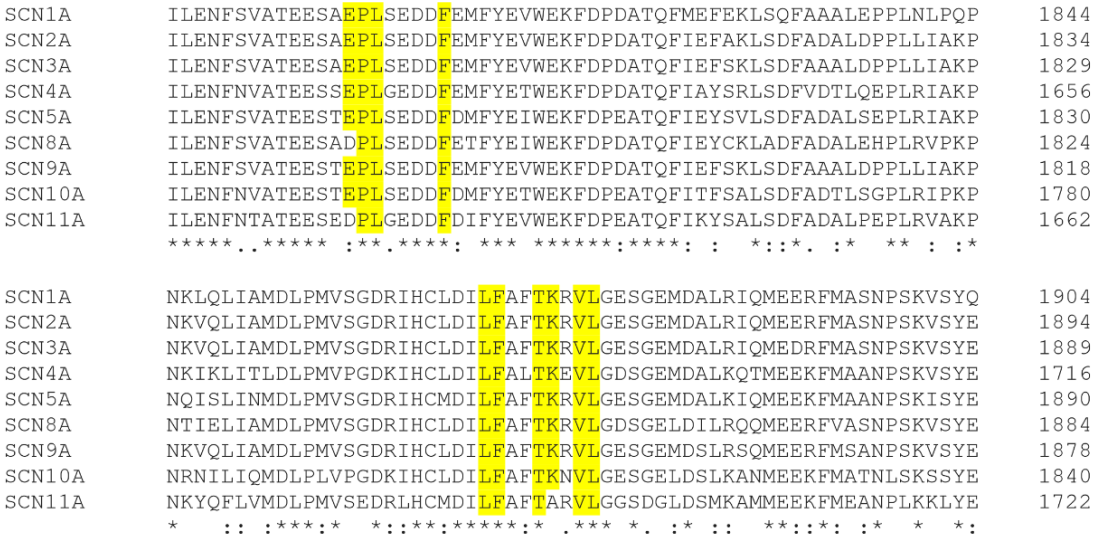

Figure 6.9 Clustal alignment of amino acid sequences of $Na_v1.2$ (SCN2A) and $Na_v1.5$ (SCN5A).
ESL was proposed previously (Shaikh *et al.*, 2014) to interact with the highlighted amino acids in $Na_v1.2$. An alignment of $Na_v1.2$ (UniProtKB - Q99250 (SCN2A_HUMAN)) with $Na_v1.1$ (UniProtKB - P35498 (SCN1A_HUMAN)), $Na_v1.3$ (UniProtKB - Q9NY46 (SCN3A_HUMAN)), $Na_v1.4$ (UniProtKB - P35499 (SCN4A_HUMAN)), $Na_v1.5$ (UniProtKB - Q14524 (SCN5A_HUMAN)) $Na_v1.6$ (UniProtKB - Q9UQD0 (SCN8A_HUMAN)), $Na_v1.7$ (UniProtKB - Q15858 (SCN9A_HUMAN)), $Na_v1.8$ (UniProtKB - Q9Y5Y9 (SCN10A_HUMAN)), and $Na_v1.9$ (UniProtKB - Q9UI33 (SCN11A_HUMAN)) shows that the interacting amino acids highlighted in yellow are conserved between $Na_v1.2$ and $Na_v1.5$, along with most other isoforms. Asterisks indicate conserved residues. Colon indicates conservation between groups of strongly similar properties - scoring > 0.5 in the Gonnet PAM 250 matrix. Period indicates conservation between groups of weakly similar properties - scoring ≤ 0.5 in the Gonnet PAM 250 matrix.

in ESL and S-lic transport. In one study both drugs were shown to be substrates of Pgp (Zhang *et al.*, 2011), but others showed no effect of inhibition of Pgp or another ABC transporter, the multidrug resistance protein MRP on trans-intestinal transport of S-Lic or plasma:brain concentration ratio (Soares-da-Silva *et al.*, 2015).

In both cell lines S-lic inhibition of Na^+ current was less reversible than ESL inhibition. This could be due to higher affinity of S-lic to its binding site on $Na_v1.5$, or to greater trapping of S-lic in the cytoplasm, since the lipid solubility of S-lic is less than that of ESL (Bialer & Soares-da-Silva, 2012). The concentration of ESL and S-Lic used in most of this chapter was higher than that found in patient plasma samples but it was considered relevant in previous *in vitro* studies because S-Lic is highly lipophilic (with a 50:1 lipid:water partition coefficient) so it will concentrate in membranes and may therefore be found at higher concentration in tissues than in plasma (Bialer & Soares-da-Silva, 2012). Importantly, ESL and S-lic both inhibited the transient and persistent Na^+ current through $Na_v1.5$, at concentrations which would be found in the plasma of patients (Hebeisen *et al.*, 2015).

In both cell lines, both the prodrug ESL and the main metabolite S-Lic inhibited Na^+ currents by a greater proportion when the holding voltage was -80 mV rather than -120 mV. This indicates that both drugs preferentially bind to channels in the open or inactivated state, and will therefore exert more effect on $Na_v1.5$ in cells with a more depolarised V_m, for example cancer cells (Yang & Brackenbury, 2013). In this way, the drugs may target $Na_v1.5$ in cancer cells and leave cardiomyocytes relatively unaffected.

In general, both the activation and inactivation curves were shifted to more negative potentials, although this was not statistically significant in every case. This explains why both drugs reduced the persistent current at -10 mV (Table 6.1 and Table 6.2), because it moved the "window current" to more negative potentials than -10 mV. This would reduce the persistent current at the relatively depolarised resting membrane potential of most cancer

cells (Yang & Brackenbury, 2013). The reduction in persistent current caused by ESL or S-Lic treatment is likely to be the most important effect of these drugs on VGSCs in cancer cells, since these cells are not likely to have the rapid changes in V_m needed to elicit transient Na^+ currents. Breast cancer cells are however likely to have a fluctuating V_m given that fluctuations in field potentials are seen in MCF7 and MDA-MB-231 cells in culture (Ribeiro *et al.*, 2020).

It is interesting that the prodrug ESL is just as potent an inhibitor of $Na_v1.5$ as the metabolite S-Lic. ESL was designed by selecting an active metabolite of oxcarbazepine, licarbazepine, and then choosing the most blood-brain barrier permeable stereoisomer of this, S-licarbazepine (Bialer & Soares-da-Silva, 2012). An acetate group was added, presumably to improve its absorption across the intestine. The acetate group clearly does not interfere with the drug's ability to bind $Na_v1.5$ or neuronal VGSC isoforms since its VGSC-inhibitory effects have been studied *in vitro* previously as well as in this study (Bonifacio *et al.*, 2001). The docking of ESL to $Na_v1.2$ was modelled in (Shaikh *et al.*, 2014) and the acetate group was predicted to interact with a threonine residue in $Na_v1.2$. This interaction cannot be present between S-Lic and the VGSC so it may not be necessary for ESL inhibition of the VGSC. In any case, the effects of ESL given orally are likely mostly due to the metabolite S-Lic since ESL is rapidly hydrolysed to this form in first pass metabolism (Almeida *et al.*, 2005; Falcão *et al.*, 2007; Maia *et al.*, 2008; Perucca *et al.*, 2011).

Patch clamp recording from both adult and neonatal splice variants of $Na_v1.5$, from two cell lines indicated very similar results. This gives a high level of confidence in the findings that both transient and persistent $Na_v1.5$ current are inhibited by ESL and S-Lic. In both cell lines β1-subunits were absent, so the effect of ESL and S-Lic on heteromeric channels could not be assessed. In particular, it would be useful to assessing the likely effect of ESL and S-Lic with the β-subunits normally associated with cardiac $Na_v1.5$. To properly assess the likelihood of cardiac side effects of ESL and S-Lic treatment, recovery from inactivation

should be assessed with a pulse repetition rate within the same order of magnitude as a human heart rate (Sokolov *et al.*, 2013). Since tumours have a low pH_e (White *et al.*, 2017) it would be useful to assess the effect of pH_e on $Na_v1.5$ inhibition by ESL and S-Lic. Another VGSC inhibitor, ranolazine was less effective at inhibiting $Na_v1.5$ at pH_e 6.0 than at pH_e 7.4 (Sokolov *et al.*, 2013). If ESL and S-Lic show a similar reduction in efficacy at low pH_e, they may not act as selectively on cancer cells as predicted.

The aim of this chapter was to characterise a drug to assess the potential for ESL to be used to treat breast cancer *in vivo*. After electrophysiological assessment of the effect of S-Lic, the next experiments which would be of use would be *in vitro* migration and invasion assays, and then assessment of tumour growth and metastasis in the mouse, as previously performed with ranolazine and phenytoin (Driffort *et al.*, 2014; Nelson *et al.*, 2015a). If ESL shows promise in these studies, the eventual goal would be to assess its efficacy in breast cancer patients.

7 General Discussion

7.1 Summary of findings

The main findings from this thesis were that total tissue [Na^+] was elevated in MDA-MB-231 xenograft breast tumours compared to normal mammary glands, but $[Na^+]_e$ was normal. This indicated that $[Na^+]_i$ may be elevated in these tumours. The overall pH_e in xenograft tumours was more acidic than normal physiological pH, and lower pH correlated with peripheral, highly proliferative regions of the tumour. Low pH_e leads to increased persistent Na^+ current through $Na_v1.5$ into MDA-MB-231 cells. VGSC activity may increase lactate production in MDA-MB-231 cells, although more work is needed to confirm this. Inhibition of glycolysis in MDA-MB-231 cells led to rapid Na^+ accumulation but inhibition of oxidative phosphorylation did not, indicating that NKA in these cells relies on ATP derived from glycolysis. Findings from an RNAseq experiment comparing wild-type MDA-MB-231 tumours with $Na_v1.5$-knock down tumours suggested that presence of $Na_v1.5$ is associated with expression of genes involved in ROS detoxification, pH regulation, Ca^{2+} signalling, immune system interactions and angiogenesis. $Na_v1.5$ was shown to be an indicator of poor prognosis in breast cancer in a breast cancer tissue microarray. Protein expression of $Na_v1.5$ correlated with increased metastasis in particular. When electrophysiological recordings were made from patient breast cancer tissue and primary cells, small inward currents consistent with VGSCs were present in some samples. The anti-epileptic drug ESL was shown to be an effective inhibitor of the transient and persistent Na^+ current through $Na_v1.5$ *in vitro.*

7.2 Prognostic importance and functional expression of $Na_v1.5$ in breast cancer

Although there have been several previous reports indicating that VGSCs are likely to be important prognostic indicators of breast cancer (Fraser *et al.*, 2005; Yang *et al.*, 2012; Nelson *et al.*, 2015b), no studies have examined VGSC protein expression in a large number of cancer patients. Until this immunohistochemical study examining $Na_v1.5$ expression in a

large cohort of breast cancer patients, VGSC protein expression in cancer has mostly been extrapolated from experiments on cell lines with differing metastatic potential (Diss *et al.*, 1998; Fraser *et al.*, 2005; Roger *et al.*, 2007) and small cohorts of patients (Fraser *et al.*, 2005; Diaz *et al.*, 2007; Hernandez-Plata *et al.*, 2012; Nelson *et al.*, 2015b; Yamaci *et al.*, 2017). The results from this TMA experiment confirmed the expectation that $Na_v1.5$ expression is associated with poorer prognosis and increased metastasis in breast cancer. $Na_v1.5$ expression also correlated with many measures of breast cancer severity, including primary tumour size, grade and lymph node status. These findings show that oncogenic actions of VGSCs discovered experimentally are likely to be clinically relevant.

In the breast cancer TMA, $Na_v1.5$ staining appeared to be cytoplasmic in most samples. It cannot be determined from this data whether there are functional channels at the plasma membrane. It is therefore important to show whether VGSC currents can be measured in patient tissue as well as in cell lines. Small inward currents, consistent with VGSC currents were recorded in breast cancer biopsies and primary cell cultures from breast cancer patients, although the small current size did not permit confirmation of the identity of the channels using TTX inhibition. To our knowledge this is the first time that VGSC currents have been recorded in primary cell cultures. In two related studies, (Diaz *et al.*, 2007) and (Hernandez-Plata *et al.*, 2012) VGSC recordings were made from three samples of cervical cancer cells; however, these cells had been passaged multiple times before recording. Since it was not possible to characterise the inward currents seen in breast biopsies or primary cultures in this thesis, it would be desirable to continue recording from patient samples. VGSC currents may be larger in certain culture conditions. For example currents could be affected by the serum concentration in the cell culture medium, since higher concentrations of serum reduced VGSC currents in prostate cancer cell lines (Ding & Djamgoz, 2004). Future optimisation of the storage and culture conditions may reveal VGSC currents are larger or more common than found in this study.

A further question which needs exploration is whether VGSC currents are maintained or changed as cells move out of the primary tumour to form distant metastases. No samples of metastatic tumours were present in the breast cancer TMA or in the primary breast cancer cell cultures in which small VGSC currents were measured. In contrast, the established breast cancer cell lines used in *in vitro* and xenograft experiments in this thesis were derived from metastatic pleural effusions (Table 3.1). Since VGSCs increase metastasis *in vivo* (Nelson *et al.*, 2015b) and VGSC expression correlates with increased metastasis in patients (Figure 5.2 E), it might be expected that VGSC currents would be larger in metastases than in primary tumours. VGSC Na^+ currents were measured in xenograft primary tumours and lung metastases in this thesis and no difference was seen between the currents in each location (Figure 3.3 G), however the cells implanted to form the primary tumours were derived from a human pleural effusion, so had already undergone changes necessary for distant colonisation, as well as changes necessary for proliferation *in vitro*. To avoid this problem, better models of breast cancer metastasis, for example MMTV-PyMT transgenic mice, would be required to address the hypothesis that VGSC currents are larger in metastases than in primary tumours. The model in question would need to express VGSCs in at least some of the cancer cells in either the primary or secondary tumours.

Since $Na_v1.5$ is a negative prognostic indicator in breast cancer, and its expression increases tumour growth rate and metastasis (Nelson *et al.*, 2015b), it is a promising therapeutic target for breast cancer. Indeed, inhibition of this channel has been shown to decrease tumour growth and metastasis in the MDA-MB-231 xenograft model of breast cancer (Driffort *et al.*, 2014; Nelson *et al.*, 2015a). In this thesis electrophysiological effects of an antiepileptic drug, ESL, were assessed in breast cancer cells, since ESL has an improved safety profile compared to phenytoin which was shown previously to reduce metastasis. If ESL had similar inhibitory effects to phenytoin on breast cancer, the improved safety profile would mean that ESL would be a better choice of drug to use in clinical trials. The purpose of this study was to confirm that ESL inhibited Na^+ current (in particular the persistent current)

through $Na_v1.5$. ESL inhibition was assessed both on the neonatal splice variant of $Na_v1.5$, naturally expressed in MDA-MB-231 cells and on the adult variant stably expressed in HEK-293 cells. Both ESL and the active metabolite eslicarbazepine inhibited the persistent current through $Na_v1.5$ in both neonatal and adult splice variants, indicating that they may be similarly effective to phenytoin. In addition ESL and eslicarbazepine preferentially inhibited channels in the open or inactivated state (Figure 6.2 and Figure 6.4). This means that VGSC inhibition would be greater in cancer cells with their relatively depolarised V_m than in cardiomyocytes or neurons. This feature would increase the therapeutic window of plasma concentrations of the drug. Future work is needed to test the anti-cancer effects of ESL *in vivo* before any clinical trials could be considered.

7.3 VGSC regulation of tumour Na^+ homeostasis

By allowing a persistent Na^+ current into cancer cells at a steady state, VGSCs might increase tissue $[Na^+]$ in tumours. There is limited but growing evidence that total tissue $[Na^+]$ and $[Na^+]_i$ are elevated in cancer, as measured by ^{23}Na MRI (Ouwerkerk *et al.*, 2003; Jacobs *et al.*, 2004; Ouwerkerk *et al.*, 2007). This elevation may be due an increase in extracellular fluid volume fraction in tumours, since extracellular fluid contains an order of magnitude more Na^+ than intracellular fluid (Hille, 2001). Alternatively, it could be due to an increased $[Na^+]$ in either the extracellular or intracellular fluid compartments. There is some evidence from x-ray dispersion studies and ^{23}Na MRI that the increase in $[Na^+]$ seen in tumours is due to an increase in *intracellular* $[Na^+]$ (Cameron *et al.*, 1980; Hürter *et al.*, 1982; Madelin *et al.*, 2014; Zaric *et al.*, 2016).

To test the theory that VGSCs increase $[Na^+]_i$ and thereby also total $[Na^+]$ in tumours, the total tumour $[Na^+]$ was measured using ICP-MS in normal and $Na_v1.5$ knock-down xenograft tumours. There was no difference in the total tumour $[Na^+]$ with $Na_v1.5$ knock-down. The same breast cancer tumours were analysed by ^{23}Na MRI by Andrew James and found to have no difference in total tissue $[Na^+]$ when the mean tumour $[Na^+]$ was examined

(unpublished data). Together, these experiments showed no evidence that $Na_v1.5$ increased total $[Na^+]$. It is possible that these techniques were not sensitive enough to detect small changes in total $[Na^+]$, and it is also possible that taking average concentrations from bulk tissue means that localised areas of $[Na^+]$ elevation are missed. In support of this ^{23}Na MRI was able to detect changes in maximal $[Na^+]$ but not mean $[Na^+]$ between tumours and healthy tissue (James *et al.*, 2022).

The $[Na^+]_e$ in xenograft tumours was found to be within the normal physiological range for mouse plasma. Ideally $[Na^+]_i$ would be assessed in tumours, but this is challenging to measure accurately. There is, however, evidence of elevated $[Na^+]_i$ in *ex-vivo* slices from xenograft tumours measured using SBFI-AM (James *et al.*, 2022). There is published evidence from isolated cells that VGSC activity increases $[Na^+]_i$, in lung and breast cancer cells (Campbell *et al.*, 2013; Yang *et al.*, 2020). To address this further, knockout of $Na_v1.5$ was attempted using CRISPR-Cas9 in MDA-MB-231 cells, however the effects of $Na_v1.5$ deletion on $[Na^+]_i$ were difficult to resolve, since CRISPR knock-out of $Na_v1.5$ decreased $[Na^+]_i$ in a clonal population of cells but not in a polyclonal population (Appendix III.iii).

Where present, an elevation of $[Na^+]_i$ in cancer is likely due to changes in several Na^+ transport mechanisms, in addition to VGSCs. There are several proteins involved in Na^+ transport which have altered expression in cancer, discussed in (Leslie *et al.*, 2019). Of these, the most important regulator of $[Na^+]_i$ is NKA. A reduction in the NKA activity or sensitivity of NKA to $[Na^+]_i$ would certainly lead to elevated $[Na^+]_i$, whereas changes in other mechanisms of Na^+ transport could be counteracted by NKA. Future work should consider the role of $Na_v1.5$ in the context of other Na^+ transport mechanisms to evaluate how these work together to control $[Na^+]_i$.

7.4 Mechanisms of $Na_v1.5$-induced metastasis in breast cancer

The most commonly reported function which has been ascribed to VGSCs in cancer is increasing invasion *in vitro* (Grimes *et al.*, 1995; Laniado *et al.*, 1997; Roger *et al.*, 2003; Fraser *et al.*, 2005) and tumour growth and metastasis *in vitro* (Driffort *et al.*, 2014; Nelson *et al.*, 2015a; Nelson *et al.*, 2015b). Other effects of VGSC activity in cancer cells are production of an elongated, mesenchymal phenotype and increased migration (Fulgenzi *et al.*, 2006; Isbilen *et al.*, 2006; Brackenbury & Djamgoz, 2007; Ding *et al.*, 2008; Chioni *et al.*, 2010; Nelson *et al.*, 2015b; Gradek *et al.*, 2019). Understanding the mechanisms behind these functions may help to develop new cancer treatments targeting VGSC signalling pathways. The following sections consider three main consequences of VGSC activity in breast cancer cells implicated by the results of this thesis.

7.4.1 Acidifying the extracellular environment

Reducing the extracellular pH in tumours promotes cancer progression by increasing activity of enzymes that degrade the extracellular matrix such as cysteine cathepsins and MMPs (Brisson *et al.*, 2011). This allows cancer cells to invade out of the primary tumour. Extracellular acidification via NHE1-mediated H^+ extrusion is increased by VGSC activity in MDA-MB-231 cells. (Brisson *et al.*, 2011; Brisson *et al.*, 2013). The authors hypothesised that this is due to an allosteric interaction between VGSCs and NHE1 and they showed evidence that VGSCs and NHE1 colocalised in caveolae to support this theory. In this thesis, an alternative explanation for VGSC-induced H^+ extrusion was proposed: Na^+ entry through VGSCs would increase the activity of NKA to remove the excess Na^+. NKA is a major consumer of ATP (McBride & Early, 1989) and increased production of ATP is required to power NKA when VGSCs are active. Both oxidative and glycolytic ATP production increase acidic metabolites, in the form of carbonic acid and lactic acid respectively. However, glycolytic respiration reduces pH more than oxidative phosphorylation to produce the same amount of ATP. Intriguingly, NKA predominantly utilises ATP derived from glycolysis in several tissues including breast cancer cells (Epstein *et al.*, 2014), vascular

smooth muscle (Paul *et al.*, 1979) and cardiomyocytes (Sepp *et al.*, 2014). Using similar cell culture and recording conditions to those in (Brisson *et al.*, 2011; Brisson *et al.*, 2013), this project suggests that NKA in MDA-MB-231 and MCF7 cells is strongly reliant on glycolysis. In fact, inhibiting mitochondrial respiration did not affect viability or $[Na^+]_i$ (Figure 3.18), suggesting that NKA could function as normal without mitochondrial respiration. In contrast, inhibition of glycolysis induced a large increase in $[Na^+]_i$ similar to that caused by ouabain, and also rapidly led to cell death (Figure 3.18). It is therefore possible that VGSC activity increased the rate of glycolysis in the previously published studies where VGSC activity was shown to increase extracellular acidification (Brisson *et al.*, 2011; Brisson *et al.*, 2013).

It has been shown by others that increasing $[Na^+]_i$ via non-VGSC routes increases the rate of glycolysis in breast cancer (Epstein *et al.*, 2014), as well as in other cell types such as skeletal and cardiac muscle (James *et al.*, 1996; Aksentijevic *et al.*, 2018). Additional evidence pointing towards a likely effect of VGSC activity on glycolysis is shown by a non-voltage-gated isoform of the α subunit, Na_x, encoded by *SCN7A*. This α subunit is used as an extracellular $[Na^+]$ sensor in the CNS and it mediates lactate signalling via direct interactions with NKA (Shimizu *et al.*, 2007; Berret *et al.*, 2013).

To test the theory that VGSC activity increases the glycolytic rate in breast cancer cells, lactate was measured as a proxy for glycolytic rate. Experiments in this thesis suggested a possible decrease in glycolysis due to VGSC inhibition with TTX in MDA-MB-231 cells (Figure 3.17 I), however this result was not statistically significant ($P = 0.052$). Since lactate production was reduced with TTX treatment in every experiment, it seems probable that a significant effect would have been seen with more than three experimental repeats. Interestingly, no change in lactate was seen with TTX treatment of MCF7 cells (Figure 3.17 E), which would be expected since this cell line does not have detectable VGSC Na^+ currents. Further lactate assays and a Seahorse assay measuring the rates of H^+ production

and O_2 consumption with VGSC inhibitors and openers would be important next experiments to further address this mechanism.

High $[Na^+]_i$ increased glycolytic flux and reduced oxidative metabolism in cardiomyocytes (Aksentijevic *et al.*, 2018). In this study, the authors collected metabolomic data which gave a detailed overview of the respiration changes due to elevated $[Na^+]_i$. Similar data in cancer cells may help show whether VGSC activity or elevation of $[Na^+]_i$ disrupts mitochondrial respiration in cancer cells, and at which enzyme-controlled steps. In addition, the effect of VGSC activity on mitochondrial membrane potential could be investigated using an indicator such as TMRE (Crowley *et al.*, 2016). Moreover, in this project the effect of VGSC activity on the rate of NKA activity was not measured, so this is an obvious future study which needs to be performed. NKA activity can be measured using cellular $^{86}Rb^+$ accumulation since Rb^+ can take the place of K^+ in this pump (Xie *et al.*, 1999).

As part of the evidence for VGSC regulation of NHE1, Brisson *et al.* showed that NHE1 co-localised with $Na_v1.5$ in caveolae in invadopodia (Brisson *et al.*, 2011; Brisson *et al.*, 2013). Interestingly, NKA immunoprecipitates with caveolin 1 in renal cells (Josef *et al.*, 2016) so NKA is likely also to be found in caveolae in cancer cells. Also, the α-subunit Na_x coded for by *SCN7A* interacts directly with NKA in glial cells (Shimizu *et al.*, 2007), raising the possibility that other VGSC α-subunits may have direct interactions with NKA. It is therefore conceivable that NKA is involved in the local interactions between $Na_v1.5$ and NHE1 in caveolae. This theory could be investigated using immunocytochemistry and confocal microscopy, as well as with FRET experiments using labelled NKA, VGSCs and NHE1.

Extracellular acidification increases malignancy of cancers in more ways than just aiding ECM degradation. As discussed in Section 1.6.5, low pH leads to activation of several G-protein coupled receptors and ASIC channels which increase mitogenic intracellular

signalling. In addition, a reduced extracellular pH also leads to an immunosuppressive tumour microenvironment (Calcinotto *et al.*, 2012; Bellone *et al.*, 2013). In this thesis, MDA-MB-231 xenografts were found to have a lower pH_e than found in normal tissue (Section 3.2.5), which is consistent with several previous studies of solid tumours, reviewed in (White *et al.*, 2017). In particular, the pH was lower in peripheral regions of the tumour which also exhibited more proliferation and less apoptosis. This was unexpected, since it has generally been thought that pH_e reduction occurs due to hypoxia, both in skeletal muscle and in tumours (Estrella *et al.*, 2013). However, when tumours are examined at high resolution, it appears that low pH_e can occur in the absence of hypoxia. A surprisingly poor association between hypoxic and acidic microdomains of tumours was noticed in the 1990s when ratiometric fluorescent imaging was used to measure pH_e and phosphorescence quenching microscopy was used to estimate the partial pressure of oxygen in tumours *in vivo* (Helmlinger *et al.*, 1997). NHE1 and MCT1 (both important for removing H^+ from the cytoplasm) localised to the invading edges in glioma, rather than the hypoxic core as might have been expected (Grillon *et al.*, 2011; Grillon *et al.*, 2015). Similarly, in a study of breast cancer xenograft tumours, the spatial distribution of the "pH-stat" enzyme carbonic anhydrase 9 (CAIX) and the hypoxia marker pimonidazole did overlap partially, but the CAIX staining extended much more peripherally than pimonidazole staining. The authors concluded that that acidic pH_e occurred even in non-hypoxic, more viable areas, whereas the hypoxia marker co-registered well with necrotic areas of the tumour (Jardim-Perassi *et al.*, 2019). In another recent study, a fluorescent pH-sensitive peptide "pHLIP" was highly retained at the invading edges rather than the hypoxic centres of mouse mammary tumours and lung metastases. pHLIP retention correlated strongly with CAIX and lysosome-associated membrane protein 2 (LAMP-2) staining, adding confidence to the conclusion that the actively invading edges of tumours have a low pH_e (Rohani *et al.*, 2019).

Results from Section 3.2.6 show that the persistent Na^+ current through VGSCs will be increased when the pH_e is more acidic. This indicates that VGSC activity, and its

downstream effects on increasing invasive cell behaviour will be increased in solid tumours, particularly in areas with lower pH_e: hypoxic regions and invading edges of tumours.

In summary, there is some evidence to suggest that VGSC activity increases the rate of glycolysis in breast cancer cells, which would in turn increase H^+ extrusion through pH regulators such as NHE1. This may explain why VGSC activity was previously shown to increase NHE1-mediated H^+ extrusion, leading to ECM degradation in breast cancer (Brisson *et al.*, 2011; Brisson *et al.*, 2013). There is also evidence that extracellular acidification in breast tumours occurs particularly in the highly proliferative peripheral region of tumours. Since the persistent current through $Na_v1.5$ is larger in acidic conditions, more Na^+ would enter breast cancer cells through VGSCs at the invading edges of the tumour. These cellular mechanisms are illustrated in Figure 7.1.

7.4.2 ROS and VEGF signalling: due to hypoxia?

Data from the RNAseq experiment showed that knock-down of $Na_v1.5$ decreased expression of many antioxidant genes involved in ROS detoxification. This can be interpreted in two ways: reduction of these genes could lead to an increase in ROS present in the $Na_v1.5$ knock-down cells, or perhaps more likely, it could indicate a reduced need for ROS detoxification when $Na_v1.5$ is knocked down, due to reduced ROS production. Cancer cells produce more ROS than normal cells due to increased metabolic rate and relative hypoxia, and they upregulate antioxidant production in response to this (Perillo *et al.*, 2020). ROS have a concentration-dependent effect in cancer. At moderate concentrations ROS increase angiogenesis and promote survival and proliferation via the src, MAPK/ERK1/2, p38 and PI3K/Akt pathways, whereas at higher concentrations they lead to cancer cell apoptosis (Aggarwal *et al.*, 2019; Perillo *et al.*, 2020). Investigation into targeting redox homeostasis for cancer treatment and prevention is therefore an active area of research. There is no published information on the effect of $Na_v1.5$ on ROS signalling, although there is plenty of evidence of the reciprocal relationship. ROS lead to decreased transient current through

$Na_v1.5$ in cardiomyocytes (Liu *et al.*, 2010), possibly because of reduced $Na_v1.5$ expression (Mao *et al.*, 2012), however ROS also oxidise CAM kinase which increases the persistent Na^+ current in cardiomyocytes (Wagner *et al.*, 2011). The effect of ROS on Na^+ current through $Na_v1.5$ should be studied in cancer cells, since the relative importance of the signalling mechanisms discovered in cardiomyocytes may be different in other tissues and ROS signalling is important in cancer development (Aggarwal *et al.*, 2019). In addition, based on findings from the RNAseq experiment, it would be important to investigate the potential effects of $Na_v1.5$ on ROS production in cancer cells. To speculate on a possible mechanism by which $Na_v1.5$ expression could affect ROS signalling, it could be due to disruption of normal electron transport chain function, for example by interfering with mitochondrial inner membrane fluidity (Hernansanz-Agustín *et al.*, 2020). Increased ROS production could also be because of increased hypoxia in $Na_v1.5$-expressing tumours since hypoxia leads to increased mitochondrial ROS production in many tissues (Chen *et al.*, 2018; Aggarwal *et al.*, 2019). One gene ontology term which was enriched in the downregulated gene set with $Na_v1.5$-knockdown was NK-κB signalling. This can be induced by ROS (Li *et al.*, 1998), which adds evidence to the theory that $Na_v1.5$ expression may increase ROS production, rather than just increase transcription of antioxidants.

Another consequence of hypoxia in tumours is increased angiogenic signalling (Hanahan & Weinberg, 2000) , and this may be affected by VGSC activity. In HUVEC vascular endothelial cells, $Na_v1.5$ activity leads to VEGF signalling and thus angiogenesis (Andrikopoulos *et al.*, 2011). Conversely in MDA-MB-231 tumours there was no effect on angiogenesis with $Na_v1.5$ knock-down (Nelson *et al.*, 2015b). Overexpression of the VGSC β1 subunit did however increase VEGF secretion into cell culture medium and number of endothelial vessel structures in xenograft tumours (Nelson *et al.*, 2014). Since VEGF signalling was an enriched term in the Reactome analysis in this project, and $Na_v1.5$ knockdown decreased expression of stromal oxygen carrying genes, $Na_v1.5$ activity may promote VEGF signalling in breast cancer cells. Since VEGF signalling is linked to hypoxia

(Minchenko *et al.*, 1994), it is possible that VEGF signalling occurs downstream of mitochondrial or redox disturbances caused by Na^+ entry through $Na_v1.5$. This may be mediated through ROS-induced NF-κB which increases VEGF signalling (Schmidt *et al.*, 2007). Alternatively, since VGSC expression increases tumour growth rate (Nelson *et al.*, 2015b), it may simply increase the size of the hypoxic regions in the tumour.

In conclusion, this thesis has provided transcriptomics evidence that $Na_v1.5$ has a role in ROS regulation in breast cancer cells and may also increase angiogenic signalling. These two systems are usually linked to hypoxia in tumours, so there may be a link between $Na_v1.5$ activity and tumour hypoxia which needs further investigation.

7.4.3 V_m modulation and direct protein interactions

As well as regulating pH_e, VGSCs have been shown to promote migration of cancer cells by depolarisation of the V_m. They also engage in direct interactions with other molecules through both α and β subunits to promote migration and invasion. These mechanisms will be discussed in turn alongside evidence from this project which contributes to our understanding of each mechanism.

The notion of VGSC-induced depolarisation of V_m is intriguing, given the evidence that more proliferative cells have a less negative V_m (Yang & Brackenbury, 2013). Inhibition of VGSCs with TTX in MDA-MB-231 cells and H460 non-small cell lung cancer cells hyperpolarised the V_m (Campbell *et al.*, 2013; Yang *et al.*, 2020). A change in V_m would be expected to have a multitude of effects on the cell, since it would change the driving force for all ions across the plasma membrane and could affect electrostatic forces involved in protein structure and molecular interactions at the membrane. One such interaction that has been shown to be affected by VGSC activity is the nanoclustering and activation of the small GTPase Rac1 in the inner leaflet of the plasma membrane (Yang *et al.*, 2020).

In this thesis, the effect of β1 expression on V_m was investigated. The tumorigenic effects of β1 subunits include promotion of a mesenchymal phenotype and membrane outgrowths in cancer cells, as well as increased metastasis in the MDA-MB-231 xenograft model of breast cancer (Nelson *et al.*, 2014). The hypothesis was that since β1 increases transient Na^+ current in MDA-MB-231 cells, it would depolarise the V_m. This hypothesis was not supported by the data since there was no difference between the V_m of control and β1-overexpressing cells (Figure 3.2 H). It has since been shown that the induced Na^+ current in β1-overexpressing MDA-MB-231 cells is TTX-sensitive, unlike that in wild-type MDA-MB-231 cells (Haworth *et al.*, 2021). This indicates that β1 induces expression of a different α subunit from that which is normally present in MDA-MB-231 cells. It is possible that this TTX-sensitive α subunit passes a smaller persistent Na^+ current than $Na_v1.5$, meaning that it would not alter the resting V_m in MDA-MB-231 cells. Alternatively, β1 may alter inactivation gating of α subunits to reduce the persistent Na^+ current. In support of this theory, it was shown that although β1 increased the transient Na^+ current, it reduced the persistent Na^+ current when co-expressed with $Na_v1.1$ in HEK293 cells (Aman *et al.*, 2009). Results from this thesis show that β1 is unlikely to act through depolarisation of the V_m in cancer cells. Nor did β1 appear to act via increasing Na^+ current since this *in vitro* effect of β1 (Chioni *et al.*, 2009) was not found *in vivo* (Figure 3.3 E). It is therefore likely that β1 increases invasive cell behaviour through direct interactions with CAMs on other cells and with ECM components, via its Ig loop (McEwen & Isom, 2004). These interactions stimulate β1-regulated intracellular signalling pathways involving ankyrin recruitment (Malhotra *et al.*, 2000), fyn kinase and contactin (Brackenbury *et al.*, 2008) or other pathways as yet unidentified.

One pro-migratory function of $Na_v1.5$ in breast cancer cells is increasing cortactin phosphorylation (Brisson *et al.*, 2013) which then activates the Arp2/3 complex to initiate branching of actin required for cell motility (MacGrath & Koleske, 2012). In this thesis, RNAseq revealed that $Na_v1.5$ knock-down upregulated *ARPC3* which codes for one subunit

of the Arp2/3 complex. Alone, this seems to disagree with the finding that $Na_v1.5$ activates Arp2/3, however activity of Arp2/3 may not follow expression changes. Also, many more cytoskeletal genes were downregulated with knock-down of $Na_v1.5$ than were upregulated (Table 4.4, Table 4.7 and Figure 4.6 A). The STRING database was consulted to assess downregulated genes where the gene product interacts directly with $Na_v1.5$, and four out of five genes were involved in the cytoskeleton (Figure 4.12).

Another function of VGSCs which has been shown in cancer is increasing activity of src (Brisson *et al.*, 2013) and fyn, a member of the src family of tyrosine kinases which are important in mitogenic signalling (Brackenbury *et al.*, 2008; Brackenbury *et al.*, 2010). There were no significant changes in expression of any members of the src family with $Na_v1.5$ knock-down except strong downregulation of *JAK3* (Table 4.4). This does not exclude the possibility that src and fyn are less activated with $Na_v1.5$ knock-down however. Since MAPK signalling has been shown to be linked by VGSC activity in colon cancer (House *et al.*, 2010; House *et al.*, 2015), expression of genes in this pathway could be altered by knock down of $Na_v1.5$ in breast cancer cells. Indeed, three MAPK genes were differentially expressed in $Na_v1.5$ knock-down tumours, although two of these were upregulated. Again, it seems likely that activity does not correlate with activity in these genes, given that phosphorylation status rather than concentration controls activation of each member of the pathway. House *et al* (2015) showed that *WNT9A* was upregulated when VGSCs were opened by veratridine in colon cancer cells. Since the wnt pathway is important for cancer cell invasion and is activated downstream of the MAPK mitogenic cascade (House *et al.*, 2015), this was an important finding. *WNT3* was downregulated with $Na_v1.5$ knock-down in this RNAseq experiment indicating that a similar mechanism may be present in breast cancer cells.

The RNAseq data in this thesis suggest a role for VGSCs in regulating Ca^{2+} signalling via the ryanodine receptor, TRPV4 and the VGCC regulatory subunit $\alpha_2\delta$. There is little

published evidence of a direct link between VGSCs and Ca^{2+} signalling in non-excitable cancer cells, although there are several possible mechanisms by which $[Na^+]_i$ could affect $[Ca^{2+}]$, such as via depolarisation of the V_m which would reduce the inward driving force for Ca^{2+} but could also open any VGCCs which are present. In addition, Na^+ and Ca^{2+} are exchanged across the plasma membrane by NCX and across the mitochondrial membrane by NCLX. Although small and localised increases in cytosolic Ca^{2+} can increase cell migration (Prevarskaya *et al.*, 2011), a large increase in cytosolic Ca^{2+} initiates apoptosis (Akl & Bultynck, 2013). Large increases are often mediated by ER release of Ca^{2+} via the IP3R, and in cancer cells this mechanism of Ca^{2+} release is usually associated with induction of apoptosis (Akl & Bultynck, 2013). Further work is required to investigate the link between VGSC activity and the Ca^{2+} channels identified in this project. This could involve Ca^{2+} imaging with confocal microscopy and pharmacological regulation of each type of Ca^{2+} channel in turn to assess localised changes in Ca^{2+} upon opening of VGSCs.

As mentioned above, a significantly downregulated gene in $Na_v1.5$ tumours is a member of the src family, *JAK3*. This normally mediates intracellular signalling downstream of cytokine receptors in immune cells (Leonard & O'Shea, 1998). It is possible that a decrease in *JAK3* expression indicates a reduction in inflammatory cytokine signalling in $Na_v1.5$ knock-down tumours. Other evidence for this is shown by the downregulation of genes involved in interferon signalling (Figure 4.5), and the changes in expression of genes involved in antigen presentation (Table 4.9 and Figure 4.5). A reduction in inflammatory signalling in a severely immunocompromised host is difficult to interpret. It is however possible that $Na_v1.5$ expression in cancer cells influences interactions with the immune system, for example through ROS signalling, reduced pH_e, changes in antigen presentation or via increasing expression of co-stimulatory molecules which induce immune tolerance.

In summary, the RNAseq data, together with the mechanistic findings from the in vitro physiological studies, suggest that $Na_v1.5$ expression and activity in breast cancer xenografts

may affect ROS signalling, NF-κB signalling, VEGF signalling and the hypoxia/low pH marker CAIX. These are all linked to hypoxia, and changes in metabolism, which would fit with an increased rate of glycolysis in cells expressing $Na_v1.5$. In mechanistic experiments with breast cancer cells, NKA was highly reliant on glycolysis but not oxidative phosphorylation. Logically, this would mean that Na^+ entry via VGSCs would increase the rate of glycolysis to power NKA. Reciprocally, the reduction in pH_e caused by VGSC activity serves to increase Na^+ entry into breast cancer cells via $Na_v1.5$. Together, these mechanisms, shown in Figure 7.1 could lead to a positive feedback loop linking Na^+ entry and extracellular acidification.

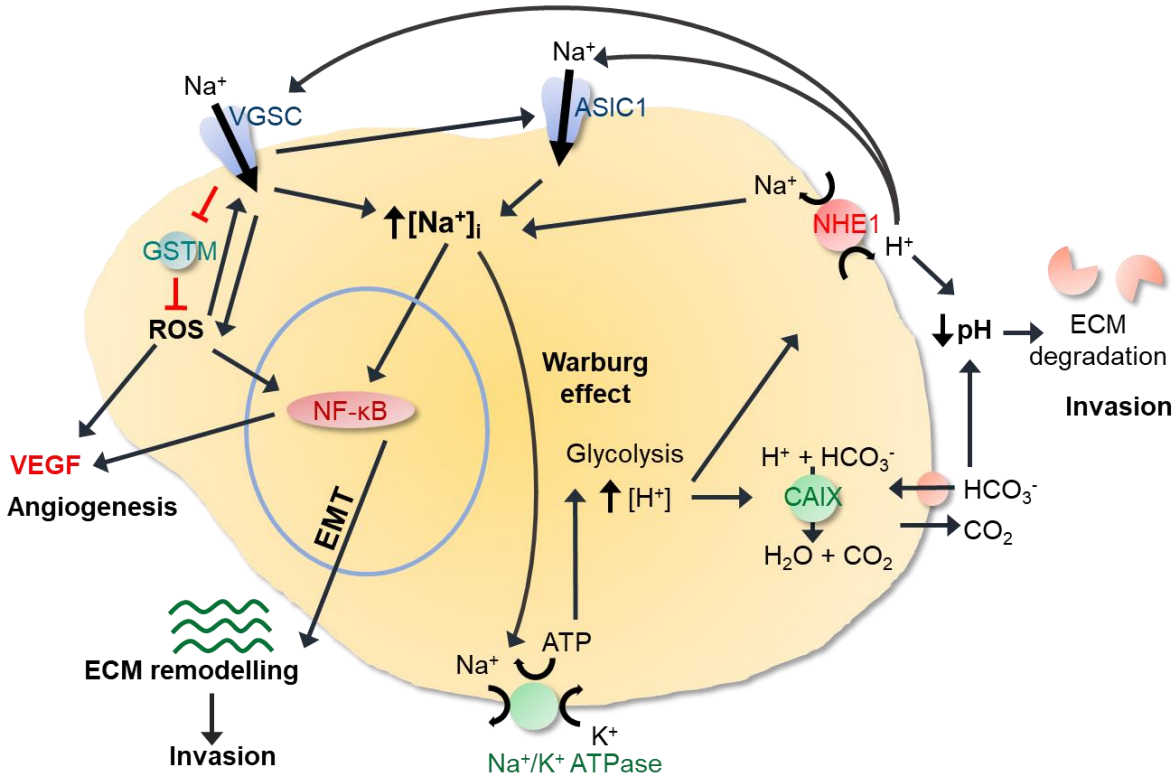

Figure 7.1 Hypothetical mechanisms of VGSC promotion of extracellular acidication and invasion, updated to include new findings from this thesis.
This includes the hypothesis from Figure 3.1, whereby VGSCs increase NKA activity, increasing the rate of glycolysis and cytosolic H^+ production, with removal of H^+ through NHE1. Additional mechanisms are: 1. Upregulation of ASIC1 which, like $Na_v1.5$ allows Na^+ into the cell in low pH_e. 2. Removal of intracellular H^+ via CAIX as well as by NHE1. 3. Upregulation of ROS signalling via GSTM downregulation, with positive feedback on persistent Na^+ current through VGSCs. 4. Upregulation of NF-κB signalling which promotes EMT, including the production of ECM components. 5. Upregulation of angiogenesis, perhaps via ROS and/or NF-κB. Angiogenic signalling alongside upregulation of CAIX is associated with aerobic glycolysis (the Warburg effect). 6. Reciprocally, acidic pH_e increases persistent Na^+ current into cancer cells through the VGSC $Na_v1.5$.

7.5 Future directions

Experiments which have been highlighted above as desirable next steps include optimisation of culture conditions to measure VGSC currents in primary breast cancer cells, and to obtain primary cultures of metastatic cells, for example cells from pleural effusions in breast cancer patients. It is important to make electrophysiological recordings from metastatic cells because there is evidence that $Na_v1.5$ is linked to metastatic ability, and large VGSC currents have only been recorded from breast cancer cell lines obtained from pleural effusions. To examine whether VGSC currents are larger in metastases than in primary tumours, electrophysiological recordings would need to be performed in primary and metastatic cells from a better mouse model of breast cancer metastasis such as the MMTV-PyMT model, if this model expresses VGSC currents.

ESL was shown to inhibit currents through $Na_v1.5$ in MDA-MB-231 cells, so the next steps to investigate its potential as an anti-cancer therapy would be to perform *in vitro* studies to assess the effect of ESL on migration and invasion of breast cancer cells. These could be performed as in (Yang *et al.*, 2012) using a wound-healing assay and a Matrigel invasion assay. If these assays are successful, the drug could be tested in an *in vivo* study similar to (Nelson *et al.*, 2015a). The eventual goal of these experiments is to find a suitable drug for a clinical trial of a VGSC inhibitor in breast cancer patients.

Since no relationship was found in this project between VGSC activity and total tissue $[Na^+]$, but small studies on isolated cancer cells showed that $[Na^+]_i$ is reduced with TTX (Campbell *et al.*, 2013; Yang *et al.*, 2020), it is still unclear whether VGSC activity affects $[Na^+]$ in tumours. Na^+ entry via VGSCs is likely to be counteracted by NKA, but the amount of extracellular Na^+ entering cells through all mechanisms may still be increased with VGSC activity, and this could be assessed if extracellular Na^+ could be labelled. The isotope ^{22}Na emits positrons and is therefore detectable by positron emission tomography (Murata *et al.*, 2016). There might be a way of using this physical feature of ^{22}Na to measure intracellular

Na^+ accumulation in breast cancer cells *in vitro* and thereby assess the relative importance of various Na^+ transport mechanisms on regulation of $[Na^+]_i$.

This thesis provided some evidence of heterogeneous extracellular pH in xenograft tumours. In particular, the region with lower pH correlated with the more proliferative edges of the tumour. ^{23}Na MRI studies have shown that $[Na^+]$ is also heterogeneous in tumours (Ouwerkerk *et al.*, 2007; James *et al.*, 2021). Given the evidence from this thesis that Na^+ and pH^+ regulation are linked, it would be extremely useful to determine whether there is any correlation between the distributions of these two ions. pH can be assessed by MRI *in vivo* using a phosphorus coil or by MRI-CEST, so imaging of Na^+ and using CAIX staining or the hypoxia probe pimonidazole. Co-registration of histological sections and ^{23}Na MRI images is possible if great care is taken to preserve the orientation of the tumour as in (Jardim-Perassi *et al.*, 2019).

Further work needed to test the hypothesis that VGSCs affect extracellular acidification via NKA would include measurement of the rate of NKA activity with VGSC channel modulators. NKA activity would be best measured by an $^{86}Rb^+$ uptake assay. The effect of VGSC modulators on the rate of glycolysis needs to be tested by further lactate assays as in this thesis. It can also be measured using a Seahorse analyser which measures real-time extracellular acidification rate as well as oxygen consumption rate, isolating the source of extra ATP used by NKA upon opening of VGSCs.

Again, to further test the hypothesised mechanism of VGSC-induced H^+ extrusion through NHE1, it would be useful to assess the degree of co-localisation of VGSCs and NKA on the plasma membrane using immunofluorescence and confocal microscopy. In breast cancer cells, $Na_v1.5$ has been shown to co-localise with NHE1 to increase extracellular acidification (Brisson *et al.*, 2013). The VGSC-related α subunit Na_x co-localises with NKA in CNS neurons to produce lactate signalling (Berret *et al.*, 2013). It is therefore possible that NKA

might co-localise with $Na_v1.5$ and NHE1 in caveolae in breast cancer cells, and if so, it would add confidence to the theory that $Na_v1.5$ acts through NKA to increase glycolytic H^+ production and therefore H^+ extrusion through NHE1.

In the RNAseq experiment, several glutathione-S-transferase gene mRNAs were downregulated with knock-down of $Na_v1.5$. This is of note because glutathione removes cellular ROS, and ROS signalling is disrupted in cancer. The downregulation of these genes should be confirmed with qPCR and a glutathione assay might show a change in glutathione activity with knock-down of $Na_v1.5$. Antioxidant genes are expressed in response to oxidative stress (Lu, 2009) so ROS production may be decreased with knock-down of $Na_v1.5$. It would be sensible to perform ROS assays in $Na_v1.5$ knock-down cells, but also in cells treated acutely with TTX or veratridine to assess effects of VGSCs on ROS production before any changes in gene expression have taken place. If $Na_v1.5$ activity is shown to increase expression of glutathione-S-transferase genes, the signalling pathway leading to this regulation should also be investigated. There is RNAseq evidence that NF-κB signalling is disrupted with $Na_v1.5$ knock-down and this pathway has been shown to regulate glutathione expression, so activation of genes in this pathway could be investigated through qPCR and Western blot for example.

7.6 Conclusion

This thesis has provided significant evidence that VGSCs are important in breast cancer metastasis. It has also provided some evidence that VGSCs in cancer cells reduce pH_e via increasing glycolytic flux, contributing to tumour aerobic glycolysis. Interestingly, $Na_v1.5$ allows a larger steady-state Na^+ current into cancer cells in acidic conditions. Together these findings lead to a positive feedback loop which acts both to increase intracellular $[Na^+]$ and extracellular $[H^+]$ in tumours.

Appendices

Appendix I Calculation to explain tissue [Na^+] difference in normal and cancerous mammary glands

This calculation was performed to assess whether the milk content of normal lactating mammary glands explains the difference between total tissue [Na^+] between normal glands and breast tumours. Mouse milk has a [Na^+] of 26 mM (Berga & Neville, 1985), slightly less than the total [Na^+] of the normal mammary glands measured by ICP-MS (~30 mM). It is therefore possible that non-lactating mammary glands might have had a slightly higher total [Na^+] than these glands. If the milk content were the sole reason for the difference in total [Na^+] between the normal and cancerous tissues, it would be possible to calculate the proportion of the tissue made up of milk:

Milk proportion (p) x milk [Na^+] + tissue proportion (1-p) x tissue [Na^+] = 30 mM.

$p \times 26 + (1-p) \times 46 = 30$

$p = 0.8$

In order for the milk content to decrease the total [Na^+] from 46 mM as in the tumours to 30 mM, it would be necessary for 80% of the normal lactating mammary gland to be made up of milk. In (Berga & Neville, 1985) the milk was calculated to make up 0.064 ml/g tissue (~6%) of the lactating mouse mammary gland. Therefore, the difference between tumour [Na^+] and normal gland [Na^+] is not likely to be just due to the milk content of the normal glands.

Appendix II Primers

II.i Primers to detect selected K^+ channel mRNA:

Appendix table I PCR primers used to detect mRNA for selected K^+ channels in breast cells.

***KCNA3* (K_v1.3)**	FWD	5'-AAA AAC GGG CAA TTC CAC TGC-3′
Self-designed	REV	5'-AAC AAG GGC ATA GGC AGA CC-3′
	Length 282 bp	Gene contains only one exon
***KCNH1* (K_v10.1)**	FWD in exon 18	5'-CCT GGA GGT GAT CCA AGA TG-3'
(Ramirez *et al.*, 2013)	REV in exon 19	5'-CCA AAC ACG TCT CCT TTT CC-3'
	Length 60 bp	
***KCNH2* (K_v11.1)**	FWD in exon 9	5'-GTG CTA AGG GCT TCC CTG AG-3'
(Gong *et al.*, 2014)	REV in exon 11	5′-CCG ACT GAA GCC ACC CTC TAA C-3′
	Length 504 bp	
***KCNMA1* (K_{Ca}1.1 or BK_{Ca})**	FWD in exon 69	5'-TGC AAA GGA GGT TAT AAA GTT ACG-3'
(Khaitan *et al.*, 2009)	REV in exon 69	5'-ATT TCA CAA AAG TTT TCA CAA GGA C-3'
	Length 248 bp	
***KCNN4* (K_{Ca}3.1 or IK_{Ca})**	FWD in exon 10	5'-CTG CTG CGT CTC TAC CTG G-3'
(Thurber *et al.*, 2017)	REV in exon 10	5'- AGG GTG CGT GTT CAT GTA AAG-3'
	Length 144 bp	

Appendix III CRISPR knock out of *SCN5A* in MDA-MB-231 cells

The gene coding for Na_v1.5, *SCN5A* was knocked out in MDA-MB-231 cells using CRISPR-Cas9 technology, in preparation for *in vitro* and *in vivo* experiments assessing the functions of Na_v1.5 in breast cancer. CRISPR was chosen for this purpose as it has fewer and more predictable off-target effects than RNA interference techniques (Smith *et al.*, 2017).

III.i Choosing CRISPR target sequences in *SCN5A*

The online Zhang lab CRISPR design tool (CRISPR.mit.edu) was used to find suitably unique CRISPR target sequence sequences in *SCN5A*. It is advisable to target near to the beginning of the gene to achieve reliable disruption of protein function. Target sequences for exons 3. 8 and 9 were designed (Appendix III.v.x). First, the MDA-MB-231 genome was sequenced around each possible target in exons 3, 8 and 9, to make sure that this cell line did

not have mutations making the targets unsuitable. Sequencing primers were designed (Appendix III.v.ix). The sequences for *SCN5A* exons 3, 8 and 9 in MDA-MB-231 cells matched the NCBI sequences.

III.ii Creating CRISPR plasmids and transfection of MDA-MB-231 cells

The CRISPR plasmid px459 (Appendix figure I) was engineered to target exons 3, 8 or 9 by inserting a target sequence into the guide RNA scaffold. The inserts were designed to be flanked by sticky ends which were complementary to the BbsI-restricted px459 plasmid. Forward and reverse oligonucleotides to make each insert were annealed then ligated into the BbsI-restricted px459 plasmid. After amplification of the plasmid in bacteria and purification of DNA, the plasmids inserts were sequenced to confirm correct recombination. Engineered plasmids targeting one of three exons in *SCN5A* were transfected into MDA-MB-231 cells and wild-type px459 plasmids were transfected into control cells. Puromycin treatment was applied for 7 days to kill all untransfected cells.

III.iii Characterisation of CRISPR-treated clones

After transfection of the px459 CRISPR plasmid engineered to target exon 3 of *SCN5A*, some CRISPR-treated cells were frozen down. Five clones were expanded from single cells by plating at a density of 1 cell/well in 96 well plates and removing wells containing more than one cell for the first three days. The genomic region around the target sequence was amplified by PCR, and this amplicon was sent for Sanger sequencing. The chromatograms that were obtained showed a disruption of the sequence in all five clones at the expected location of the double stranded break (e.g. Appendix figure II A). The chromatograms were deconvoluted into the likely sequences present in each allele of the gene by the online program CRISP-ID (Dehairs *et al.*, 2016). MDA-MB-231 cells can have 1-3 copies of chromosome 3 (Watson *et al.*, 2004), but for the purposes of using CRISP-ID, it was assumed that there were two copies in these MDA-MB-231 cells.

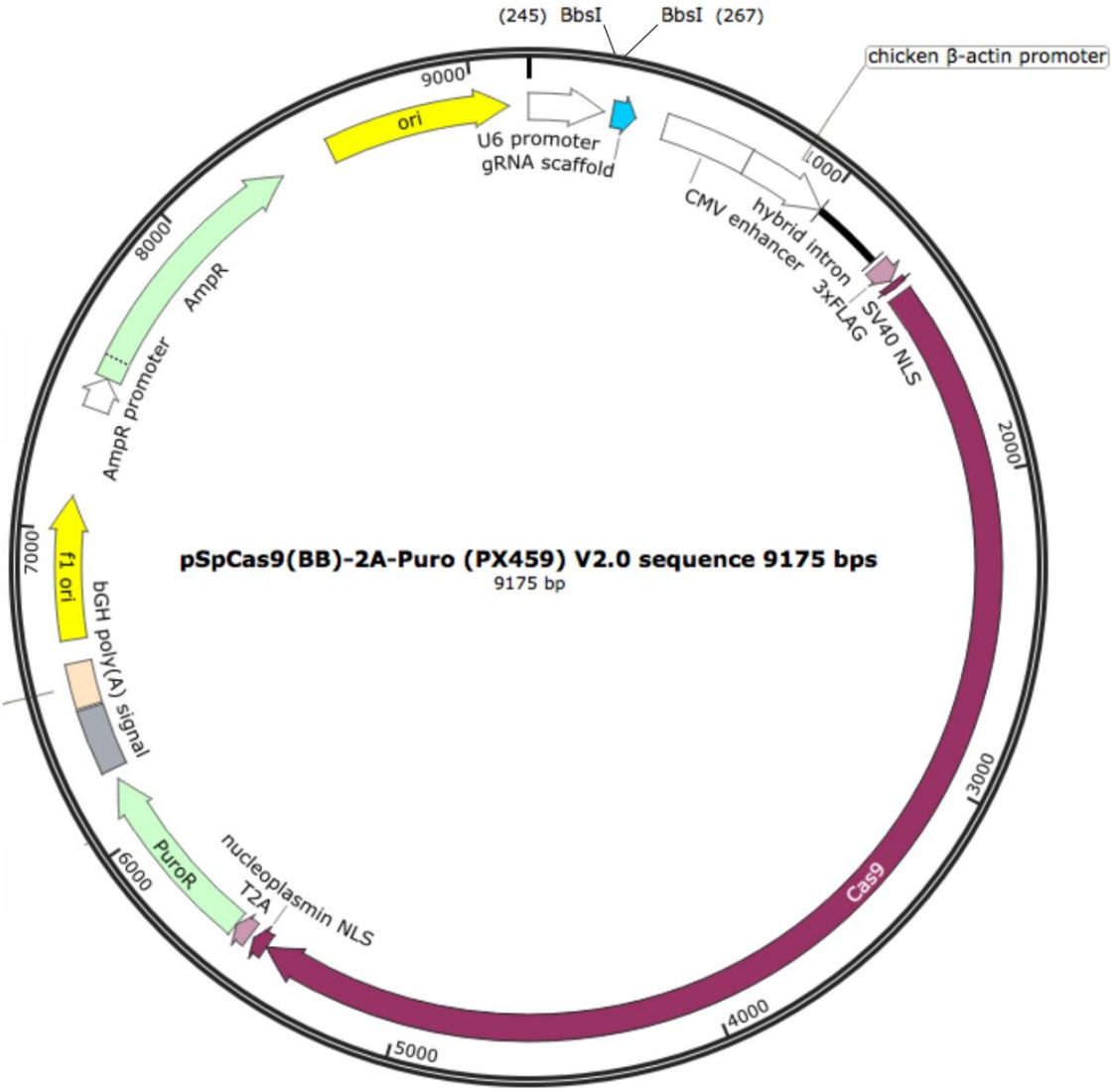

Appendix figure I Plasmid map of px459 V2.0.
This plasmid contains the gene coding for the CRISPR endonuclease enzyme Cas9 and a scaffold for a guide RNA to direct Cas9 to a location where it will make a double stranded DNA break. Image made with Snapgene.

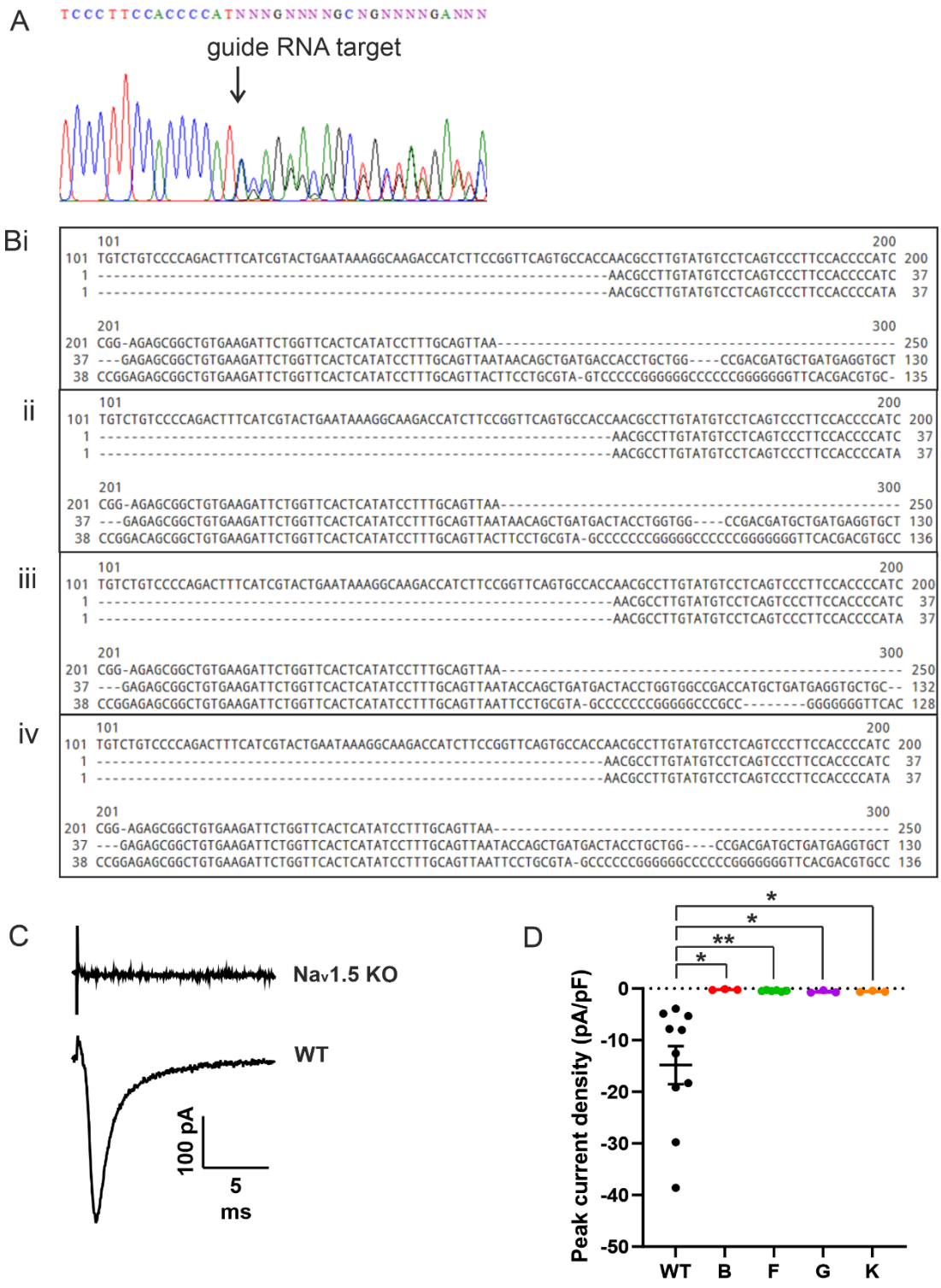

Appendix figure II Assessing $Na_v1.5$ KO in four clonal populations of MDA-MB-231 cells. **A**. Chromatogram showing that the sequence becomes altered at the point of the expected double-strand break in exon 3. **B**. Alignment of the wild-type DNA sequence (top line in each box) to the sequenced PCR product from four *SCN5A* knock-out clones, using the online deconvolution tool CRISP-ID (Dehairs *et al.*, 2016). This shows gene disruption of both alleles of the gene (middle and bottom lines in each box) in all clones. **C**. Example VGSC Na^+ currents measured using whole cell patch clamp in control (WT) MDA-MB-231 cells and from one *SCN5A*/$Na_v1.5$ knock-out clone. **D**. Peak current density of control (WT) MDA-MB-231 cell and $Na_v1.5$ knock-out clones B, F, G & K (n = 3-10). Results are mean ± SEM, one way ANOVA with Dunnett's multiple comparisons test.

Four knock-out clones with unique gene disruptions (called B, F, G and K) were found out of the five tested (Appendix figure II.Bi-iv). Whole-cell patch clamp recordings confirmed that there were no detectable voltage-sensitive Na^+ currents in any of the clones (Appendix figure II.C and D).

The sequencing and patch clamp evidence was sufficient to show that the CRISPR knock-out of $Na_v1.5$ had been successful. However CRISPR gene editing can have off-target effects. The Zhang lab online CRISPR design tool (Ran *et al.*, 2013) specified the most likely off-targets that could be affected for each target sequence that it identified (Appendix table III). The top 10 most likely off-target regions were amplified by PCR using self-designed primers (Section III.v.xii) and these were sequenced. All of these sequences matched the reference genome sequences, showing that the top 10 most likely off-targets had not been affected by CRISPR.

The four $Na_v1.5$ knock-out clones were next assessed for phenotypic changes. First a proliferation assay was performed, using a sulforhodamine B assay (Section III.v.vii) to quantify protein (Appendix figure III A). There was no statistically significant difference between any of the clones and the control cells, even at day 5 ($P = 0.13$; $n = 6$ experiments each with 8 wells per condition; Appendix figure III B). Next, morphology of the $Na_v1.5$ knock-out cells was assessed (Section III.v.viii) since $Na_v1.5$ expression has been previously associated with an elongated, mesenchymal-like morphology (Nelson *et al.*, 2015b). Circularity of cell perimeter was used as an indicator of cell shape as this had been used in (Nelson *et al.*, 2015b). Surprisingly, the $Na_v1.5$ knock-out clones' circularity did not differ from the control cells, except one clone, 'K', which was more elongated than the control cells with a circularity score of 0.40 ± 0.02 compared to 0.58 ± 0.03 ($P < 0.01$; $n = 6$ experimental repeats; Appendix figure III C). Finally, $[Na^+]_i$ was measured using SBFI-AM in $Na_v1.5$ knock-out clone B compared to control cells (Appendix figure III D and E). This showed that $[Na^+]_i$ was lower in $Na_v1.5$ knock-out clone B cells (2.6 ± 0.5 mM) than in the

controls (8.0 ± 1.2 mM) ($P < 0.05$; n = 3 or 4 experimental repeats each with 40 cells; unpaired *t* test; Appendix figure III E).

It was hypothesised that growing colonies from single cells might select for more mesenchymal-type cells which were less prone to anoikis. To mitigate for this possibility, experiments were performed using polyclonal CRISPR $Na_v1.5$ knock-out cells frozen down prior to clonal selection. There were no detectable voltage-gated Na^+ currents detected by whole cell patch clamp in the 14 polyclonal cells tested (Appendix figure IV A and B). There was no significant difference in circularity between the polyclonal knock-out cells and controls ($P = 0.20$; n = 8 experimental repeats; unpaired *t* test; Appendix figure IV C). Next $[Na^+]_i$ was measured in the polyclonal knock-out cells compared to wild type cells. Instead of SBFI-AM fluorescence being measured with a microscope and camera as with a clonal population of $Na_v1.5$ knock-out cells, in this experiment SBFI-AM fluorescence was measured using a plate reader so that control and knock-out cells could be assessed concurrently. The polyclonal $Na_v1.5$ knock-out cells did not have a detectably different $[Na^+]_i$ from control cells (7.93 ± 0.42 vs 6.46 ± 0.53 mM; $P = 0.58$; n = 5 experimental repeats; unpaired *t* test; Appendix figure IV D and E).

In summary, the CRISPR knock out of *SCN5A* from MDA-MB-231 cells was successful, efficient and there was no evidence of off-target effects. However, growing clones from single cells selects for those cells which are particularly resilient and therefore clones may show a different phenotype from the original population of cells. Due to an unforeseen lack of time and resources due to covid-19, no further experiments were performed with the *SCN5A* knock-out cell in this project.

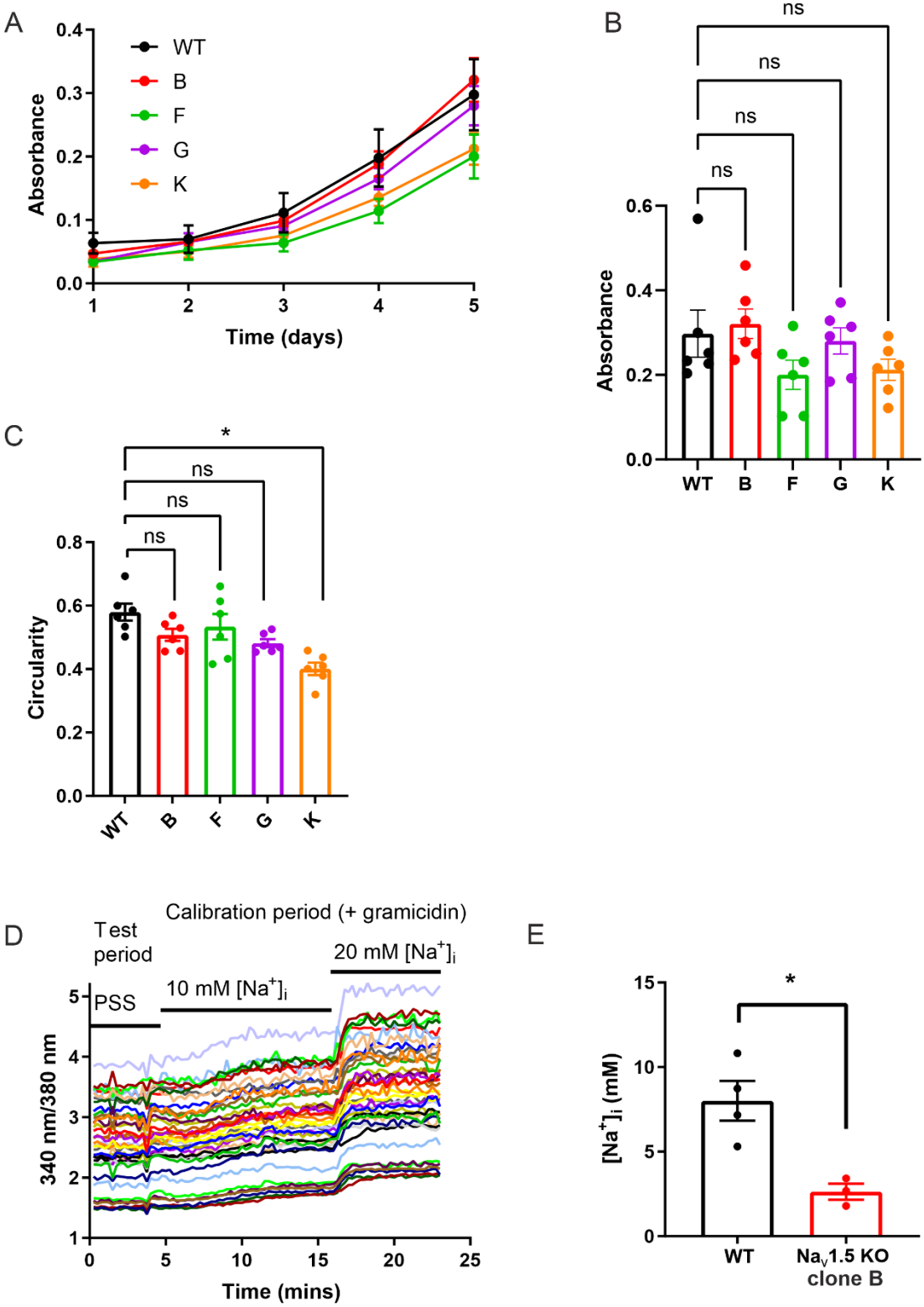
A
Absorbance
Time (days)
WT
B
F
G
K
B
Absorbance
ns
C
Circularity
*
D
Test period
Calibration period (+ gramicidin)
PSS
10 mM [Na+]i
20 mM [Na+]i
340 nm/380 nm
Time (mins)
E
[Na+]i (mM)
WT
Nav1.5 KO clone B

Appendix figure III Characteristics of clonal populations of MDA-MB-231 cells with CRISPR knock out of $Na_v1.5$.
A. Proliferation assay (sulforhodamine B protein assay), examining growth of $Na_v1.5$ knock-out clones compared to control (WT) MDA-MB-231 cells over five days (n = 6 experiments, with 8 wells per condition). **B**. Comparison of growth of clones on day 5 of the proliferation assay in **A**. ($P = 0.13$; n = 6 experiments; one-way ANOVA with Dunnett's multiple comparisons test) **C**. Circularity of cells from each of the $Na_v1.5$ knock-out clones compared to WT MDA-MB-231 cells (n = 6 experiments, each an average of 50 cells; one-way ANOVA with Dunnett's multiple comparisons test). **D**. Example calibration of SBFI-AM measurement of $[Na^+]_i$ in $Na_v1.5$ knock-out MDA-MB-231 cells on a coverslip. Each cell's $[Na^+]_i$ was calibrated separately using a two-point calibration at the end of the test period. **E**. SBFI-AM measurement of $[Na^+]_i$ in $Na_v1.5$ knock-out clone B vs WT MDA-MB-231 cells ($P < 0.05$; n = 3-4 experiments per cell line, each an average of 40 cells; unpaired *t* test). Results are mean ± SEM.

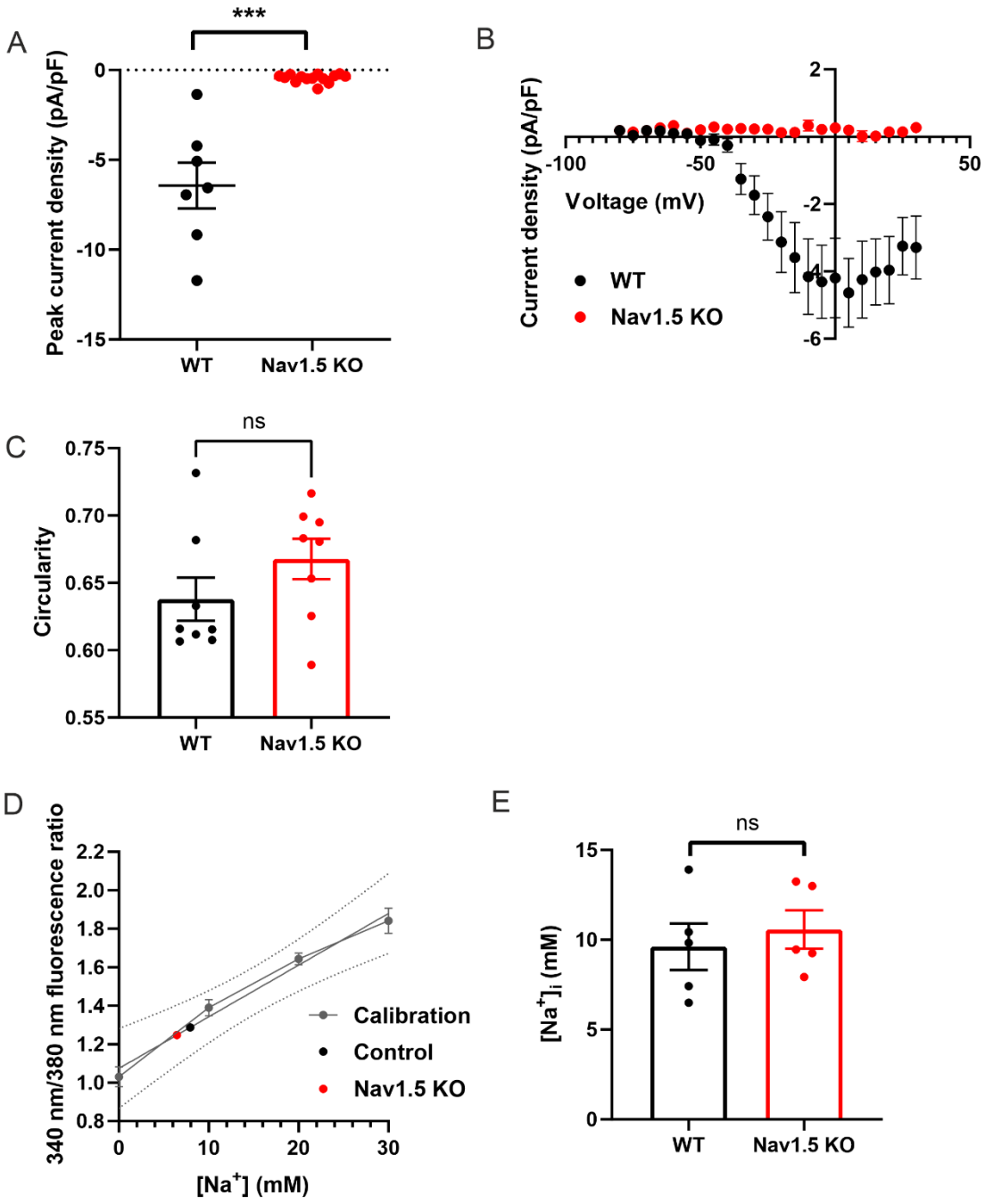

Appendix figure IV Assessment of polyclonal MDA-MB-231 cells with CRISPR knock out of $Na_v1.5$.

A. Peak current density of control (WT) and polyclonal $Na_v1.5$ knock-out MDA-MB-231 cells ($P < 0.0001$; n = 7 WT and 14 KO cells; unpaired *t* test). **B**. Current/voltage relationship of VGSC Na^+ currents in polyclonal $Na_v1.5$ KO and control MDA-MB-231 cells. **C**. Circularity of polyclonal $Na_v1.5$ KO and control MDA-MB-231 cells ($P = 0.20$; n = 8 experiments each of 50 cells; unpaired *t* test). **D**. Average calibrations of SBFI-AM in plate reader experiments, with the averaged results of control and *SCN5A*/$Na_v1.5$ KO cells, showing where these data points lie on the calibration curves. (To calculate $[Na^+]_i$, in each experiment, test wells were compared a calibration curve from the same plate rather than an averaged calibration curve). **E**. SBFI-AM measurement of $[Na^+]_i$ in polyclonal $Na_v1.5$ knock-out and control MDA-MB-231 cells ($P = 0.58$; n = 5 experiments, each an average of 5 wells, each containing 2.5×10^4 cells; unpaired *t* test). Results are mean ± SEM.

III.iv CRISPR project discussion

The finding that $Na_v1.5$ knockout did not cause a detectable change in steady-state $[Na^+]_i$ in a polyclonal population was surprising, since an shRNA construct targeting *SCN5A* was shown to decrease $[Na^+]_i$ in MDA-MB-231 cells, albeit only by 4 mM (Yang *et al.*, 2020). Perhaps it should not be particularly surprising that knock-out of $Na_v1.5$ did not change $[Na^+]_i$ detectably in this study. VGSCs are one of many transport systems affecting the $[Na^+]_i$ and changes in $[Na^+]_i$ are rapidly counteracted by Na^+/K^+ ATPases (NKAs) to maintain homeostasis. It is possible that rather than increasing steady-state $[Na^+]_i$, the main consequence of VGSC activity is increased flux of Na^+ into and out of the cell, with the effect of increasing NKA activity (main hypothesis from Chapter 3).

As shown in this chapter, selection of a clonal population of cells results in a different phenotype from that of a polyclonal population of cells. The fact that the $Na_v1.5$ knock-out clones were not behaving as expected based on the literature suggested that there could be selection for particularly aggressive cells when clonal colonies were grown from single cells, as described in Jurkat T cells (Hanlon *et al.*, 2019). These authors showed that non-genetically edited clonal populations were phenotypically different from the parental population and did not revert back to the parental phenotype. Epigenetic changes caused by single-cell selection were long lasting. Given that clonal selection is a very common technique in cell biology, these findings indicate that experiments using clones should be interpreted with care.

III.v CRISPR project methods

III.v.i Plasmid engineering

Oligonucleotides were designed to create inserts with sticky ends for the guide RNA scaffold to target the previously identified target sequences in *SCN5A* (Appendix III.v.x). The forward and reverse oligonucleotides (1 μl of 100 μM stock) were annealed in 10 μl T4 ligase buffer to make inserts by holding at 95 °C for 5 min then ramping down the

temperature by 0.1 °C per second to 25 °C. The px459 plasmid was restricted with BbsI (Thermo Scientific ER1011) at 37 °C for 16 h then BbsI was inactivated at 65 °C for 20 min. The inserts were then ligated into the BbsI-restricted px459 plasmid using T4 ligase (New England Biolabs M2020) in a reaction containing 1 µl T4 ligase, 20 ng of restricted px459 and 30 pmol annealed primers in a reaction volume of 10 µl. The px459 plasmid was amplified in bacteria and sequenced using primer LKO.1_5 (Appendix III.v.xi) to check for proper insertion of the insert (e.g. Appendix figure V C).

III.v.ii Transformation of bacteria

XL1-blue competent cells (Stratagene) were used for amplification of plasmids. An aliquot of XL1 competent cells was thawed and resuspended, then 50 µl was added to each 14 ml pre-cooled tube. Experimental plasmid DNA (~30 ng) was added to one tube and 0.1 ng of pUC18 (positive control plasmid) DNA was added to the other tube. Tubes were mixed and incubated on ice for 20 minutes, heat pulsed to 42 °C for 45 s, then put back in ice for 2 minutes. 0.9 ml S.O.C. medium (Thermo Scientific) preheated to 42 °C was added to each tube and tubes were incubated at 37 °C for 30 minutes with shaking at 225 rpm. 100-200 µl from each tube was spread onto LB agar plates containing ampicillin at 100 µg/ml.

III.v.iii Bacterial culture

Plates of transformed bacteria were incubated at 37 °C overnight and colonies were picked. Each colony was added to 5 ml LB broth with 100 µg/ml ampicillin in a 14 ml tube. Tubes were incubated at 37 °C for 24 h and shaken at 225 rpm. Glycerol stocks were made by adding 500 µl bacterial suspension to 250 µl glycerol and 250 µl water then frozen at -80 °C.

III.v.iv DNA purification

Plasmid DNA was purified in small quantities for sequencing using a NucleoSpin plasmid clean up kit (Macherey-Nagel). For transfection quality plasmid DNA, a HiSpeed plasmid midiprep kit (Qiagen) was used. Genomic DNA was purified using a NucleoSpin tissue

clean up kit (Macherey-Nagel). PCR products were purified using a Nucleospin Gel and PCR clean up kit (Macherey-Nagel). DNA was assessed for purity and concentration using Nanodrop ND-1000 (Thermo). DNA was used if the concentration was >100 ng/µl and absorbance readings were 260nm/280nm >1.8 and 260nm/230nm >2.0.

III.v.v Transfection of mammalian cells

Cells were grown in 24-well plate wells until they were at 50-80% confluency. JetPRIME transfection reagent (Polyplus) was used for all transfections. 500 ng plasmid DNA was added to 1 µl JetPRIME and made up to 50 µl with JetPRIME buffer in a microcentrifuge tube. The mixture was vortexed, incubated at room temperature for 5 minutes then vortexed again. The mixture was added to a well of cells containing 0.5 ml serum-containing medium and the cells were incubated at 37 °C and 5 % CO_2 for 4 h. After this, the medium was replaced with fresh medium.

III.v.vi Antibiotic treatment and clone selection

Before transfection of plasmids into MDA-MB-231 cells, a puromycin kill curve was performed to choose the optimal dose for selection, and this was determined to be 1 µg/ml puromycin which killed non-transfected cells after 5 days. Following transfection of MDA-MB-231 cells, puromycin treatment (1 µg/ml) was started after 48 h and continued for 7 days until all untransfected cells had died. Wild-type px459, not including the target sequence specific for *SCN5A* was transfected into CRISPR control cells.

Cells were then plated in 96 well plates at a concentration of 5 cells/ml, meaning that each well had on average 1 cell in a volume of 200 µl. Wells were examined daily after seeding. Wells in which there were two or more cells in the first 48 h were excluded, and wells in which there were two or more colonies at later timepoints were excluded. Only clones that had grown from single cells were kept. These were transferred to larger wells when approaching confluency and frozen down.

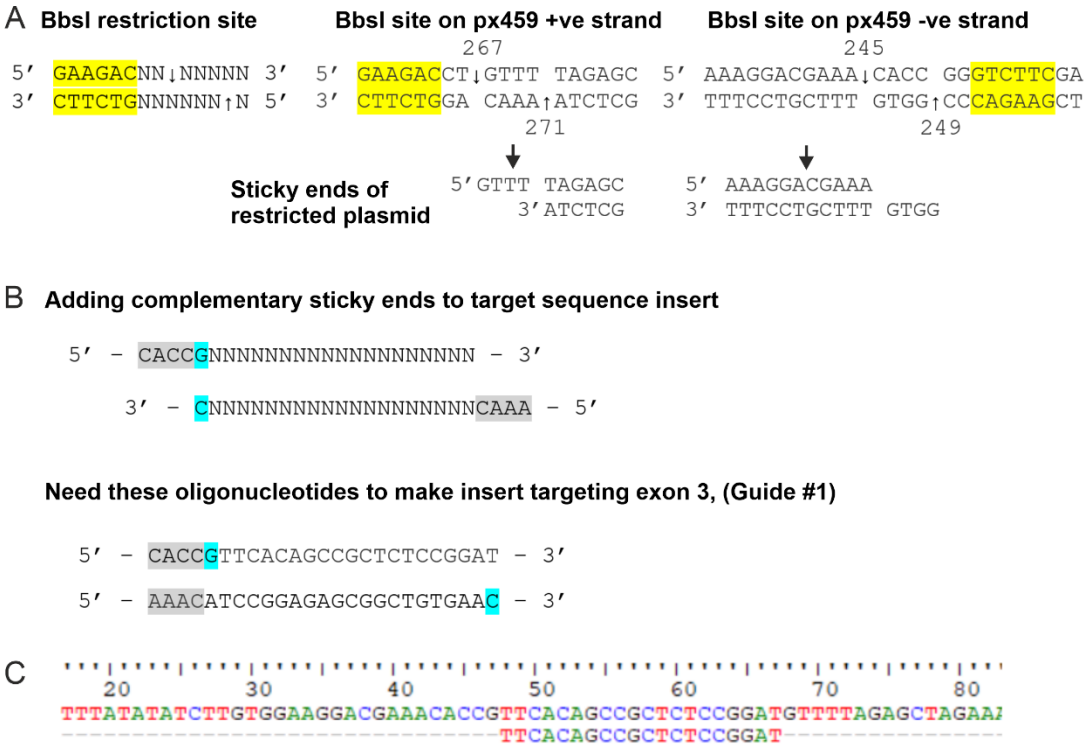

Appendix figure V Creating a plasmid to target exon 3 of *SCN5A*.
A. Restriction site of BbsI which does not cut within the recognised sequence and how this will affect the vector px459, leaving sticky ends. **B**. Design of oligonucleotides needed to create an insert with sticky ends complementary to the BbsI-restricted px459 vector. A G-C base pair (in blue) needs to be added at the 5′ end of the guide sequence for U6 transcription. **C**. Alignment of the exon 3 target sequence against recombinant px459 into which the target sequence for exon 3 of *SCN5A* has been ligated.

III.v.vii Sulforhodamine B proliferation assay

Cells were seeded at 4 x 10^4 cells/well in 5 x 96 well plates, and one plate was fixed every 24 h after seeding. The first plate was fixed after 2 h to allow cells to adhere. To fix plates, 100 µl of 10% TCA was added to the culture medium in each well and the plates were incubated at 4°C for 1 h. The plates were then rinsed gently and dried. At the end of the experiment, 100 µl of 0.057% sulforhodamine B (Sigma S1307) was added to each well and plates were incubated at room temperature for 30 minutes. Plates were then drained, rinsed thoroughly in 1% acetic acid and dried. The dye was solubilized by adding 200 µl of Tris-base solution (pH 10.5) in each well and the absorbance was measured at 510 nm in a BMG Clariostar plate reader. Readings were corrected for absorbance of wells which had contained culture medium but no cells.

III.v.viii Morphology assay

Cells were seeded at 1 x 10^4 cells/well of a 4 well plate, and three days later they were imaged in the plate on Nikon Eclipse TE200 fluorescent microscope using phase contrast brightfield imaging at 20X magnification. Photomicrographs were recorded using a RoleraXR Fast1394 charge-coupled device (CCD) camera (QImaging) and SimplePCI 6.0 software and images were saved as 8-bit .tif files. After blinding the experimenter to cell type, the images were analysed in NIH ImageJ 1.53c (Schindelin *et al.*, 2012), by drawing around the perimeter of each cell and measuring circularity. Each experimental repeat was the mean of 50 cells from one plate.

III.v.ix Primers for sequencing wild-type MDA-MB-231 genome around CRISPR target sequences (and later for sequencing CRISPR-treated cells)

Exon 3: FWD: 5'-CTG ACC TGC CAA ATG TGC TG-3', REV 5'-AAT CAG CGC TAC TCT CAC TCC-3' Expected fragment length 398 bp

Exon 8: FWD: 5'-AGG GAC AGA TCA GCA GCA AC-3', REV: 5'-ACT GGC AGC AGG ATG TCT TC-3' Expected fragment length 662 bp

Exon 9: FWD: 5’-CTT GTG TAG CCT GGA CCC TG-3’, REV: 5’-GGG CAG AAG GGA

GCT TGA TT-3’ Expected fragment length 461 bp

III.v.x Primers used to make inserts for px459 to target exon 3 of *SCN5A*

Exon 3: FWD: 5’-CAC-CGT TCA CAG CCG CTC TCC GGA T-3’, REV: 5’- AAA CAT CCG GAG AGC GGC TGT GAA C-3’

Exon 8: FWD: 5’-CAC CGC AGA GGT GCC GTT GAG C-3’, REV: 5’-AAA CGC TCA AGA ACG GCA CCT CTG C-3’

Exon 9: FWD: 5’-CAC CGG GAG GGC TAC CGG TGC CTA C-3’, REV: 5’-AAA CTT AGG CAC CGG TAG CCC TCC C-3’

III.v.xi Sequencing primer for plasmid

The inserts in px459 were sequenced using the primer LKO.1_5: 5’-GAC TAT CAT ATG

CTT ACC GT-3’ which binds at 172-191 bp, in the U6 promoter region of px459.

III.v.xii Primers for sequencing genome of *SCN5A*-KO MDA-MB-231 cells for off-target effects

Off target 1: FWD: 5’-ACG CAT GTC TGT GAC TCT GG-3’, REV: 5’- ATC TCC CAG GCA GCT GAA AC-3’ Expected fragment length 121 bp

Off target 2: FWD: 5’-ACG CAG GCA AAA CGG ATT TC-3’, REV: 5’-CTG CAC AGA CCC AGA ACA GA-3’ Expected fragment length 600 bp

Off target 3: FWD: 5’-ATC ACA AAG CCA AAG CAC AGT C-3’, REV: 5’-CCT GTT TAA AGT CTC GGA CGC-3’ Expected fragment length 843 bp

Off target 4: FWD: 5’-GTG CAC AAC AAC TTA CGG GG-3’, REV: 5’-AAA TAC CTG GCT GGC ATC TCT T-3’ Expected fragment length 828 bp

Off target 5: FWD: 5’-GGA CCT CTA GGC ACA ACT GA-3’, REV: 5’-AAC GGT ACC TGT ACT GCG AT-3’ Expected fragment length 327 bp

Off target 6: FWD: 5’-GAG CTG CCG GTA CAC TCT AT -3’, REV: 5’-GCC CCT TTA TTT CTC TTG CGG-3’ Expected fragment length 735 bp

Off target 7: FWD: 5’-CAG CTC CAC TGC CTT CTT GA-3’, REV: 5’-TAC CAG AGG GAA GGA TGG GG-3’ Expected fragment length 891 bp

Off target 8: FWD: 5’-TTT AGA CGT GGC GAG AAG CC -3’, REV: 5’-AGG GCA GCA TTA TTG GGT CC-3’ Expected fragment length 757 bp

Off target 9: FWD: 5'-TGA ATA GAG GGA CCA GGG GTT-3', REV: 5'-GCC TCT GAT TCT CTT CGG GA-3' Expected fragment length 818 bp

Off target 10 FWD: 5'-AAG ATG ACC CCA CCC AAA CC-3', REV: 5'- GCC TCT CTC TGT GGT CAA GG-3' Expected fragment length 643 bp

III.v.xiii CRISPR target sequences

Appendix table II Target sequences designed by an online CRISPR design tool for exon 3 of *SCN5A.*
The PAM sequence is in green. (This is necessary to be present in the genome for Cas9 to work but is not included in the target sequence of the gRNA.) The score is a measure of inverse likelihood of off-target effects. CRISPR design tool: CRISPR.mit.edu (Ran *et al.*, 2013)

	Score	Sequence
Guide #1	90	TTCACAGCCGCTCTCCGGAT**GGG**
Guide #2	86	ACTGAGGACATACAAGGCGT**TGG**
Guide #3	86	TCACAGCCGCTCTCCGGATG**GGG**
Guide #4	84	GAGGACATACAAGGCGTTGG**TGG**
Guide #5	84	CTTCACAGCCGCTCTCCGGA**TGG**

III.v.xiv Checking for off-target effects of CRISPR

Appendix table III Top 10 most likely off target effects of Guide #1 for exon 3 of *SCN5A*.

sequence	score	mismatches	UCSC gene	locus
GTCACAGCAGCTCTCCTGATTAG	0.8	3MMs [1:9:17]		chr14:-42040187
ATCACAGGCCCTCTCCGGACCAG	0.7	4MMs [1:8:10:20]	NM_015576	chr3:-55733401
TTAAAAGCCACTCTCCTGATAAG	0.5	4MMs [3:5:10:17]		chr8:-90121333
GTCAGGGCTGCTCTCCGGATAGG	0.5	4MMs [1:5:6:9]	NM_012302	chr1:-82456589
TGGACAGCCCCTCTCCGGCTCAG	0.5	4MMs [2:3:10:19]		chr9:-4228331
TTCACAAGCTCTCTCCTGATTAG	0.4	4MMs [7:8:10:17]		chr6:-138053873
GTCACAGAAGCTCTCCGGTTAAG	0.3	4MMs [1:8:9:19]		chr1:+55411555
TTCACGGACACTCTCCGGGTCGG	0.3	4MMs [6:8:10:19]	NR_033265	chr17:-80348263
TCCACAGAAGCTCTTCGGATTAG	0.3	4MMs [2:8:9:15]		chr7:+34162521
TTCCCATCAGCTCTCCTGATGAG	0.2	4MMs [4:7:9:17]	NM_153676	chr11:-17548340

Appendix IV ImageJ macro for counting nuclei and IHC-stained cells

```
// To run this macro, put RGB TIFFs into a folder called "rawdata"
and specify the path to this folder in line 36 below


// Create a folder called DAPI_output for the nuclei count csv files
to go into and specify the path to this folder in line 37 below


// Create a folder called red_nomask_output for the red particle
count csv files to go into and specify the path to this folder in
line 38 below


// Create a folder called red_mask_output for the red particles
which colocalise with nuclei count csv files to go into and specify
the path to this folder in line 39 below


// change the lower threshold in line 17 to choose just positive
cells. This threshold will be used for all ROIs in the input folder.
Make sure to use the same thresholds for all analyses on the same
section.


function Analysis(input, DAPI_output, red_nomask_output,
red_mask_output, filename) {
      open(input + filename);
      run("Split Channels");
      selectWindow(filename + " (green)");
      close();
      selectWindow(filename + " (blue)");
      setAutoThreshold("Default dark");
      setOption("BlackBackground", false);
      run("Convert to Mask");
```

```
	run("Watershed");
	run("Create Mask");
	run("Analyze Particles...", "size=50-Infinity pixel display
clear include add in_situ");
	saveAs("Results", DAPI_output + filename + ".csv");
	selectWindow(filename + " (red)");
	setAutoThreshold("Default dark");
	run("Threshold...");
	setThreshold(65, 255);
	run("Convert to Mask");run("Convert to Mask");
	run("Analyze Particles...", "size=50-Infinity pixel display
clear include add in_situ");
	saveAs("Results", red_nomask_output + filename + ".csv");
	selectWindow(filename + " (blue)");
	run("Create Selection");
	selectWindow(filename + " (red)");
	run("Restore Selection");
	run("Analyze Particles...", "size=50-Infinity pixel display
clear include add in_situ");
	saveAs("Results", red_mask_output + filename + ".csv");
	close();
}

input = "C:\\Users\\Name\\Folder1\\Folder2\\rawdata\\";
DAPI_output = "C:\\Users\\Name\\Folder1\\Folder2\\DAPIcount\\";
red_nomask_output =
"C:\\Users\\Name\\Folder1\\Folder2\\redNoMaskCount\\";
red_mask_output =
"C:\\Users\\Name\\Folder1\\Folder2\\redMaskCount\\";

list = getFileList(input);

run("Close All");

for (i = 0; i < list.length; i++){
	Analysis(input, DAPI_output, red_nomask_output,
red_mask_output, list[i]);
}

run("Close All");
```

IV.i Thresholds chosen:

Ki67

H261/RN	50-255
H261/LN	65-255
H261/RLN	95-255
H492/RN	100-255
H492/LN	85-255
H492/RLN	85-255
H493/RN	80-255
Mouse 4-10-19	85-255
Mouse 27-9-19	65-255

Caspase 3

H261/RN	61-255
H261/LN	45-255
H261/RLN	105-255
H492/RN	60-255
H492/LN	78-255
H492/RLN	85-255
H493/RN	85-255
Mouse 4-10-19	110-255
Mouse 27-9-19	100-255

Appendix V Assessment of SBFI-AM use in emission peak shift mode

In order to measure absolute $[Na^+]_i$ accurately in tissue, it would be necessary to use SBFI-AM with confocal microscopy. However, most confocal microscopes only have one UV laser, so dual excitation at 340 and 380 nm is not possible. Minta and Tsien showed that the emission peak for SBFI-AM shifts depending on Na^+ binding (Minta & Tsien, 1989). To test the feasibility of using SBFI-AM to detect $[Na^+]_i$ in this way, to allow its use with confocal microscopy, I examined the emission profile of SBFI at different $[Na^+]_i$.

V.i Determination of optimal excitation wavelength for SBFI-AM

MDA-MB-231 cells (3×10^4) were seeded into wells of an 8 well chamber slide (Ibidi 80807). Cells were incubated with 5 μM SBFI with 0.05% Pluronic F-127 in DMEM for 2 hours at 37 °C. Slides were rinsed twice with PBS and left in PBS for 30 minutes for remaining esterified dye to diffuse out of the cells. The chamber slide was viewed on a Zeiss LSM 780 multiphoton microscope. The optimal excitation wavelength was determined by

exciting at 700, 720, 740, 760, 780 or 800 nm (approximately double the normal UV excitation wavelength). The brightest emission was found with 720 nm excitation so this was chosen for the emission profile. In one well, the PSS was replaced with 0 mM Na^+ with K^+ as the replacement ion, and in another well it was replaced with ordinary 144 mM Na^+ PSS. Both of these solutions contained 20 μM gramidicin D (Sigma G5002) to equilibrate intracellular and extracellular [Na^+]. Fluorescence was collected in 8.7 nm wide bins between 417 nm and 678 nm from each well. 14 cells were chosen from each well and average fluorescence from each cell was measured. There was negligible autofluorescence. As can be seen in Appendix figure VI there was only a 10 nm shift of emission peak with a 144 mM change in $[Na^+]_i$. Given that differences in $[Na^+]_i$ would be expected to be 10 mM or less, it was decided that emission peak shift would not be a useful to measure $[Na^+]_i$ in this study.

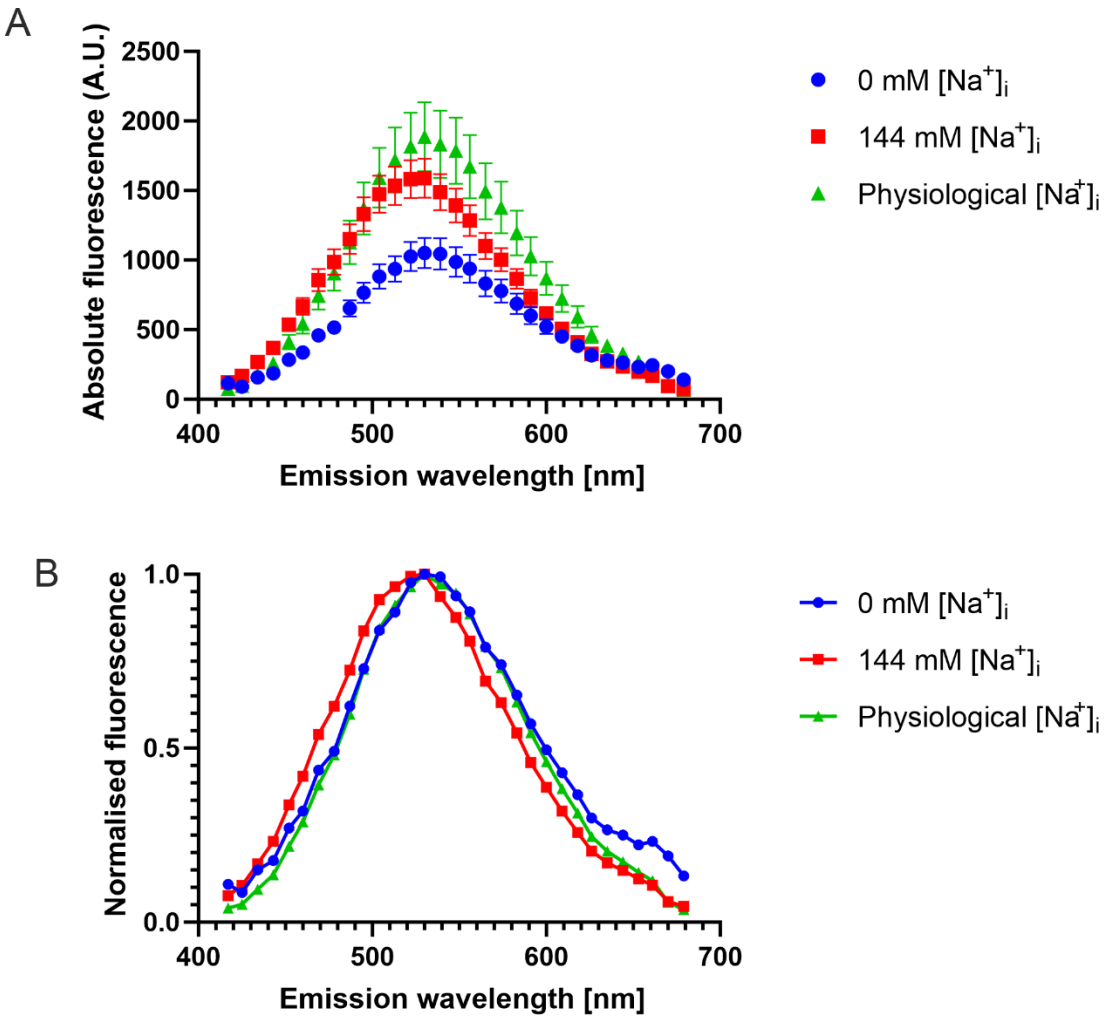

Appendix figure VI. Emission profile for SBFI-AM.
A. Absolute fluorescence with multiphoton excitation at 720 nm of SBFI-loaded MDA-MB-231 cells containing 0 mM, physiological or 144 mM intracellular [Na^+]. **B**. Fluorescence as in **A**. but normalised to maximal fluorescence to better view the wavelength at which there is maximal emission.

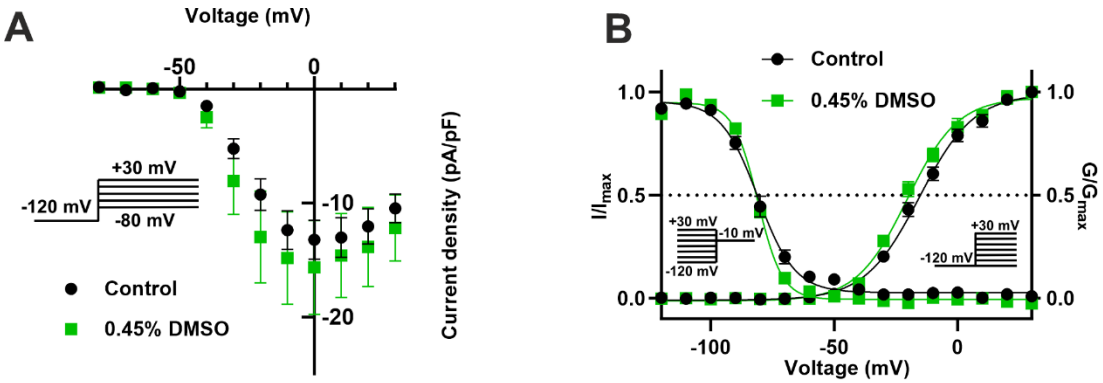

Appendix figure VII. Effect of 0.45% DMSO on VGSC current-voltage relationship and gating in MDA-MB-231 cells.
A. Current-voltage (I-V) plots of Na+ currents in MDA-MB-231 cells in physiological saline solution (PSS; black circles) and in PSS with 0.45% DMSO (0.45% DMSO; green squares). Currents were elicited using 10 mV depolarising steps from -80 to +30 mV for 30 ms, from a holding potential of -120 mV. Results are mean ± SEM (n = 13-17). **B**. Activation and steady-state inactivation in physiological saline solution (PSS; black circles) and in PSS with 0.45% DMSO (0.45% DMSO; green squares). For activation, normalised conductance (G/Gmax) was calculated from the current data and plotted as a function of voltage. For steady-state inactivation, normalised current (I/Imax), elicited by 50 ms test pulses at -10 mV following 250 ms conditioning voltage pulses between -120 mV and +30 mV, applied from a holding potential of -120 mV, was plotted as a function of the prepulse voltage. Results are mean ± SEM (n = 10-13). Activation and inactivation curves are fitted with Boltzmann functions.

Abbreviations

ANOVA	Analysis of variance
Arp2/3	Actin-related protein 2/3
ASIC	Acid-sensing ion channel
ATP	Adenosine triphosphate
BAM	Binary alignment map
BRCA1	Breast cancer type 1 susceptibility protein
CAM	Cell adhesion molecule
CaM	Calmodulin
cAMP	Cyclic adenosine monophosphate
CCD	Charge coupled device
CD44	Cluster of differentiation 44
CNS	Central nervous system
Cx43	Connexin 43
DAPI	4',6-diamidino-2-phenylindole
DEG	Differentially expressed genes
DMEM	Dulbecco's modified eagle medium
DMSO	Dimethyl sulfoxide
DO	Disease ontology
ECM	Extracellular matrix
EDTA	Ethylenediaminetetraacetic acid
EGF	Epidermal growth factor
EGFR	Epidermal growth factor receptor
EMT	Epithelial to mesenchymal transition
ENaC	Epithelial Na^+ channel
ER	Endoplasmic reticulum
ERK	Extracellular-signal-regulated kinase
FASTQ	Text file containing sequence information and sequencing quality scores
FBS	Foetal bovine serum
FDR	False discovery rate
FPKM	Fragments per kilobase of exon per million mapped fragments
FRET	Förster resonance energy transfer
GFP	Green fluorescent protein
GO	Gene ontology
HEK-293 cells	Human embryonic kidney cells
HEPES	4-(2-hydroxyethyl)-1-piperazineethanesulfonic acid
HER2	Human epidermal growth factor receptor 2
HRP	Horseradish peroxidase
IC50	The concentration of drug at which half of its maximal effect occurs
Ig	Immunoglobulin
IL	Interleukin
IP3	Inositol 1,4,5-trisphosphate
IPS	Intracellular pipette solution
ISME	Ion-sensitive microelectrode
JAK	Janus kinase
k	Slope factor
kDa	Kilodalton
LAMP	Lysosome associated membrane protein
MAPK	Mitogen-activated protein kinase
MCF-7	Michigan cancer foundation-7
MDA-MB-231	M.D. Anderson metastatic breast cancer 231
MEK	Mitogen-activated protein kinase kinase
MMP	Matrix metalloproteinase

MRI	Magnetic resonance imaging
$[Na^+]_i$	Intracellular Na+ concentration
$[Na^+]_e$	Extracellular Na+ concentration
NCX	Na^+/Ca^{2+} exchanger
NFAT5	Nuclear factor of activated T cells 5
NHE1	Na^+/H^+ exchanger
NKA	Na^+/K^+ ATPase
NMDG	N-methyl-d-glucamine
PB	Phosphate buffer
PBS	Phosphate buffered saline
PBTGS	PB, Triton X-100, goat serum
PCR	Polymerase chain reaction
PFA	Paraformaldehyde
pH_i	Intracellular pH
pH_e	Extracellular pH
PI3K	Phosphotidylinositol-3-kinase
PKA	Protein kinase A
PKN-γ	Protein kinase N-gamma
PNS	Peripheral nervous system
PR	Progesterone receptor
PSS	Physiological saline solution
PTEN	Phosphate and tensin homologue
PyMT	polyoma middle T
qPCR	Real-time, quantitative PCR
Rac1	Member of the Rho family of GTPases
ROI	Region of interest
ROS	Reactive oxygen species
SEM	Standard error of the mean
shRNA	Small hairpin RNA
SIK1	Salt-inducible kinase 1
Src	A tyrosine kinase proto-oncogene
TNBC	Triple negative breast cancer
TNF	Tumour necrosis factor
T_p	Time to peak
TRP	Transient receptor potential
TTX	Tetrodotoxin
$V_{1/2}$	The voltage at which half-maximal conductance or availability occurs
V_a	Activation voltage
VEGF	Vascular endothelial growth factor
VGCC	Voltage-gated Ca^{2+} channel
VGSC	Voltage-gated Na^+ channel
V_h	Holding voltage
V_m	Plasma membrane potential
V_{rev}	Reversal potential

8 References

Abdul M & Hoosein N. (2002). Voltage-gated sodium ion channels in prostate cancer: expression and activity. *Anticancer Res* **22,** 1727-1730.

Abdul M, Ramlal S & Hoosein N. (2008). Ryanodine receptor expression correlates with tumor grade in breast cancer. *Pathol Oncol Res* **14,** 157-160.

Abdul M, Santo A & Hoosein N. (2003). Activity of potassium channel-blockers in breast cancer. *Anticancer Res* **23,** 3347-3351.

Abriel H & Kass RS. (2005). Regulation of the voltage-gated cardiac sodium channel Nav1.5 by interacting proteins. *Trends Cardiovasc Med* **15,** 35-40.

Adachi K, Toyota M, Sasaki Y, Yamashita T, Ishida S, Ohe-Toyota M, Maruyama R, Hinoda Y, Saito T, Imai K, Kudo R & Tokino T. (2004). Identification of SCN3B as a novel p53-inducible proapoptotic gene. *Oncogene* **23,** 7791-7798.

Aggarwal V, Tuli HS, Varol A, Thakral F, Yerer MB, Sak K, Varol M, Jain A, Khan MA & Sethi G. (2019). Role of Reactive Oxygen Species in Cancer Progression: Molecular Mechanisms and Recent Advancements. *Biomolecules* **9**.

Agullo-Pascual E, Lin X, Leo-Macias A, Zhang M, Liang FX, Li Z, Pfenniger A, Lübkemeier I, Keegan S, Fenyö D, Willecke K, Rothenberg E & Delmar M. (2014). Super-resolution imaging reveals that loss of the C-terminus of connexin43 limits microtubule plus-end capture and NaV1.5 localization at the intercalated disc. *Cardiovasc Res* **104,** 371-381.

Ahern CA, Zhang JF, Wookalis MJ & Horn R. (2005). Modulation of the Cardiac Sodium Channel NaV1.5 by Fyn, a Src Family Tyrosine Kinase. *Circulation research* **96**.

Ahmadzadeh M, Johnson LA, Heemskerk B, Wunderlich JR, Dudley ME, White DE & Rosenberg SA. (2009). Tumor antigen-specific CD8 T cells infiltrating the tumor express high levels of PD-1 and are functionally impaired. *Blood* **114,** 1537-1544.

Ahmed AR. (2016). HER2 expression is a strong independent predictor of nodal metastasis in breast cancer. *J Egypt Natl Canc Inst* **28,** 219-227.

Akl H & Bultynck G. (2013). Altered Ca(2+) Signaling in Cancer Cells: Proto-Oncogenes and Tumor Suppressors Targeting IP3 Receptors. *Biochimica et biophysica acta* **1835**.

Aksentijevic D, O'Brien BA, Eykyn TR & Shattock MJ. (2018). Is there a causal link between intracellular Na elevation and metabolic remodelling in cardiac hypertrophy? *Biochem Soc Trans* **46,** 817-827.

Al-Sabi A, Shamotienko O, Dhochartaigh SN, Muniyappa N, Le Berre M, Shaban H, Wang J, Sack JT & Dolly JO. (2010). Arrangement of Kv1 α subunits dictates sensitivity to tetraethylammonium. *J Gen Physiol* **136,** 273-282.

Allen DH, Lepple-Wienhues A & Cahalan MD. (1997). Ion channel phenotype of melanoma cell lines. *J Membr Biol* **155,** 27-34.

Allred DC, Harvey JM, Berardo M & Clark GM. (1998). Prognostic and predictive factors in breast cancer by immunohistochemical analysis. *Mod Pathol* **11,** 155-168.

Almeida L, Falcao A, Maia J, Mazur D, Gellert M & Soares-da-Silva P. (2005). Single-dose and steady-state pharmacokinetics of eslicarbazepine acetate (BIA 2-093) in healthy elderly and young subjects. *J Clin Pharmacol* **45,** 1062-1066.

Alzheimer C, Schwindt PC & Crill WE. (1993). Modal gating of Na+ channels as a mechanism of persistent Na+ current in pyramidal neurons from rat and cat sensorimotor cortex. *J Neurosci* **13,** 660-673.

Aman TK, Grieco-Calub TM, Chen C, Rusconi R, Slat EA, Isom LL & Raman IM. (2009). Regulation of persistent Na current by interactions between β subunits of voltage-gated Na channels. *J Neurosci* **29,** 2027-2042.

Amara S, Alotaibi D & Tiriveedhi V. (2016). NFAT5/STAT3 interaction mediates synergism of high salt with IL-17 towards induction of VEGF-A expression in breast cancer cells. *Oncol Lett* **12,** 933-943.

Amith SR, Fong S, Baksh S & Fliegel L. (2015). Na (+)/H (+)exchange in the tumour microenvironment: does NHE1 drive breast cancer carcinogenesis? *Int J Dev Biol* **59,** 367-377.

An WF, Bowlby MR, Betty M, Cao J, Ling HP, Mendoza G, Hinson JW, Mattsson KI, Strassle BW, Trimmer JS & Rhodes KJ. (2000). Modulation of A-type potassium channels by a family of calcium sensors. *Nature* **403,** 553-556.

Anders S & Huber W. (2010). Differential expression analysis for sequence count data. *Genome Biol* **11,** R106.

Anderson JD, Hansen TP, Lenkowski PW, Walls AM, Choudhury IM, Schenck HA, Friehling M, Holl GM, Patel MK, Sikes RA & Brown ML. (2003). Voltage-gated sodium channel blockers as cytostatic inhibitors of the androgen-independent prostate cancer cell line PC-3. *Mol Cancer Ther* **2,** 1149-1154.

Andrikopoulos P, Fraser SP, Patterson L, Ahmad Z, Burcu H, Ottaviani D, Diss JK, Box C, Eccles SA & Djamgoz MB. (2011). Angiogenic Functions of Voltage-gated Na+ Channels in Human Endothelial Cells: Modulation of vascular endothelial growth factor (VEGF) signaling. *J Biol Chem* **286,** 16846-16860.

Anemone A, Consolino L, Conti L, Irrera P, Hsu MY, Villano D, Dastrù W, Porporato PE, Cavallo F & Longo DL. (2021). Tumour acidosis evaluated in vivo by MRI-CEST pH imaging reveals breast cancer metastatic potential. *Br J Cancer* **124,** 207-216.

Arcangeli A & Becchetti A. (2017). hERG Channels: From Antitargets to Novel Targets for Cancer Therapy. *Clin Cancer Res* **23,** 3-5.

Armstrong CM & Bezanilla F. (1977). Inactivation of the sodium channel. II. Gating current experiments. *J Gen Physiol* **70,** 567-590.

Ashby BS. (1966). pH studies in human malignant tumours. *Lancet* **288,** 312-315.

Attwell D & Laughlin SB. (2001). An energy budget for signaling in the grey matter of the brain. *J Cereb Blood Flow Metab* **21,** 1133-1145.

Avula UMR, Dridi H, Chen BX, Yuan Q, Katchman AN, Reiken SR, Desai AD, Parsons S, Baksh H, Ma E, Dasrat P, Ji R, Lin Y, Sison C, Lederer WJ, Joca HC, Ward C, Greiser M, Marks AR, Marx SO & Wan EY. (2021). Attenuating persistent sodium current induced atrial myopathy and fibrillation by preventing mitochondrial oxidative stress. *JCI Insight*.

Aydar E, Stratton D, Fraser SP, Djamgoz MB & Palmer C. (2016). Sigma-1 receptors modulate neonatal Na. *Eur Biophys J* **45,** 671-683.

Balasubramaniam S, Gopalakrishnapillai A, Gangadharan V, Duncan R & Barwe S. (2015). Sodium-Calcium Exchanger 1 Regulates Epithelial Cell Migration via Calcium-dependent Extracellular Signal-regulated Kinase Signaling. *J Biol Chem* **290,** 12463-12473.

Balasubramaniam SL, Gopalakrishnapillai A, Petrelli NJ & Barwe SP. (2017). Knockdown of sodium-calcium exchanger 1 induces epithelial-to-mesenchymal transition in kidney epithelial cells. *J Biol Chem* **292,** 11388-11399.

Balasuriya D, Stewart AP, Crottès D, Borgese F, Soriani O & Edwardson JM. (2012). The sigma-1 receptor binds to the Nav1.5 voltage-gated Na+ channel with 4-fold symmetry. *J Biol Chem* **287,** 37021-37029.

Banerjee D. (2016). Connexin's Connection in Breast Cancer Growth and Progression. *Int J Cell Biol* **2016,** 9025905.

Bao L. (2015). Trafficking regulates the subcellular distribution of voltage-gated sodium channels in primary sensory neurons. *Mol Pain* **11,** 61.

Bao Y, Willis BC, Frasier CR, Lopez-Santiago LF, Lin X, Ramos-Mondragón R, Auerbach DS, Chen C, Wang Z, Anumonwo J, Valdivia HH, Delmar M, Jalife J & Isom LL. (2016). Scn2b Deletion in Mice Results in Ventricular and Atrial Arrhythmias. *Circ Arrhythm Electrophysiol* **9**.

Barann M, Göthert M, Brüss M & Bönisch H. (1999). Inhibition by steroids of [14C]-guanidinium flux through the voltage-gated sodium channel and the cation channel of the 5-HT3 receptor of N1E-115 neuroblastoma cells. *Naunyn Schmiedebergs Arch Pharmacol* **360,** 234-241.

Barker A, Jaffe L & Vanable J. (1982). The Glabrous Epidermis of Cavies Contains a Powerful Battery. *The American journal of physiology* **242**.

Barratt LJ. (1976). The effect of amiloride on the transepithelial potential difference of the distal tubule of the rat kidney. *Pflugers Arch* **361,** 251-254.

Barrett T, Riemer F, McLean MA, Kaggie J, Robb F, Tropp JS, Warren A, Bratt O, Shah N, Gnanapragasam VJ, Gilbert FJ, Graves MJ & Gallagher FA. (2018). Quantification of Total and Intracellular Sodium Concentration in Primary Prostate Cancer and Adjacent Normal Prostate Tissue With Magnetic Resonance Imaging. *Invest Radiol* **53,** 450-456.

Barry PH. (1994). JPCalc, a software package for calculating liquid junction potential corrections in patch-clamp, intracellular, epithelial and bilayer measurements and for correcting junction potential measurements. *J Neurosci Methods* **51,** 107-116.

Bellone M, Calcinotto A, Filipazzi P, De Milito A, Fais S & Rivoltini L. (2013). The acidity of the tumor microenvironment is a mechanism of immune escape that can be overcome by proton pump inhibitors. *Oncoimmunology* **2,** e22058.

Benjamini Y & Hochberg Y. (1995). Controlling the false discovery rate: a practical and powerful approach to multiple testing. *J Royal Statist Soc B* **57,** 289-300.

Bennett ES, Smith BA & Harper JM. (2004). Voltage-gated Na^+ channels confer invasive properties on human prostate cancer cells. *Pflugers Arch* **447,** 908-914.

Berga SE & Neville MC. (1985). Sodium and potassium distribution in the lactating mouse mammary gland in vivo. *J Physiol* **361,** 219-230.

Berret E, Nehmé B, Henry M, Toth K, Drolet G & Mouginot D. (2013). Regulation of central Na+ detection requires the cooperative action of the NaX channel and α1 Isoform of Na+/K+-ATPase in the Na+-sensor neuronal population. *J Neurosci* **33,** 3067-3078.

Bers D & Ginsburg K. (2007). Na:Ca Stoichiometry and Cytosolic Ca-dependent Activation of NCX in Intact Cardiomyocytes. *Annals of the New York Academy of Sciences* **1099**.

Bezanilla F & Armstrong CM. (1977). Inactivation of the sodium channel. I. Sodium current experiments. *J Gen Physiol* **70,** 549-566.

Bialer M & Soares-da-Silva P. (2012). Pharmacokinetics and drug interactions of eslicarbazepine acetate. *Epilepsia* **53,** 935-946.

Blesneac I, Chemin J, Bidaud I, Huc-Brandt S, Vandermoere F & Lory P. (2015). Phosphorylation of the Cav3.2 T-type calcium channel directly regulates its gating properties. *Proc Natl Acad Sci U S A* **112,** 13705-13710.

Boedtkjer E, Moreira JMA, Mele M, Vahl P, Wielenga VT, Christiansen PM, Jensen VED, Pedersen SF & Aalkjaer C. (2013). Contribution of Na+,HCO3(-)-cotransport to

cellular pH control in human breast cancer: a role for the breast cancer susceptibility locus NBCn1 (SLC4A7). *Int J Cancer* **132,** 1288-1299.

Boehmer C, Wilhelm V, Palmada M, Wallisch S, Henke G, Brinkmeier H, Cohen P, Pieske B & Lang F. (2003). Serum and glucocorticoid inducible kinases in the regulation of the cardiac sodium channel SCN5A. *Cardiovasc Res* **57,** 1079-1084.

Bon E, Driffort V, Gradek F, Martinez-Caceres C, Anchelin M, Pelegrin P, Cayuela ML, Marionneau-Lambot S, Oullier T, Guibon R, Fromont G, Gutierrez-Pajares JL, Domingo I, Piver E, Moreau A, Burlaud-Gaillard J, Frank PG, Chevalier S, Besson P & Roger S. (2016). SCN4B acts as a metastasis-suppressor gene preventing hyperactivation of cell migration in breast cancer. *Nat Commun* **7,** 13648.

Bonifacio MJ, Sheridan RD, Parada A, Cunha RA, Patmore L & Soares-da-Silva P. (2001). Interaction of the novel anticonvulsant, BIA 2-093, with voltage-gated sodium channels: comparison with carbamazepine. *Epilepsia* **42,** 600-608.

Bordey A & Sontheimer H. (1998). Electrophysiological properties of human astrocytic tumor cells In situ: enigma of spiking glial cells. *J Neurophysiol* **79,** 2782-2793.

Borgens R, Vanable J & Jaffe L. (1977). Bioelectricity and Regeneration: Large Currents Leave the Stumps of Regenerating Newt Limbs. *Proceedings of the National Academy of Sciences of the United States of America* **74**.

Borowiec AS, Hague F, Harir N, Guenin S, Guerineau F, Gouilleux F, Roudbaraki M, Lassoued K & Ouadid-Ahidouch H. (2007). IGF-1 activates hEAG K(+) channels through an Akt-dependent signaling pathway in breast cancer cells: role in cell proliferation. *J Cell Physiol* **212,** 690-701.

Boscardin E, Alijevic O, Hummler E, Frateschi S & Kellenberger S. (2016). The function and regulation of acid-sensing ion channels (ASICs) and the epithelial Na channel (ENaC): IUPHAR Review 19. *Br J Pharmacol* **173,** 2671-2701.

Bourguignon LY, Singleton PA & Diedrich F. (2004). Hyaluronan-CD44 Interaction With Rac1-dependent Protein Kinase N-gamma Promotes Phospholipase Cgamma1 Activation, Ca(2+) Signaling, and Cortactin-Cytoskeleton Function Leading to Keratinocyte Adhesion and Differentiation. *The Journal of biological chemistry* **279**.

Bourguignon LY, Zhu H, Shao L & Chen YW. (2001). CD44 Interaction With c-Src Kinase Promotes Cortactin-Mediated Cytoskeleton Function and Hyaluronic Acid-Dependent Ovarian Tumor Cell Migration. *The Journal of biological chemistry* **276**.

Bouza AA, Edokobi N, Hodges SL, Pinsky AM, Offord J, Piao L, Zhao YT, Lopatin AN, Lopez-Santiago LF & Isom LL. (2021). Sodium channel β1 subunits participate in regulated intramembrane proteolysis-excitation coupling. *JCI Insight* **6**.

Brackenbury WJ. (2012). Voltage-gated sodium channels and metastatic disease. *Channels (Austin)* **6,** 352-361.

Brackenbury WJ, Calhoun JD, Chen C, Miyazaki H, Nukina N, Oyama F, Ranscht B & Isom LL. (2010). Functional reciprocity between Na+ channel Nav1.6 and beta1 subunits in the coordinated regulation of excitability and neurite outgrowth. *Proc Natl Acad Sci U S A* **107,** 2283-2288.

Brackenbury WJ, Chioni AM, Diss JK & Djamgoz MB. (2007). The neonatal splice variant of Nav1.5 potentiates in vitro invasive behaviour of MDA-MB-231 human breast cancer cells. *Breast Cancer Res Treat* **101,** 149-160.

Brackenbury WJ, Davis TH, Chen C, Slat EA, Detrow MJ, Dickendesher TL, Ranscht B & Isom LL. (2008). Voltage-gated Na+ channel beta1 subunit-mediated neurite outgrowth requires Fyn kinase and contributes to postnatal CNS development in vivo. *J Neurosci* **28,** 3246-3256.

Brackenbury WJ & Djamgoz MB. (2006). Activity-dependent regulation of voltage-gated Na^+ channel expression in Mat-LyLu rat prostate cancer cell line. *J Physiol* **573,** 343-356.

Brackenbury WJ & Djamgoz MB. (2007). Nerve growth factor enhances voltage-gated Na+ channel activity and Transwell migration in Mat-LyLu rat prostate cancer cell line. *J Cell Physiol* **210,** 602-608.

Brackenbury WJ & Isom LL. (2011). Na Channel β Subunits: Overachievers of the Ion Channel Family. *Front Pharmacol* **2,** 53.

Bray F, Ferlay J, Soerjomataram I, Siegel RL, Torre LA & Jemal A. (2018). Global cancer statistics 2018: GLOBOCAN estimates of incidence and mortality worldwide for 36 cancers in 185 countries. *CA Cancer J Clin* **68,** 394-424.

Bray F, McCarron P & Parkin DM. (2004). The Changing Global Patterns of Female Breast Cancer Incidence and Mortality. *Breast cancer research : BCR* **6**.

Breuer EK, Fukushiro-Lopes D, Dalheim A, Burnette M, Zartman J, Kaja S, Wells C, Campo L, Curtis KJ, Romero-Moreno R, Littlepage LE, Niebur GL, Hoskins K, Nishimura MI & Gentile S. (2019). Potassium channel activity controls breast cancer metastasis by affecting β-catenin signaling. *Cell Death Dis* **10,** 180.

Brisson L, Driffort V, Benoist L, Poet M, Counillon L, Antelmi E, Rubino R, Besson P, Labbal F, Chevalier S, Reshkin SJ, Gore J & Roger S. (2013). NaV1.5 Na(+) channels allosterically regulate the NHE-1 exchanger and promote the activity of breast cancer cell invadopodia. *J Cell Sci* **126,** 4835-4842.

Brisson L, Gillet L, Calaghan S, Besson P, Le Guennec JY, Roger S & Gore J. (2011). Na(V)1.5 enhances breast cancer cell invasiveness by increasing NHE1-dependent H(+) efflux in caveolae. *Oncogene* **30,** 2070-2076.

Buchanan PJ & McCloskey KD. (2016). CaV channels and cancer: canonical functions indicate benefits of repurposed drugs as cancer therapeutics. *Eur Biophys J* **45,** 621-633.

Bultynck G & Campanella M. (2017). Tumor Suppressive Ca 2+ Signaling Is Driven by IP 3 Receptor Fitness. *Cell stress* **1**.

Busco G, Cardone RA, Greco MR, Bellizzi A, Colella M, Antelmi E, Mancini MT, Dell'Aquila ME, Casavola V, Paradiso A & Reshkin SJ. (2010). NHE1 promotes invadopodial ECM proteolysis through acidification of the peri-invadopodial space. *FASEB J* **24,** 3903-3915.

Bushnell B. (2021). BBTools. sourceforge.net/projects/bbmap/.

Calcinotto A, Filipazzi P, Grioni M, Iero M, De Milito A, Ricupito A, Cova A, Canese R, Jachetti E, Rossetti M, Huber V, Parmiani G, Generoso L, Santinami M, Borghi M, Fais S, Bellone M & Rivoltini L. (2012). Modulation of microenvironment acidity reverses anergy in human and murine tumor-infiltrating T lymphocytes. *Cancer Res* **72,** 2746-2756.

Cameron IL, Smith NK, Pool TB & Sparks RL. (1980). Intracellular concentration of sodium and other elements as related to mitogenesis and oncogenesis in vivo. *Cancer Res* **40,** 1493-1500.

Campbell TM, Main MJ & Fitzgerald EM. (2013). Functional expression of the voltage-gated Na(+)-channel Nav1.7 is necessary for EGF-mediated invasion in human non-small cell lung cancer cells. *J Cell Sci* **126,** 4939-4949.

Cardone RA, Casavola V & Reshkin SJ. (2005). The role of disturbed pH dynamics and the Na+/H+ exchanger in metastasis. *Nat Rev Cancer* **5,** 786-795.

Cardoso F, Costa A, Norton L, Cameron D, Cufer T, Fallowfield L, Francis P, Gligorov J, Kyriakides S, Lin N, Pagani O, Senkus E, Thomssen C, Aapro M, Bergh J, Di Leo A, El Saghir N, Ganz PA, Gelmon K, Goldhirsch A, Harbeck N, Houssami N, Hudis C, Kaufman B, Leadbeater M, Mayer M, Rodger A, Rugo H, Sacchini V, Sledge G, van't Veer L, Viale G, Krop I & Winer E. (2012). 1st International consensus guidelines for advanced breast cancer (ABC 1). *Breast* **21,** 242-252.

Carrithers MD, Chatterjee G, Carrithers LM, Offoha R, Iheagwara U, Rahner C, Graham M & Waxman SG. (2009). Regulation of podosome formation in macrophages by a splice variant of the sodium channel SCN8A. *J Biol Chem* **284,** 8114-8126.

Carrithers MD, Dib-Hajj S, Carrithers LM, Tokmoulina G, Pypaert M, Jonas EA & Waxman SG. (2007). Expression of the voltage-gated sodium channel NaV1.5 in the macrophage late endosome regulates endosomal acidification. *J Immunol* **178,** 7822-7832.

Catacuzzeno L, Fioretti B & Franciolini F. (2012). Expression and Role of the Intermediate-Conductance Calcium-Activated Potassium Channel KCa3.1 in Glioblastoma. *J Signal Transduct* **2012,** 421564.

Chatton JY, Marquet P & Magistretti PJ. (2000). A quantitative analysis of L-glutamate-regulated Na+ dynamics in mouse cortical astrocytes: implications for cellular bioenergetics. *Eur J Neurosci* **12,** 3843-3853.

Chen J, Lu L, Feng Y, Wang H, Dai L, Li Y & Zhang P. (2011). PKD2 mediates multi-drug resistance in breast cancer cells through modulation of P-glycoprotein expression. *Cancer Lett* **300,** 48-56.

Chen R, Lai UH, Zhu L, Singh A, Ahmed M & Forsyth NR. (2018). Reactive Oxygen Species Formation in the Brain at Different Oxygen Levels: The Role of Hypoxia Inducible Factors. *Front Cell Dev Biol* **6,** 132.

Chioni AM, Brackenbury WJ, Calhoun JD, Isom LL & Djamgoz MB. (2009). A novel adhesion molecule in human breast cancer cells: voltage-gated Na+ channel beta1 subunit. *Int J Biochem Cell Biol* **41,** 1216-1227.

Chioni AM, Shao D, Grose R & Djamgoz MB. (2010). Protein kinase A and regulation of neonatal Nav1.5 expression in human breast cancer cells: activity-dependent positive feedback and cellular migration. *Int J Biochem Cell Biol* **42,** 346-358.

Clarke RJ, Humphrey PA, Lüpfert C, Apell HJ & Cornelius F. (2003). Kinetic investigations of the mechanism of the rate-determining step of the Na+,K+-ATPase pump cycle. *Ann N Y Acad Sci* **986,** 159-162.

Cock PJ, Fields CJ, Goto N, Heuer ML & Rice PM. (2010). The Sanger FASTQ file format for sequences with quality scores, and the Solexa/Illumina FASTQ variants. *Nucleic Acids Res* **38,** 1767-1771.

Collier DM & Snyder PM. (2009). Extracellular protons regulate human ENaC by modulating Na+ self-inhibition. *J Biol Chem* **284,** 792-798.

Cone CD, Jr. (1970). Variation of the transmembrane potential level as a basic mechanism of mitosis control. *Oncology* **24,** 438-470.

Cone CD, Jr. & Tongier M, Jr. (1971). Control of somatic cell mitosis by simulated changes in the transmembrane potential level. *Oncology* **25,** 168-182.

Consortium U. (2019). UniProt: a worldwide hub of protein knowledge. *Nucleic Acids Res* **47,** D506-D515.

Couchonnal LF & Anderson ME. (2008). The role of calmodulin kinase II in myocardial physiology and disease. *Physiology (Bethesda)* **23,** 151-159.

Crowley LC, Christensen ME & Waterhouse NJ. (2016). Measuring Mitochondrial Transmembrane Potential by TMRE Staining. *Cold Spring Harb Protoc* **2016**.

Cusdin FS, Nietlispach D, Maman J, Dale TJ, Powell AJ, Clare JJ & Jackson AP. (2010). The sodium channel {beta}3-subunit induces multiphasic gating in NaV1.3 and affects fast inactivation via distinct intracellular regions. *J Biol Chem* **285,** 33404-33412.

Dai JL, Wang L, Sahin AA, Broemeling LD, Schutte M & Pan Y. (2004). NHERF (Na+/H+ exchanger regulatory factor) gene mutations in human breast cancer. *Oncogene* **23,** 8681-8687.

Damaghi M, Wojtkowiak JW & Gillies RJ. (2013). pH sensing and regulation in cancer. *Front Physiol* **4,** 370.

Davis TH, Chen C & Isom LL. (2004). Sodium channel beta1 subunits promote neurite outgrowth in cerebellar granule neurons. *J Biol Chem* **279,** 51424-51432.

Dehairs J, Talebi A, Cherifi Y & Swinnen JV. (2016). CRISP-ID: decoding CRISPR mediated indels by Sanger sequencing. *Sci Rep* **6,** 28973.

Diaz D, Delgadillo DM, Hernandez-Gallegos E, Ramirez-Dominguez ME, Hinojosa LM, Ortiz CS, Berumen J, Camacho J & Gomora JC. (2007). Functional expression of voltage-gated sodium channels in primary cultures of human cervical cancer. *J Cell Physiol* **210,** 469-478.

Dillies MA, Rau A, Aubert J, Hennequet-Antier C, Jeanmougin M, Servant N, Keime C, Marot G, Castel D, Estelle J, Guernec G, Jagla B, Jouneau L, Laloë D, Le Gall C, Schaëffer B, Le Crom S, Guedj M, Jaffrézic F & Consortium FS. (2013). A comprehensive evaluation of normalization methods for Illumina high-throughput RNA sequencing data analysis. *Brief Bioinform* **14,** 671-683.

Ding Y, Brackenbury WJ, Onganer PU, Montano X, Porter LM, Bates LF & Djamgoz MB. (2008). Epidermal growth factor upregulates motility of Mat-LyLu rat prostate cancer cells partially via voltage-gated Na^+ channel activity. *J Cell Physiol* **215,** 77-81.

Ding Y & Djamgoz MB. (2004). Serum concentration modifies amplitude and kinetics of voltage-gated Na^+ current in the Mat-LyLu cell line of rat prostate cancer. *Int J Biochem Cell Biol* **36,** 1249-1260.

Diss JK, Archer SN, Hirano J, Fraser SP & Djamgoz MB. (2001). Expression profiles of voltage-gated Na(+) channel alpha-subunit genes in rat and human prostate cancer cell lines. *Prostate* **48,** 165-178.

Diss JK, Fraser SP, Walker MM, Patel A, Latchman DS & Djamgoz MB. (2008). Beta-subunits of voltage-gated sodium channels in human prostate cancer: quantitative in vitro and in vivo analyses of mRNA expression. *Prostate Cancer Prostatic Dis* **11,** 325-333.

Diss JK, Stewart D, Fraser SP, Black JA, Dib-Hajj S, Waxman SG, Archer SN & Djamgoz MB. (1998). Expression of skeletal muscle-type voltage-gated Na+ channel in rat and human prostate cancer cell lines. *FEBS Lett* **427,** 5-10.

Diss JK, Stewart D, Pani F, Foster CS, Walker MM, Patel A & Djamgoz MB. (2005). A potential novel marker for human prostate cancer: voltage-gated sodium channel expression in vivo. *Prostate Cancer Prostatic Dis* **8,** 266-273.

Djamgoz M, Mycielska M, Madeja Z, Fraser SP & Korohoda W. (2001). Directional movement of rat prostate cancer cells in direct-current electric field: involvement of voltagegated Na+ channel activity. *J Cell Sci* **114,** 2697-2705.

Dobin A, Davis CA, Schlesinger F, Drenkow J, Zaleski C, Jha S, Batut P, Chaisson M & Gingeras TR. (2013). STAR: ultrafast universal RNA-seq aligner. *Bioinformatics* **29,** 15-21.

Doeser A, Dickhof G, Reitze M, Uebachs M, Schaub C, Pires NM, Bonifacio MJ, Soares-da-Silva P & Beck H. (2015). Targeting pharmacoresistant epilepsy and epileptogenesis with a dual-purpose antiepileptic drug. *Brain* **138,** 371-387.

Doeser A, Soares-da-Silva P, Beck H & Uebachs M. (2014). The effects of eslicarbazepine on persistent Na^+ current and the role of the Na^+ channel β subunits. *Epilepsy Res* **108,** 202-211.

Dolinska M, Dybel A, Zablocka B & Albrecht J. (2003). Glutamine transport in C6 glioma cells shows ASCT2 system characteristics. *Neurochem Int* **43,** 501-507.

Dolphin AC. (2018). Voltage-gated calcium channel αlpha2delta subunits: and assessment of proposed novel roles. *F1000Res* **7**.

Dong H, Shim KN, Li JM, Estrema C, Ornelas TA, Nguyen F, Liu S, Ramamoorthy SL, Ho S, Carethers JM & Chow JY. (2010). Molecular mechanisms underlying Ca2+-mediated motility of human pancreatic duct cells. *Am J Physiol Cell Physiol* **299,** C1493-1503.

Driffort V, Gillet L, Bon E, Marionneau-Lambot S, Oullier T, Joulin V, Collin C, Pages JC, Jourdan ML, Chevalier S, Bougnoux P, Le Guennec JY, Besson P & Roger S. (2014). Ranolazine inhibits NaV1.5-mediated breast cancer cell invasiveness and lung colonization. *Mol Cancer* **13,** 264.

du Bois-Reymond E. (1843). Vorläufiger Abriss einer Untersuchung über den sogenannten Froschstrom und über die elektromotorischen Fische. *Ann Physik U Chemie* **58,** 1-30.

Dutka TL & Lamb GD. (2007). Na+-K+ pumps in the transverse tubular system of skeletal muscle fibers preferentially use ATP from glycolysis. *Am J Physiol Cell Physiol* **293,** C967-977.

Edwards FA & Konnerth A. (1992). Patch-clamping cells in sliced tissue preparations. *Methods Enzymol* **207,** 208-222.

Eijkelkamp N, Linley JE, Baker MD, Minett MS, Cregg R, Werdehausen R, Rugiero F & Wood JN. (2012). Neurological perspectives on voltage-gated sodium channels. In *Brain*, pp. 2585-2612.

Elmore SA, Dixon D, Hailey JR, Harada T, Herbert RA, Maronpot RR, Nolte T, Rehg JE, Rittinghausen S, Rosol TJ, Satoh H, Vidal JD, Willard-Mack CL & Creasy DM. (2016). Recommendations from the INHAND Apoptosis/Necrosis Working Group. *Toxicol Pathol* **44,** 173-188.

Epstein T, Xu L, Gillies RJ & Gatenby RA. (2014). Separation of metabolic supply and demand: aerobic glycolysis as a normal physiological response to fluctuating energetic demands in the membrane. *Cancer Metab* **2,** 7.

Estrella V, Chen T, Lloyd M, Wojtkowiak J, Cornnell HH, Ibrahim-Hashim A, Bailey K, Balagurunathan Y, Rothberg JM, Sloane BF, Johnson J, Gatenby RA & Gillies RJ. (2013). Acidity generated by the tumor microenvironment drives local invasion. *Cancer Res* **73,** 1524-1535.

Fairhurst C, Watt I, Martin F, Bland M & Brackenbury WJ. (2015). Sodium channel-inhibiting drugs and survival of breast, colon and prostate cancer: a population-based study. *Sci Rep* **5,** 16758.

Falcao A, Fuseau E, Nunes T, Almeida L & Soares-da-Silva P. (2012). Pharmacokinetics, drug interactions and exposure-response relationship of eslicarbazepine acetate in adult patients with partial-onset seizures: population pharmacokinetic and pharmacokinetic/pharmacodynamic analyses. *CNS Drugs* **26,** 79-91.

Falcão A, Maia J, Almeida L, Mazur D, Gellert M & Soares-da-Silva P. (2007). Effect of gender on the pharmacokinetics of eslicarbazepine acetate (BIA 2-093), a new voltage-gated sodium channel blocker. *Biopharm Drug Dispos* **28,** 249-256.

Farias LM, Ocaña DB, Díaz L, Larrea F, Avila-Chávez E, Cadena A, Hinojosa LM, Lara G, Villanueva LA, Vargas C, Hernández-Gallegos E, Camacho-Arroyo I, Dueñas-González A, Pérez-Cárdenas E, Pardo LA, Morales A, Taja-Chayeb L, Escamilla J,

Sánchez-Peña C & Camacho J. (2004). Ether a go-go potassium channels as human cervical cancer markers. *Cancer Res* **64,** 6996-7001.

Fong Y, Evans J, Brook D, Kenkre J, Jarvis P & Gower-Thomas K. (2015). The Nottingham Prognostic Index: five- and ten-year data for all-cause survival within a screened population. *Ann R Coll Surg Engl* **97,** 137-139.

Fraser SP, Ding Y, Liu A, Foster CS & Djamgoz MB. (1999). Tetrodotoxin suppresses morphological enhancement of the metastatic MAT-LyLu rat prostate cancer cell line. *Cell Tissue Res* **295,** 505-512.

Fraser SP, Diss JK, Lloyd LJ, Pani F, Chioni AM, George AJ & Djamgoz MB. (2004). T-lymphocyte invasiveness: control by voltage-gated Na^+ channel activity. *FEBS Lett* **569,** 191-194.

Fraser SP, Diss JKJ, Chioni AM, Mycielska ME, Pan HY, Yamaci RF, Pani F, Siwy Z, Krasowska M, Grzywna Z, Brackenbury WJ, Theodorou D, Koyuturk M, Kaya H, Battaloglu E, De Bella MT, Slade MJ, Tolhurst R, Palmieri C, Jiang J, Latchman DS, Coombes RC & Djamgoz MBA. (2005). Voltage-gated sodium channel expression and potentiation of human breast cancer metastasis. *Clin Cancer Res* **11,** 5381-5389.

Fraser SP, Hemsley F & Djamgoz MBA. (2016). Caffeic acid phenethyl ester: Inhibition of metastatic cell behaviours via voltage-gated sodium channel in human breast cancer in vitro. *Int J Biochem Cell Biol* **71,** 111-118.

Fraser SP, Ozerlat-Gunduz I, Brackenbury WJ, Fitzgerald EM, Campbell TM, Coombes RC & Djamgoz MB. (2014). Regulation of voltage-gated sodium channel expression in cancer: hormones, growth factors and auto-regulation. *Philos Trans R Soc Lond B Biol Sci* **369,** 20130105.

Fraser SP, Ozerlat-Gunduz I, Onkal R, Diss JK, Latchman DS & Djamgoz MB. (2010). Estrogen and non-genomic upregulation of voltage-gated Na(+) channel activity in MDA-MB-231 human breast cancer cells: role in adhesion. *J Cell Physiol* **224,** 527-539.

Fraser SP, Salvador V, Manning EA, Mizal J, Altun S, Raza M, Berridge RJ & Djamgoz MB. (2003). Contribution of functional voltage-gated Na+ channel expression to cell behaviors involved in the metastatic cascade in rat prostate cancer: I. Lateral motility. *J Cell Physiol* **195,** 479-487.

Fujii T, Shimizu T, Katoh M, Nagamori S, Koizumi K, Fukuoka J, Tabuchi Y, Sawaguchi A, Okumura T, Shibuya K, Takeshima H & Sakai H. (2021). Survival of detached cancer cells is regulated by movement of intracellular Na. *iScience* **24,** 102412.

Fujita K & Nonomura N. (2019). Role of Androgen Receptor in Prostate Cancer: A Review. *World J Mens Health* **37,** 288-295.

Fulgenzi G, Graciotti L, Faronato M, Soldovieri MV, Miceli F, Amoroso S, Annunziato L, Procopio A & Taglialatela M. (2006). Human neoplastic mesothelial cells express voltage-gated sodium channels involved in cell motility. *Int J Biochem Cell Biol* **38,** 1146-1159.

Galiana GL, Gauthier AC & Mattson RH. (2017). Eslicarbazepine Acetate: A New Improvement on a Classic Drug Family for the Treatment of Partial-Onset Seizures. *Drugs R D* **17,** 329-339.

Gao R, Shen Y, Cai J, Lei M & Wang Z. (2010). Expression of voltage-gated sodium channel alpha subunit in human ovarian cancer. *Oncol Rep* **23,** 1293-1299.

Gatenby RA & Gillies RJ. (2004). Why do cancers have high aerobic glycolysis? *Nat Rev Cancer* **4,** 891-899.

Gavillet B, Rougier JS, Domenighetti AA, Behar R, Boixel C, Ruchat P, Lehr HA, Pedrazzini T & Abriel H. (2006). Cardiac sodium channel Nav1.5 is regulated by a multiprotein complex composed of syntrophins and dystrophin. *Circ Res* **99,** 407-414.

Ghovanloo MR, Peters CH & Ruben PC. (2018). Effects of acidosis on neuronal voltage-gated sodium channels: Nav1.1 and Nav1.3. *Channels (Austin)* **12,** 367-377.

Gillet L, Roger S, Besson P, Lecaille F, Gore J, Bougnoux P, Lalmanach G & Le Guennec JY. (2009). Voltage-gated Sodium Channel Activity Promotes Cysteine Cathepsin-dependent Invasiveness and Colony Growth of Human Cancer Cells. *J Biol Chem* **284,** 8680-8691.

Gong Q, Stump MR, Deng V, Zhang L & Zhou Z. (2014). Identification of Kv11.1 Isoform Switch as a Novel Pathogenic Mechanism of Long QT Syndrome. *Circ Cardiovasc Genet* **7,** 482-490.

Gradek F, Lopez-Charcas O, Chadet S, Poisson L, Ouldamer L, Goupille C, Jourdan ML, Chevalier S, Moussata D, Besson P & Roger S. (2019). Sodium Channel *Na v 1.5* Controls Epithelial-to-Mesenchymal Transition and Invasiveness in Breast Cancer Cells Through its Regulation by the Salt-Inducible Kinase-1. *Sci Rep* **9,** 18652.

Grieco TM, Malhotra JD, Chen C, Isom LL & Raman IM. (2005). Open-channel block by the cytoplasmic tail of sodium channel beta4 as a mechanism for resurgent sodium current. *Neuron* **45,** 233-244.

Grillon E, Farion R, Fablet K, De Waard M, Tse CM, Donowitz M, Rémy C & Coles JA. (2011). The spatial organization of proton and lactate transport in a rat brain tumor. *PLoS One* **6,** e17416.

Grillon E, Farion R, Reuveni M, Glidle A, Rémy C & Coles JA. (2015). Spatial profiles of markers of glycolysis, mitochondria, and proton pumps in a rat glioma suggest coordinated programming for proliferation. *BMC Res Notes* **8,** 207.

Grimes JA, Fraser SP, Stephens GJ, Downing JEG, Laniado ME, Foster CS, Abel PD & Djamgoz MBA. (1995). Differential expression of voltage-activated Na+ currents in 2 prostatic tumor cell lines - Contribution to invasiveness in-vitro. *Febs Letters* **369,** 290-294.

Gupta SC, Singh R, Asters M, Liu J, Zhang X, Pabbidi MR, Watabe K & Mo YY. (2016). Regulation of breast tumorigenesis through acid sensors. *Oncogene* **35,** 4102-4111.

Guy HR & Seetharamulu P. (1986). Molecular model of the action potential sodium channel. *Proc Natl Acad Sci U S A* **83,** 508-512.

Guzel RM, Ogmen K, Ilieva KM, Fraser SP & Djamgoz MBA. (2018). Colorectal cancer invasiveness in vitro: Predominant contribution of neonatal Nav1.5 under normoxia and hypoxia. *J Cell Physiol*.

Hanahan D & Weinberg RA. (2000). The hallmarks of cancer. *Cell* **100,** 57-70.

Hanlon K, Thompson A, Pantano L, Hutchinson JN, Al-Obeidi A, Wang S, Bliss-Moreau M, Helble J, Alexe G, Stegmaier K, Bauer DE & Croker BA. (2019). Single-cell cloning of human T-cell lines reveals clonal variation in cell death responses to chemotherapeutics. *Cancer Genet* **237,** 69-77.

Haque A, Engel J, Teichmann SA & Lönnberg T. (2017). A practical guide to single-cell RNA-sequencing for biomedical research and clinical applications. *Genome Med* **9,** 75.

Hassanein M, Hoeksema MD, Shiota M, Qian J, Harris BK, Chen H, Clark JE, Alborn WE, Eisenberg R & Massion PP. (2013). SLC1A5 mediates glutamine transport required for lung cancer cell growth and survival. *Clin Cancer Res* **19,** 560-570.

Haworth A. (2019). The contribution of secretase cleavage to voltage-gated Na+ channel β1-subunit function in breast cancer cells. In *Department of Biology*. University of York.

Haworth A, Hodges S, Isom L, Baumann C & Brackenbury W. (2021). Subcellular dynamics and functional activity of the cleaved Na+ channel β1 subunit intracellular domain. *BioRxiv*.

Hebeisen S, Pires N, Loureiro AI, Bonifacio MJ, Palma N, Whyment A, Spanswick D & Soares-da-Silva P. (2015). Eslicarbazepine and the enhancement of slow inactivation of voltage-gated sodium channels: a comparison with carbamazepine, oxcarbazepine and lacosamide. *Neuropharmacology* **89,** 122-135.

Helmlinger G, Yuan F, Dellian M & Jain RK. (1997). Interstitial pH and pO2 gradients in solid tumors in vivo: high-resolution measurements reveal a lack of correlation. *Nat Med* **3,** 177-182.

Hernandez-Plata E, Ortiz CS, Marquina-Castillo B, Medina-Martinez I, Alfaro A, Berumen J, Rivera M & Gomora JC. (2012). Overexpression of NaV 1.6 channels is associated with the invasion capacity of human cervical cancer. *Int J Cancer* **130,** 2013-2023.

Hernansanz-Agustín P, Choya-Foces C, Carregal-Romero S, Ramos E, Oliva T, Villa-Piña T, Moreno L, Izquierdo-Álvarez A, Cabrera-García JD, Cortés A, Lechuga-Vieco AV, Jadiya P, Navarro E, Parada E, Palomino-Antolín A, Tello D, Acín-Pérez R, Rodríguez-Aguilera JC, Navas P, Cogolludo Á, López-Montero I, Martínez-Del-Pozo Á, Egea J, López MG, Elrod JW, Ruíz-Cabello J, Bogdanova A, Enríquez JA & Martínez-Ruiz A. (2020). Na + controls hypoxic signalling by the mitochondrial respiratory chain. *Nature* **586,** 287-291.

Hille B. (2001). *Ion channels of excitable membranes*. Sinauer Associates Inc. , Sunderland, Massachusetts.

Holliday DL & Speirs V. (2011). Choosing the right cell line for breast cancer research. *Breast Cancer Res* **13,** 215.

Hompoonsup S, Chambers D, Doherty P & Williams G. (2019). No transcriptional evidence for active Nav channels in two classes of cancer cell. *Channels (Austin)* **13,** 311-320.

House CD, Vaske CJ, Schwartz AM, Obias V, Frank B, Luu T, Sarvazyan N, Irby R, Strausberg RL, Hales TG, Stuart JM & Lee NH. (2010). Voltage-gated Na+ channel SCN5A is a key regulator of a gene transcriptional network that controls colon cancer invasion. *Cancer Res* **70,** 6957-6967.

House CD, Wang BD, Ceniccola K, Williams R, Simaan M, Olender J, Patel V, Baptista-Hon DT, Annunziata CM, Gutkind JS, Hales TG & Lee NH. (2015). Voltage-gated Na+ Channel Activity Increases Colon Cancer Transcriptional Activity and Invasion Via Persistent MAPK Signaling. *Sci Rep* **5,** 11541.

Hu F, Wang Q, Wang P, Wang W, Qian W, Xiao H & Wang L. (2012). 17β-Estradiol regulates the gene expression of voltage-gated sodium channels: role of estrogen receptor α and estrogen receptor β. *Endocrine* **41,** 274-280.

Huczyński A, Janczak J, Lowicki D & Brzezinski B. (2012). Monensin A acid complexes as a model of electrogenic transport of sodium cation. *Biochim Biophys Acta* **1818,** 2108-2119.

Humphrey PA, Lüpfert C, Apell HJ, Cornelius F & Clarke RJ. (2002). Mechanism of the rate-determining step of the Na(+),K(+)-ATPase pump cycle. *Biochemistry* **41,** 9496-9507.

Hürter T, Bröcker W & Bosma HJ. (1982). Investigations on vasogenic and cytotoxic brain edema, comparing results from X-ray microanalysis and flame photometry. *Microsc Acta* **85,** 285-293.

Iamshanova O, Mariot P, Lehen'kyi V & Prevarskaya N. (2016). Comparison of fluorescence probes for intracellular sodium imaging in prostate cancer cell lines. *Eur Biophys J* **45,** 765-777.

Isbilen B, Fraser SP & Djamgoz MBA. (2006). Docosahexaenoic acid (omega-3) blocks voltage-gated sodium channel activity and migration of MDA-MB-231 human breast cancer cells. *Int J Biochem Cell Biol* **38,** 2173-2182.

Ishikawa N, Oguri T, Isobe T, Fujitaka K & Kohno N. (2001). SGLT gene expression in primary lung cancers and their metastatic lesions. *Jpn J Cancer Res* **92,** 874-879.

Isom LL, De Jongh KS, Patton DE, Reber BF, Offord J, Charbonneau H, Walsh K, Goldin AL & Catterall WA. (1992). Primary structure and functional expression of the beta 1 subunit of the rat brain sodium channel. *Science* **256,** 839-842.

Isom LL, Ragsdale DS, De Jongh KS, Westenbroek RE, Reber BF, Scheuer T & Catterall WA. (1995a). Structure and function of the beta 2 subunit of brain sodium channels, a transmembrane glycoprotein with a CAM motif. *Cell* **83,** 433-442.

Isom LL, Scheuer T, Brownstein AB, Ragsdale DS, Murphy BJ & Catterall WA. (1995b). Functional co-expression of the beta 1 and type IIA alpha subunits of sodium channels in a mammalian cell line. *J Biol Chem* **270,** 3306-3312.

Iwai Y, Ishida M, Tanaka Y, Okazaki T, Honjo T & Minato N. (2002). Involvement of PD-L1 on tumor cells in the escape from host immune system and tumor immunotherapy by PD-L1 blockade. *Proc Natl Acad Sci U S A* **99,** 12293-12297.

Jacobs MA, Ouwerkerk R, Kamel I, Bottomley PA, Bluemke DA & Kim HS. (2009). Proton, diffusion-weighted imaging, and sodium (23Na) MRI of uterine leiomyomata after MR-guided high-intensity focused ultrasound: a preliminary study. *J Magn Reson Imaging* **29,** 649-656.

Jacobs MA, Ouwerkerk R, Wolff AC, Stearns V, Bottomley PA, Barker PB, Argani P, Khouri N, Davidson NE, Bhujwalla ZM & Bluemke DA. (2004). Multiparametric and multinuclear magnetic resonance imaging of human breast cancer: current applications. *Technol Cancer Res Treat* **3,** 543-550.

Jacobs MA, Stearns V, Wolff AC, Macura K, Argani P, Khouri N, Tsangris T, Barker PB, Davidson NE, Bhujwalla ZM, Bluemke DA & Ouwerkerk R. (2010). Multiparametric Magnetic Resonance Imaging, Spectroscopy and Multinuclear (23Na) Imaging Monitoring of Preoperative Chemotherapy for Locally Advanced Breast Cancer. *Acad Radiol* **17,** 1477-1485.

James AD, Leslie TK, Kaggie JD, Wiggins L, Patten L, Murphy O'Duinn J, Langer S, Labarthe MC, Riemer F, Baxter G, McLean MA, Gilbert FJ, Kennerley AJ & Brackenbury WJ. (2022). Sodium accumulation in breast cancer predicts malignancy and treatment response. *Br J Cancer*.

James AD, Leslie TK, Kaggie JD, Wiggins L, Patten L, O'Duinn JM, Langer S, Labarthe M-C, Riemer F, Baxter G, McLean MA, Gilbert FJ, Kennerley AJ & Brackenbury WJ.

(2021). Sodium accumulation in breast cancer predicts malignancy and treatment response. *BioRxiv*.

James AD, Patel W, Butt Z, Adiamah M, Dakhel R, Latif A, Uggenti C, Swanton E, Imamura H, Siriwardena AK & Bruce JIE. (2015). The Plasma Membrane Calcium Pump in Pancreatic Cancer Cells Exhibiting the Warburg Effect Relies on Glycolytic ATP. *J Biol Chem* **290,** 24760-24771.

James JH, Fang CH, Schrantz SJ, Hasselgren PO, Paul RJ & Fischer JE. (1996). Linkage of aerobic glycolysis to sodium-potassium transport in rat skeletal muscle. Implications for increased muscle lactate production in sepsis. *J Clin Invest* **98,** 2388-2397.

Jang SH, Choi SY, Ryu PD & Lee SY. (2011). Anti-proliferative effect of Kv1.3 blockers in A549 human lung adenocarcinoma in vitro and in vivo. *Eur J Pharmacol* **651,** 26-32.

Jang SH, Kang KS, Ryu PD & Lee SY. (2009). Kv1.3 voltage-gated K(+) channel subunit as a potential diagnostic marker and therapeutic target for breast cancer. *BMB Rep* **42,** 535-539.

Jansson KH, Lynch JE, Lepori-Bui N, Czymmek KJ, Duncan RL & Sikes RA. (2012). Overexpression of the VSSC-associated CAM, β-2, enhances LNCaP cell metastasis associated behavior. *Prostate* **72,** 1080-1092.

Jardim-Perassi BV, Huang S, Dominguez-Viqueira W, Poleszczuk J, Budzevich MM, Abdalah MA, Pillai SR, Ruiz E, Bui MM, Zuccari DAPC, Gillies RJ & Martinez GV. (2019). Multiparametric MRI and Coregistered Histology Identify Tumor Habitats in Breast Cancer Mouse Models. *Cancer Res* **79,** 3952-3964.

Jenkins SM & Bennett V. (2001). Ankyrin-G coordinates assembly of the spectrin-based membrane skeleton, voltage-gated sodium channels, and L1 CAMs at Purkinje neuron initial segments. *J Cell Biol* **155,** 739-746.

Jones DK, Peters CH, Tolhurst SA, Claydon TW & Ruben PC. (2011). Extracellular proton modulation of the cardiac voltage-gated sodium channel, Nav1.5. *Biophys J* **101,** 2147-2156.

Josef E, Katz A, Peleg Y, Mehlman T & Karlish S. (2016). Do Src Kinase and Caveolin Interact Directly with Na,K-ATPase? *Membrane Biology* **291,** 11736-11750.

Kaminota T, Yano H, Shiota K, Nomura N, Yaguchi H, Kirino Y, Ohara K, Tetsumura I, Sanada T, Ugumori T, Tanaka J & Hato N. (2017). Elevated Na(+)/H(+) exchanger-1 expression enhances the metastatic collective migration of head and neck squamous cell carcinoma cells. *Biochem Biophys Res Commun* **486,** 101-107.

Kazarinova-Noyes K, Malhotra JD, McEwen DP, Mattei LN, Berglund EO, Ranscht B, Levinson SR, Schachner M, Shrager P, Isom LL & Xiao ZC. (2001). Contactin associates with Na+ channels and increases their functional expression. *J Neurosci* **21,** 7517-7525.

Kazen-Gillespie KA, Ragsdale DS, D'Andrea MR, Mattei LN, Rogers KE & Isom LL. (2000). Cloning, localization, and functional expression of sodium channel beta1A subunits. *J Biol Chem* **275,** 1079-1088.

Khaitan D, Sankpal UT, Weksler B, Meister EA, Romero IA, Couraud PO & Ningaraj NS. (2009). Role of KCNMA1 gene in breast cancer invasion and metastasis to brain. *BMC Cancer* **9,** 258.

Khan A, Kyle JW, Hanck DA, Lipkind GM & Fozzard HA. (2006). Isoform-dependent interaction of voltage-gated sodium channels with protons. *J Physiol* **576,** 493-501.

Khan A, Romantseva L, Lam A, Lipkind G & Fozzard HA. (2002). Role of outer ring carboxylates of the rat skeletal muscle sodium channel pore in proton block. *J Physiol* **543,** 71-84.

Kim DY, Carey BW, Wang H, Ingano LA, Binshtok AM, Wertz MH, Pettingell WH, He P, Lee VM, Woolf CJ & Kovacs DM. (2007a). BACE1 regulates voltage-gated sodium channels and neuronal activity. *Nat Cell Biol* **9,** 755-764.

Kim J, Ghosh S, Liu H, Tateyama M, Kass RS & Pitt GS. (2004). Calmodulin mediates Ca^{2+} sensitivity of sodium channels. *J Biol Chem* **279,** 45004-45012.

Kim JW, Gao P & Dang CV. (2007b). Effects of hypoxia on tumor metabolism. *Cancer Metastasis Rev* **26,** 291-298.

Klein JP, Tendi EA, Dib-Hajj SD, Fields RD & Waxman SG. (2003). Patterned electrical activity modulates sodium channel expression in sensory neurons. *J Neurosci Res* **74,** 192-198.

Kwakye AK, Kampo S, Lv J, Ramzan MN, Richard SA, Falagán AA, Agudogo J, Atito-Narh E, Yan Q & Wen QP. (2020). Levobupivacaine inhibits proliferation and promotes apoptosis of breast cancer cells by suppressing the PI3K/Akt/mTOR signalling pathway. *BMC Res Notes* **13,** 386.

Laedermann CJ, Syam N, Pertin M, Decosterd I & Abriel H. (2013). β1- and β3- voltage-gated sodium channel subunits modulate cell surface expression and glycosylation of Nav1.7 in HEK293 cells. *Front Cell Neurosci* **7**.

Laniado ME, Lalani EN, Fraser SP, Grimes JA, Bhangal G, Djamgoz MB & Abel PD. (1997). Expression and functional analysis of voltage-activated Na^+ channels in human prostate cancer cell lines and their contribution to invasion in vitro. *Am J Pathol* **150,** 1213-1221.

Lee A, Fraser SP & Djamgoz MBA. (2019a). Propranolol inhibits neonatal Nav1.5 activity and invasiveness of MDA-MB-231 breast cancer cells: Effects of combination with ranolazine. *J Cell Physiol* **234,** 23066-23081.

Lee GH, Yan C, Shin S-J, Hong S-C, Ahn T, Moon A, Park SJ, Lee YC, Yoo WH, Kim H-T, Kim D-S, Chae S-W, Kim H-R & Chae H-J. (2010). BAX inhibitor-1 enhances cancer metastasis by altering glucose metabolism and activating the sodium-hydrogen exchanger: the alteration of mitochondrial function. *Oncogene* **29,** 2130-2141.

Lee S, Mele M, Vahl P, Christiansen PM, Jensen VE & Boedtkjer E. (2015). Na+,HCO3- -cotransport is functionally upregulated during human breast carcinogenesis and required for the inverted pH gradient across the plasma membrane. *Pflugers Arch* **467,** 367-377.

Lee SY, Ju MK, Jeon HM, Lee YJ, Kim CH, Park HG, Han SI & Kang HS. (2019b). Reactive oxygen species induce epithelial-mesenchymal transition, glycolytic switch, and mitochondrial repression through the Dlx-2/Snail signaling pathways in MCF-7 cells. *Mol Med Rep* **20,** 2339-2346.

Leonard WJ & O'Shea JJ. (1998). Jaks and STATs: biological implications. *Annu Rev Immunol* **16,** 293-322.

Leslie EM, Deeley RG & Cole SP. (2005). Multidrug resistance proteins: role of P-glycoprotein, MRP1, MRP2, and BCRP (ABCG2) in tissue defense. *Toxicol Appl Pharmacol* **204,** 216-237.

Leslie TK, James AD, Zaccagna F, Grist JT, Deen S, Kennerley A, Riemer F, Kaggie JD, Gallagher FA, Gilbert FJ & Brackenbury WJ. (2019). Sodium homeostasis in the tumour microenvironment. *Biochim Biophys Acta Rev Cancer* **1872,** 188304.

Li JJ, Oberley LW, Fan M & Colburn NH. (1998). Inhibition of AP-1 and NF-kappaB by manganese-containing superoxide dismutase in human breast cancer cells. *FASEB J* **12,** 1713-1723.

Li W, Zhou K, Li M, Hu Q, Wei W, Liu L & Zhao Q. (2022). Identification of SCN7A as the key gene associated with tumor mutation burden in gastric cancer. *BMC Gastroenterol* **22,** 45.

Li X, Cheng Y, Wang Z, Zhou J, Jia Y, He X, Zhao L, Dong Y, Fan Y, Yang X, Shen B, Wu X, Wang J, Xiong C & Wei L. (2020). Calcium and TRPV4 promote metastasis by regulating cytoskeleton through the RhoA/ROCK1 pathway in endometrial cancer. *Cell Death Dis* **11,** 1009.

Li X, Yang J, Peng L, Sahin AA, Huo L, Ward KC, O'Regan R, Torres MA & Meisel JL. (2017). Triple-negative breast cancer has worse overall survival and cause-specific survival than non-triple-negative breast cancer. *Breast Cancer Res Treat* **161,** 279-287.

Liberti MV & Locasale JW. (2016). The Warburg Effect: How Does it Benefit Cancer Cells? *Trends Biochem Sci* **41,** 211-218.

Liu C, Wu P, Zhang A & Mao X. (2021). Advances in Rodent Models for Breast Cancer Formation, Progression, and Therapeutic Testing. *Front Oncol* **11,** 593337.

Liu M, Liu H & Dudley SC. (2010). Reactive oxygen species originating from mitochondria regulate the cardiac sodium channel. *Circ Res* **107,** 967-974.

Liu M, Wang X, Wang L, Ma X, Gong Z, Zhang S & Li Y. (2018). Targeting the IDO1 pathway in cancer: from bench to bedside. *J Hematol Oncol* **11,** 100.

Lobikin M, Chernet B, Lobo D & Levin M. (2012). Resting potential, oncogene-induced tumorigenesis, and metastasis: the bioelectric basis of cancer in vivo. *Phys Biol* **9,** 065002.

Lopez-Santiago LF, Meadows LS, Ernst SJ, Chen C, Malhotra JD, McEwen DP, Speelman A, Noebels JL, Maier SK, Lopatin AN & Isom LL. (2007). Sodium channel Scn1b null mice exhibit prolonged QT and RR intervals. *J Mol Cell Cardiol* **43,** 636-647.

Lopez-Santiago LF, Pertin M, Morisod X, Chen C, Hong S, Wiley J, Decosterd I & Isom LL. (2006). Sodium Channel β2 Subunits Regulate Tetrodotoxin-Sensitive Sodium Channels in Small Dorsal Root Ganglion Neurons and Modulate the Response to Pain. *J Neurosci* **26,** 7984-7994.

Lu SC. (2009). Regulation of glutathione synthesis. *Mol Aspects Med* **30,** 42-59.

Lustig M, Zanazzi G, Sakurai T, Blanco C, Levinson SR, Lambert S, Grumet M & Salzer JL. (2001). Nr-CAM and neurofascin interactions regulate ankyrin G and sodium channel clustering at the node of Ranvier. *Curr Biol* **11,** 1864-1869.

Ly JD, Grubb DR & Lawen A. (2003). The mitochondrial membrane potential (deltapsi(m)) in apoptosis; an update. *Apoptosis* **8,** 115-128.

Lynch RM & Balaban RS. (1987a). Coupling of aerobic glycolysis and Na+-K+-ATPase in renal cell line MDCK. *Am J Physiol* **253,** C269-276.

Lynch RM & Balaban RS. (1987b). Energy metabolism of renal cell lines, A6 and MDCK: regulation by Na-K-ATPase. *Am J Physiol* **252,** C225-231.

MacGrath SM & Koleske AJ. (2012). Cortactin in cell migration and cancer at a glance. *J Cell Sci* **125,** 1621-1626.

Madelin G, Kline R, Walvick R & Regatte RR. (2014). A method for estimating intracellular sodium concentration and extracellular volume fraction in brain in vivo using sodium magnetic resonance imaging. *Sci Rep* **4,** 4763.

Magnus CJ, Lee PH, Atasoy D, Su HH, Looger LL & Sternson SM. (2011). Chemical and genetic engineering of selective ion channel-ligand interactions. *Science* **333,** 1292-1296.

Maia J, Almeida L, Falcao A, Soares E, Mota F, Potgieter MA, Potgieter JH & Soares-da-Silva P. (2008). Effect of renal impairment on the pharmacokinetics of eslicarbazepine acetate. *Int J Clin Pharmacol Ther* **46,** 119-130.

Maleno I, López-Nevot MA, Cabrera T, Salinero J & Garrido F. (2002). Multiple mechanisms generate HLA class I altered phenotypes in laryngeal carcinomas: high frequency of HLA haplotype loss associated with loss of heterozygosity in chromosome region 6p21. *Cancer Immunol Immunother* **51,** 389-396.

Malhotra JD, Kazen-Gillespie K, Hortsch M & Isom LL. (2000). Sodium channel beta subunits mediate homophilic cell adhesion and recruit ankyrin to points of cell-cell contact. *J Biol Chem* **275,** 11383-11388.

Malhotra JD, Thyagarajan V, Chen C & Isom LL. (2004). Tyrosine-phosphorylated and nonphosphorylated sodium channel beta1 subunits are differentially localized in cardiac myocytes. *J Biol Chem* **279,** 40748-40754.

Mao W, You T, Ye B, Li X, Dong HH, Hill JA, Li F & Xu H. (2012). Reactive oxygen species suppress cardiac NaV1.5 expression through Foxo1. *PLoS One* **7,** e32738.

Marx A, Siara J & Rudel R. (1991). Sodium and potassium channels in epithelial cells from thymus glands and thymomas of myasthenia gravis patients. *Pflugers Arch* **417,** 537-539.

McBride BW & Early RJ. (1989). Energy expenditure associated with sodium/potassium transport and protein synthesis in skeletal muscle and isolated hepatocytes from hyperthyroid sheep. *Br J Nutr* **62,** 673-682.

McCormick KA, Isom LL, Ragsdale D, Smith D, Scheuer T & Catterall WA. (1998). Molecular determinants of Na^+ channel function in the extracellular domain of the beta1 subunit. *J Biol Chem* **273,** 3954-3962.

McEwen DP & Isom LL. (2004). Heterophilic interactions of sodium channel beta1 subunits with axonal and glial cell adhesion molecules. *J Biol Chem* **279,** 52744-52752.

McEwen DP, Meadows LS, Chen C, Thyagarajan V & Isom LL. (2004). Sodium channel beta1 subunit-mediated modulation of Nav1.2 currents and cell surface density is dependent on interactions with contactin and ankyrin. *J Biol Chem* **279,** 16044-16049.

McGranahan N, Rosenthal R, Hiley CT, Rowan AJ, Watkins TBK, Wilson GA, Birkbak NJ, Veeriah S, Van Loo P, Herrero J, Swanton C & Consortium T. (2017). Allele-Specific HLA Loss and Immune Escape in Lung Cancer Evolution. *Cell* **171,** 1259-1271.e1211.

McLean LA, Roscoe J, Jorgensen NK, Gorin FA & Cala PM. (2000). Malignant gliomas display altered pH regulation by NHE1 compared with nontransformed astrocytes. *Am J Physiol Cell Physiol* **278,** C676-688.

Meadows L, Malhotra JD, Stetzer A, Isom LL & Ragsdale DS. (2001). The intracellular segment of the sodium channel beta 1 subunit is required for its efficient association with the channel alpha subunit. *J Neurochem* **76,** 1871-1878.

Minchenko A, Bauer T, Salceda S & Caro J. (1994). Hypoxic stimulation of vascular endothelial growth factor expression in vitro and in vivo. *Lab Invest* **71,** 374-379.

Minta A & Tsien RY. (1989). Fluorescent indicators for cytosolic sodium. *J Biol Chem* **264,** 19449-19457.

Mohammed FH, Khajah MA, Yang M, Brackenbury WJ & Luqmani YA. (2016). Blockade of voltage-gated sodium channels inhibits invasion of endocrine-resistant breast cancer cells. *Int J Oncol* **48,** 73-83.

Mokhtar N, Sharuddin N, Che Wahab N, Dominguez A, Sarmiento M, Mohd Nor N & Yaccob N. (2019). Evaluation of mouse polyclonal antibody against nNav1.5 to recognize

nNav1.5 protein in human breast cancer cells using fluorescence

immunostaining. In *Proceedings of the European Society for Medical Oncology (ESMO)*. Barcelona, Spain.

Molecular-Devices. (2012). *The Axon Guide; Electrophysiology and Biophysics Laboratory Techniques*. 1311 Orleans Drive, Sunnyvale, California, United States of America 94089.

Monk M & Holding C. (2001). Human embryonic genes re-expressed in cancer cells. *Oncogene* **20,** 8085-8091.

Motoike HK, Liu H, Glaaser IW, Yang AS, Tateyama M & Kass RS. (2004). The Na+ channel inactivation gate is a molecular complex: a novel role of the COOH-terminal domain. *J Gen Physiol* **123,** 155-165.

Murata T, Miwa K, Miyaji N, Wagatsuma K, Hasegawa T, Oda K, Umeda T, Iimori T, Masuda Y, Terauchi T & Koizumi M. (2016). Evaluation of spatial dependence of

point spread function-based PET reconstruction using a traceable point-like 22Na source. *EJNMMI Phys* **3,** 26.

Murtadha AH, Azahar IIM, Sharudin NA, Che Has AT & Mokhtar NF. (2021). Influence of nNav1.5 on MHC class I expression in breast cancer. *J Biosci* **46**.

Mycielska ME & Djamgoz MB. (2004). Cellular mechanisms of direct-current electric field effects: galvanotaxis and metastatic disease. *J Cell Sci* **117,** 1631-1639.

Nelson M, Millican-Slater R, Forrest LC & Brackenbury WJ. (2014). The sodium channel β1 subunit mediates outgrowth of neurite-like processes on breast cancer cells and promotes tumour growth and metastasis. *Int J Cancer* **135,** 2338-2351.

Nelson M, Yang M, Dowle AA, Thomas JR & Brackenbury WJ. (2015a). The sodium channel-blocking antiepileptic drug phenytoin inhibits breast tumour growth and metastasis. *Mol Cancer* **14,** 13.

Nelson M, Yang M, Millican-Slater R & Brackenbury WJ. (2015b). Nav1.5 regulates breast tumor growth and metastatic dissemination in vivo. *Oncotarget* **6,** 32914-32929.

Nishimura K, Isseroff R & Nuccitelli R. (1996). Human Keratinocytes Migrate to the Negative Pole in Direct Current Electric Fields Comparable to Those Measured in Mammalian Wounds. *Journal of cell science* **109 (Pt 1)**.

Noda M, Shimizu S, Tanabe T, Takai T, Kayano T, Ikeda T, Takahashi H, Nakayama H, Kanaoka Y & Minamino N. (1984). Primary structure of Electrophorus electricus sodium channel deduced from cDNA sequence. *Nature* **312,** 121-127.

Nomura K, Hiyama TY, Sakuta H, Matsuda T, Lin CH, Kobayashi K, Kuwaki T, Takahashi K, Matsui S & Noda M. (2019). [Na +] Increases in Body Fluids Sensed by Central Na x Induce Sympathetically Mediated Blood Pressure Elevations via H + -Dependent Activation of ASIC1a. *Neuron* **101,** 60-75.e66.

O'Connell KE, Mikkola AM, Stepanek AM, Vernet A, Hall CD, Sun CC, Yildirim E, Staropoli JF, Lee JT & Brown DE. (2015). Practical murine hematopathology: a comparative review and implications for research. *Comp Med* **65,** 96-113.

Onganer PU & Djamgoz MB. (2005). Small-cell lung cancer (human): potentiation of endocytic membrane activity by voltage-gated Na(+) channel expression in vitro. *J Membr Biol* **204,** 67-75.

Onkal R, Fraser SP & Djamgoz MBA. (2019). Cationic Modulation of Voltage-Gated Sodium Channel (Nav1.5): Neonatal Versus Adult Splice Variants-1. Monovalent (H. *Bioelectricity* **1,** 139-147.

Ono K, Fozzard HA & Hanck DA. (1993). Mechanism of cAMP-dependent modulation of cardiac sodium channel current kinetics. *Circ Res* **72,** 807-815.

Onuma EK & Hui SW. (1988). Electric field-directed cell shape changes, displacement, and cytoskeletal reorganization are calcium dependent. *J Cell Biol* **106,** 2067-2075.

Ou SW, Kameyama A, Hao LY, Horiuchi M, Minobe E, Wang WY, Makita N & Kameyama M. (2005). Tetrodotoxin-resistant Na^+ channels in human neuroblastoma cells are encoded by new variants of Nav1.5/SCN5A. *Eur J Neurosci* **22,** 793-801.

Ouadid-Ahidouch H, Ahidouch A & Pardo LA. (2016). Kv10.1 K(+) channel: from physiology to cancer. *Pflugers Arch* **468,** 751-762.

Ouadid-Ahidouch H, Roudbaraki M, Delcourt P, Ahidouch A, Joury N & Prevarskaya N. (2004). Functional and molecular identification of intermediate-conductance Ca(2+)-activated K(+) channels in breast cancer cells: association with cell cycle progression. *Am J Physiol Cell Physiol* **287,** C125-134.

Ouwerkerk R, Bleich KB, Gillen JS, Pomper MG & Bottomley PA. (2003). Tissue sodium concentration in human brain tumors as measured with 23Na MR imaging. *Radiology* **227,** 529-537.

Ouwerkerk R, Jacobs MA, Macura KJ, Wolff AC, Stearns V, Mezban SD, Khouri NF, Bluemke DA & Bottomley PA. (2007). Elevated tissue sodium concentration in malignant breast lesions detected with non-invasive 23Na MRI. *Breast Cancer Res Treat* **106,** 151-160.

Pan X, Li Z, Zhou Q, Shen H, Wu K, Huang X, Chen J, Zhang J, Zhu X, Lei J, Xiong W, Gong H, Xiao B & Yan N. (2018). Structure of the human voltage-gated sodium channel Na. *Science* **362**.

Pancrazio JJ, Viglione MP, Tabbara IA & Kim YI. (1989). Voltage-dependent ion channels in small-cell lung cancer cells. *Cancer Res* **49,** 5901-5906.

Pardo LA & Stuhmer W. (2014). The roles of K(+) channels in cancer. *Nat Rev Cancer* **14,** 39-48.

Park J & Schwarzbauer JE. (2014). Mammary epithelial cell interactions with fibronectin stimulate epithelial-mesenchymal transition. *Oncogene* **33,** 1649-1657.

Parks SK, Chiche J & Pouysségur J. (2013). Disrupting proton dynamics and energy metabolism for cancer therapy. *Nat Rev Cancer* **13,** 611-623.

Patino GA, Brackenbury WJ, Bao Y, Lopez-Santiago LF, O'Malley HA, Chen C, Calhoun JD, Lafrenière RG, Cossette P, Rouleau GA & Isom LL. (2011). Voltage-gated Na+ channel β1B: a secreted cell adhesion molecule involved in human epilepsy. *J Neurosci* **31,** 14577-14591.

Paul RJ, Bauer M & Pease W. (1979). Vascular smooth muscle: aerobic glycolysis linked to sodium and potassium transport processes. *Science* **206,** 1414-1416.

Payandeh J, Scheuer T, Zheng N & Catterall WA. (2011). The crystal structure of a voltage-gated sodium channel. *Nature* **475,** 353-358.

Pellerin L & Magistretti PJ. (1994). Glutamate uptake into astrocytes stimulates aerobic glycolysis: a mechanism coupling neuronal activity to glucose utilization. *Proc Natl Acad Sci U S A* **91,** 10625-10629.

Perillo B, Di Donato M, Pezone A, Di Zazzo E, Giovannelli P, Galasso G, Castoria G & Migliaccio A. (2020). ROS in cancer therapy: the bright side of the moon. *Exp Mol Med* **52,** 192-203.

Perucca E, Elger C, Halász P, Falcão A, Almeida L & Soares-da-Silva P. (2011). Pharmacokinetics of eslicarbazepine acetate at steady-state in adults with partial-onset seizures. *Epilepsy Res* **96,** 132-139.

Phan NN, Wang CY, Chen CF, Sun Z, Lai MD & Lin YC. (2017). Voltage-gated calcium channels: Novel targets for cancer therapy. *Oncol Lett* **14,** 2059-2074.

Philipson KD, Bersohn MM & Nishimoto AY. (1982). Effects of pH on Na -Ca2 exchange in canine cardiac sarcolemmal vesicles. *Circ Res* **50,** 287-293.

Pollock NI & Grandis JR. (2015). HER2 as a therapeutic target in head and neck squamous cell carcinoma. *Clin Cancer Res* **21,** 526-533.

Prevarskaya N, Skryma R & Shuba Y. (2011). Calcium in tumour metastasis: new roles for known actors. *Nat Rev Cancer* **11,** 609-618.

Pristerà A, Baker MD & Okuse K. (2012). Association between tetrodotoxin resistant channels and lipid rafts regulates sensory neuron excitability. *PLoS One* **7,** e40079.

Pullar C, Baier B, Kariya Y, Russell A, Horst B, Marinkovich M & Isseroff R. (2006). beta4 Integrin and Epidermal Growth Factor Coordinately Regulate Electric Field-Mediated Directional Migration via Rac1. *Molecular biology of the cell* **17**.

Pusch M, Ludewig U, Rehfeldt A & Jentsch TJ. (1995). Gating of the voltage-dependent chloride channel CIC-0 by the permeant anion. *Nature* **373,** 527-531.

Ramirez A, Hinojosa LM, Gonzales J, Montante-Montes D, Martinez-Benitez B, Aguilar-Guadarrama R, Gamboa-Dominguez A, Morales F, Carrillo-Garcia A, Lizano M, Garcia-Becerra R, Diaz L, Vazquez-Sanchez AY & Camacho J. (2013). KCNH1 potassium channels are expressed in cervical cytologies from pregnant patients and are regulated by progesterone. *Reproduction* **146,** 615-623.

Ran FA, Hsu PD, Wright J, Agarwala V, Scott DA & Zhang F. (2013). Genome engineering using the CRISPR-Cas9 system. *Nat Protoc* **8,** 2281-2308.

Ratcliffe CF, Westenbroek RE, Curtis R & Catterall WA. (2001). Sodium channel beta1 and beta3 subunits associate with neurofascin through their extracellular immunoglobulin-like domain. *J Cell Biol* **154,** 427-434.

Reshkin SJ, Bellizzi A, Caldeira S, Albarani V, Malanchi I, Poignee M, Alunni-Fabbroni M, Casavola V & Tommasino M. (2000). Na+/H+ exchanger-dependent intracellular alkalinization is an early event in malignant transformation and plays an essential role in the development of subsequent transformation-associated phenotypes. *Faseb j* **14,** 2185-2197.

Rhett JM, Ongstad EL, Jourdan J & Gourdie RG. (2012). Cx43 associates with Na(v)1.5 in the cardiomyocyte perinexus. *J Membr Biol* **245,** 411-422.

Ribeiro M, Elghajiji A, Fraser SP, Burke ZD, Tosh D, Djamgoz MBA & Rocha PRF. (2020). Human Breast Cancer Cells Demonstrate Electrical Excitability. *Front Neurosci* **14,** 404.

Riva R, Albani F, Contin M & Baruzzi A. (1996). Pharmacokinetic interactions between antiepileptic drugs. Clinical considerations. *Clin Pharmacokinet* **31,** 470-493.

Rofstad EK, Mathiesen B, Kindem K & Galappathi K. (2006). Acidic extracellular pH promotes experimental metastasis of human melanoma cells in athymic nude mice. *Cancer Res* **66,** 6699-6707.

Roger S, Besson P & Le Guennec JY. (2003). Involvement of a novel fast inward sodium current in the invasion capacity of a breast cancer cell line. *Biochim Biophys Acta* **1616,** 107-111.

Roger S, Rollin J, Barascu A, Besson P, Raynal PI, Iochmann S, Lei M, Bougnoux P, Gruel Y & Le Guennec JY. (2007). Voltage-gated sodium channels potentiate the invasive capacities of human non-small-cell lung cancer cell lines. *Int J Biochem Cell Biol* **39,** 774-786.

Rohani N, Hao L, Alexis MS, Joughin BA, Krismer K, Moufarrej MN, Soltis AR, Lauffenburger DA, Yaffe MB, Burge CB, Bhatia SN & Gertler FB. (2019). Acidification of Tumor at Stromal Boundaries Drives Transcriptome Alterations Associated with Aggressive Phenotypes. *Cancer Res* **79,** 1952-1966.

Royeck M, Horstmann MT, Remy S, Reitze M, Yaari Y & Beck H. (2008). Role of axonal NaV1.6 sodium channels in action potential initiation of CA1 pyramidal neurons. *J Neurophysiol* **100,** 2361-2380.

Rudy B. (1978). Slow inactivation of the sodium conductance in squid giant axons. Pronase resistance. *J Physiol* **283,** 1-21.

Sachs HG, Stambrook PJ & Ebert JD. (1974). Changes in membrane potential during the cell cycle. *Exp Cell Res* **83,** 362-366.

Saint DA. (2008). The cardiac persistent sodium current: an appealing therapeutic target? *Br J Pharmacol* **153,** 1133-1142.

Sanchez-Sandoval AL & Gomora JC. (2019). Contribution of voltage-gated sodium channel beta-subunits to cervical cancer cells metastatic behavior. *Cancer Cell Int* **19,** 35.

Santos-Sacchi J. (1991). Isolated supporting cells from the organ of Corti: some whole cell electrical characteristics and estimates of gap junctional conductance. *Hear Res* **52,** 89-98.

Savio-Galimberti E, Gollob MH & Darbar D. (2012). Voltage-gated sodium channels: biophysics, pharmacology, and related channelopathies. *Front Pharmacol* **3,** 124.

Schickling BM, England SK, Aykin-Burns N, Norian LA, Leslie KK & Frieden-Korovkina VP. (2015). BKCa channel inhibitor modulates the tumorigenic ability of hormone-independent breast cancer cells via the Wnt pathway. *Oncol Rep* **33,** 533-538.

Schindelin J, Arganda-Carreras I, Frise E, Kaynig V, Longair M, Pietzsch T, Preibisch S, Rueden C, Saalfeld S, Schmid B, Tinevez JY, White DJ, Hartenstein V, Eliceiri K, Tomancak P & Cardona A. (2012). Fiji: an open-source platform for biological-image analysis. *Nat Methods* **9,** 676-682.

Schmidt D, Textor B, Pein OT, Licht AH, Andrecht S, Sator-Schmitt M, Fusenig NE, Angel P & Schorpp-Kistner M. (2007). Critical role for NF-kappaB-induced JunB in VEGF regulation and tumor angiogenesis. *EMBO J* **26,** 710-719.

Schnitt SaL, SR, World Health Organisation. (2014). *World Cancer Report*. International Agency for Research on Cancer, 150 cours Albert Thomas, 69372 Lyon Cedex 08, France.

Schrey M, Codina C, Kraft R, Beetz C, Kalff R, Wolfl S & Patt S. (2002). Molecular characterization of voltage-gated sodium channels in human gliomas. *Neuroreport* **13,** 2493-2498.

Selvik LK, Rao S, Steigedal TS, Haltbakk I, Misund K, Bruland T, Prestvik WS, Lægreid A & Thommesen L. (2014). Salt-inducible kinase 1 (SIK1) is induced by gastrin and inhibits migration of gastric adenocarcinoma cells. *PLoS One* **9,** e112485.

Sepp M, Sokolova N, Jugai S, Mandel M, Peterson P & Vendelin M. (2014). Tight coupling of Na+/K+-ATPase with glycolysis demonstrated in permeabilized rat cardiomyocytes. *PLoS One* **9,** e99413.

Sepp M, Vendelin M, Vija H & Birkedal R. (2010). ADP compartmentation analysis reveals coupling between pyruvate kinase and ATPases in heart muscle. *Biophys J* **98,** 2785-2793.

Shaikh S, Rizvi SM, Hameed N, Biswas D, Khan M, Shakil S & Kamal MA. (2014). Aptiom (eslicarbazepine acetate) as a dual inhibitor of beta-secretase and voltage-gated sodium channel: advancement in Alzheimer's disease-epilepsy linkage via an enzoinformatics study. *CNS Neurol Disord Drug Targets* **13,** 1258-1262.

Shannon P, Markiel A, Ozier O, Baliga NS, Wang JT, Ramage D, Amin N, Schwikowski B & Ideker T. (2003). Cytoscape: a software environment for integrated models of biomolecular interaction networks. *Genome Res* **13,** 2498-2504.

Shimizu H, Watanabe E, Hiyama TY, Nagakura A, Fujikawa A, Okado H, Yanagawa Y, Obata K & Noda M. (2007). Glial Nax channels control lactate signaling to neurons for brain [Na+] sensing. *Neuron* **54,** 59-72.

Shirahata E, Iwasaki H, Takagi M, Lin C, Bennett V, Okamura Y & Hayasaka K. (2006). Ankyrin-G Regulates Inactivation Gating of the Neuronal Sodium Channel, Nav1.6. *Journal of neurophysiology* **96**.

Shiraishi S, Yokoo H, Yanagita T, Kobayashi H, Minami S, Saitoh T, Takasaki M & Wada A. (2003). Differential effects of bupivacaine enantiomers, ropivacaine and lidocaine on up-regulation of cell surface voltage-dependent sodium channels in adrenal chromaffin cells. *Brain Res* **966,** 175-184.

Sinke AP, Caputo C, Tsaih SW, Yuan R, Ren D, Deen PM & Korstanje R. (2011). Genetic analysis of mouse strains with variable serum sodium concentrations identifies the Nalcn sodium channel as a novel player in osmoregulation. *Physiol Genomics* **43,** 265-270.

Sjöström M, Stenström K, Eneling K, Zwiller J, Katz AI, Takemori H & Bertorello AM. (2007). SIK1 is part of a cell sodium-sensing network that regulates active sodium transport through a calcium-dependent process. *Proc Natl Acad Sci U S A* **104,** 16922-16927.

Smith I, Greenside PG, Natoli T, Lahr DL, Wadden D, Tirosh I, Narayan R, Root DE, Golub TR, Subramanian A & Doench JG. (2017). Evaluation of RNAi and CRISPR Technologies by Large-Scale Gene Expression Profiling in the Connectivity Map. *PLoS biology* **15**.

Soares-da-Silva P, Pires N, Bonifácio MJ, Loureiro AI, Palma N & Wright LC. (2015). Eslicarbazepine acetate for the treatment of focal epilepsy: an update on its proposed mechanisms of action. *Pharmacol Res Perspect* **3**.

Sokolov S, Peters CH, Rajamani S & Ruben PC. (2013). Proton-dependent inhibition of the cardiac sodium channel Nav1.5 by ranolazine. *Front Pharmacol* **4,** 78.

Srinivasan J, Schachner M & Catterall WA. (1998). Interaction of voltage-gated sodium channels with the extracellular matrix molecules tenascin-C and tenascin-R. *Proc Natl Acad Sci U S A* **95,** 15753-15757.

Srinivasan Y, Elmer L, Davis J, Bennett V & Angelides K. (1988). Ankyrin and spectrin associate with voltage-dependent sodium channels in brain. *Nature* **333,** 177-180.

Stelzer G, Rosen N, Plaschkes I, Zimmerman S, Twik M, Fishilevich S, Stein TI, Nudel R, Lieder I, Mazor Y, Kaplan S, Dahary D, Warshawsky D, Guan-Golan Y, Kohn A, Rappaport N, Safran M & Lancet D. (2016). The GeneCards Suite: From Gene Data Mining to Disease Genome Sequence Analyses. *Curr Protoc Bioinformatics* **54,** 1.30.31-31.30.33.

Subik K, Lee JF, Baxter L, Strzepek T, Costello D, Crowley P, Xing L, Hung MC, Bonfiglio T, Hicks DG & Tang P. (2010). The Expression Patterns of ER, PR, HER2, CK5/6, EGFR, Ki-67 and AR by Immunohistochemical Analysis in Breast Cancer Cell Lines. *Breast Cancer (Auckl)* **4,** 35-41.

Subramanian A, Tamayo P, Mootha VK, Mukherjee S, Ebert BL, Gillette MA, Paulovich A, Pomeroy SL, Golub TR, Lander ES & Mesirov JP. (2005). Gene set enrichment analysis: a knowledge-based approach for interpreting genome-wide expression profiles. *Proc Natl Acad Sci U S A* **102,** 15545-15550.

Sukumar M, Liu J, Ji Y, Subramanian M, Crompton JG, Yu Z, Roychoudhuri R, Palmer DC, Muranski P, Karoly ED, Mohney RP, Klebanoff CA, Lal A, Finkel T, Restifo NP & Gattinoni L. (2013). Inhibiting glycolytic metabolism enhances CD8+ T cell memory and antitumor function. *J Clin Invest* **123,** 4479-4488.

Tajada S & Villalobos C. (2020). Calcium Permeable Channels in Cancer Hallmarks. *Front Pharmacol* **11,** 968.

Talhouk RS, Fares MB, Rahme GJ, Hariri HH, Rayess T, Dbouk HA, Bazzoun D, Al-Labban D & El-Sabban ME. (2013). Context dependent reversion of tumor phenotype by connexin-43 expression in MDA-MB231 cells and MCF-7 cells: role of beta-catenin/connexin43 association. *Exp Cell Res* **319,** 3065-3080.

Tamayo P, Steinhardt G, Liberzon A & Mesirov JP. (2016). The limitations of simple gene set enrichment analysis assuming gene independence. *Stat Methods Med Res* **25,** 472-487.

Teleki I, Szasz AM, Maros ME, Gyorffy B, Kulka J, Meggyeshazi N, Kiszner G, Balla P, Samu A & Krenacs T. (2014). Correlations of differentially expressed gap junction connexins Cx26, Cx30, Cx32, Cx43 and Cx46 with breast cancer progression and prognosis. *PLoS One* **9,** e112541.

Thurber AE, Nelson M, Frost CL, Levin M, Brackenbury WJ & Kaplan DL. (2017). IK channel activation increases tumor growth and induces differential behavioral responses in two breast epithelial cell lines. *Oncotarget* **8,** 42382-42397.

Tomayko MM & Reynolds CP. (1989). Determination of subcutaneous tumor size in athymic (nude) mice. *Cancer Chemother Pharmacol* **24,** 148-154.

Turk B, Dolenc I, Lenarcic B, Krizaj I, Turk V, Bieth JG & Bjork I. (1999). Acidic pH as a physiological regulator of human cathepsin L activity. *Eur J Biochem* **259,** 926-932.

Uebachs M, Opitz T, Royeck M, Dickhof G, Horstmann MT, Isom LL & Beck H. (2010). Efficacy loss of the anticonvulsant carbamazepine in mice lacking sodium channel beta subunits via paradoxical effects on persistent sodium currents. *J Neurosci* **30,** 8489-8501.

Uphoff CC, Gignac SM & Drexler HG. (1992). Mycoplasma contamination in human leukemia cell lines. I. Comparison of various detection methods. *J Immunol Methods* **149,** 43-53.

van Bemmelen MX, Rougier JS, Gavillet B, Apotheloz F, Daidie D, Tateyama M, Rivolta I, Thomas MA, Kass RS, Staub O & Abriel H. (2004). Cardiac voltage-gated sodium channel Nav1.5 is regulated by Nedd4-2 mediated ubiquitination. *Circ Res* **95,** 284-291.

van den Berg AP, Wike-Hooley JL, van den Berg-Blok AE, van der Zee J & Reinhold HS. (1982). Tumour pH in human mammary carcinoma. *Eur J Cancer Clin Oncol* **18,** 457-462.

van Geldermalsen M, Wang Q, Nagarajah R, Marshall AD, Thoeng A, Gao D, Ritchie W, Feng Y, Bailey CG, Deng N, Harvey K, Beith JM, Selinger CI, O'Toole SA, Rasko JEJ & Holst J. (2016). ASCT2/SLC1A5 controls glutamine uptake and tumour growth in triple-negative basal-like breast cancer. *Oncogene* **35,** 3201-3208.

Vander Heiden MG, Cantley LC & Thompson CB. (2009). Understanding the Warburg effect: the metabolic requirements of cell proliferation. *Science* **324,** 1029-1033.

Vassilev PM, Scheuer T & Catterall WA. (1988). Identification of an intracellular peptide segment involved in sodium channel inactivation. *Science* **241,** 1658-1661.

Vaz-Da-Silva M, Nunes T, Almeida L, Gutierrez MJ, Litwin JS & Soares-Da-Silva P. (2012). Evaluation of Eslicarbazepine acetate on cardiac repolarization in a thorough QT/QTc study. *J Clin Pharmacol* **52,** 222-233.

Vilin YY, Peters CH & Ruben PC. (2012). Acidosis differentially modulates inactivation in na(v)1.2, na(v)1.4, and na(v)1.5 channels. *Front Pharmacol* **3,** 109.

Vilin YY & Ruben PC. (2001). Slow inactivation in voltage-gated sodium channels: molecular substrates and contributions to channelopathies. *Cell Biochem Biophys* **35,** 171-190.

Voipio J, Pasternack M & MacLeod K. (1994). Ion-sensitive microelectrodes. In *Microelectrode Techniques; the Plymouth Workshop Handbook*, 2nd edn, ed. Ogden DC, pp. 275-316. The Company of Biologists Ltd, Cambridge.

Wagner S, Ruff HM, Weber SL, Bellmann S, Sowa T, Schulte T, Anderson ME, Grandi E, Bers DM, Backs J, Belardinelli L & Maier LS. (2011). Reactive oxygen species-activated Ca/calmodulin kinase IIδ is required for late I(Na) augmentation leading to cellular Na and Ca overload. *Circ Res* **108,** 555-565.

Wanajo A, Sasaki A, Nagasaki H, Shimada S, Otsubo T, Owaki S, Shimizu Y, Eishi Y, Kojima K, Nakajima Y, Kawano T, Yuasa Y & Akiyama Y. (2008). Methylation of the calcium channel-related gene, CACNA2D3, is frequent and a poor prognostic factor in gastric cancer. *Gastroenterology* **135,** 580-590.

Wang CY, Lai MD, Phan NN, Sun Z & Lin YC. (2015a). Meta-Analysis of Public Microarray Datasets Reveals Voltage-Gated Calcium Gene Signatures in Clinical Cancer Patients. *PLoS One* **10,** e0125766.

Wang HJ, Li YL, Zhang LB, Zucker IH, Gao L, Zimmerman MC & Wang W. (2011a). Endogenous reactive oxygen species modulates voltage-gated sodium channels in dorsal root ganglia of rats. *J Appl Physiol (1985)* **110,** 1439-1447.

Wang J, Ou SW & Wang YJ. (2017). Distribution and function of voltage-gated sodium channels in the nervous system. *Channels (Austin)* **11,** 534-554.

Wang W, Liu Y & Liao K. (2011b). Tyrosine phosphorylation of cortactin by the FAK-Src complex at focal adhesions regulates cell motility. *BMC Cell Biol* **12,** 49.

Wang YY, Zhao R & Zhe H. (2015b). The emerging role of CaMKII in cancer. *Oncotarget* **6,** 11725-11734.

Warburg O. (1925). The Metabolism of Carcinoma Cells. *J Cancer Res* **9(1),** 148:163.

Watson MB, Greenman J, Drew PJ, Lind MJ & Cawkwell L. (2004). *Variation between independently cultured strains of the MDA-MB-231 breast cancer cell line identified by multicolour fluorescence in situ hybridisation*, vol. 2.

Weigelt B, Peterse JL & van't Veer LJ. (2005). Breast cancer metastasis: markers and models. *Nature Reviews Cancer* **5,** 591-602.

Westenbroek RE, Merrick DK & Catterall WA. (1989). Differential subcellular localization of the RI and RII Na+ channel subtypes in central neurons. *Neuron* **3,** 695-704.

White KA, Grillo-Hill BK & Barber DL. (2017). Cancer cell behaviors mediated by dysregulated pH dynamics at a glance. *J Cell Sci* **130,** 663-669.

Wike-Hooley JL, van den Berg AP, van der Zee J & Reinhold HS. (1985). Human tumour pH and its variation. *Eur J Cancer Clin Oncol* **21,** 785-791.

Witte D, Ali N, Carlson N & Younes M. (2002). Overexpression of the neutral amino acid transporter ASCT2 in human colorectal adenocarcinoma. *Anticancer Res* **22,** 2555-2557.

Xiao ZC, Ragsdale DS, Malhotra JD, Mattei LN, Braun PE, Schachner M & Isom LL. (1999). Tenascin-R is a functional modulator of sodium channel beta subunits. *J Biol Chem* **274,** 26511-26517.

Xie Z, Kometiani P, Liu J, Li J, Shapiro JI & Askari A. (1999). Intracellular reactive oxygen species mediate the linkage of Na+/K+-ATPase to hypertrophy and its marker genes in cardiac myocytes. *J Biol Chem* **274,** 19323-19328.

Xu S, Liu C, Ma Y, Ji HL & Li X. (2016). Potential Roles of Amiloride-Sensitive Sodium Channels in Cancer Development. *Biomed Res Int* **2016,** 2190216.

Yamaci RF, Fraser SP, Battaloglu E, Kaya H, Erguler K, Foster CS & Djamgoz MBA. (2017). Neonatal Nav1.5 protein expression in normal adult human tissues and breast cancer. *Pathol Res Pract* **213,** 900-907.

Yamashita N, Hamada H, Tsuruo T & Ogata E. (1987). Enhancement of voltage-gated Na+ channel current associated with multidrug resistance in human leukemia cells. *Cancer Res* **47,** 3736-3741.

Yang M & Brackenbury W. (2013). Membrane potential and cancer progression. *Front Physiol* **4,** 185.

Yang M, James AD, Suman R, Kasprowicz R, Nelson M, O'Toole PJ & Brackenbury WJ. (2020). Voltage-dependent activation of Rac1 by Nav1.5 channels promotes migration. *J Cell Physiol* **235,** 3950-3972.

Yang M, Kozminski DJ, Wold LA, Modak R, Calhoun JD, Isom LL & Brackenbury WJ. (2012). Therapeutic potential for phenytoin: targeting Na(v)1.5 sodium channels to reduce migration and invasion in metastatic breast cancer. *Breast Cancer Res Treat* **134,** 603-615.

Yang X, Wang D, Dong W, Song Z & Dou K. (2011). Expression and modulation of Na(+) /H(+) exchanger 1 gene in hepatocellular carcinoma: A potential therapeutic target. *J Gastroenterol Hepatol* **26,** 364-370.

Yao L, Fan P, Jiang Z, Viatchenko-Karpinski S, Wu Y, Kornyeyev D, Hirakawa R, Budas GR, Rajamani S, Shryock JC & Belardinelli L. (2011). Nav1.5-dependent persistent Na+ influx activates CaMKII in rat ventricular myocytes and N1325S mice. *Am J Physiol Cell Physiol* **301,** C577-586.

Yarbrough TL, Lu T, Lee HC & Shibata EF. (2002). Localization of cardiac sodium channels in caveolin-rich membrane domains: regulation of sodium current amplitude. *Circ Res* **90,** 443-449.

Yarov-Yarovoy V, Baker D & Catterall WA. (2006). Voltage sensor conformations in the open and closed states in ROSETTA structural models of K(+) channels. *Proc Natl Acad Sci U S A* **103,** 7292-7297.

Yildirim S, Altun S, Gumushan H, Patel A & Djamgoz MB. (2012). Voltage-gated sodium channel activity promotes prostate cancer metastasis in vivo. *Cancer Lett* **323,** 58-61.

Yoon JY, Ho WK, Kim ST & Cho H. (2009). Constitutive CaMKII activity regulates Na+ channel in rat ventricular myocytes. *J Mol Cell Cardiol* **47,** 475-484.

Yu FH, Mantegazza M, Westenbroek RE, Robbins CA, Kalume F, Burton KA, Spain WJ, McKnight GS, Scheuer T & Catterall WA. (2006). Reduced sodium current in GABAergic interneurons in a mouse model of severe myoclonic epilepsy in infancy. *Nat Neurosci* **9,** 1142-1149.

Yu G, Wang LG, Han Y & He QY. (2012). clusterProfiler: an R package for comparing biological themes among gene clusters. *OMICS* **16,** 284-287.

Yuan P, Rao W, Lin Z, Liu S, Lin X, Wu C, Hu Z & Ye W. (2022). Genomic analyses reveal SCN7A is associated with the prognosis of esophageal squamous cell carcinoma. *Esophagus*.

Zaccara G, Giovannelli F, Cincotta M, Carelli A & Verrotti A. (2015). Clinical utility of eslicarbazepine: current evidence. *Drug Des Devel Ther* **9,** 781-789.

Zaric O, Pinker K, Zbyn S, Strasser B, Robinson S, Minarikova L, Gruber S, Farr A, Singer C, Helbich TH, Trattnig S & Bogner W. (2016). Quantitative Sodium MR Imaging at 7 T: Initial Results and Comparison with Diffusion-weighted Imaging in Patients with Breast Tumors. *Radiology* **280,** 39-48.

Zattarin E, Leporati R, Ligorio F, Lobefaro R, Vingiani A, Pruneri G & Vernieri C. (2020). Hormone Receptor Loss in Breast Cancer: Molecular Mechanisms, Clinical Settings, and Therapeutic Implications. *Cells* **9**.

Zhang C, Zuo Z, Kwan P & Baum L. (2011). In vitro transport profile of carbamazepine, oxcarbazepine, eslicarbazepine acetate, and their active metabolites by human P-glycoprotein. *Epilepsia* **52,** 1894-1904.

Zhang GH & Melvin JE. (1993). Membrane Potential Regulates Ca2+ Uptake and Inositol Phosphate Generation in Rat Sublingual Mucous Acini. *Cell calcium* **14**.

Zhao M, Song B, Pu J, Wada T, Reid B, Tai G, Wang F, Guo A, Walczysko P, Gu Y, Sasaki T, Suzuki A, Forrester JV, Bourne HR, Devreotes PN, McCaig CD & Penninger JM. (2006). Electrical signals control wound healing through phosphatidylinositol-3-OH kinase-gamma and PTEN. *Nature* **442,** 457-460.

Zhou D, Lambert S, Malen PL, Carpenter S, Boland LM & Bennett V. (1998). AnkyrinG is required for clustering of voltage-gated Na channels at axon initial segments and for normal action potential firing. *J Cell Biol* **143,** 1295-1304.

Zhou X, Ferraris JD, Cai Q, Agarwal A & Burg MB. (2005). Increased reactive oxygen species contribute to high NaCl-induced activation of the osmoregulatory transcription factor TonEBP/OREBP. *Am J Physiol Renal Physiol* **289,** F377-385.

Zhou Y, Wong CO, Cho KJ, van der Hoeven D, Liang H, Thakur DP, Luo J, Babic M, Zinsmaier KE, Zhu MX, Hu H, Venkatachalam K & Hancock JF. (2015). SIGNAL TRANSDUCTION. Membrane potential modulates plasma membrane phospholipid dynamics and K-Ras signaling. *Science* **349,** 873-876.

Zhou Z, Song J, Li W, Liu X, Cao L, Wan L, Tan Y, Ji S, Liang Y & Gong F. (2017). The acid-sensing ion channel, ASIC2, promotes invasion and metastasis of colorectal cancer under acidosis by activating the calcineurin/NFAT1 axis. In *J Exp Clin Cancer Res*.

Zhu G, Zhang L, Dan J & Zhu Q. (2020). Differential Effects and Mechanisms of Local Anesthetics on Esophageal Carcinoma Cell Migration, Growth, Survival and Chemosensitivity. *BMC anesthesiology* **20**.

Zhu S, Zhou H-Y, Deng S-C, Deng S-J, He C, Li X, Chen J-Y, Jin Y, Hu Z-L, Wang F, Wang C-Y & Zhao G. (2017). ASIC1 and ASIC3 contribute to acidity-induced EMT of pancreatic cancer through activating Ca/RhoA pathway. *Cell Death Dis* **8,** e2806.

Zirlik K & Duyster J. (2018). Anti-Angiogenics: Current Situation and Future Perspectives. *Oncol Res Treat* **41,** 166-171.

Zybura AS, Baucum AJ, Rush AM, Cummins TR & Hudmon A. (2020). CaMKII enhances voltage-gated sodium channel Nav1.6 activity and neuronal excitability. *J Biol Chem* **295,** 11845-11865.

Özerlat I. (2009). Effects of estrogen on voltage-gated sodium channel expression and function in human breast cancer cell lines. University of London, London, UK.